UNIVERSITY OF SOUTHAMPTON

Faculty of Engineering and Physical Sciences

Cell designs and methods for characterisation of lithium protective membranes, solid electrolytes and beyond

Nina Catherine Meddings

Thesis for the degree of Doctor of Philosophy

June 2020

UNIVERSITY OF SOUTHAMPTON

ABSTRACT

Faculty of Engineering and Physical Sciences

School of Chemistry

Doctor of Philosophy

Cell designs and methods for characterisation of lithium protective membranes, solid electrolytes and beyond

By Nina Catherine Meddings

Battery systems employing a lithium metal negative electrode are attractive due to their high theoretical specific energy. However, it is necessary to protect the lithium electrode from crossover species such as polysulfides in Li-S systems, redox mediators in Li-O_2 cells or dissolved cathode species in high voltage Li-ion batteries. Lithium conducting membranes and solid electrolytes can address this and other issues such as lithium dendrite growth. This work focuses on some of the key properties governing performance of such components: ion selectivity and transference number, interfacial resistance, and redox kinetics (mass transport of reactants and/or electron transfer). A number of novel cell designs and methods are developed for the evaluation of these properties. Firstly, a convenient, in-situ method is presented for evaluating the ability of membranes to block crossover species. The method employs a novel 'Swagelok' cell design equipped with a glassy carbon probe for voltammetric detection of crossover species, and is demonstrated using a model redox system. Building on this work, a cell design and method is presented for evaluating membrane selectivity and transference under operando conditions, that is, when a current is applied across the cell. By fitting of a simple analytical model to measurements with and without current, values are obtained for the diffusive permeability and transference number of crossover species in the membrane, and also for the lithium transference number in the case of highly selective membranes. Moving on to interfacial resistance, the rate of lithium ion transfer between a solid lithium conductor and liquid electrolytes is studied using 4-probe impedance measurements. An approach is illustrated for identifying the rate-limiting step, which may be desolvation of lithium ions or transport through a solid-liquid electrolyte interphase. Focusing next on the Li-S system, a Swagelok cell equipped with glassy carbon electrode is used to study solid polymer electrolytes for Li-S batteries, providing direct observation and measurement of polysulfide intermediates for the first time. Finally, a similar cell design is used to investigate the application of GITT to soluble redox reactants whose concentration is unknown, as is the case for polysulfides in Li-S batteries.

Contents

Academic Thesis: Declaration Of Authorship

Nina Catherine Meddings

Cell designs and methods for characterisation of lithium protective membranes, solid electrolytes and beyond

I declare that this thesis and the work presented in it are my own and has been generated by me as the result of my own original research.

I confirm that:

1. This work was done wholly or mainly while in candidature for a research degree at this University;

2. Where any part of this thesis has previously been submitted for a degree or any other qualification at this University or any other institution, this has been clearly stated;

3. Where I have consulted the published work of others, this is always clearly attributed;

4. Where I have quoted from the work of others, the source is always given. With the exception of such quotations, this thesis is entirely my own work;

5. I have acknowledged all main sources of help;

6. Where the thesis is based on work done by myself jointly with others, I have made clear exactly what was done by others and what I have contributed myself;

7. Either none of this work has been published before submission, or parts of this work have been published as:

- N. Meddings, J. R. Owen and N. Garcia-Araez, Journal of Power Sources, 2017, DOI: 10.1016/j.jpowsour.2017.08.004
- N. Meddings, J. R. Owen and N. Garcia-Araez, ChemElectroChem, 2018, DOI: 10.1002/celc.201801372.
- J. W. Dibden, N. Meddings, J. R. Owen and N. Garcia-Araez, ChemElectroChem, 2017, DOI: 10.1002/celc.201701004

Signed: ……

Date: …….

Acknowledgements

I would like to thank my supervisors, Dr. Nuria Garcia-Araez and Prof. John Owen, for giving me the opportunity to work with them, and for their guidance, support and encouragement throughout my PhD. I am grateful to them for making it such an enjoyable and rewarding experience. The same goes for past and present members and visitors of the Garcia-Araez/Owen research group, especially Jimmy for all his help at the beginning, Mike, Will; James and Tom, my conference buddies in Japan; Dan, Liam, Rinaldo and Vivek, Sam, Niamh and everyone else in this and the wider Southampton Electrochemistry Group. Thanks for your help in the lab, scientific discussions, tea-break crosswords, group meals and generally being such a friendly and supportive bunch. Thank you to the machinists and glass-blowers in the Chemistry department, especially Alan, Shamack and Lee for putting the designs in this thesis into practise, and to the team at CIC Energigune for allowing me to test their polymer electrolytes. Thanks also to everyone involved with the Energy Storage CDT, especially my fellow students in the first cohort. Special thanks to Tom for helping out with emergency accommodation (!) and to my eventual Avenue Place flatmates for sharing a home from home over the last three years. Thank you to all my friends for sticking with me along the way (especially during the reclusive final months!) and last but by no means least, to my family and Kevin for the love and support that has made it all possible.

I would also like to acknowledge the UK Engineering and Physical Sciences Research Council (EPSRC) for financial support through the Centre for Doctoral Training in Energy Storage and its Applications (Grant No. EP/L016818/1).

Abbreviations

General abbreviations

BV	Butler Volmer
CV	cyclic voltammogram
DBBQ	di-tert-butyl benzoquinone
DC	direct current
DEC	diethyl carbonate
DMC	dimethyl carbonate
DME	1,2-dimethoxyethane (diglyme)
DoD	depth of discharge
DOL	1,3-dioxolane
EC	ethylene carbonate
EDX	energy dispersive x-ray spectroscopy
EIS	electrochemical impedance spectroscopy
EO	ethylene oxide
EtV	ethyl viologen
FEP	fluorinated ethylene propylene
GC	glassy carbon
GITT	galvanostatic intermittent titration technique
HPLC	high performance liquid chromatography
LAGP	$Li_{1.5}Al_{0.5}Ge_{1.5}(PO_4)_3$
LATP	$Li_{1+x}Al_xTi_{2-x}(PO_4)_3$
Li-S	lithium-sulfur
LIB	lithium ion battery
LICGC	lithium-ion conducting glass ceramic
LICM	lithium ion conducting membrane
LiPON	lithium phosphorous oxy-nitride
LISICON	lithium super ionic conductor
LiS_n	lithium polysulfide of chain length n
LiTFSI	lithium (bis)trifluoromethanesulfonylimide
LLTa	$Li_5La_3Ta_2O_{12}$
LLTO	$Li_{3x}La_{(2/3)-x}TiO_3$
LLZO	$Li_7La_3Zr_2O_{12}$
MOF	metal organic framework
NASICON	sodium (Na) super ionic conductor
NMR	nuclear magnetic resonance
OER	oxygen evolution reaction
OCP/OCV	open-circuit potential/open-circuit voltage
ORR	oxygen reduction reaction
OTf	triflate
PC	polyethylene carbonate
PEO	polyethylene oxide
PPO	polyphenylene oxide

PTFE	polytetrafluoroethylene
PVdF	polyvinylidene fluoride
Pyr14TFSI	1-butyl-1-methylpyrrolidinium bis(trifluoromethanesulfonyl)imide
SEI	solid electrolyte interphase
SEM	scanning electron microscopy
SLEI	solid-liquid electrolyte interphase
SPE	solid polymer electrolyte
SWV	square wave voltammetry
TEGDME	tetraethylene glycol dimethyl ether (tetraglyme)
TEM	transmission electron microscopy
TTf	tetrathiafulvalene
UV-vis	ultraviolet-visible spectroscopy
XANES	x-ray absorption near-edge spectroscopy
XAS	x-ray absorption spectroscopy
XPS	x-ray photoelectron spectroscopy
XRD	x-ray diffraction

Mathematical symbols and subscripts

$_a$	anodic
A	area
$_c$	cathodic or crossover species
c	concentration
C	capacitance
c^*	initial or bulk concentration
CPE	constant phase element
$_{ct}$	charge transfer
D	diffusion coefficient
$_{dl}$	double layer
e^-	electron
E	potential
$E_{1/2}$	half-wave potential
$E_{p/2}$	half-peak potential
E_e	equilibrium potential
E°	standard electrode potential
$E^{0'}$	formal potential
f	frequency
F	Faraday's constant (96485 C mol^{-1})
i	current
I	current density
I_0	exchange current density
j	square root of -1
J	flux
k^0	standard rate constant

K	sorption coefficient
l	liquid electrolyte
L	thickness / distance between phase boundaries or inductance
m	membrane
m	molality
M	molarity
n	number of electrons involved in electrode reaction or number of moles crossing membrane
O	oxidised species
q/Q	charge
p	peak or pulse
P_m	diffusive permeability of membrane
R	reduced species, resistance or ideal gas constant (8.314 J K^{-1} mol^{-1})
s	step
T	Temperature
T_x	transport number
t	time
t_p	pulse duration in square wave voltammetry
t_x	transference number
V	voltage or volume
wt%	percentage by mass
x	distance into the electrolyte from the electrode/electrolyte interface
z	charge number
Z	impedance
Z_W	Warburg impedance
α	transfer coefficient or CPE exponent
γ	Walden exponent ($0 \leq \gamma \leq 1$)
Δ	change in or difference
η	overpotential
Λ	molar conductivity
ν	scan rate
ρ	resistivity
σ	conductivity or Warburg coefficient
τ	time constant, transition time or duration of current pulse
φ	potential within phase
ω	angular frequency

Units

Prefixes to units: M = mega (10^6), k = kilo (10^3), d = deci (10^{-1}), c = centi (10^{-2}), m = milli (10^{-3}), µ = micro (10^{-6}), n = nano (10^{-9})

A	ampere
F	farad
g	gram
h	hour

J	Joule
K	kelvin
L	litre
m	metre or molal (mol kg^{-1})
M	molar (mol dm^{-3})
min	minute
Pa	pascal
ppm	parts per million
s	second
S	siemens
V	volt
W	watt
Ω	ohm

1 Introduction

1.1 Fundamentals of electrochemical energy storage

Portable energy storage is an essential part of today's society, whose role is set to increase in the future with the increasing electrification of transport as an alternative to polluting internal combustion engines, as well as ever-growing demand for mobile IT devices.[1-5]

Batteries are energy storage devices able to convert chemical energy to electrical energy, and vice versa in the case of secondary (rechargeable) batteries. Commercial batteries consist of a number of individual electrochemical cells, each of which contains two electrodes separated by an electrolyte. During discharge, the active material at the negative electrode (i.e. the electrode with the more negative electrochemical potential) is oxidised, transferring electrons via an external circuit to the positive electrode (i.e. the electrode with the more positive electrochemical potential), where reduction occurs. Positive ions pass through the electrolyte in the same direction, to maintain charge neutrality. The opposite process happens during charge.[1, 2, 6]

Although strictly speaking the anode in an electrochemical cell refers to the electrode being oxidised and the cathode to the one being reduced, which in the case of a rechargeable battery depends on whether it is being charged or discharged, the terms anode and cathode are generally applied to the negative electrode and positive electrode respectively.[7]

The open circuit voltage, or equilibrium potential, of the cell is determined by the difference in the electrochemical potential of each electrode:[2, 6, 8, 9]

$$E_{cell} = E_a - E_c \qquad \text{(Eq. 1.1)}$$

The cell potential is related to the Gibbs free energy of the overall reaction taking place: [6, 8, 9]

$$\Delta G = -nFE_{cell} \qquad \text{(Eq. 1.2)}$$

where n is the number of electrons transferred.

During operation, kinetic or mass transport limitations of the reactions as well as Ohmic losses from internal cell resistance reduce the output voltage during discharge and increase the voltage required to charge the cell, relative to the equilibrium potential.[2, 6] These effects will be larger at higher currents or C-rates (where xC means a full (dis)charge in 1/x hours).[6]

The theoretical capacity of each electrode (i.e. the amount of charge that can be stored, in Coulombs or mA h) is given by:[6]

$$Q_{theoretical} = nFm \quad \text{(Eq. 1.3)}$$

where m is the number of moles of active species present.

The amount of energy that can be stored by the cell is the product of the cell voltage and capacity, and is generally expressed in terms of the mass (specific energy, W h kg^{-1}) or volume (energy density, W h L^{-1}), of either the active materials, electrodes, or of the cell as a whole.

As with voltage, the amount of charge that is stored/released during charge/discharge may be affected by kinetic or mass transport limitations of the electrode reactions. The energy available from a fully charged cell for a given discharge current is given by[2, 6]:

$$energy = \int_0^{\Delta t} IV(t)dt = \int_0^{Q} V_{dis}(q)dq \quad \text{(Eq. 1.4)}$$

Where V is the cell voltage, Δt is the time required for full discharge, Q is the total charge obtained and q represents state of charge.

The energy efficiency of a single charge/discharge cycle is given by:[2, 6]

$$\frac{\int_0^{Q} V_{dis}(q)dq}{\int_0^{Q} V_{ch}(q)dq} \quad \text{(Eq. 1.5)}$$

The Coulombic efficiency is simply the ratio of charge output to charge input:[2, 6]

$$\frac{Q_{dis}}{Q_{ch}} \quad \text{(Eq. 1.6)}$$

Coulombic efficiency may be less than unity due to parasitic electrode-electrolyte reactions or to electrode volume or other changes during cycling, leading to irreversible capacity fade. The cycle life of a cell is the number of cycles until the cell fails, or the capacity falls to a given percentage of its initial value. Energy density/specific energy, rate performance, energy efficiency, Coulombic efficiency and cycle life are all key figures of merit for rechargeable batteries, along with cost and safety.[2-4, 6]

1.2 Lithium ion batteries

Since their commercialisation by Sony in 1991, lithium ion batteries (LIBs) have become ubiquitous in portable electronics and also power today's electric and hybrid vehicles, as well as finding application in stationary energy storage. State-of-the-art cells can reach a specific capacity

of ~250 Wh kg^{-1}.[10] LIBs are based on the intercalation (insertion) of lithium ions within crystalline host electrodes. The majority of modern cells consist of a graphite negative electrode and a metal oxide or phosphate positive electrode with either layered ($LiMO_2$, M = Co, Ni, Mn), spinel ($LiMn_2O$) or olivine ($LiFePO_4$) structures.[2, 3]

Graphite has a theoretical capacity of 372 mA h g^{-1} (corresponding to one Li ion per six carbon atoms) and a redox potential close to that of Li/Li^+ (~0.1 V vs Li/Li^+).[11] At this potential, the electrolytes employed (typically 1 M $LiPF_6$ in a mixture of carbonate solvents) are thermodynamically unstable towards reduction; however the formation of a self-limiting layer (the solid-electrolyte interphase or SEI, comprising a mosaic of inorganic and organic reduction productions) during the first cell charge allows stable operation.[11-15] Silicon, which undergoes an alloying (rather than intercalation) reaction with lithium, has been investigated as an alternative anode material due to its high theoretical capacity (>4,000 mAh g^{-1}). However the huge volume changes that take place during lithiation/delithiation lead to pulverisation of the active material and an unstable SEI, severely hampering cycle life. Blending Si (typically <5wt%) with graphite has been used to give modest increases in the charge storage capacity of practical cells.[3, 4]

Amongst positive electrode materials, the layered structures give the highest capacities, with $LiNi_{1/3}Mn_{1/3}Co_{1/3}O_2$ (NMC111) a common representative.[3, 4] However, its sloping potential profile means that only half the lithium can be removed below ca. 4.3 V, giving a practical capacity of ca. 150 mA h g^{-1}, well below the theoretical value of ca. 275 mA h g^{-1}. Above this, the cathode-electrolyte interface is not stable. Additionally, structural instabilities prevent further removal of lithium.[16-18] Layered Ni-rich have been investigated since they allow more lithium to be extracted within the same voltage window, giving capacities up to 220 mAh g^{-1}, but structural (cation mixing, phase transition) and chemical (transition metal dissolution, electrolyte attack) instabilities continue to affect cycle life.[3, 4, 16-20] Li- and Mn-rich layered oxides offer even higher capacity linked to the contribution of reversible oxygen redox activity, but suffer from voltage degradation during cycling.[4, 21] Strategies including doping, surface coating and concentration-gradient structures are being explored to address these issues.[3, 4, 20, 21] High voltage cathodes such as the ordered spinel $LiNi_{0.5}Mn_{1.5}O_4$ (LNMO), which has a flat nominal voltage profile around 4.7 V, are another avenue of research for increasing the energy density of LIBs, but also suffer from transition metal dissolution and electrolyte oxidation. Surface coatings, electrolyte additives which induce a stable CEI (cathode electrolyte interphase) layer, or solid electrolytes are possible routes for preventing these degradation mechanisms.[3, 4, 22]. As well as degradation of the cathode active material, crossover/shuttling of dissolved transition metal cations and electrolyte oxidation products can also have deleterious effects on the anode.[23] Functional separators which block this

crossover have therefore also been explored, e.g. using a Li^+/Mn^{2+} ion-exchangeable lithiated Nafion coating as a Mn^{2+} capturing layer applied to a conventional polypropylene separator. [24]

1.3 Next generation lithium batteries

Whilst further improvements to LIBs can be made, ultimately their energy density is limited by the theoretical capacity of intercalation materials. Matching the range of electric vehicles with conventional ones will require an increase in energy density beyond what is possible for LIBs. One solution is to replace the graphite anode in LIBs with lithium metal, whose theoretical specific capacity is over ten times higher (3860 mAh g^{-1} cf. 372 mAh g^{-1}). [5, 10, 25] However, formation of dendrites on the lithium surface during charging can lead to short circuits, which, combined with the use of flammable organic electrolyte solvents, presents a serious fire hazard.[26] Dendrite growth also leads to active material loss through continuous regeneration of the SEI which forms spontaneously on the lithium metal surface.[12] At the same time, cracking of the SEI due to volume changes during cycling promotes dendrite growth.[10]

Much effort has been directed at mitigating these issues using strategies such as electrolyte additives, highly concentrated electrolytes, solid electrolytes (polymer, ceramic, composite), lithium protective coatings, as well as nano-structuring of the anode. These strategies are designed, variously, to prevent concentration gradients, a precursor to dendrite formation, from developing in the cell (e.g. in the case of highly concentrated electrolytes and single-ion conducting solid electrolytes), to promote uniform current flux (e.g. in the case of electrolyte additives, which alter the physico-chemical properties of the SEI, or lithium protective coatings which form a uniform, artificial SEI), to minimise local current density (e.g. in the case of anode structuring to increase surface area), or to physically block dendrite propagation as well as to mitigate safety hazards if dendrites do lead to short circuit (e.g. in the case of non-flammable solid electrolytes).[10, 25-29] Examples of each of these approaches are discussed in the following sections.

Besides employing a lithium metal anode, a further step-change in theoretical energy density relative to LIBs can be achieved by replacing the intercalation reaction at the cathode with a conversion reaction.[5, 25] Two chemistries in particular – lithium-sulfur and lithium-oxygen – have been intensively researched in recent years and are discussed next.

1.4 Lithium-sulfur batteries

The overall redox reaction for Li-S cells is:

$$S_8 + 16Li^+ + 16e^- \leftrightarrow 8Li_2S \qquad \text{(Eq. 1.7)}$$

The average voltage of the redox reaction is 2.15 V vs. Li. This is lower than for lithium intercalation into positive electrode materials, but, since the sulfur cathode has the highest theoretical specific capacity of all known solid cathodes (1672 mAh g^{-1}), Li-S cells still offer a significantly higher theoretical energy density than conventional LIBs (~2500 W h kg^{-1} by weight, ~2800 W h l^{-1} by volume of active materials). (The real values are lower as conductive additives such as carbon must be combined with the insulating sulfur and Li_2S end products.) Another advantage of Li-S batteries is low cost, since sulfur is an abundant and cheap natural material.[30, 31]

A typical discharge profile in an organic electrolyte is shown in Figure 1.1 and exhibits two clear plateaus. Although the mechanisms are still not well understood, the first plateau, typically between 2.4 and 2.2 V, is usually attributed to reduction of sulfur to long chain, soluble polysulfide species. The second plateau at ca. 2.1 V is associated with reduction of these species to shorter chain polysulfides and eventual precipitation of Li_2S. In addition to electrochemical reduction, various chemical association and dissociation reactions are known to take place between polysulfide species. On charge, a small knee in the voltage profile signals oxidation of solid Li_2S to lithium polysulfides, which are then oxidised to S_8^{2-} over a long plateau at ~2.3 V, before the last step at 2.4 V, during which S_8^{2-} is oxidised to S_8.[31, 32]

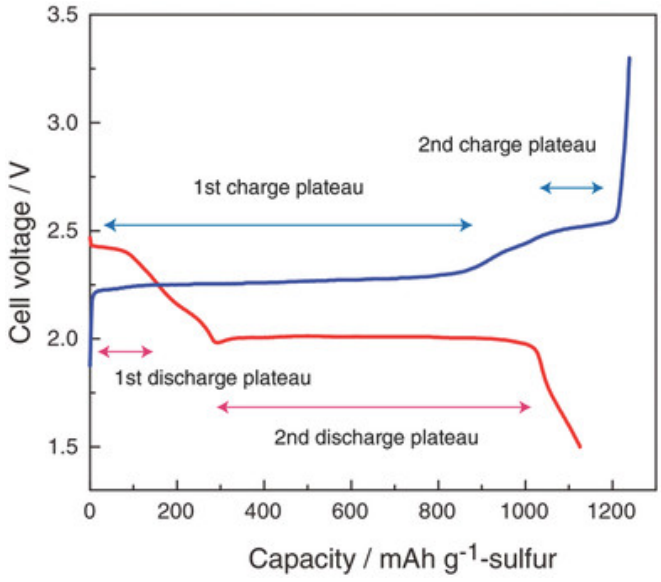

Figure 1.1: Typical charge–discharge curves of Li–S cell with 1 M LiTFSI in TEGDME. Reproduced with permission.[33] Copyright (2015) Wiley.

Whilst it offers several advantages, the Li-S cell also presents some challenges in additional to those discussed already in relation to lithium metal anodes. The insoluble and

insulating nature of the discharge product leads to passivation and loss of active material at the cathode, resulting in capacity fade. Loss of active material and capacity fade also arises due to large volume changes at the cathode during cycling. All these issues are exacerbated at the high sulfur loadings (ca. 7 mg cm^{-2}) that are needed for Li-S cells to exhibit the high energy density and low cost required for transport applications, [34] due to difficulties in creating a continuous conduction pathway over thick cathodes and in protecting the anode from dendrite formation at high currents.[35, 36] Perhaps the most serious problem, however, is the solubility of the long chain polysulfide intermediates (S_n^{2-}) which can diffuse through the separator from the sulfur cathode to the lithium metal anode. Here they are reduced to insoluble Li_2S or Li_2S_2, leading to passivation and loss of active material at the anode. Moreover, further S_n^{2-} react with the fully reduced sulfides to form lower order polysulfides (S_{n-x}^{2-}) which become concentrated at the anode side, diffuse back to the cathode and are then re-oxidized into S_n^{2-}. This parasitic process takes place repeatedly, creating an internal 'shuttle' which leads to low Coulombic efficiency and problems with self-discharge (although it does also provide protection against overcharge).[31, 32, 37-39]

Approaches for preventing the polysulfide shuttle include trapping polysulfides within the cathode, using electrolytes with limited polysulfide solubility, using electrolyte additives to create a protective barrier on the lithium electrode and prevent reaction with polysulfides, or employing a barrier (functional separator) to prevent cross-over.[33, 35, 40, 41]

Whilst physically confining polysulfides in a porous carbon host has been demonstrated, this is typically effective only for a few hundred cycles; moreover, a large electrolyte volume is required to wet the porous carbon, reducing the cell energy density. For these reasons, host materials that show strong chemical interactions with polysulfides have also been explored as a route to longer term cycling stability.[35, 42]

In the area of electrolyte design, electrolytes with low polysulfide solubility may be used as an alternative to conventional ether-based ones. Examples include room-temperature ionic liquids[43] and highly-concentrated 'solvent-in-salt' electrolytes.[44] As well as suppressing the polysulfide shuttle, both show high electrochemical stability, and are non-flammable and non-volatile; ultra-concentrated electrolytes can additionally suppress dendrite formation.[44] However, rate capability in both cases is relatively poor due to relatively low Li^+ conductivity. Use of electrolytes with high polysulfide solubility (and thus enhanced reaction kinetics), coupled with a protected lithium anode, may therefore be preferable for high performance cells.[33, 35, 45, 46] $LiNO_3$ is commonly used as an additive in ether-based electrolytes to create a protective film on the lithium anode surface[47, 48], though its irreversible reduction can occur at voltages below 1.8 V with adverse effects on cathode reversibility.[49] A kinetically stable Li_3N protection layer formed on the

surface of the Li anode by direct reaction with N_2 gas has also been shown to suppress the polysulfide shuttle.[50]

An alternative means for protecting the anode is the use of a functional separator or interlayer. Examples employed in Li-S cells include lithium-selective membranes[28, 51] (e.g. lithiated Nafion, whose sulfonate groups allow transport of Li^+ but not polysulfides[52-55]), polysulfide-capturing (e.g. carbon-based[56, 57]) coatings or a combination of these approaches[58, 59], whilst coating of a polypropylene separator with an inorganic solid electrolyte material (LAGP) has also been demonstrated.[60] In all cases, polysulfides are (to varying degrees) localised on the cathode side resulting in enhanced Coulombic efficiency and cycle performance.[28, 61] It is worth mentioning that the ability of such membranes to block crossover of polysulfides has generally relied on ex-situ analysis, typically via visual inspection or spectroscopic analysis of electrolytes in (or from) a two-compartment, H-type cell[52, 60, 62, 63], whilst only a handful of studies have used in-situ electrochemical approaches.[64-68]

Starting with Li_2S–P_2S_5 glass–ceramic[69], inorganic solid electrolytes have also been explored for Li-S cells, as they can prevent the dissolution and diffusion of polysulfides, as well as avoiding safety issues associated with liquid electrolytes. The main challenges are achieving acceptable room-temperature conductivity and, in all-solid-state cells, forming an effective solid-electrolyte/solid-electrode interface for electrochemical reactions, which affects rate capability, sulfur utilisation and cyclability.[33, 70, 71] A hybrid approach, where inorganic Li-ion conductors are combined with a liquid electrolyte, offers a potential solution.[70, 72] For example, a hybrid cell employing a garnet (LLZO) solid electrolyte with 1 M LiTFSI in DOL-DME liquid electrolyte, with sulfur loading of 1.2 g cm^{-2}, delivered capacities of ~1000 mAh g^{-1} (sulfur) and 550 mAh g^{-1} (sulfur) at C/8 and C/2 respectively, with close to 100% Coulombic efficiency and negligible capacity fade over 60 cycles at the lower rate. Polysulfides in the liquid electrolyte were found to react with the garnet forming a ~5 nm thick interphase which served as a protective layer to prevent further reaction.[73] On the other hand, lithium polysulfide solution in contact LATP was found to react to form a surface layer of Li_2CO_3 blocking lithium-ion transport between the liquid and solid electrolytes. Moreover, lithiation of the LATP caused anisotropic expansion of the crystal structure, leading to cracking and corrosion of grain boundaries and allowing polysulfide diffusion from the cathode to anode side of the cell.[74] Clearly, for the hybrid approach to be viable, the solid and liquid electrolytes must be stable in contact, as well as having a low interfacial resistance.[72] This interfacial resistance may stem from the formation a solid electrolyte-liquid electrolyte interphase as well as the activation barrier for lithium ion transfer between the liquid and the solid phase, which necessarily involves a (de-)solvation step.[72, 75] For both functional

separator and hybrid electrolyte approaches, the additional layers should be thin, in order to minimise associated reductions in energy density, as well as low-cost.[76]

Polymer electrolytes have attracted considerable attention as a means to suppress the polysulfide shuttle, as well as increasing safety relative to liquid electrolytes.[77] Polymer electrolytes reported for Li-S cells typically comprise PEO as a base polymer and LiTFSI as the conducting salt.[37] Their main drawback is low conductivity at room temperature, resulting in Li–S batteries with relatively low reversible capacity and rate performance.[33] The addition of inactive or active fillers to improve the conductivity of solid polymer electrolytes in general has been explored.[78] Recently, a Li-S cell with bilayer PEO-LiTFSI electrolyte containing Al_2O_3 filler on the anode side and LATP filler on the cathode side was demonstrated. No enhancement in conductivity was found, but the Al_2O_3 filler was found to reduce the Li/electrolyte interface resistance, whilst the LATP filler improved sulfur utilisation and areal capacity.[78] Polymer gel electrolytes, where large amounts of liquid electrolyte are immobilized in a polymer matrix, show higher conductivity, but suffer greater capacity fade during cycling, as the high liquid content facilitates polysulfide dissolution and diffusion.[33, 37] On the other hand, a thin gel polymer coating on the solid electrolyte was used to improve interfacial contact with the lithium electrode in a high-energy density Li-S battery employing a 3-D bilayer garnet solid electrolyte, with a sulfur cathode loading >7 mg cm^{-2} and Coulombic efficiency >99%.[79]

Interestingly, although the mechanisms of Li-S redox reactions in liquid electrolytes have been studied extensively[32, 80], there have been few studies on polysulfide chemistry in solid polymer electrolytes. Marceau et al[81] used in-operando SEM and UV-vis spectroscopy to study a cell with PEO-based electrolyte containing 7 wt% $LiClO_4$ and 12 wt% SiO_2 nanoparticles, whilst Wujcik et al[82] used XAS to study Li-S cells containing a diblock copolymer electrolyte polystyrene-poly(ethylene oxide) with $LiClO_4$ (Li:EO = 0.085). To the author's knowledge there have been no studies employing electrochemical techniques.

1.5 Lithium-oxygen batteries

In lithium-oxygen batteries, energy is released via the reaction between lithium and oxygen. The latter can, in theory, come from the air rather than being carried on-board. Theoretical specific energy of up to 11,426 Wh kg^{-1} based on the mass of lithium alone has therefore been quoted. However, the mass of the battery will increase significantly during discharge and more realistic figures for specific energy take the mass of the discharge product into account.[83] The discharge product varies depending on the electrolyte system. In aprotic

electrolytes, the main discharge product is lithium peroxide, giving a theoretical specific energy in the discharged state of 3,457 Wh kg^{-1}:

$2Li + O_2 \leftrightarrow Li_2O_2$ E^0 = 2.959 V (Eq. 1.8)

An alternative discharge product in aprotic electrolytes is Li_2O (Eq. 1.9), whilst in aqueous electrolytes the main discharge product is lithium hydroxide (Eq. 1.10):

$2Li + ½ O_2 \leftrightarrow Li_2O$ E^0 = 2.913 V (Eq. 1.9)

$4Li + 6H_2O + O_2 \leftrightarrow 4(LiOH \cdot H_2O)$ E^0 = 2.982 V (Eq. 1.10)

Aprotic electrolytes tend to be favoured as they have a wider voltage stability window, and avoid the need to protect the lithium electrode from violent reaction with water (see below).[83] A schematic of a Li-O_2 cell with aprotic electrolyte is shown in Figure 1.2.

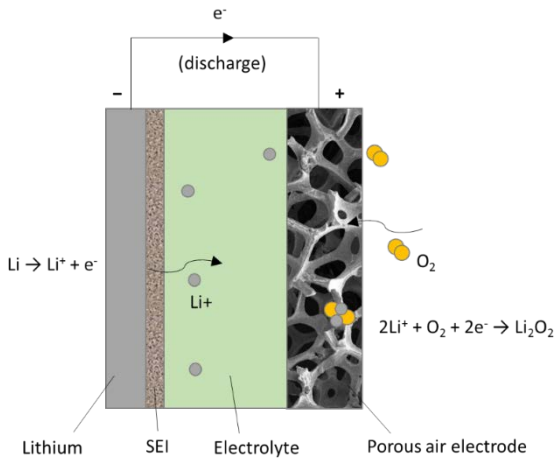

Figure 1.2: Schematic of Li-O_2 cell

Whilst promising, Li-O_2 batteries currently suffer from a number of issues. Passivation of the oxygen electrode in aprotic electrolytes by insoluble and electrically insulating Li_2O_2 leads to lower discharge voltage as a result of IR drop, and to reduced battery capacity and eventual failure as the oxygen electrode pores are irreversibly filled with discharge product. Significant overpotentials for both the oxygen reduction reaction (ORR) and the oxygen evolution reaction (OER) lead to low round trip efficiency, decreased specific energy and power, and degradation of solvents and oxygen electrode materials as a result of high charge voltages.[83-89]

Electrolyte degradation may also occur as a result of attack by superoxide radical anions during discharge. Rather than direct formation of Li_2O_2 via a 2-electron transfer, the discharge reaction mechanism can involve formation of lithium superoxide as an intermediate:[87, 89, 90]

$Li + O_2 \leftrightarrow LiO_2$ (Eq. 1.11)

$LiO_2 + Li \leftrightarrow Li_2O_2$ (Eq. 1.12)

$2LiO_2 \leftrightarrow Li_2O_2 + O_2$ (Eq. 1.13)

Various solutions to these issues have been proposed. For discharge, incorporation of catalysts into the air electrode can promote reduction of superoxide to peroxide, reducing the superoxide lifetime and allowing a wider range of electrolyte and electrode materials. However, it also speeds up passivation of the oxygen electrode by Li_2O_2.[87] An alternative is the use of redox shuttles, proposed and demonstrated by Owen et al using ethyl violgen.[91] These are soluble redox active species which are reduced at the electrode surface and diffuse into the liquid electrolyte where they, in turn, reduce oxygen (and are regenerated into their oxidised form). Redox shuttles or mediators have also been widely studied for reducing the overpotential of the charge reaction.[84, 90, 92, 93]. Inclusion of shuttles/mediators could, however, lead to problems similar to polysulfide shuttling in Li-S cells, and some form of lithium protection is likely to be required in Li-O_2 cells also[94, 95] (for example, a MOF-based separator in conjunction with a dual-mediator system (DBBQ for ORR mediation and TTF for OER mediation) was recently demonstrated)[96]. In fact, this is the case even without redox mediators, to protect against crossover of dissolved oxygen or mositure.[97-99] The concept of the protected lithium electrode for lithium-air batteries was proposed by Visco et al of PolyPlus Battery Company.[100] It also offers an alternative to the use of mediators for addressing the slow oxygen redox kinetics in non-aqueous electrolytes, by allowing the use of an aqueous electrolyte on the cathode side, separated from the anode by a solid state electrolyte.[101, 102] An additional layer of organic, ionic liquid or polymer electrolyte may be used between the lithium metal and solid state electrolyte in hybrid cells, either to reduce interfacial resistance[103, 104], or where the latter is not stable in contact with lithium (as in the case of the frequently used LATP).[5, 70, 99, 102, 105]

Solid rather than liquid electrolytes may also be used to improve safety and suppress dendrite formation in Li-O_2 cells and all solid-state cells have been demonstrated for Li-O_2 cells using both polymer and ceramic electrolytes.[70, 106, 107] Recently, a hybrid polymer-ceramic solid electrolyte, combining the mechanical stability of the former with the higher ionic conductivity of the latter, was demonstrated in a cell operated at 50 °C, and showed a cycle life of 350 cycles at 1000 mAh g^{-1}(Li_2O_2), although energy efficiency was relatively low (68% initially, falling to 57%).[108]

1.6 Membranes, thin films and solid electrolytes in lithium metal batteries

As discussed, lithium protective membranes, coatings or solid electrolytes may be used to protect the lithium electrode in lithium metal batteries. The term membrane is used here to mean a self-standing structure in contact with liquid (or polymer) electrolyte on both sides. Depending on the stability of the material towards lithium, however, it may be used directly against the negative electrode (with liquid electrolyte on the positive electrode side only). In this case, the material may be deposited as a thin film onto the lithium (or vice versa) in order to improve interfacial contact. Alternatively, a completely solid-state battery may be constructed by using the material as a solid electrolyte. Many of the key materials requirements are the same for all of these formats and include high Li^+ conductivity, high Li^+ transference number, high ion selectivity, low electronic conductivity, wide electrochemical stability window, high chemical stability towards and low interfacial resistance with electrolytes and/or electrodes, good thermal and mechanical stability, low cost and environmental impact, and easy fabrication and device integration.[26, 70, 109]

Good conductivity, both bulk and interfacial, is essential for efficient battery operation since any kind of internal cell resistance will decrease the discharge voltage and increase the voltage required for charge, thus reducing energy efficiency, power output and practical charge capacity (e.g. as a result of reaching cut-off voltages early).[6] Some recent studies have suggested that in hybrid electrolyte systems, the formation of a resistive solid-liquid electrolyte interphase could dominate the overall cell impedance, providing a much larger contribution than de-solvation at lithium concentrations relevant for battery operation (ca. 1 M).[72, 75]

A number of materials exhibit good Li^+ conductivity, including inorganic oxides (perovskite-type, NASICON-type, garnet-type, and γ-Li_3PO_4), non-oxide inorganic compounds (e.g. sulfides) and polymers/polymer-ceramic composites. Inorganic materials may be crystalline (ceramic), glassy or glass-ceramic.[110] The mechanism for Li^+ conduction varies depending on the type of material e.g. in crystalline oxides, Li^+ ions migrate via vacant and/or interstitial sites with conductivity dependent on crystal structure and lattice parameters; in polymers Li^+ conductivity arises from short-range ionic hopping enabled by local liquid-like relaxation processes above the glass transition temperature.[70, 105, 107] Table 1.1 compares the properties of the main classes of material.

	Oxide	Sulfide	Polymer
Ionic conductivity	✓✓	✓✓✓	✓
Ion selectivity	✓✓✓	✓✓✓	✓*
Electrochemical window	✓✓✓	✓✓	✓
Chemical stability	✓✓	✓	✓✓
Thermal stability	✓✓✓	✓✓	✓
Mechanical properties	✓✓	✓✓	✓✓
Processing cost	✓✓	✓✓	✓✓✓
Device integration	✓	✓✓	✓✓✓

Table 1.1: Performance of different solid electrolyte materials.[70] *Conventional polymer electrolytes – see section 1.6.2

1.6.1 Inorganic materials

The representative perovskite-type oxide is $Li_{3x}La_{(2/3)-x}TiO_3$ (LLTO) which has a bulk Li^+ conductivity of over 10^{-3} S cm^{-1} at room temperature. NASICON-type oxides have the general formula $LiM_2(PO_4)_3$ (M^{4+}) with a structure similar to NASICON (sodium super ionic conductor). In particular the $LiTi_2(PO_4)_3$ system has been widely investigated; conductivity can be enhanced by substitution of Ti with Al to form $Li_{1+x}Al_xTi_{2-x}(PO_4)_3$ (LATP)[70, 107]. Ohara glass-ceramic is a commercial material marketed by Ohara Inc. which has two NASICON-type crystalline phases ($Li_{1+x}Al_xGe_zTi_{2-x-z}P_3O_{12}$ and $Li_{1+x+y}Al_x(Ge,Ti)_{2-x}Si_yP_{3-y}O_{12}$) with a further crystalline phase of $AlPO_4$. Nano-scale lithium-ion conductive polycrystalline particles are isotropically dispersed within an amorphous glass matrix. [111] Ohara Inc. report the following properties for their "AG-01" product (Table 1.2).

Ionic conductivity	1 - 4 x 10^{-4} S/cm at room temperature Li-ion transport number of 1
Chemical properties	Stable in air and water
Mechanical properties	Bending Strength (4 points) 140 N mm^{-2} Prevents dendrite penetration
Thermal properties	Thermally Stable up to 600°C Non-flammable Coefficients of thermal expansion (x10^{-7} K^{-1}): 94 (30-350 °C), 82 (350-600 °C)

Table 1.2: Properties of commercial Ohara glass-ceramic reported by Ohara Inc.[111]

The titanium in their composition means that both LLTO and LATP are readily reduced by Li and so an interlayer between the ceramic membrane and negative electrode is needed. On the other hand, garnet-type oxides, in particular $Li_7La_3Zr_2O_{12}$ (LLZO) and $Li_5La_3Ta_2O_{12}$ (LLTa) have been shown to be stable against Li, with high Li^+ conductivity when stabilised in the cubic phase vs. the more thermodynamically stable tetragonal structure.[70, 105] A room temperature conductivity of 1.3 mS cm^{-1} was demonstrated for a Ga-substituted LLZO sintered under dry O_2 conditions to give a high density ceramic material and avoid degradation due to exchange of Li^+ by H^+ from atmospheric moisture.[112] However, garnet solid electrolytes generally have high interfacial resistance with Li metal, due to poor wetting. Various strategies to engineer the Li-garnet interface have been proposed e.g. coating the garnet with Al (to form a Li-Al alloy with Li) or Al_2O_3 (which has higher binding energy with Li).[113, 114] Recently a new type of composite electrolyte was proposed in which conducting ceramic (Ta-substituted LLZO) nanoparticles form a percolating network in a salt-free insulating PEO matrix, to give a flexible composite membrane with Li^+ conductivity of 2 x 10^{-4} S cm^{-1} at room temperature and ability to suppress dendrite growth.[115]

Li^+ conducting sulfide glasses/glass-ceramics such as the Li_2S-SiS_2 and Li_2S-P_2S_5 systems are also stable against lithium metal, have a wide electrochemical stability window, and demonstrate high conductivities (~10^{-3} S cm^{-1}) at room temperature, with $Li_7P_3S_{11}$ demonstrating a value as high as 10^{-2} S cm^{-1}. However the Li_2S-P_2S_5 materials are sensitive to humidity, generating H_2S, and must be handled in a dry atmosphere.[70, 105]

Some solid electrolyte materials can be fabricated as thin films via physical or chemical vapour deposition. The first thin film electrolytes were developed by Bates et al by radio frequency magnetron sputtering of lithium silicates and phosphates. Sputtering of Li_3PO_4 in N_2 produced LiPON, an amorphous analogue to LISICON.[116] Thin-film batteries with Li anodes and LiPON electrolyte demonstrated high cycle life. Here, the LiPON was deposited over the cathode material on a substrate, and the Li deposited on top of the LiPON via thermal evaporation.[116-118] It is also possible to deposit LiPON onto a copper substrate, and form the Li anode in situ by electrodeposition. This was demonstrated in a Li-S cell.[119]

1.6.2 Polymers

Polymer electrolytes are ionically conducting solid phases formed (usually) by the dissolution of salts in ion-coordinating macromolecules.[120] The first ion-conducting polymer, polyethylene oxide (PEO) complexed with alkali metal salt, was discovered over 40 years ago[121]. Since then there have been numerous studies, using various techniques, into their structure,

morphology and ionic motion as a function of temperature, salt type and concentration, polymer molecular weight, end groups and additives, as well as into the properties of the polymer/electrode interface.[109, 122-126]

Various categories of solid polymer electrolyte (SPE) exist. *Conventional polymer-salt complex (dry)* SPEs are prepared by dissolving ionic salts into coordinating polar polymer hosts, such as PEO, with low glass transition temperature. Films/membranes can be produced either by traditional solution-casting or by a novel hot-press technique. *Polymer gel* electrolytes comprise liquid solvent/plasticiser in a polymer matrix, with an increase in room temperature ionic conductivity at the expense of mechanical integrity and stability towards the metal electrode. *'Polymer-in-salt'* electrolytes comprise a large amount of salt mixed with a small amount of polymer. They can demonstrate high conductivity (up to 10^{-2} S cm^{-1}) but suffer from a tendency of the complexed salt to crystallise. *Composite polymer* electrolytes are prepared by dispersing a small fraction of micro- or nano-sized ceramic or organic filler particles into a conventional SPE, usually with an improvement in ionic conductivity, mechanical integrity and interfacial activity.[109, 126]

The majority of conventional SPEs employ a PEO or PPO polymer host, while a wide variety of lithium salts can be complexed. The basic structure consists of polymer chains coiled around Li^+ ions, separating them from their counter anions. Li^+ transport comes generally from local relaxation and segmental motion of the polymer chains; this is facilitated by a high degree of amorphicity, with conductivity-temperature dependence following Vogel–Tamman–Fulcher or "free volume" behaviour. For PEO-based SPEs, conductivity >= 10^{-4} S cm^{-1} is achievable in the temperature range 70-90 ^oC (i.e. above the melting temperature), although much research has been done to increase the amorphous volume fraction and hence conductivity at room temperature. Both ionic conductivity and Li^+ transference number (see below) tend to decrease as salt concentration is increased due to hindrance of polymer chain motion as well as the formation of ion pairs[109, 120], although an increase in Li^+ transference number with increasing salt concentration has also been reported.[127] Salts such as LiTFSI, containing large organic anions which act as a plasticiser due to highly delocalised electrons, can increase conductivity with minimum anion migration. Still, conventional SPEs generally have cation transference numbers much lower than unity (the majority <=0.5).[26, 109, 120] However, single lithium-ion conducting SPEs with Li^+ transport numbers close to unity are being pursued using strategies including covalently bonding anions to the polymer backbone or adding trapping agents for anions to dual-ion conducting SPEs.[26, 128]

It is worth mentioning that the terms transference and transport number are often used interchangeably; however these quantities are distinct. Transport number, T, is the fraction of the total current carried by a particular species (Li^+, X^-, $[LiX]^0$, $[Li_2X]^+$, $[LiX_2]^-$ etc.), whilst transference number, t, of a constituent cation (Li^+) or anion (X^-) of the salt is defined as the net number of Faradays carried by migration by that constituent, in the direction of the cathode or anode, respectively, on the passage of 1 Faraday of charge through the cell. Transference number is related to individual transport numbers according to:

$$t_{Li^+} = T_{Li^+} + 2T_{[Li_2X]^+} - T_{[LiX_2]^-} \quad \text{(Eq. 1.14)}$$

Similarly

$$t_{X^-} = T_{X^-} - T_{[Li_2X]^+} + 2T_{[LiX_2]^-} \quad \text{(Eq. 1.15)}$$

The sum of the cation and anion transference numbers is equal to unity. For a fully dissociated salt, transference number and transport numbers are identical.[129, 130]. A low Li^+ transference/transport number will result in anion build-up at one electrode and depletion at the other, leading to a salt concentration gradient in the cell with adverse effects on cell performance. These include voltage losses due to concentration polarisation, higher internal impedance due to changes in electrolyte conductivity, side reactions, salt precipitation and promotion of dendrite growth. [131-133]

One of the most common methods for measuring transport number is the one developed by Bruce and Vincent for polymer electrolytes (though it has also been applied to liquid electrolytes[134, 135]), which involves applying a small DC voltage across a symmetric Li/electrolyte/Li cell (see Appendix B for more details).[136, 137] Strictly, however, the analysis is valid only in the dilute limit where ion interaction can be neglected (i.e. conductivity follows the Nernst-Einstein equation), a condition that is often overlooked. [131, 134, 138-140] When applied to concentrated electrolytes, the result is neither the lithium transport number nor true transference number (due to the contribution of neutral ion pairs)[129], though it is still a relevant quantity for Li cells, and may be referred to as the effective transference number[141] (Bruce and Vincent suggested the term 'limiting current fraction'[142]). However, the method relies on a stable lithium-electrolyte interface and an absence of convection which is difficult to achieve totally in liquid electrolytes.[135, 141, 143] Ma et al developed a method for determining a complete set of transport properties (salt diffusion coefficient, activity coefficient, transference number and conductivity) without the assumption of a dilute or ideal solution. However the method involves three separate measurements (in two different cell geometries) as well as differentiation of experimental data as part of the analysis,

and is therefore susceptible to experimental error.[140] As with the Bruce-Vincent method, the electrolyte must be stable in contact with lithium. The Hittorf method involves passing charge through a symmetric Li/electrolyte/Li cell, dividing the electrolyte into four sections and measuring the change in salt concentration in the sections closest to the electrodes. Provided no concentration gradient has developed in the central sections then any change in concentration in the end sections is due to migration only and can be used to calculate the anion transference number ($T_- = -\Delta m_{Li} F/Q$) and from that the lithium transference number. Again, however, the electrolyte must be stable in contact with lithium, and there are also practical difficulties in applying the technique to polymer electrolytes.[138]

1.7 Aims and objectives

The use of lithium protective membranes/separators, coatings and solid electrolytes can address key issues associated with lithium metal batteries. This work focuses on some of the key properties for good performance of such components: ion selectivity, transference number, interface resistance and, in the case of polymer electrolytes for Li-S batteries, the mechanisms of Li-S redox reactions. The main focus of this research project has been to develop appropriate cell designs and techniques for the evaluation of these properties, via fast, easy, reliable, reproducible, quantitative and *in-situ*/*operando* measurement. Other applications of the cell designs and/or techniques developed, to gain further insight into the mechanisms Li-S batteries, have also be explored. There are five mains sections in this work:

i. **New method to measure the rate of transport of redox species through membranes**. A new quantitative, *in-situ* method is presented which employs a glassy carbon working electrode designed to fit a standard 'Swagelok' cell. The method is tested using a model and well-behaved electrochemical system to demonstrate its sensitivity, reproducibility and reliability.
ii. **New method for evaluating selectivity and transference number in lithium conducting membranes**. A novel *operando* approach, employing a modified version of the aforementioned cell, is presented for the evaluation of the selectivity and transference numbers of membranes under practically relevant conditions, including application of a current through the membrane. Using a model system, it is shown that standard *ex-situ* methods (without current flow) provide a considerable overestimation of the capability of the membrane to block crossover species.
iii. **Contributions to the resistance of lithium ion transfer at the solid-liquid electrolyte interface**. Four-point impedance measurements of a solid lithium ion conductor immersed in

different liquid electrolytes are used to study the rate of ion transfer through the solid-liquid electrolyte interface. An approach is illustrated for identifying the rate-limiting step, which may be desolvation of lithium ions or transport through a solid-liquid electrolyte interphase.

iv. **Electrochemical observation of polysulfide species in solid polymer electrolytes in lithium-sulfur batteries**. Using a novel, three-electrode 'Swagelok' cell design, direct observation and measurement of sulfur and intermediate polysulfide species in solid polymer electrolytes is made for the first time using electrochemical methods, providing insights into mass transport properties and mechanisms of the associated redox reactions.

v. **Characterising mass transport coefficients: the use of GITT for soluble redox species.** Using a model redox system, the cell design developed for measuring membrane selectivity is used to investigate the suitability of the galvanic intermittent titration technique (GITT) for determining quantitative information on mass transport of soluble species such as polysulfides in liquid-electrolyte Li-S batteries.

1.8 References

1. Armand, M.; Tarascon, J. M., Building better batteries. *Nature* **2008**, *451*, 652.
2. Goodenough, J. B.; Park, K. S., The Li-ion rechargeable battery: a perspective. *J Am Chem Soc* **2013**, *135*, 1167-76.
3. Manthiram, A., An Outlook on Lithium Ion Battery Technology. *ACS Cent Sci* **2017**, *3*, 1063-1069.
4. Choi, J. W.; Aurbach, D., Promise and reality of post-lithium-ion batteries with high energy densities. *Nature Reviews Materials* **2016**, *1*.
5. Bruce, P. G.; Freunberger, S. A.; Hardwick, L. J.; Tarascon, J. M., Li-O_2 and Li-S batteries with high energy storage. *Nat Mater* **2011**, *11*, 19-29.
6. Vincent, C. A., 2 - Theoretical background. In *Modern Batteries (Second Edition)*, Vincent, C. A.; Scrosati, B., Eds. Butterworth-Heinemann: Oxford, 1997; pp 18-64.
7. Glossary. In *Modern Batteries (Second Edition)*, Vincent, C. A.; Scrosati, B., Eds. Butterworth-Heinemann: Oxford, 1997; pp 333-340.
8. Bard, A. J.; Faulkner, L. R., *Electrochemical Methods: Fundamentals and Applications, 2nd Edition*; Wiley Textbooks, 2000.
9. Pletcher, D., *A first course in electrode processes*; Royal Society of Chemistry, 2009, p 316.
10. Lin, D.; Liu, Y.; Cui, Y., Reviving the lithium metal anode for high-energy batteries. *Nat Nanotechnol* **2017**, *12*, 194-206.

11. Fong, R.; von Sacken, U.; Dahn, J. R., Studies of Lithium Intercalation into Carbons Using Nonaqueous Electrochemical Cells. *Journal of The Electrochemical Society* **1990**, *137*, 2009-2013.

12. Peled, E.; Menkin, S., Review—SEI: Past, Present and Future. *Journal of The Electrochemical Society* **2017**, *164*, A1703-A1719.

13. An, S. J.; Li, J.; Daniel, C.; Mohanty, D.; Nagpure, S.; Wood, D. L., The state of understanding of the lithium-ion-battery graphite solid electrolyte interphase (SEI) and its relationship to formation cycling. *Carbon* **2016**, *105*, 52-76.

14. Etacheri, V.; Marom, R.; Elazari, R.; Salitra, G.; Aurbach, D., Challenges in the development of advanced Li-ion batteries: a review. *Energy & Environmental Science* **2011**, *4*.

15. Gauthier, M., et al., Electrode–Electrolyte Interface in Li-Ion Batteries: Current Understanding and New Insights. *The Journal of Physical Chemistry Letters* **2015**, *6*, 4653-4672.

16. Noh, H.-J.; Youn, S.; Yoon, C. S.; Sun, Y.-K., Comparison of the structural and electrochemical properties of layered $Li[Ni_xCo_yMn_z]O_2$ (x = 1/3, 0.5, 0.6, 0.7, 0.8 and 0.85) cathode material for lithium-ion batteries. *Journal of Power Sources* **2013**, *233*, 121-130.

17. Schipper, F.; Erickson, E. M.; Erk, C.; Shin, J.-Y.; Chesneau, F. F.; Aurbach, D., Review—Recent Advances and Remaining Challenges for Lithium Ion Battery Cathodes. *Journal of The Electrochemical Society* **2016**, *164*, A6220-A6228.

18. Jung, R.; Metzger, M.; Maglia, F.; Stinner, C.; Gasteiger, H. A., Oxygen Release and Its Effect on the Cycling Stability of $LiNi_xMn_yCo_zO_2$ (NMC) Cathode Materials for Li-Ion Batteries. *Journal of The Electrochemical Society* **2017**, *164*, A1361-A1377.

19. Li, J.; Downie, L. E.; Ma, L.; Qiu, W.; Dahn, J. R., Study of the Failure Mechanisms of $LiNi_{0.8}Mn_{0.1}Co_{0.1}O_2$ Cathode Material for Lithium Ion Batteries. *Journal of The Electrochemical Society* **2015**, *162*, A1401-A1408.

20. Liu, W.; Oh, P.; Liu, X.; Lee, M. J.; Cho, W.; Chae, S.; Kim, Y.; Cho, J., Nickel-rich layered lithium transition-metal oxide for high-energy lithium-ion batteries. *Angew Chem Int Ed Engl* **2015**, *54*, 4440-57.

21. Pan, H.; Zhang, S.; Chen, J.; Gao, M.; Liu, Y.; Zhu, T.; Jiang, Y., Li- and Mn-rich layered oxide cathode materials for lithium-ion batteries: a review from fundamentals to research progress and applications. *Molecular Systems Design & Engineering* **2018**, *3*, 748-803.

22. Hu, M.; Pang, X.; Zhou, Z., Recent progress in high-voltage lithium ion batteries. *Journal of Power Sources* **2013**, *237*, 229-242.

23. Li, W.; Song, B.; Manthiram, A., High-voltage positive electrode materials for lithium-ion batteries. *Chemical Society Reviews* **2017**, *46*, 3006-3059.

24. Shi, J.; Xia, Y.; Yuan, Z.; Hu, H.; Li, X.; Jiang, H.; Zhang, H.; Liu, Z., Composite membrane with ultra-thin ion exchangeable functional layer: a new separator choice for manganese-based cathode material in lithium ion batteries. *Journal of Materials Chemistry A* **2015**, *3*, 7006-7013.

25. Shen, X.; Liu, H.; Cheng, X.-B.; Yan, C.; Huang, J.-Q., Beyond lithium ion batteries: Higher energy density battery systems based on lithium metal anodes. *Energy Storage Materials* **2018**, *12*, 161-175.

26. Zhang, H.; Li, C.; Piszcz, M.; Coya, E.; Rojo, T.; Rodriguez-Martinez, L. M.; Armand, M.; Zhou, Z., Single lithium-ion conducting solid polymer electrolytes: advances and perspectives. *Chemical Society Reviews* **2017**, *46*, 797-815.

27. Zhang, H.; Eshetu, G. G.; Judez, X.; Li, C.; Rodriguez-Martinez, L. M.; Armand, M., Electrolyte Additives for Lithium Metal Anodes and Rechargeable Lithium Metal Batteries: Progress and Perspectives. *Angew Chem Int Ed Engl* **2018**, *57*, 15002-15027.

28. Pan, Y.; Chou, S.; Liu, H. K.; Dou, S. X., Functional membrane separators for next-generation high-energy rechargeable batteries. *National Science Review* **2017**, *4*, 917-933.

29. Xu, X.; Wang, S.; Wang, H.; Xu, B.; Hu, C.; Jin, Y.; Liu, J.; Yan, H., The suppression of lithium dendrite growth in lithium sulfur batteries: A review. *Journal of Energy Storage* **2017**, *13*, 387-400.

30. Nazar, L. F.; Cuisinier, M.; Pang, Q., Lithium-sulfur batteries. *MRS Bulletin* **2014**, *39*, 436-442.

31. Ji, X.; Nazar, L. F., Advances in Li-S batteries. *Journal of Materials Chemistry* **2010**, *20*, 9821-9826.

32. Wild, M.; O'Neill, L.; Zhang, T.; Purkayastha, R.; Minton, G.; Marinescu, M.; Offer, G. J., Lithium sulfur batteries, a mechanistic review. *Energy & Environmental Science* **2015**, *8*, 3477-3494.

33. Zhang, S.; Ueno, K.; Dokko, K.; Watanabe, M., Recent Advances in Electrolytes for Lithium-Sulfur Batteries. *Advanced Energy Materials* **2015**, *5*.

34. Eroglu, D.; Zavadil, K. R.; Gallagher, K. G., Critical Link between Materials Chemistry and Cell-Level Design for High Energy Density and Low Cost Lithium-Sulfur Transportation Battery. *Journal of The Electrochemical Society* **2015**, *162*, A982-A990.

35. Pang, Q.; Liang, X.; Kwok, C. Y.; Nazar, L. F., Advances in lithium–sulfur batteries based on multifunctional cathodes and electrolytes. *Nature Energy* **2016**, *1*, 16132.

36. Bonnick, P.; Nagai, E.; Muldoon, J., Perspective—Lithium-Sulfur Batteries. *Journal of The Electrochemical Society* **2017**, *165*, A6005-A6007.

37. Urbonaite, S.; Poux, T.; Novák, P., Progress Towards Commercially Viable Li–S Battery Cells. *Advanced Energy Materials* **2015**, *5*.

38. Mikhaylik, Y. V.; Akridge, J. R., Polysulfide Shuttle Study in the Li/S Battery System. *Journal of The Electrochemical Society* **2004**, *151*, A1969-A1976.

39. Lin, Z.; Liang, C., Lithium–sulfur batteries: from liquid to solid cells. *Journal of Materials Chemistry A* **2015**, *3*, 936-958.

40. Fang, R.; Zhao, S.; Sun, Z.; Wang, D. W.; Cheng, H. M.; Li, F., More Reliable Lithium-Sulfur Batteries: Status, Solutions and Prospects. *Adv Mater* **2017**, *29*.

41. Ren, W.; Ma, W.; Zhang, S.; Tang, B., Recent advances in shuttle effect inhibition for lithium sulfur batteries. *Energy Storage Materials* **2019**.

42. Pang, Q.; Liang, X.; Kwok, C. Y.; Nazar, L. F., Review—The Importance of Chemical Interactions between Sulfur Host Materials and Lithium Polysulfides for Advanced Lithium-Sulfur Batteries. *Journal of The Electrochemical Society* **2015**, *162*, A2567-A2576.

43. Wang, L.; Byon, H. R., N-Methyl-N-propylpiperidinium bis(trifluoromethanesulfonyl)imide-based organic electrolyte for high performance lithium–sulfur batteries. *Journal of Power Sources* **2013**, *236*, 207-214.

44. Suo, L.; Hu, Y. S.; Li, H.; Armand, M.; Chen, L., A new class of Solvent-in-Salt electrolyte for high-energy rechargeable metallic lithium batteries. *Nature Communications* **2013**, *4*, 1481.

45. Li, G.; Li, Z.; Zhang, B.; Lin, Z., Developments of Electrolyte Systems for Lithium-Sulfur Batteries: A Review. *Frontiers in Energy Research* **2015**, *3*.

46. Barghamadi, M.; Best, A. S.; Bhatt, A. I.; Hollenkamp, A. F.; Musameh, M.; Rees, R. J.; Rüther, T., Lithium–sulfur batteries—the solution is in the electrolyte, but is the electrolyte a solution? *Energy Environ. Sci.* **2014**, *7*, 3902-3920.

47. Aurbach, D.; Pollak, E.; Elazari, R.; Salitra, G.; Kelley, C. S.; Affinito, J., On the Surface Chemical Aspects of Very High Energy Density, Rechargeable Li–Sulfur Batteries. *Journal of The Electrochemical Society* **2009**, *156*, A694-A702.

48. Li, W.; Yao, H.; Yan, K.; Zheng, G.; Liang, Z.; Chiang, Y. M.; Cui, Y., The synergetic effect of lithium polysulfide and lithium nitrate to prevent lithium dendrite growth. *Nat Commun* **2015**, *6*, 7436.

49. Zhang, S. S., Effect of Discharge Cutoff Voltage on Reversibility of Lithium/Sulfur Batteries with LiNO3-Contained Electrolyte. *Journal of The Electrochemical Society* **2012**, *159*, A920-A923.

50. Ma, G.; Wen, Z.; Wu, M.; Shen, C.; Wang, Q.; Jin, J.; Wu, X., A lithium anode protection guided highly-stable lithium-sulfur battery. *Chem Commun (Camb)* **2014**, *50*, 14209-12.

51. Shaibani, M.; Hollenkamp, A. F.; Hill, M. R.; Majumder, M., Permselective membranes in lithium–sulfur batteries. *Current Opinion in Chemical Engineering* **2017**, *16*, 31-38.

52. Huang, J.-Q.; Zhang, Q.; Peng, H.-J.; Liu, X.-Y.; Qian, W.-Z.; Wei, F., Ionic shield for polysulfides towards highly-stable lithium–sulfur batteries. *Energy & Environmental Science* **2014**, *7*, 347-353.

53. Bauer, I.; Thieme, S.; Brückner, J.; Althues, H.; Kaskel, S., Reduced polysulfide shuttle in lithium–sulfur batteries using Nafion-based separators. *Journal of Power Sources* **2014**, *251*, 417-422.

54. Jin, Z.; Xie, K.; Hong, X.; Hu, Z.; Liu, X., Application of lithiated Nafion ionomer film as functional separator for lithium sulfur cells. *Journal of Power Sources* **2012**, *218*, 163-167.

55. Yu, X.; Joseph, J.; Manthiram, A., Polymer lithium–sulfur batteries with a Nafion membrane and an advanced sulfur electrode. *Journal of Materials Chemistry A* **2015**, *3*, 15683-15691.

56. Chung, S.-H.; Manthiram, A., Bifunctional Separator with a Light-Weight Carbon-Coating for Dynamically and Statically Stable Lithium-Sulfur Batteries. *Advanced Functional Materials* **2014**, *24*, 5299-5306.

57. Zhu, J.; Ge, Y.; Kim, D.; Lu, Y.; Chen, C.; Jiang, M.; Zhang, X., A novel separator coated by carbon for achieving exceptional high performance lithium-sulfur batteries. *Nano Energy* **2016**, *20*, 176-184.

58. Hao, Z.; Yuan, L.; Li, Z.; Liu, J.; Xiang, J.; Wu, C.; Zeng, R.; Huang, Y., High performance lithium-sulfur batteries with a facile and effective dual functional separator. *Electrochimica Acta* **2016**, *200*, 197-203.

59. Zeng, F.; Jin, Z.; Yuan, K.; Liu, S.; Cheng, X.; Wang, A.; Wang, W.; Yang, Y.-s., High performance lithium–sulfur batteries with a permselective sulfonated acetylene black modified separator. *Journal of Materials Chemistry A* **2016**, *4*, 12319-12327.

60. Wu, X.-l.; Zong, J.; Xu, H.; Wang, W.; Liu, X.-j., Effects of LAGP electrolyte on suppressing polysulfide shuttling in Li-S cells. *RSC Advances* **2016**, *6*, 57346-57356.

61. Deng, N.; Kang, W.; Liu, Y.; Ju, J.; Wu, D.; Li, L.; Hassan, B. S.; Cheng, B., A review on separators for lithium sulfur battery: Progress and prospects. *Journal of Power Sources* **2016**, *331*, 132-155.

62. Conder, J.; Forner-Cuenca, A.; Gubler, E. M.; Gubler, L.; Novák, P.; Trabesinger, S., Performance-Enhancing Asymmetric Separator for Lithium–Sulfur Batteries. *ACS Applied Materials & Interfaces* **2016**, *8*, 18822-18831.

63. Yu, X.; Bi, Z.; Zhao, F.; Manthiram, A., Hybrid Lithium–Sulfur Batteries with a Solid Electrolyte Membrane and Lithium Polysulfide Catholyte. *ACS Applied Materials & Interfaces* **2015**, *7*, 16625-16631.

64. Cui, Y.; Fu, Y., Polysulfide transport through separators measured by a linear voltage sweep method. *Journal of Power Sources* **2015**, *286*, 557-560.

65. Dominko, R.; Demir-Cakan, R.; Morcrette, M.; Tarascon, J.-M., Analytical detection of soluble polysulphides in a modified Swagelok cell. *Electrochemistry Communications* **2011**, *13*, 117-120.

66. Lacey, M. J.; Edström, K.; Brandell, D., Analysis of soluble intermediates in the lithium–sulfur battery by a simple in situ electrochemical probe. *Electrochemistry Communications* **2014**, *46*, 91-93.

67. Li, C.; Ward, A. L.; Doris, S. E.; Pascal, T. A.; Prendergast, D.; Helms, B. A., Polysulfide-Blocking Microporous Polymer Membrane Tailored for Hybrid Li-Sulfur Flow Batteries. *Nano Letters* **2015**, *15*, 5724-5729.

68. Vizintin, A.; Patel, M. U. M.; Genorio, B.; Dominko, R., Effective Separation of Lithium Anode and Sulfur Cathode in Lithium–Sulfur Batteries. *ChemElectroChem* **2014**, *1*, 1040-1045.

69. Hayashi, A.; Ohtomo, T.; Mizuno, F.; Tadanaga, K.; Tatsumisago, M., All-solid-state Li/S batteries with highly conductive glass–ceramic electrolytes. *Electrochemistry Communications* **2003**, *5*, 701-705.

70. Manthiram, A.; Yu, X.; Wang, S., Lithium battery chemistries enabled by solid-state electrolytes. *Nature Reviews Materials* **2017**, *2*, 16103.

71. Ohno, S.; Koerver, R.; Dewald, G.; Rosenbach, C.; Titscher, P.; Steckermeier, D.; Kwade, A.; Janek, J.; Zeier, W. G., Observation of Chemomechanical Failure and the Influence of Cutoff Potentials in All-Solid-State Li–S Batteries. *Chemistry of Materials* **2019**.

72. Busche, M. R.; Drossel, T.; Leichtweiss, T.; Weber, D. A.; Falk, M.; Schneider, M.; Reich, M. L.; Sommer, H.; Adelhelm, P.; Janek, J., Dynamic formation of a solid-liquid electrolyte interphase and its consequences for hybrid-battery concepts. *Nature Chemistry* **2016**, *8*, 426-34.

73. Fu, K. K., et al., Stabilizing the Garnet Solid-Electrolyte/Polysulfide Interface in Li–S Batteries. *Chemistry of Materials* **2017**, *29*, 8037-8041.

74. Wang, S.; Ding, Y.; Zhou, G.; Yu, G.; Manthiram, A., Durability of the $Li_{1+x}Ti_{2-x}Al_x(PO_4)_3$ Solid Electrolyte in Lithium–Sulfur Batteries. *ACS Energy Letters* **2016**, *1*, 1080-1085.

75. Schleutker, M.; Bahner, J.; Tsai, C. L.; Stolten, D.; Korte, C., On the interfacial charge transfer between solid and liquid Li^+ electrolytes. *Phys Chem Chem Phys* **2017**, *19*, 26596-26605.

76. Berg, E. J.; Trabesinger, S., Viability of Polysulfide-Retaining Barriers in Li–S Battery. *Journal of The Electrochemical Society* **2017**, *165*, A5001-A5005.

77. Judez, X.; Zhang, H.; Li, C.; Eshetu, G. G.; González-Marcos, J. A.; Armand, M.; Rodriguez-Martinez, L. M., Review—Solid Electrolytes for Safe and High Energy Density Lithium-Sulfur

Batteries: Promises and Challenges. *Journal of The Electrochemical Society* **2018**, *165*, A6008-A6016.

78. Judez, X.; Zhang, H.; Li, C.; Eshetu, G. G.; Zhang, Y.; González-Marcos, J. A.; Armand, M.; Rodriguez-Martinez, L. M., Polymer-Rich Composite Electrolytes for All-Solid-State Li–S Cells. *The Journal of Physical Chemistry Letters* **2017**, *8*, 3473-3477.

79. Fu, K., et al., Three-dimensional bilayer garnet solid electrolyte based high energy density lithium metal–sulfur batteries. *Energy & Environmental Science* **2017**, *10*, 1568-1575.

80. Zheng, D.; Wang, G.; Liu, D.; Si, J.; Ding, T.; Qu, D.; Yang, X.; Qu, D., The Progress of Li–S Batteries—Understanding of the Sulfur Redox Mechanism: Dissolved Polysulfide Ions in the Electrolytes. *Advanced Materials Technologies* **2018**, *3*, 1700233.

81. Marceau, H., et al., In operando scanning electron microscopy and ultraviolet–visible spectroscopy studies of lithium/sulfur cells using all solid-state polymer electrolyte. *Journal of Power Sources* **2016**, *319*, 247-254.

82. Wujcik, K. H.; Pascal, T. A.; Pemmaraju, C. D.; Devaux, D.; Stolte, W. C.; Balsara, N. P.; Prendergast, D., Characterization of Polysulfide Radicals Present in an Ether-Based Electrolyte of a Lithium–Sulfur Battery During Initial Discharge Using In Situ X-Ray Absorption Spectroscopy Experiments and First-Principles Calculations. *Advanced Energy Materials* **2015**, *5*, 1500285.

83. Garcia-Araez, N.; Novák, P., Critical aspects in the development of lithium–air batteries. *Journal of Solid State Electrochemistry* **2013**, *17*, 1793-1807.

84. Chen, Y.; Freunberger, S. A.; Peng, Z.; Fontaine, O.; Bruce, P. G., Charging a Li–O_2 battery using a redox mediator. *Nature Chemistry* **2013**, *5*, 489-494.

85. Lim, H. D., et al., Superior rechargeability and efficiency of lithium-oxygen batteries: hierarchical air electrode architecture combined with a soluble catalyst. *Angew Chem Int Ed Engl* **2014**, *53*, 3926-31.

86. Liu, T.; Leskes, M.; Yu, W.; Moore, A. J.; Zhou, L.; Bayley, P. M.; Kim, G.; Grey, C. P., Cycling Li-O_2 batteries via LiOH formation and decomposition. *Science* **2015**, *350*, 530-533.

87. Lodge, A. W.; Lacey, M. J.; Fitt, M.; Garcia-Araez, N.; Owen, J. R., Critical appraisal on the role of catalysts for the oxygen reduction reaction in lithium-oxygen batteries. *Electrochimica Acta* **2014**, *140*, 168-173.

88. Yoon, T. H.; Park, Y. J., New strategy toward enhanced air electrode for Li-air batteries: apply a polydopamine coating and dissolved catalyst. *RSC Advances* **2014**, *4*, 17434-17442.

89. Kwak, W.-J., et al., Understanding the behavior of Li-oxygen cells containing LiI. *Journal of Materials Chemistry A* **2015**, *3*, 8855-8864.

90. Yang, L.; Frith, J. T.; Garcia-Araez, N.; Owen, J. R., A new method to prevent degradation of lithium-oxygen batteries: reduction of superoxide by viologen. *Chemical Communications* **2015**, *51*, 1705-1708.

91. Lacey, M. J.; Frith, J. T.; Owen, J. R., A redox shuttle to facilitate oxygen reduction in the lithium air battery. *Electrochemistry Communications* **2013**, *26*, 74-76.

92. Landa-Medrano, I.; Lozano, I.; Ortiz-Vitoriano, N.; Ruiz de Larramendi, I.; Rojo, T., Redox mediators: a shuttle to efficacy in metal–O_2 batteries. *Journal of Materials Chemistry A* **2019**, *7*, 8746-8764.

93. Park, J.-B.; Lee, S. H.; Jung, H.-G.; Aurbach, D.; Sun, Y.-K., Redox Mediators for Li–O_2 Batteries: Status and Perspectives. *Advanced Materials* **2018**, *30*, 1704162.

94. Ha, S.; Kim, Y.; Koo, D.; Ha, K.-H.; Park, Y.; Kim, D.-M.; Son, S.; Yim, T.; Lee, K. T., Investigation into the stability of Li metal anodes in Li–O_2 batteries with a redox mediator. *Journal of Materials Chemistry A* **2017**, *5*, 10609-10621.

95. Bergner, B. J.; Busche, M. R.; Pinedo, R.; Berkes, B. B.; Schroder, D.; Janek, J., How To Improve Capacity and Cycling Stability for Next Generation Li-O_2 Batteries: Approach with a Solid Electrolyte and Elevated Redox Mediator Concentrations. *ACS Applied Materials & Interfaces* **2016**, *8*, 7756-65.

96. Qiao, Y.; He, Y.; Wu, S.; Jiang, K.; Li, X.; Guo, S.; He, P.; Zhou, H., MOF-Based Separator in an Li–O_2 Battery: An Effective Strategy to Restrain the Shuttling of Dual Redox Mediators. *ACS Energy Letters* **2018**, *3*, 463-468.

97. Li, Y.; Lu, J., Metal–Air Batteries: Will They Be the Future Electrochemical Energy Storage Device of Choice? *ACS Energy Letters* **2017**, *2*, 1370-1377.

98. Lu, J.; Li, L.; Park, J.-B.; Sun, Y.-K.; Wu, F.; Amine, K., Aprotic and Aqueous Li–O_2 Batteries. *Chemical Reviews* **2014**, *114*, 5611-5640.

99. Visco, S. J.; Nimon, V. Y.; Petrov, A.; Pridatko, K.; Goncharenko, N.; Nimon, E.; De Jonghe, L.; Volfkovich, Y. M.; Bograchev, D. A., Aqueous and nonaqueous lithium-air batteries enabled by water-stable lithium metal electrodes. *Journal of Solid State Electrochemistry* **2014**, *18*, 1443-1456.

100. Visco, S. J.; Nimon, Y. S.; Katz, B. Li/air non-aqueous batteries. US8652692B2, 2014.

101. Visco, S. J.; Nimon, Y. S. Active metal/aqueous electrochemical cells and systems. US7645543B2, 2012.

102. Manthiram, A.; Li, L., Hybrid and Aqueous Lithium-Air Batteries. *Advanced Energy Materials* **2015**, *5*, 1401302.

103. Safanama, D.; Adams, S., High efficiency aqueous and hybrid lithium-air batteries enabled by Li1.5Al0.5Ge1.5(PO4)3 ceramic anode-protecting membranes. *Journal of Power Sources* **2017**, *340*, 294-301.

104. Zhou, H.; Wang, Y.; Li, H.; He, P., The development of a new type of rechargeable batteries based on hybrid electrolytes. *ChemSusChem* **2010**, *3*, 1009-1019.

105. Sun, Y., Lithium ion conducting membranes for lithium-air batteries. *Nano Energy* **2013**, *2*, 801-816.

106. Yi, J.; Guo, S.; He, P.; Zhou, H., Status and prospects of polymer electrolytes for solid-state Li–O_2 (air) batteries. *Energy & Environmental Science* **2017**, *10*, 860-884.

107. Sun, C.; Liu, J.; Gong, Y.; Wilkinson, D. P.; Zhang, J., Recent advances in all-solid-state rechargeable lithium batteries. *Nano Energy* **2017**, *33*, 363-386.

108. Yi, J.; Liu, Y.; Qiao, Y.; He, P.; Zhou, H., Boosting the Cycle Life of Li–O_2 Batteries at Elevated Temperature by Employing a Hybrid Polymer–Ceramic Solid Electrolyte. *ACS Energy Letters* **2017**, *2*, 1378-1384.

109. Agrawal, R. C.; Pandey, G. P., Solid polymer electrolytes: materials designing and all-solid-state battery applications: an overview. *Journal of Physics D: Applied Physics* **2008**, *41*, 223001.

110. Tatsumisago, M.; Nagao, M.; Hayashi, A., Recent development of sulfide solid electrolytes and interfacial modification for all-solid-state rechargeable lithium batteries. *Journal of Asian Ceramic Societies* **2013**, *1*, 17-25.

111. Nakajima, K.; Katoh, T.; Inda, Y.; Hoffman, B., Lithium Ion Conductive Glass Ceramics: Properties and Application in Lithium Metal Batteries. In *Symposium on Energy Storage Beyond Lithium Ion; Materials Perspective*, Oak Ridge National Laboratory, 2010.

112. Bernuy-Lopez, C.; Manalastas, W.; Lopez del Amo, J. M.; Aguadero, A.; Aguesse, F.; Kilner, J. A., Atmosphere Controlled Processing of Ga-Substituted Garnets for High Li-Ion Conductivity Ceramics. *Chemistry of Materials* **2014**, *26*, 3610-3617.

113. Fu, K., et al., Toward garnet electrolyte–based Li metal batteries: An ultrathin, highly effective, artificial solid-state electrolyte/metallic Li interface. *Science Advances* **2017**, *3*, e1601659.

114. Han, X., et al., Negating interfacial impedance in garnet-based solid-state Li metal batteries. *Nat Mater* **2016**, *16*, 572.

115. Zhang, J.; Zhao, N.; Zhang, M.; Li, Y.; Chu, P. K.; Guo, X.; Di, Z.; Wang, X.; Li, H., Flexible and ion-conducting membrane electrolytes for solid-state lithium batteries: Dispersion of garnet nanoparticles in insulating polyethylene oxide. *Nano Energy* **2016**, *28*, 447-454.

116. Bates, J. B.; Dudney, N. J.; Gruzalski, G. R.; Zuhr, R. A.; Choudhury, A.; Luck, C. F.; Robertson, J. D., Fabrication and characterization of amorphous lithium electrolyte thin films and rechargeable thin-film batteries. *Journal of Power Sources* **1993**, *43*, 103-110.

117. Bates, J. B.; Dudney, N. J.; Lubben, D. C.; Gruzalski, G. R.; Kwak, B. S.; Yu, X.; Zuhr, R. A., Thin-film rechargeable lithium batteries. *Journal of Power Sources* **1995**, *54*, 58-62.

118. Bates, J. B.; Dudney, N. J.; Neudecker, B.; Ueda, A.; Evans, C. D., Thin-film lithium and lithium-ion batteries. *Solid State Ionics* **2000**, *135*, 33-45.

119. Chu, M.-Y.; Visco, S. J.; De Jonghe, L. C. Plating metal negative electrodes under protective coatings. US6402795B1, 2002.

120. Bruce, P. G.; Vincent, C. A., Polymer electrolytes. *Journal of the Chemical Society, Faraday Transactions* **1993**, *89*, 3187-3203.

121. Armand, M., Polymer solid electrolytes - an overview. *Solid State Ionics* **1983**, *9-10*, 745-754.

122. Vallée, A.; Besner, S.; Prud'Homme, J., Comparative study of poly(ethylene oxide) electrolytes made with $LiN(CF_3SO_2)_2$, $LiCF_3SO_3$ and $LiClO_4$: Thermal properties and conductivity behaviour. *Electrochimica Acta* **1992**, *37*, 1579-1583.

123. Devaux, D.; Bouchet, R.; Glé, D.; Denoyel, R., Mechanism of ion transport in PEO/LiTFSI complexes: Effect of temperature, molecular weight and end groups. *Solid State Ionics* **2012**, *227*, 119-127.

124. Croce, F.; Appetecchi, G. B.; Persi, L.; Scrosati, B., Nanocomposite polymer electrolytes for lithium batteries. *Nature* **1998**, *394*, 456-458.

125. Benrabah, D.; Baril, D.; Sanchez, J.-Y.; Armand, M.; Gard, G. G., Comparative electrochemical study of new poly(oxyethylene)–Li salt complexes. *Journal of the Chemical Society, Faraday Transactions* **1993**, *89*, 355-359.

126. Appetecchi, G. B.; Croce, F.; Persi, L.; Ronci, F.; Scrosati, B., Transport and interfacial properties of composite polymer electrolytes. *Electrochimica Acta* **2000**, *45*, 1481-1490.

127. Ghosh, A.; Wang, C.; Kofinas, P., Block Copolymer Solid Battery Electrolyte with High Li-Ion Transference Number. *Journal of The Electrochemical Society* **2010**, *157*, A846-A849.

128. Strauss, E.; Menkin, S.; Golodnitsky, D., On the way to high-conductivity single lithium-ion conductors. *Journal of Solid State Electrochemistry* **2017**, *21*, 1879-1905.

129. Bruce, P. G.; Gray, F. M., Polymer electrolytes II: Physical principles. In *Solid State Electrochemistry*, Bruce, P. G., Ed. Cambridge University Press: Cambridge, UK, 1994; pp 119-162.

130. Mindemark, J.; Lacey, M. J.; Bowden, T.; Brandell, D., Beyond PEO—Alternative host materials for Li^+-conducting solid polymer electrolytes. *Progress in Polymer Science* **2018**, *81*, 114-143.

131. Diederichsen, K. M.; McShane, E. J.; McCloskey, B. D., Promising Routes to a High Li^+ Transference Number Electrolyte for Lithium Ion Batteries. *ACS Energy Letters* **2017**, *2*, 2563-2575.

132. Doyle, M.; Fuller, T. F.; Newman, J., The importance of the lithium ion transference number in lithium/polymer cells. *Electrochimica Acta* **1994**, *39*, 2073-2081.

133. Brissot, C.; Rosso, M.; Chazalviel, J. N.; Lascaud, S., Dendritic growth mechanisms in lithium/polymer cells. *Journal of Power Sources* **1999**, *81-82*, 925-929.

134. Zugmann, S.; Fleischmann, M.; Amereller, M.; Gschwind, R. M.; Wiemhöfer, H. D.; Gores, H. J., Measurement of transference numbers for lithium ion electrolytes via four different methods, a comparative study. *Electrochimica Acta* **2011**, *56*, 3926-3933.

135. Ehrl, A.; Landesfeind, J.; Wall, W. A.; Gasteiger, H. A., Determination of Transport Parameters in Liquid Binary Electrolytes: Part II. Transference Number. *Journal of The Electrochemical Society* **2017**, *164*, A2716-A2731.

136. Bruce, P. G.; Vincent, C. A., Steady state current flow in solid binary electrolyte cells. *Journal of Electroanalytical Chemistry and Interfacial Electrochemistry* **1987**, *225*, 1-17.

137. Evans, J.; Vincent, C. A.; Bruce, P. G., Electrochemical measurement of transference numbers in polymer electrolytes. *Polymer* **1987**, *28*, 2324-2328.

138. Bruce, P. G.; Vincent, C. A., Effect of ion association on transport in polymer electrolytes. *Faraday Discussions of the Chemical Society* **1989**, *88*, 43-54.

139. Cameron, G. G.; Harvie, J. L.; Ingram, M. D., The steady state current and transference number measurements in polymer electrolytes. *Solid State Ionics* **1989**, *34*, 65-68.

140. Ma, Y.; Doyle, M.; Fuller, T. F.; Doeff, M. M.; De Jonghe, L. C.; Newman, J., The Measurement of a Complete Set of Transport Properties for a Concentrated Solid Polymer Electrolyte Solution. *Journal of The Electrochemical Society* **1995**, *142*, 1859-1868.

141. Popovic, J.; Hasegawa, G.; Moudrakovski, I.; Maier, J., Infiltrated porous oxide monoliths as high lithium transference number electrolytes. *Journal of Materials Chemistry A* **2016**, *4*, 7135-7140.

142. Vincent, C. A.; Bruce, P. G.; Hardgrave, M. T.; Shi, J., Constant-voltage polarization of symmetric polymer electrolyte cells with non-blocking electrodes. *Polymers for Advanced Technologies* **1993**, *4*, 144-151.

143. Ehrl, A.; Landesfeind, J.; Wall, W. A.; Gasteiger, H. A., Determination of Transport Parameters in Liquid Binary Lithium Ion Battery Electrolytes: I. Diffusion Coefficient. *Journal of The Electrochemical Society* **2017**, *164*, A826-A836.

2 New method to measure the rate of transport of redox species through membranes

2.1 Overview

This chapter presents a new in-situ method for measuring permeability of membranes to crossover redox species. The method employs a 'Swagelok' cell design equipped with a glassy carbon working electrode, in which crossover species are placed initially in the counter electrode compartment only. Permeability through the membrane (which separates working and counter electrodes) is determined using a square wave voltammetry technique that allows evaluation of the concentration of crossover species over time with very high precision. The method is tested using a model and well-behaved electrochemical system to demonstrate its sensitivity, reproducibility and reliability relative to alternative approaches. This new method offers advantages in terms of small electrolyte volume, and fast, facile, quantitative and in-situ measurement.

2.2 Background

As discussed in Chapter 1, lithium selective membranes have the potential to revolutionize the performance of lithium batteries. Promising post Li-ion candidates such as Li-S and Li-O_2 batteries operate with polysulfides or redox mediators that facilitate the reactions at the positive electrode, but these species are unstable at the lithium electrode, and hence protective lithium-selective membranes or coatings are required. Such membranes or coatings can also be advantageous for lithium-ion batteries to protect the anode from electrolyte oxidation products or transition metal species that have dissolved from the positive electrode. For these applications, a key property is the ability of the membrane to conduct lithium ions and block any other species.

Few studies have looked at permeability of membranes to crossover species in Li-O_2 batteries. Recently, Kim et al[1] used ex-situ XRD and XPS analysis of the lithium surface after cycling in a Li-O_2 cell to check for reaction with oxygen, water and cathode binder decomposition products. A similar approach was applied to Li-ion cells by MahootcheianAsl et al[2] who used ex-situ TEM and EDX of the graphite anode surface after cycling, to check for Mn crossover. Other, in-situ but indirect, approaches to measuring electrode 'crosstalk' have also been applied to Li-ion cells, such as analysis of the voltage drop and capacity fade during storage of graphite-$LiCoO_2$ cells.[3]

Permeability of membranes to polysulfides has been more widely studied. To date, however, this has generally relied on visual inspection (or in some cases spectroscopic analysis) of electrolytes in (or from) a two-compartment (e.g. H-type) cell (e.g. refs 4-7), ex-situ analysis of the membrane (e.g. using SEM/EDX (e.g. refs 7-8) or XAS (e.g. ref 9) to test for solubility/ trapping of polysulfides within it), and/or ex-situ analysis of the lithium anode surface after cycling to test for formation of Li_2S (e.g. refs 10-13). Suppression of polysulfide crossover is also typically inferred from cycling performance (upper plateau capacity, capacity retention, Coulombic efficiency, complete charging) or self-discharge behaviour of Li-S cells. More direct electrochemical techniques have also been applied. Li et al[14] placed a polysulfide solution in one compartment of an H-type cell, and evaluated the concentration of polysulfides in the other compartment, which was separated by a polymer membrane, using voltammetry and square wave voltammetry at a glassy carbon working electrode. Cui et al[15] employed a similar approach, in this case measuring rate of diffusion of polysulfides using linear sweep voltammetry in a two-electrode Swagelok cell with stainless steel working electrode. Dominiko et al[16] developed a method to measure polysulfide concentration in a modified, four-electrode Swagelok cell containing two perpendicular electrodes (nickel and platinum wires) in addition to the lithium and sulfur composite electrodes. Cyclic voltammograms were measured between the perpendicular electrodes at regular intervals during galvanostatic discharge of the Li-S cell and integration of the cathodic peak between 1.5 and 2.25 V used to determine the concentration of polysulfides. Vizintin et al[17] later applied this method to evaluate shuttle suppression by a functionalised graphene membrane. Lacey et al[18] developed a similar approach using a pouch cell with a platinum micro-electrode sensor to detect polysulfides during Li-S battery operation.

These approaches bring valuable insights into the mechanism of Li-S battery operation and the performance of membranes. However, interpretation of the results is difficult because of the complex electrochemistry of polysulfide species. Whilst cell designs have been reported for the detection of polysulfide crossover, none of the articles discussed tested the cell design with a model and well-behaved electrochemical system.

In this chapter, a simple, in-situ and direct approach for measuring permeability of membranes to crossover species is presented, using ethyl viologen as a model redox system to evaluate its performance. By using a model system, it is possible to identify the choice of cell design (working electrode material) and measurement technique that provides the most sensitive, stable and reproducible response.

2.3 Experimental details

Figure 2.1a illustrates the cell design developed. A glassy carbon working electrode or 'probe' (3 mm diameter, type 2, Alfa Aesar) is embedded in a 1-inch diameter glass disc attached to a glass tube. A thin copper rod in contact with the back face of the glassy carbon serves as the current collector. For some experiments, copper (1/2 inch diameter (nominal; 12.65 mm measured) HDHC rod, 99.9%, RS), stainless steel (1/2 inch diameter 316 stainless steel rod, RS) or aluminium (1/2 inch diameter 2011i aluminium rod, RS) working electrodes were used (Figure 1c).

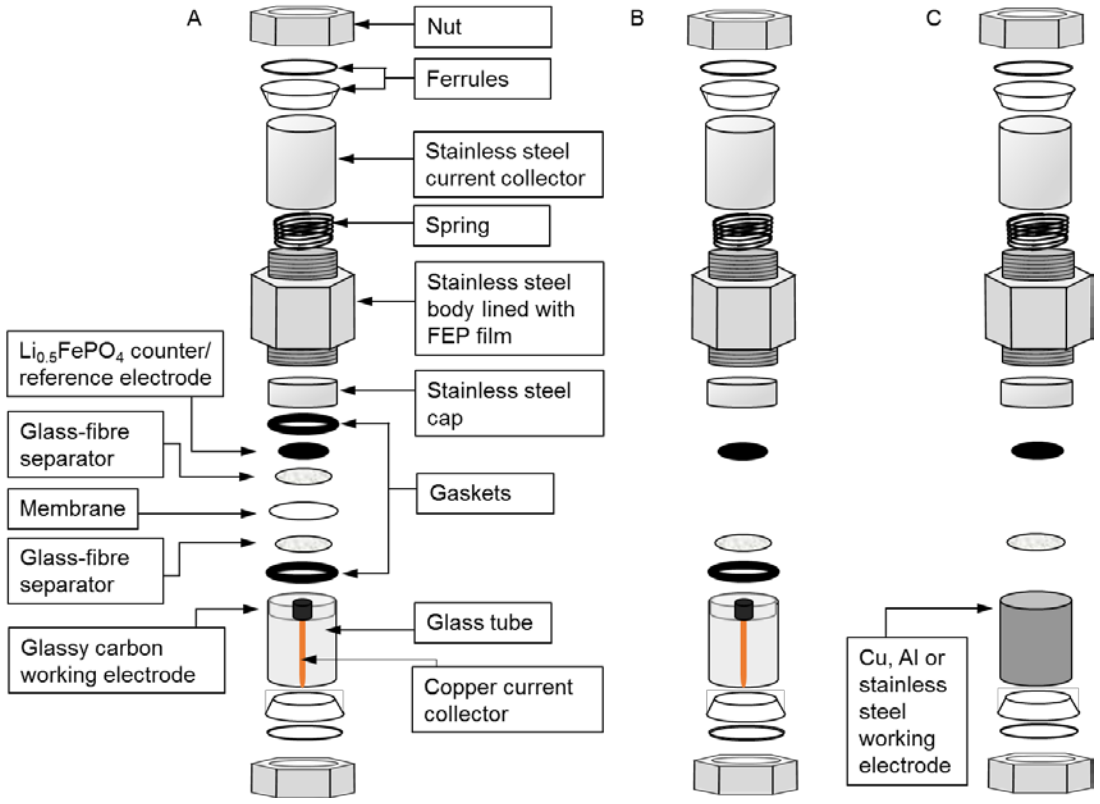

Figure 2.1: (a) sketch of Swagelok cell with glassy carbon electrode used for membrane permeability studies; (b) sketch of Swagelok cell with glassy carbon electrode used for initial voltammetric studies (c) sketch of Swagelok cell with copper working electrode.

$Li_{0.5}FePO_4$ electrodes were prepared by mixing $LiFePO_4$ (battery grade, Tatung), $FePO_4$ (prepared in-house by delithiating $LiFePO_4$)[19], carbon black (acetylene, 100% compressed, Chevron Philips) and PTFE (6CN, DuPont) in the ratio 4:4:1:4 (wt%) in a pestle and mortar. The composite material was roll-pressed to a thickness of 100 µm and punched to the required diameter (10 mm for cells with glassy carbon working electrode, 12 mm for cells with copper working electrode).

Prior to use, glassy carbon electrodes were polished with 25, 3.0 and 0.3 µm alumina powder in deionised water. Lithium ion conducting glass ceramic (LICGC™) plates (1 inch diameter, 150 µm thickness, Ohara Inc.) were sonicated in isopropyl alcohol. Both were dried under vacuum at 80 °C for a minimum of 30 minutes, along with chemically resistant gaskets (Ekraz 9655B, 24.5 mm outer diameter x 18.5 mm inner diameter x 0.5 mm thickness, supplied by Polymax Ltd.), coated with a thin layer of vacuum grease (Dow-Corning high vacuum silicone grease), which were used to prevent leakage of electrolyte around the edge of the membrane inside the cell. Copper, stainless steel and aluminium electrodes were cleaned either mechanically (sanded and polished in ethanol) or chemically (dipped in 70% nitric acid for 5 seconds, rinsed with deionised water then ethanol), and dried under vacuum at 80 °C for 10 minutes only, to minimise reformation of a surface oxide layer.

$Li_{0.5}FePO_4$ electrodes and glass fibre separators (Whatman, 300 µm thickness, punched to required 10 or 12 mm diameter) were dried under vacuum at 120 °C for 24 hours. Celgard (2320, punched to required 25 mm diameter) was dried under vacuum, unheated, for 24 hours.

For the electrolytes, ethyl viologen triflate ($EtV(OTf)_2$) was prepared in-house according to the literature[20] from ethyl viologen di-iodide ($EtVI_2$, 99%, Sigma-Aldrich) and silver triflate (AgOTf, ≥99%, Sigma-Aldrich). 1-butyl-1-methylpyrrolidinum bis(trifluoromethylsulfonyl)imide ($Pyr_{14}TFSI$) (99%, IoLiTec Ionic Liquids Technologies GmbH) and lithium bis(trifluoromethane)-sulfonamide salt (LiTFSI) (99.95%, Sigma-Aldrich) were dried and deoxygenated under vacuum at 120 °C for 24 hours. Electrolytes (0–4 mM $EtV(OTf)_2$ + 100 mM LiTFSI in $Pyr_{14}TFSI$) were prepared inside an argon filled glovebox (<1 ppm water content, < 10 ppm oxygen content, M-Braun). Cells were assembled inside the same glovebox. When assembling cells, 30 µL was used for each 10 mm separator (50 µL for 12 mm separators).

Electrochemical measurements were carried out using a Bio-logic VMP2 variable multichannel potentiostat/galvanostat. All SWV scans were carried out with the following parameters: ΔE_s = 10 mV, ΔE_p = 25 mV, t_p = 50 ms. All measurements were carried out at a controlled (external) temperature of 25 °C.

2.4 Results and discussion

2.4.1 Using square wave voltammetry to characterise crossover redox species

In conventional cyclic voltammetry, both Faradaic and non-Faradaic (e.g. double layer charging) processes contribute to the measured current. If the concentration of redox species is

low, the non-Faradaic currents can dominate. To overcome this, pulsed voltammetry techniques can be employed, which essentially strip out the non-Faradaic contribution from the signal. This is done by applying a series of potential 'pulses' and sampling the current after such time that the double-layer current has decayed but the Faradaic current is still high. The exact form the applied potential profile depends on the particular pulse technique. Square wave voltammetry (SWV) combines advantages (sensitivity, background suppression, diagnostic value) of several pulse voltammetry methods.[21]

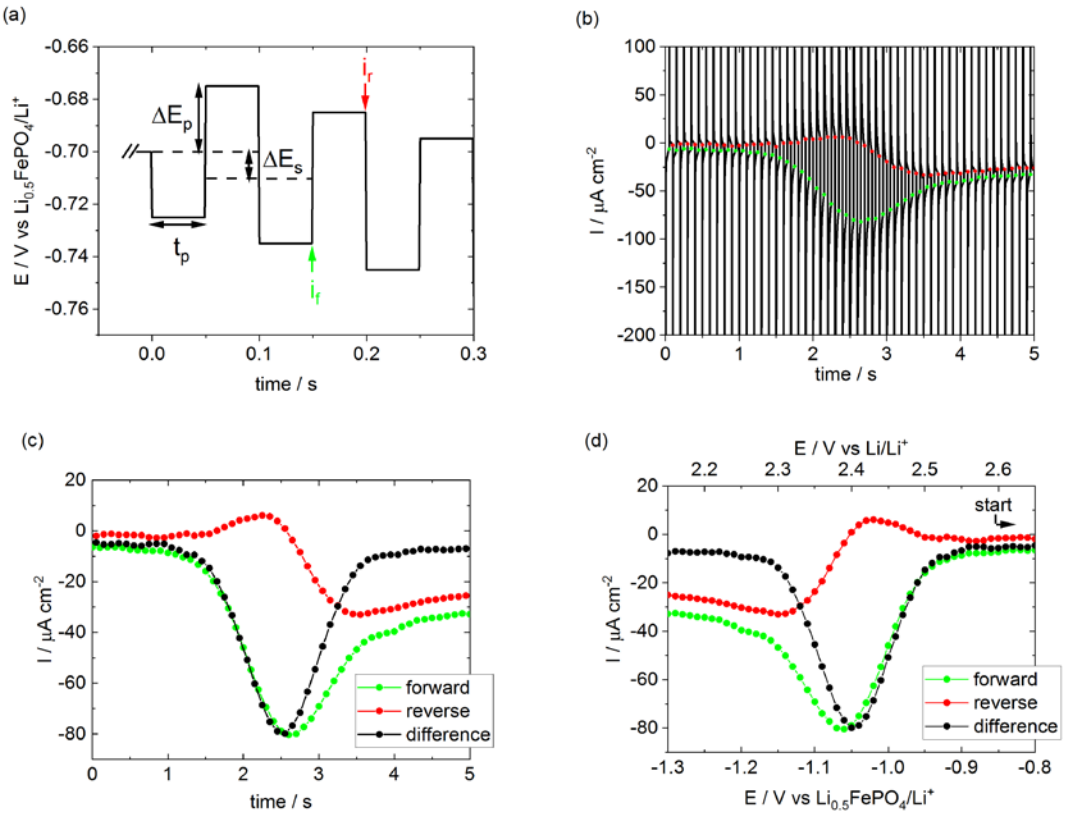

Figure 2.2: (a) Start of voltage profile applied in square wave voltammetry with ΔE_s = 10 mV, ΔE_p = 25 mV, t_p = 50 ms; (b) resulting current profile, normalised by electrode area; sampled forward (–), reverse (–) and difference (–) currents, , normalised by electrode area, as a function of (c) time and (d) electrode potential at the start of the forward and reverse pulse sequence. Data recorded in cell with glassy carbon working electrode, $Li_{0.5}FePO_4$ counter/reference electrode and 2 mM $EtV(OTf)_2$ + 100 mM LiTFSi in $Pyr_{14}TSFI$ electrolyte. See cell sketch in Figure 2.1b.

The application of SWV to a model redox system (ethyl viologen, EtV^{2+}) is illustrated in Figure 2.2. The voltage profile applied is shown in Figure 2.2a and is characterised by a 'staircase' starting well positive of the formal potential, $E^{0'}$, and with step height ΔE_s, a pulse height ΔE_p,

and a pulse width t_p. The square wave voltammogram is shown in Figure 2.2d, and equals the difference in current sampled at the end of the forward and reverse pulses, as a function of potential. Figure 2.2b shows the evolution of current vs. time. At the start of the scan, the Faradaic currents are small as the potential remains well negative of $E^{0'}$, even when the forward pulse is applied. In the middle of the scan, close to $E^{0'}$, the current depends strongly on potential: the forward pulse significantly increases the rate of reduction of EtV^{2+}, while the reverse pulse reverses the direction of current flow as EtV^{+} is oxidised back to EtV^{2+}. At the end of the scan, the staircase potential is well positive of $E^{0'}$ and the rate of reaction is diffusion-controlled, so that the potential pulses have little effect.

Current is sampled at the end of the forward and reverse pulses and a 'difference' current is calculated as $\Delta i = i_f - i_r$ as shown in Figure 2.2c. For a simple, reversible reaction, with only the oxidised species initially present in the solution, the potential at which the peak difference current occurs is given by:

$$E_{1/2} = E^{0'} + \left(RT/nF\right)\ln\left(D_R/D_O\right)^{1/2} \qquad \text{(Eq. 2.1)}$$

Where D_R and D_O are the diffusion coefficients of the reduced, and oxidized species, respectively, R is the gas constant, T is the temperature in Kelvin, n is the number of electrons and F is the Faraday constant.

The peak difference current is given by:

$$\Delta i_p = \frac{nFAD_O^{1/2}c_O^*}{\pi^{1/2}t_p^{1/2}}\Delta\psi_p \qquad \text{(Eq. 2.2)}$$

Where c_O^* is the initial concentration of the oxidized species and $\Delta\psi_p$ is a dimensionless parameter that is a function of ΔE_s and ΔE_p. Computed values for $\Delta\psi_p$ are available in the literature[22-23]; for ΔE_s = 10 mV and ΔE_p = 25 mV, $\Delta\psi_p$ = 0.569.

2.4.2 Testing of alternative probe materials and techniques

To investigate the performance of the glassy carbon probe with the SWV technique, initial experiments were conducted using a cell without a membrane, i.e. with a single glass fibre separator soaked with $EtV(OTf)_2$-containing electrolyte (Figure 2.1b). This can be done because the standard potential of the $Li_{0.5}FePO_4$ counter/reference electrode (ca. 3.45 V vs Li/Li^+) is more

positive than that of ethyl viologen (ca. 2.43 v vs Li/Li$^+$). Therefore EtV^{2+} is stable in contact with $Li_{0.5}FePO_4$. The reaction products of EtV^{2+} (i.e. EtV^+ or EtV) would be oxidised by $Li_{0.5}FePO_4$ but the timescale of the square wave voltammograms is much shorter than the timescale for these products to diffuse across the cell. In addition, the amount of EtV^+ or EtV produced is far too small to change the bulk concentration of the electrolyte within the separator.

Figure 2.3 shows multiple SWV scans of two separate cells with a glassy carbon working electrode, a $Li_{0.5}FePO_4$ counter/reference electrode and 2 mM $EtV(OTf)_2$ in the electrolyte. The initial sweep was in the cathodic direction. The EtV^{2+}/EtV^+ and EtV^+/EtV redox couples are clearly visible at ca. 2.02 V and 2.43 V vs. Li/Li$^+$. The measurements are highly stable and reproducible.

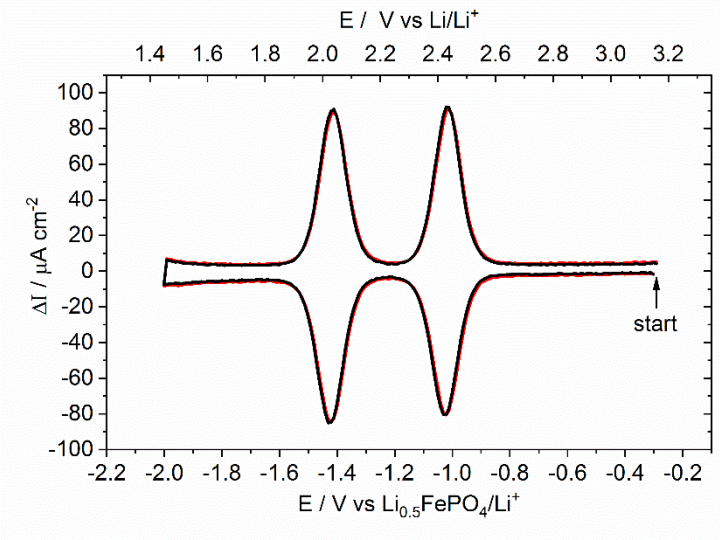

Figure 2.3: SWV scans recorded at glassy carbon electrode in two separate cells containing 2mM $EtV(OTf)_2$ in the electrolyte. Solid lines = 1st scan, dashed lines = 5th scan. All experimental conditions as in Fig. 2.2 and the cell used is sketched in Fig. 2.1b.

Similar experiments were carried out using copper working electrodes. Figure 2.4a compares SWV scans at the glassy carbon electrode and at the best-performing copper electrode, which had been treated mechanically. It can be seen that, relative to the glassy carbon electrode, the copper electrode is less sensitive (lower peak to residual double layer charging current ratio), less stable and less reliable (shows distortions from other redox processes). These distortions are even more apparent when comparing cyclic voltammograms (Figure 2.4b), with the copper electrode showing a small reduction peak at around 1.78 V vs. Li/Li$^+$ together with an additional broad oxidation peak/shoulder at ca. 2.65-3.05 V vs. Li/Li$^+$. (Based on cyclic voltammetry of a Cu-$Li_{0.5}FePO_4$ cell without $EtV(OTf)_2$ (Figure 2.5), these peaks are attributed to lithium insertion into a

residual copper oxide surface layer.[24]) Measurements with the copper working electrode were also less reproducible than those with the glassy carbon one.

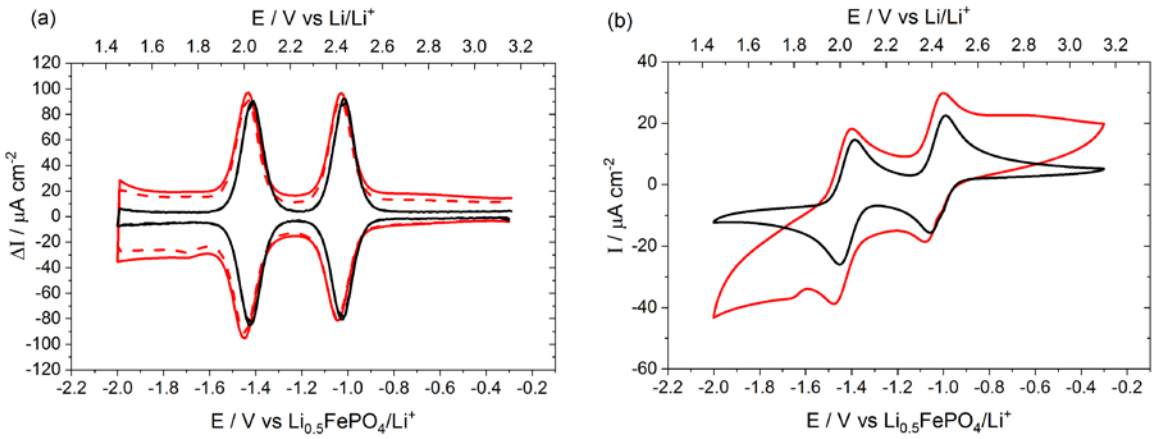

Figure 2.4: SWV scans (a) and CV scans (b), recorded at glassy carbon electrode (—) and mechanically-treated copper electrode (—) in cells containing 2mM EtV(OTf)$_2$ in the electrolyte. Solid lines = 1st scan, dashed lines = 5th scan. CV scan rate 20 mV s^{-1}. Other experimental conditions as in Fig. 2.2. The cells used are sketched in Fig. 2.1b (glassy carbon electrode) and Fig. 2.1c (copper electrode).

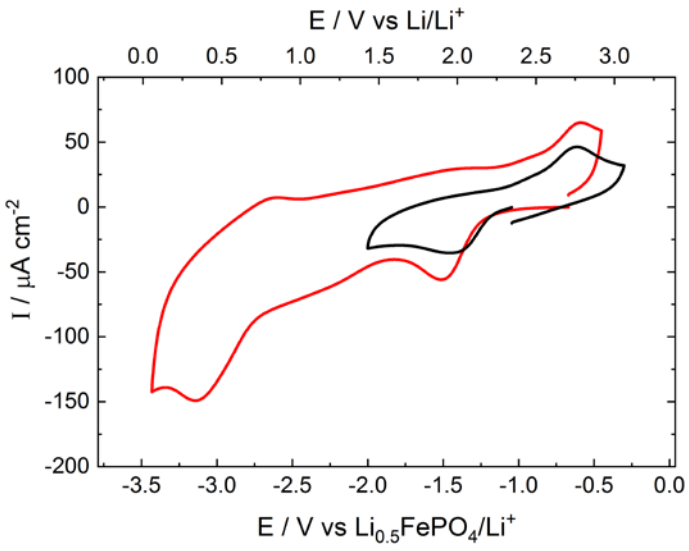

Figure 2.5: Cyclic voltammograms, with different potential limits, recorded at a copper electrode in a cell without EtV(OTf)$_2$ in the electrolyte. CV scan rate 20 mV s^{-1}. Other experimental conditions as in Fig. 2.2. The cell used is sketched in Fig. 2.1c.

The performance of chemically-treated copper electrodes showed no improvement over those treated mechanically, with the same additional peaks, large background current, and poor stability and reproducibility. The performance of (mechanically-treated) electrodes made from stainless steel or aluminium was even worse: scans recorded at stainless steel electrodes, although free from distortions, required several conditioning cycles to achieve (temporarily) stable peak heights, which nevertheless deteriorated over time (Figure 2.6a), whilst those recorded at aluminium electrodes showed very poor sensitivity (small peak to background current ratio), poor stability and large distortion at the cathodic limit (Figure 2.6b).

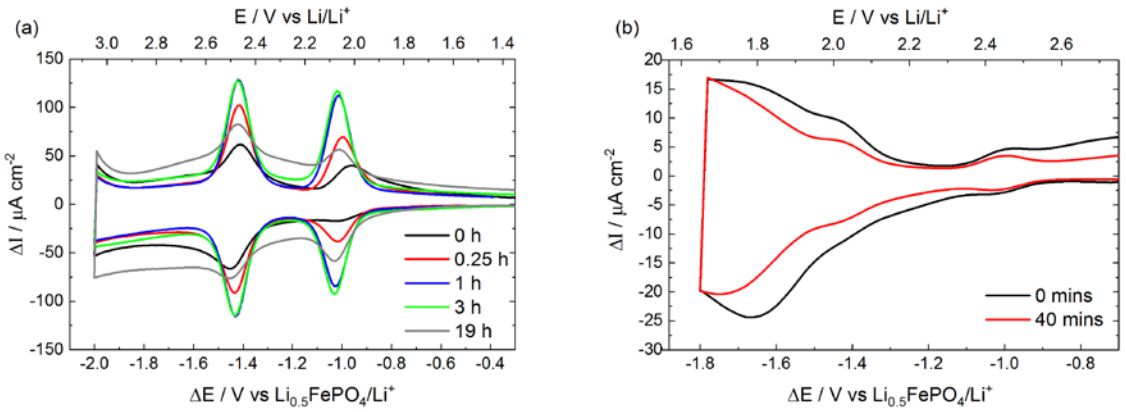

Figure 2.6: Square wave voltammograms recorded at (a) a stainless steel electrode and (b) an aluminium electrode in cells containing 4 mM EtV(OTf)$_2$ in the electrolyte. Experimental conditions as in Fig. 2.2. The cell used is sketched in Fig. 2.1c but with the copper electrode replaced by stainless steel or aluminium.

Figure 2.7 demonstrates the advantage of SWV over cyclic voltammetry at low concentrations (10 μM) of redox species using the glassy carbon electrode. Although the peaks corresponding to the ethyl viologen redox couples are weak, they are still clearly distinguishable in the SWV scan, in contrast to the cyclic voltammogram. The number of moles of EtV(OTf)$_2$ present in this cell is just 7.5 x 10^{-8}, and could be decreased further by using thinner separators and hence smaller electrolyte volume.

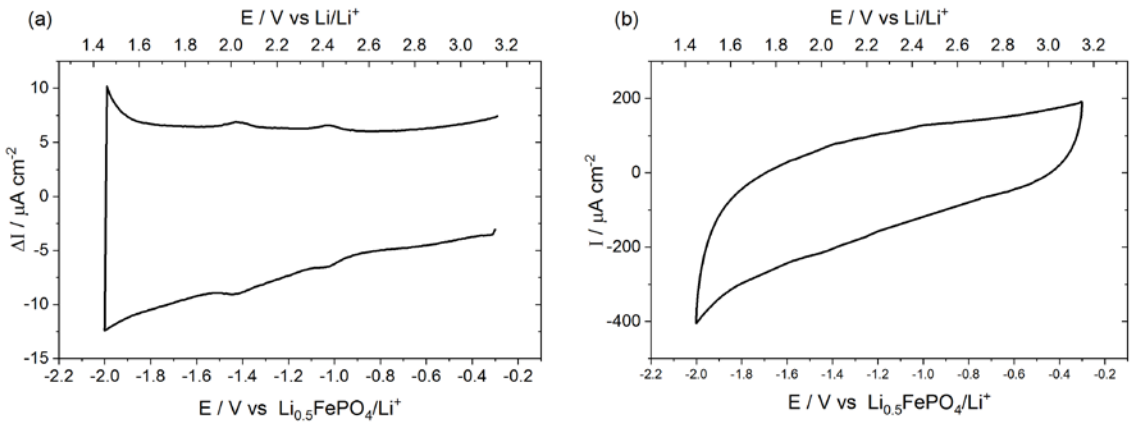

Figure 2.7: SWV scan (a) and cyclic voltammogram (b) recorded at a glassy carbon electrode in a cell containing 10 μM EtV(OTf)$_2$ in the electrolyte. CV scan rate 20 mV s^{-1}. Other experimental conditions as in Fig. 2.2. The cell used is sketched in Fig. 2.1b.

2.4.3 Testing for electrolyte leakage

In order to verify that the cell is well-sealed with gaskets, an Ohara LICGC™ plate was added to the cell, with EtV(OTf)$_2$ placed on the counter electrode side of this membrane only. LICGC™ is a single (lithium) ion conductor and therefore the only way for ethyl viologen species to pass from the counter to working electrode compartments would be via leakage of electrolyte around the membrane. However, no redox peaks relating to ethyl viologen appeared in SWV scans recorded over a two week period (Figure 2.8), confirming no such leakage.

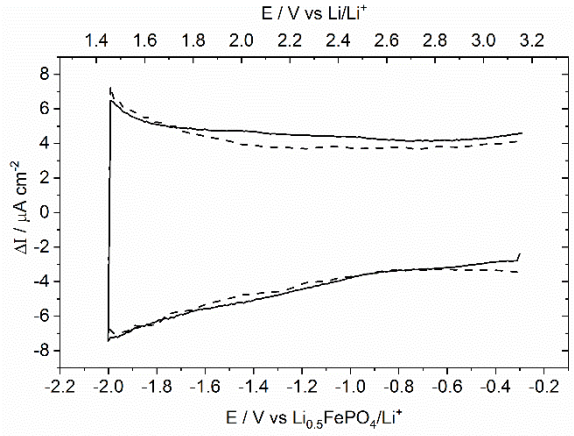

Figure 2.8: SWV scans recorded at glassy carbon electrode at the start (solid line) and end (dashed line) of a two week period, in a cell containing 2mM EtV(OTf)$_2$ in the counter/reference electrode compartment, which is separated from the working electrode compartment by a LICGC™ membrane. See cell sketch in Fig. 2.1a. Experimental conditions as in Fig. 2.2.

2.4.4 Cell calibration

According to equation 2.2, the size of the peak difference current in SWV can be used to determine the concentration of redox species if the diffusion coefficient in the electrolyte is known. In order to estimate the effective diffusion coefficient of EtV^{2+} in the present system, the glassy carbon electrode was used to record SWV scans for several known EtV^{2+} concentrations. Figure 2.9 shows the resulting plot of peak difference current versus concentration, which yields a value for the diffusion coefficient of $7.5 \cdot 10^{-8}$ cm^2 s^{-1} in the electrolyte when soaked into a glass fibre separator.

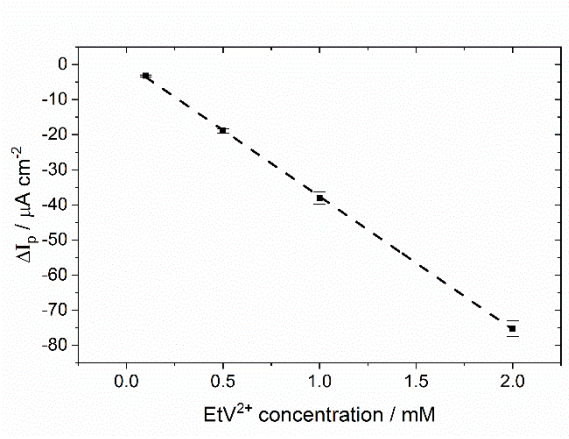

Figure 2.9: Peak difference current (net of residual double layer charging current and normalised by electrode area) for EtV^{2+}/EtV^{+} reduction from SWV scans recorded at a glassy carbon electrode in cells containing 0.1 – 2mM $EtV(OTf)_2$ in the electrolyte. Other experimental conditions as in Fig. 2.2 and the cell used is sketched in Fig. 2.1b.

2.4.5 Measuring permeability of a membrane to crossover species

As a proof of concept of the method, a cell was constructed with a permeable membrane (Celgard). As before, $EtV(OTf)_2$ was placed in the counter/reference electrode compartment only. In this case we would expect peaks corresponding to ethyl viologen redox processes to appear in voltammograms recorded at the glassy carbon electrode over time, as EtV^{2+} passes through the Celgard. Figure 2.10a demonstrates this phenomenon. No redox peaks are visible initially but gradually appear and grow as the concentration of EtV^{2+} in the working electrode compartment increases. As described above, equation 2.2 can be used to calculate this concentration from the size of the peak difference current, and as expected it tends to a value of *ca.* 2 mM (Figure 2.10b), indicating that the initial 0 mM and 4 mM concentrations in the working and counter electrode compartments respectively have equilibrated.

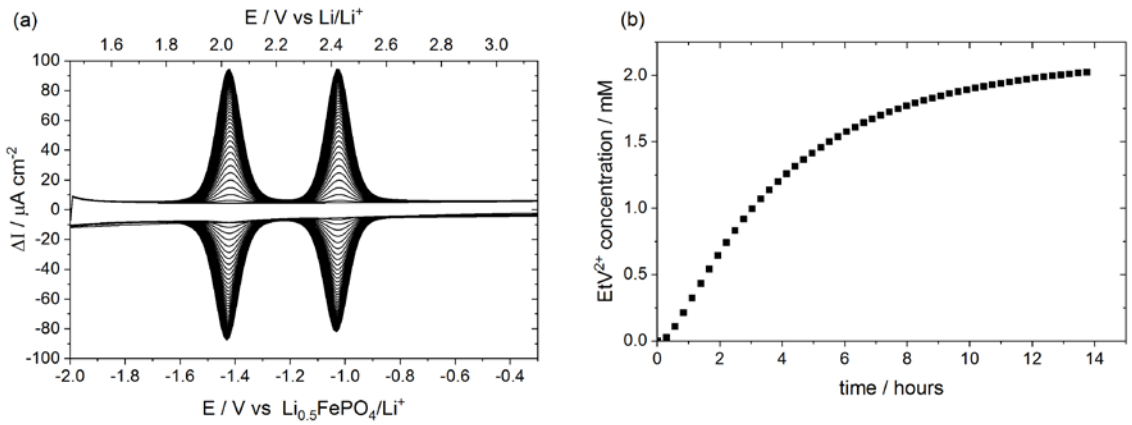

Figure 2.10: (a) SWV scans recorded at glassy carbon electrode at 15 minute intervals in a cell containing 4mM $EtV(OTf)_2$ in the counter/reference electrode compartment, which is separated from the working electrode compartment, which initially contains no $EtV(OTf)_2$, by a Celgard membrane. See cell sketch in Fig. 2.1a. Experimental conditions as in Fig. 2.2; (b) EtV^{2+} concentration in working electrode compartment over time, derived from peak difference currents in Fig. 2.10a.

2.5 Conclusions

In this chapter, a convenient, in-situ, direct and quantitative method for measuring permeability of membranes to crossover species has been demonstrated. Whilst several cell designs have been reported in the literature for the detection of polysulfide crossover in Li-S systems, none were tested with a model and well-behaved electrochemical system. By testing the present method with ethyl viologen, it has been possible to identify the electrode material that gives a more sensitive (lower limit of detection), reproducible and reliable (free from artefacts) response. It has also been possible to prove that, for crossover species with reversible redox kinetics, using a differential technique like square wave voltammetry produces a major increase in the sensitivity of the measurements, compared to other techniques such as cyclic voltammetry. This is because square wave voltammetry is able to separate the redox reaction of the crossover species from other processes such as double-layer charging.

Employing a glassy carbon electrode to record square wave voltammograms provides a sensitive, stable and reproducible means to detect crossover species. The new cell design allows testing of membrane permeability using small electrolyte volumes (35 μL) and can detect molar quantities less than 10^{-7} mole. The facile, in-situ measurement procedure makes it possible to record passage of redox species through the membrane in real time using a single cell. The quantitative nature of the measurements allows the rate of passage to be determined.

2.6 References

1. Kim, B. G.; Kim, J.-S.; Min, J.; Lee, Y.-H.; Choi, J. H.; Jang, M. C.; Freunberger, S. A.; Choi, J. W., A Moisture- and Oxygen-Impermeable Separator for Aprotic Li-O_2 Batteries. *Advanced Functional Materials* **2016**, *26*, 1747-1756.

2. MahootcheianAsl, N.; Kim, J.-H.; Pieczonka, N. P. W.; Liu, Z.; Kim, Y., Multilayer electrolyte cell: A new tool for identifying electrochemical performances of high voltage cathode materials. *Electrochemistry Communications* **2013**, *32*, 1-4.

3. Sinha, N. N.; Smith, A. J.; Burns, J. C.; Jain, G.; Eberman, K. W.; Scott, E.; Gardner, J. P.; Dahn, J. R., The Use of Elevated Temperature Storage Experiments to Learn about Parasitic Reactions in Wound $LiCoO_2$/Graphite Cells. *Journal of The Electrochemical Society* **2011**, *158*, A1194-A1201.

4. Conder, J.; Forner-Cuenca, A.; Gubler, E. M.; Gubler, L.; Novák, P.; Trabesinger, S., Performance-Enhancing Asymmetric Separator for Lithium–Sulfur Batteries. *ACS Applied Materials & Interfaces* **2016**, *8*, 18822-18831.

5. Huang, J.-Q.; Zhang, Q.; Peng, H.-J.; Liu, X.-Y.; Qian, W.-Z.; Wei, F., Ionic shield for polysulfides towards highly-stable lithium-sulfur batteries. *Energy & Environmental Science* **2014**, *7*, 347-353.

6. Wu, X.-l.; Zong, J.; Xu, H.; Wang, W.; Liu, X.-j., Effects of LAGP electrolyte on suppressing polysulfide shuttling in Li-S cells. *RSC Advances* **2016**, *6*, 57346-57356.

7. Yu, X.; Bi, Z.; Zhao, F.; Manthiram, A., Hybrid Lithium–Sulfur Batteries with a Solid Electrolyte Membrane and Lithium Polysulfide Catholyte. *ACS Applied Materials & Interfaces* **2015**, *7*, 16625-16631.

8. Cai, W.; Li, G.; He, F.; Jin, L.; Liu, B.; Li, Z., A novel laminated separator with multi functions for high-rate dischargeable lithium–sulfur batteries. *Journal of Power Sources* **2015**, *283*, 524-529.

9. Villaluenga, I.; Wujcik, K. H.; Tong, W.; Devaux, D.; Wong, D. H. C.; DeSimone, J. M.; Balsara, N. P., Compliant glass–polymer hybrid single ion-conducting electrolytes for lithium batteries. *Proceedings of the National Academy of Sciences* **2016**, *113*, 52-57.

10. Liu, M., et al., Novel gel polymer electrolyte for high-performance lithium–sulfur batteries. *Nano Energy* **2016**, *22*, 278-289.

11. Yu, X.; Joseph, J.; Manthiram, A., Polymer lithium-sulfur batteries with a Nafion membrane and an advanced sulfur electrode. *Journal of Materials Chemistry A* **2015**, *3*, 15683-15691.

12. Zeng, F.; Jin, Z.; Yuan, K.; Liu, S.; Cheng, X.; Wang, A.; Wang, W.; Yang, Y.-s., High performance lithium-sulfur batteries with a permselective sulfonated acetylene black modified separator. *Journal of Materials Chemistry A* **2016**, *4*, 12319-12327.

13. Zhu, J.; Ge, Y.; Kim, D.; Lu, Y.; Chen, C.; Jiang, M.; Zhang, X., A novel separator coated by carbon for achieving exceptional high performance lithium-sulfur batteries. *Nano Energy* **2016**, *20*, 176-184.

14. Li, C.; Ward, A. L.; Doris, S. E.; Pascal, T. A.; Prendergast, D.; Helms, B. A., Polysulfide-Blocking Microporous Polymer Membrane Tailored for Hybrid Li-Sulfur Flow Batteries. *Nano Letters* **2015**, *15*, 5724-5729.

15. Cui, Y.; Fu, Y., Polysulfide transport through separators measured by a linear voltage sweep method. *Journal of Power Sources* **2015**, *286*, 557-560.

16. Dominko, R.; Demir-Cakan, R.; Morcrette, M.; Tarascon, J.-M., Analytical detection of soluble polysulphides in a modified Swagelok cell. *Electrochemistry Communications* **2011**, *13*, 117-120.

17. Vizintin, A.; Patel, M. U. M.; Genorio, B.; Dominko, R., Effective Separation of Lithium Anode and Sulfur Cathode in Lithium–Sulfur Batteries. *ChemElectroChem* **2014**, *1*, 1040-1045.

18. Lacey, M. J.; Edström, K.; Brandell, D., Analysis of soluble intermediates in the lithium–sulfur battery by a simple in situ electrochemical probe. *Electrochemistry Communications* **2014**, *46*, 91-93.

19. Intaranont, N.; Garcia-Araez, N.; Hector, A. L.; Milton, J. A.; Owen, J. R., Selective lithium extraction from brines by chemical reaction with battery materials. *Journal of Materials Chemistry A* **2014**, *2*, 6374-6377.

20. Yang, L.; Frith, J. T.; Garcia-Araez, N.; Owen, J. R., A new method to prevent degradation of lithium-oxygen batteries: reduction of superoxide by viologen. *Chemical Communications* **2015**, *51*, 1705-1708.

21. Bard, A.; Faulkner, L., *Electrochemical Methods: Fundamentals and Applications*; John Wiley & Sons, Inc: New York, NY, USA, 2001.

22. Osteryoung, J. G.; O'Dea, J. J., In *Electroanalytical Chemistry: A Series of Advances*, Bard, A. J., Ed. Marcel Dekker Inc.: New York, NY, USA, 1986; Vol. 14, pp 209–325.

23. Osteryoung, J. G.; Osteryoung, R. A., Square wave voltammetry. *Analytical Chemistry* **1985**, *57*, 101-110.

24. Ke, F.-S.; Huang, L.; Wei, G.-Z.; Xue, L.-J.; Li, J.-T.; Zhang, B.; Chen, S.-R.; Fan, X.-Y.; Sun, S.-G., One-step fabrication of CuO nanoribbons array electrode and its excellent lithium storage performance. *Electrochimica Acta* **2009**, *54*, 5825-5829.

3 New method for evaluating selectivity and transference number in lithium conducting membranes

3.1 Overview

Building on the work in Chapter 2, this chapter presents a novel approach to evaluate the selectivity and transference numbers of lithium ion conducting membranes in-operando, under practically relevant conditions, including application of a current through the membrane. The method is illustrated with a lithiated Nafion membrane, immersed in 1 molal LiTFSI in diglyme containing 0.1 molal LiI as a model crossover species, and an accurate evaluation of both the diffusive permeability and transference number of crossover species in the membrane is reported, together with an estimate for the transference number of lithium in the membrane. It is also shown that the standard ex-situ methods of evaluation of membrane selectivity, as applied without a current passing through the membrane, provide a considerable overestimation of the capability of the membrane to block crossover species.

3.2 Background

Chapter 2 presented an in-situ method for measuring permeability of membranes to crossover species under open circuit conditions. However, membranes are used in cells in which current has to be applied. In addition to high selectivity (i.e. ability to block crossover species), key requirements thus include high Li^+ conductivity and high Li^+ transference number. As discussed in Chapter 1, the lithium transference number of membranes can in some cases be estimated via potentiostatic or galvanostatic polarization of a cell containing the membrane sandwiched between two lithium electrodes. Unfortunately, however, this method is not applicable for membranes that are unstable in contact with lithium, and it is not designed for membranes in contact with liquid electrolyte compartments (the analysis would need to be adapted to account for non-unity lithium transference number in the liquid electrolyte, and convection effects would need be eliminated, a condition which it has been shown is difficult to fulfil). On the other hand, such hybrid electrolyte systems are often employed, as they combine the advantages of liquid electrolytes, in terms of efficient wetting of the electrode and fast kinetics of the electrochemical reactions, with the protective role of lithium selective membranes in suppressing transport of crossover species.[1-13]

This chapter presents a cell design in which the crossover of species can be measured at intervals during the application of current through the membrane, applicable to the situation where the membrane is separating two liquid electrolyte compartments. A simple analytical model is presented for the variation in concentration of crossover species with time, provided that the rate of mass transport though the electrolyte can be considered to be much faster than the rate of mass transport through the membrane. By simple fitting of the model to experimental data obtained (i) under open circuit conditions and (ii) when a constant current is applied, values can be obtained for the diffusive permeability (which is related to the diffusion coefficient, see below) and transference number of crossover species in the membrane, and, for highly selective membranes, the transference number of lithium in the membrane. The approach is illustrated here for the case of a lithiated Nafion membrane and its ability to block the transport of iodide ions. Nafion membranes have been successfully used in Li-S cells to block transport of polysulfide species.[4-5, 10-11, 14-30] Iodide has a well-defined redox behaviour[31] and is used here as a model for polysulfide redox species.

3.3 Experimental details

Figure 3.1a illustrates the cell design, which is a modified version of the one used in Chapter 2 (Figure 2.1a). In this modified design, a further, ring-shaped, lithium electrode can be placed on the same side of the cell as the glassy carbon probe, with a nickel wire, embedded in the glass disc approximately 5 mm from the edge of the glassy carbon, serving as the current collector. The additional electrode allows Li^+ ions to be passed through the membrane by applying a constant current between this electrode and a lithium counter electrode on the opposite side. This current can be periodically interrupted to allow recording of voltammograms at the glassy carbon electrode at intervals in time. Figure 1b shows a simplified cell configuration used for calibration purposes.

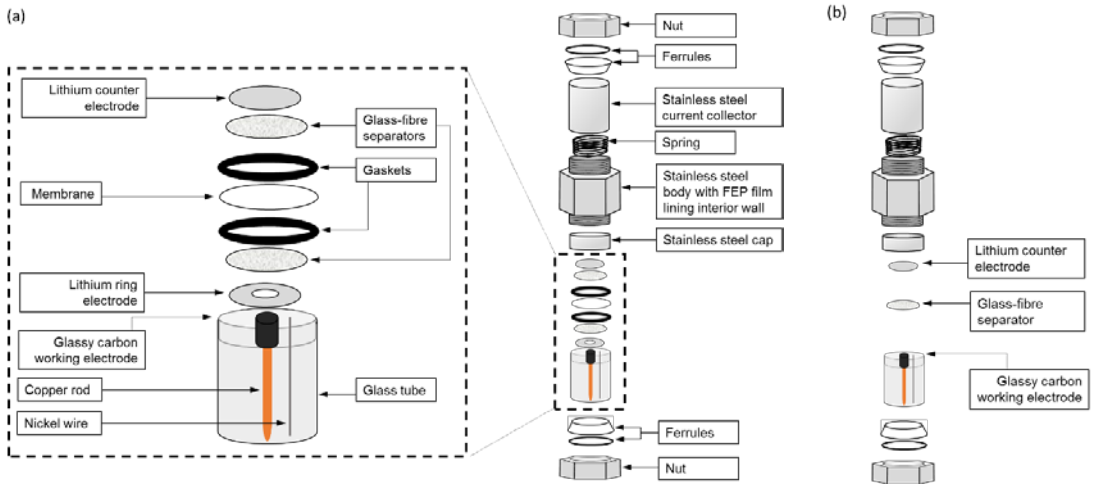

Figure 3.1 (a) Sketch of Swagelok cell with glassy carbon probe and additional electrode for passing current (b) Sketch of Swagelok cell with glassy carbon probe for cell calibration

Lithium-selective membranes were prepared by drop-coating a 1:1(vol) mixture of LiTHion™ dispersion (10-12 wt% in isopropyl alcohol, Ion Power) and isopropyl alcohol (>=99.5%, Fisher) onto both sides of a Celgard separator (Celgard 2320). Celgard sheets, ca. 40 x 40 mm, were clamped in a flat position and 110 µl of the LITHion mixture was drop-coated onto a central circular area, ca. 28 mm diameter, on one side of the sheet. This side was allowed to air-dry and the process was repeated for the other side, giving a dry mass loading of 1 mg cm^{-2} on each side. Once air-dry, the coated membranes were punched to 25 mm diameter and further dried under vacuum (unheated) for 72 hours, prior to use. Uncoated Celgard membranes were punched to the same diameter and dried in the same way. The thickness of coated membranes and of glass fibre separators was measured with a thickness gauge (Mitutoyo® ABSOLUTE Digimatic ID-C112X). In the case of glass fibre separators, which are compressible, the thickness of the compressed separator was measured immediately after cell disassembly, due to the difficulty in making a direct measurement of the thickness when under compression inside the cell, which is the relevant one for the analysis. However, previous work in the group[32] has shown that this method is accurate to within 10%. The thickness of the coated membranes was measured 24 hours after cell disassembly to allow the membranes to dry and avoid removal of the coating by the thickness gauge. However, given a stack pressure of less than 1 MPa due to the spring used in the cell (see Appendix C), and based on studies of the elastic properties of Celgard and Nafion membranes in the literature,[33-35] negligible compressive strain is expected in the membranes inside the cell.

Glass fibre separators (Whatman GF-F, punched to 14 mm diameter) were dried under vacuum at 120 ^{o}C for 24 hours. Glassy carbon electrodes were polished as described in Chapter 2 and dried, along with other cell components, under vacuum at 80 ^{o}C for a minimum of 1 hour.

For the electrolytes, lithium bis(trifluoromethane)-sulfonamide salt (LiTFSI) (99.95%, Sigma-Aldrich) and lithium iodide (LiI) (anhydrous, 99%, Sigma-Aldrich) were dried and deoxygenated under vacuum at 120 ^{o}C for 24 hours. Molecular sieves (4 Å beads, 4-8 mesh, Sigma-Aldrich) were dried under vacuum at 200 ^{o}C for 2 days and added to diethylene glycol dimethyl ether (diglyme) (anhydrous, 99.5%, Sigma-Aldrich) which was ready for use after 3 days. Electrolytes (1 molal (0.939 molar) LiTFSI in diglyme + 0–0.1 molal (0–0.0939 molar) LiI) were prepared inside an argon filled-glovebox (<1 ppm water content, < 10 ppm oxygen content, mBraun). Lithium electrode preparation and cell assembly were carried out inside the same glovebox. Lithium electrodes were punched from lithium foil (battery grade, 100 µm thickness, Rockwood Lithium), to 13 mm outer dimeter and, for the ring-shaped electrode, 5 mm inner diameter. When assembling cells, 55 µL of electrolyte was used for each glass fibre separator.

Conductivity measurements were carried out using half-inch Swagelok cells with copper current collectors. Prior to use, copper current collectors were polished in ethanol using 25, 3.0 and 0.3 µm alumina powder, sonicated in ethanol, rinsed in acetone and dried under vacuum, unheated, for 1 hour before being transferred to the glovebox. Other cell components were prepared as above. Cells were assembled containing either (a) 2 x glass fibre separators, (b) 2 x glass fibre separators with an uncoated Celgard membrane in between, or (c) 2 x glass fibre separators with a LITHion-coated Celgard membrane in between (all 12 mm diameter). 47 µL of electrolyte (1 molal LiTFSI in diglyme) was used for each glass fibre separator. Conductivity was evaluated using electrochemical impedance spectroscopy (EIS).

Electrochemical measurements were carried out using Bio-logic VMP2 and VMP3 variable multichannel potentiostat/galvanostat instruments. Cyclic voltammetry scans were carried out at a scan rate of 20 mV s^{-1}. During applied-current experiments, a constant current of 0.9 mA was applied (equivalent to 1 mA cm^{-2} at the lithium ring electrode). This current was interrupted at approximately 30 minute intervals, whilst voltammograms were recorded at the glassy carbon electrode. All measurements were carried out with the cell placed in climatic chamber (Memmert HPP110) at a temperature of 25 ^{o}C. Measurements were initiated a maximum of 2 minutes after cells were assembled.

3.4 Results and discussion

3.4.1 Simple model for the variation in concentration of crossover species with time

3.4.1.1 Under open circuit conditions

In the absence of current flow, crossover species, initially in the counter electrode compartment only, will diffuse through the membrane due to the concentration gradient across it, unless the membrane is highly selective towards lithium.

We will first consider the model sketched in Figure 3.2, in which the rate of transport of crossover species through the electrolyte impregnated in the glass fibre separator can be considered to be much faster than the rate of transport through the membrane (experimental evidence for this given in Section 3.4.2 below). This condition implies that the membrane is more efficient at suppressing the transport of crossover species than the liquid electrolyte, which should be the case for lithium protective membranes. Note, however, that this condition does not require a low conductivity of the membrane: the rate of transport of lithium ions within the membrane may indeed be very high, which should also be the case for practical applications. Mass transport is assumed to be via diffusion only, i.e. neglecting convection, which is a reasonable assumption for the present system where the liquid electrolyte is impregnated in the pores of the glass fibre separators or membrane.

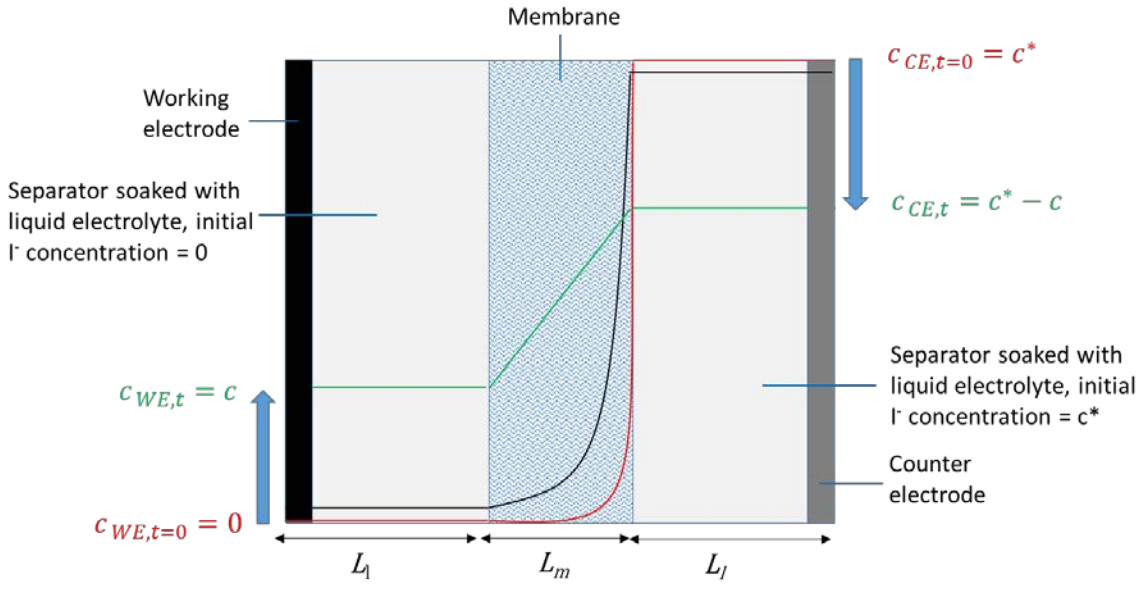

Figure 3.2: Evolution of the concentration profile as species pass through membrane, from counter electrode compartment (initial concentration = C*) to working electrode compartment (initial concentration = 0).

At short times ($t < \tau_1$), the distance travelled by crossover species through the membrane is smaller than the membrane thickness, and hence the rate of transport can be described by semi-infinite diffusion. But quickly after that ($t > \tau_1$), a linear variation of concentration over distance is established through the membrane, with the concentration of crossover species pinned at both ends of the membrane to the concentration values within the adjacent electrolyte compartments.

The flux of crossover species through the membrane is related to the variation of concentration with time inside the liquid electrolyte compartment as follows:

$$J = \frac{1}{A}\frac{dn}{dt} = \frac{V}{A}\frac{dc}{dt} = L_l \frac{dc}{dt} \qquad \text{(Eq. 3.1)}$$

where J is the flux through the membrane, A is the cross-sectional area of the membrane through which the flux passes, dn/dt is the number of moles of crossover species crossing the membrane per unit time, V is the volume of the electrolyte compartments, L_l is the thickness of the liquid electrolyte compartment (which in the present cell design equals V/A), and dc/dt is the variation of concentration of crossover species in the electrolyte compartments. All values in equation 3.1 are taken as positive, for simplicity.

For the situation in the absence of current, the flux of crossover species can also be described according to Fick's law as:

$$J = P_m \frac{c^* - 2c}{L_m} \qquad \text{(Eq. 3.2)}$$

where c^* is the initial concentration, $c^* - 2c$ is the change in concentration through the membrane, L_m is the membrane thickness and P_m is commonly referred to as the permeability coefficient or diffusive permeability.[36] (P_m is related to the diffusion coefficient of crossover species, D_c, according to $P_m = D_c K$ where K is the sorption coefficient between the liquid electrolyte and the membrane.[36]) Combining equations 3.1 and 3.2 we get:

$$J = P_m \frac{c^* - 2c}{L_m} = L_l \frac{dc}{dt} \qquad \text{(Eq. 3.3)}$$

Integration of equation 3.3 yields:

$$\frac{1}{2}\left(\ln \frac{c^*}{c^* - 2c}\right) = \frac{t - \tau_1}{\tau_2} \qquad \text{(Eq. 3.4)}$$

where $\tau_2 = L_m L_l / P_m$ and τ_1 is a fitted parameter, that includes the time required for a linear concentration profile to be established within the membrane. A plot of $\frac{1}{2}\ln\left(c^* / \left(c^* - 2c\right)\right)$ vs. $\left(t - \tau_1\right)$ should therefore be linear, with a slope of $1/\tau_2$ from which P_m can be obtained.

Rearrangement of equation 3.4 gives the following equation for the variation of concentration with time:

$$c = \frac{1}{2} c^* \left(1 - \exp\left[\frac{2\tau_1 - 2t}{\tau_2}\right]\right) \qquad \text{(Eq. 3.5)}$$

3.4.1.2 Under current flow conditions

Now, if a current is passed through the membrane, between the lithium ring electrode and the lithium counter electrode, we expect a change in the rate of the crossover due to the additional effects of migration. The change in rate will depend on the direction of the direction of the applied current and whether the crossover species is positively or negatively charged.

Assuming again that mass transport in the liquid is much faster than in the membrane, such that concentration gradients in the liquid electrolyte compartments due to the effects of migration can be neglected, then under a constant applied current density, the following equation can be proposed for the flux of crossover species:

$$J = P_m \frac{c^* - 2c}{L_m} + \frac{I t_c}{F} = L_l \frac{dc}{dt} \qquad \text{(Eq. 3.6)}$$

where I is the magnitude of the applied current density, t_c is the transference number of crossover species and F is Faraday's constant. (Equation 3.6 is similar to the Nernst-Planck equation[37], which describes the flux of ions under the influence of a concentration gradient and an electric field.) We have taken the sign convention that negative currents are those that strip lithium from the working electrode and hence speed up the transport of negatively charged crossover species (with negative values of z) from the counter to the working electrode (Figure 3.3).

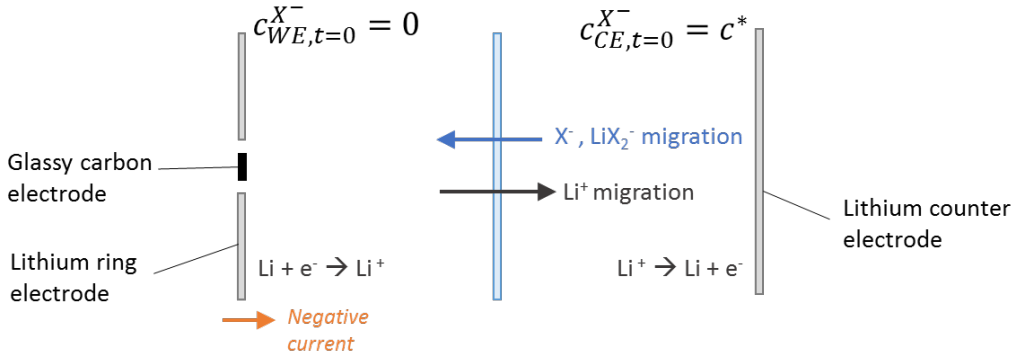

Figure 3.3. Schematic of ion transport through the membrane when current is applied. X^- represents a negatively charged crossover species.

Integration of equation 3.6 gives:

$$\frac{1}{2}\left(\ln\frac{c^* + bI}{c^* - 2c + bI}\right) = \frac{t - \tau_1}{\tau_2} \qquad \text{(Eq. 3.7)}$$

where $b = \frac{L_m}{P_m}\frac{t_c}{F} = \frac{\tau_2}{L_l}\frac{t_c}{F}$.

This gives the following equation for the variation of concentration with time:

$$c = \frac{1}{2}(c^* + bI)\left(1 - \exp\left[\frac{2\tau_1 - 2t}{\tau_2}\right]\right) \qquad \text{(Eq. 3.8)}$$

A plot of c vs. $\left[1 - \exp\left(-2\left(t - \tau_1\right)/\tau_2\right)\right]$ should therefore be linear, and b can be evaluated from its slope, since the value of applied current density I and initial concentration c^* are known. Then, t_c can be obtained by combining the value of b with τ_2 and the thickness of the liquid electrolyte compartment, L_l, as follows:

$$t_c = \frac{bP_m F}{L_m} = \frac{bL_l F}{\tau_2} \qquad \text{(Eq. 3.9)}$$

Therefore, the transference number can be evaluated using experimental data with and without current.

Finally, if we assume similar speciation (in terms of free ions vs. ions pairs and aggregates) for the lithium salt anion as for the crossover species, and similar mobilities in the membrane, we

can make the approximation that the relative rate of transport of the anion is simply proportional to its relative concentration:

$$\frac{t_{anion}}{c_{anion}} \approx \frac{t_c}{c^*} \qquad \text{(Eq. 3.10)}$$

where t_{anion} and c_{anion} are the transference number and concentration, respectively, of the lithium salt anion. (Whether in reality speciation and mobilities are similar will depend on the relative sizes (steric effect) and charge densities (electrostatic effect) of the species involved.)

Then an estimate of the transference number of lithium in the membrane, t_{Li^+}, can be made:

$$t_{Li^+} = 1 - t_c - t_{anion} \approx 1 - \left(1 + \frac{c_{anion}}{c^*}\right) t_c \qquad \text{(Eq. 3.11)}$$

Note that the above approximation is only appropriate for small values of t_c, i.e. for highly selective membranes, where the effect of the approximation on the estimation of t_{anion} and hence t_{Li^+} is small. However, the present approach for the evaluation of the transference number of crossover species, t_c, is suitable for any type of membrane.

3.4.2 Membrane conductivity

EIS was used to evaluate the conductivity of the membrane and glass fiber separators. Measurements were taken of a cell with two copper blocking electrodes containing (i) the LiTHION-coated Celgard membrane sandwiched between two separators impregnated with liquid electrolyte (Figure 3.4, black curves); (ii) an uncoated Celgard membrane plus two separators impregnated with liquid electrolyte (Figure 3.4, blue curves); (iii) only the two separators impregnated with the same liquid electrolyte used in (i) (Figure 3.4, red curves); (iii) only the two separators impregnated with the same liquid electrolyte used in (ii) (not shown). The results were fitted with an equivalent circuit comprising a constant phase element in series with a resistor, giving resistance values of (i) 30.9 ± 5.3 Ω; (ii) 9.5 ± 0.1 Ω; (iii) 7.2 ± 0.2 Ω; (iv) 8.3 ± 0.2 Ω. Error bounds were obtained from the reproducibility of the experiments. Subtracting (iii) from (i), the resistance of the coated membrane was estimated as 23.7 ± 5.3 Ω. Subtracting (iv) from (ii), the resistance of the uncoated membrane was estimated as 1.2 ± 0.2 Ω. The resistance, R_m, of the membrane coating (which is the selective part of the membrane, see below), was therefore obtained as 22.5 ± 5.3 Ω.

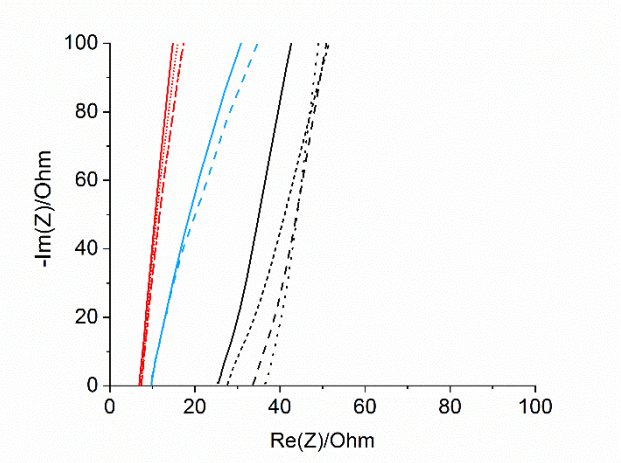

Figure 3.4. Impedance measurements recorded in half-inch Swagelok cells with copper current collectors containing (red) 2 x glass fibre separators soaked with liquid electrolyte (1 M LiTFSI in diglyme), (blue) 2 x glass fibre separators soaked with liquid electrolyte, with an uncoated Celgard membrane in between, or (black) 2 x glass fibre separators soaked with liquid electrolyte, with a LITHion-coated Celgard membrane in between. The plot shows results from repeat experiments obtained with several different cells for each condition.

The membrane coating conductivity, σ_m, could then be obtained using the following:

$$\sigma_m = \frac{L_m}{R_m A} \qquad \text{(Eq. 3.12)}$$

where L_m is the membrane coating thickness ($(1.8 \pm 0.2) \cdot 10^{-3}$ cm), obtained by comparison of the measured thicknesses of coated and uncoated membranes, and A is the membrane area (1.13 cm^2). Using equation 3.10, a value of σ_m of $(7.1 \pm 1.9) \cdot 10^{-5}$ S cm^{-1} was obtained. In addition, the conductivities of the glass fiber separator impregnated with liquid electrolyte (thickness $(35.1 \pm 0.4) \cdot 10^{-3}$ cm), and of the uncoated Celgard membrane (thickness $2.0 \cdot 10^{-3}$cm), were evaluated as $(8.6 \pm 1.0) \cdot 10^{-3}$ S cm^{-1} and $(1.4 \pm 0.2) \cdot 10^{-3}$ S cm^{-1} respectively.

The conductivity of the glass fiber separator impregnated with liquid electrolyte ($(8.6 \pm 1.0) \cdot 10^{-3}$ S cm^{-1}) is therefore much larger than the conductivity of the membrane coating ($(7.1 \pm 1.9) \cdot 10^{-5}$ cm^{-1}). Given a similar transference number in both media, this would imply that the mass transport rate of crossover species in the liquid electrolyte is much faster than in the membrane. In fact, it is reasonable to assume that the transference number of crossover species is much larger in the liquid electrolyte than in the membrane, and thus the difference in mass transport rate of crossover species is expected to be even bigger than the difference in conductivity. Experimental evidence for this is provided below.

3.4.3 Using cyclic voltammetry to measure the concentration of crossover species

Iodide was chosen as a model negatively charged redox system. From a practical point of view, iodide does not react in contact with lithium, which allows the use of lithium metal electrodes in the cell to pass current, while for other redox crossover species other electrode materials can be used (e.g. as was done in Chapter 2). Figure 3.5a shows a cyclic voltammogram recorded at the glassy carbon electrode in a cell containing 0.1 molal LiI, using the set-up shown in Figure 3.1b. There are two oxidation peaks: the I^-/I_3^- peak at ca. 3.3 V vs Li/Li^+, and the I_3^-/I_2 peak at ca. 3.9 V vs Li/Li^+. The corresponding reduction peaks are at ca. 2.4 V vs Li/Li^+ and ca. 3.6 V vs Li/Li^+ respectively.

In Chapter 2, where ethyl viologen was used as a model redox system, square wave voltammetry (SWV) was shown to produce the most sensitive response to low concentrations. This is because the ethyl viologen redox couples involve fast, highly reversible reactions. However, for the slower, irreversible reactions involved in I^- oxidation and reduction (indicated by the asymmetry and wide separation of the oxidation and reduction peaks in the voltammogram), cyclic voltammetry was found to produce a clearer response than SWV[38] (see Appendix C).

Further voltammograms of I^- recorded in the same cell as Figure 3.4a at 30 minute intervals are shown in Figure 3.5b. Some changes can be seen over time; however the peak at ca. 3.9 V associated with oxidation of I_3^- to I_2 was found to be have reasonable stability (within 15%). The reproducibility for different cells and cell designs was also within 15 % (Figure 3.5 c,d). For this reason, the I_3^-/I_2 peak was used as the basis for cell calibration (Section 3.4.4) and subsequent evaluation of iodide concentration in the working electrode compartment during crossover experiments (Section 3.4.4).

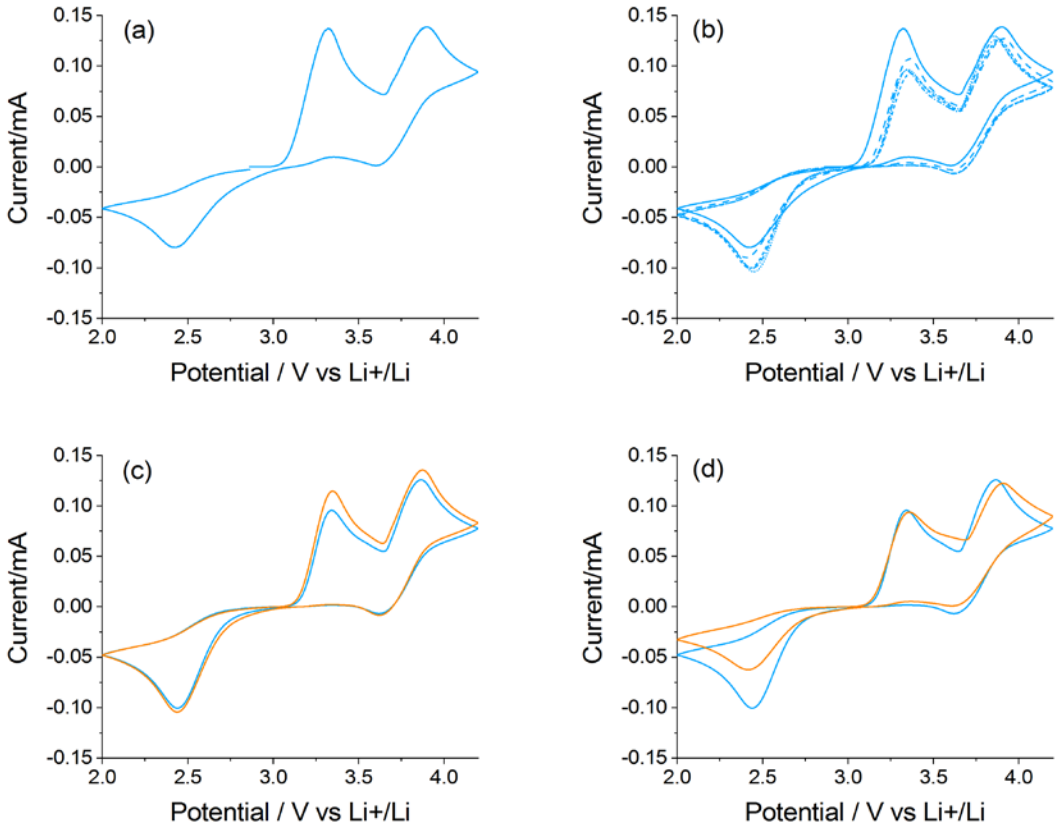

Figure 3.5 (a) Cyclic voltammogram (first cycle) recorded at a scan rate of 20 mV s^{-1} in a cell with glassy carbon working electrode, 0.1 molal LiI + 1 molal LiTFSI in diglyme electrolyte, and lithium counter electrode. Cell set-up is shown in Figure 3.1b. Forward scan in the positive direction. (b) Successive cyclic voltammograms at 30 minute intervals recorded in the same cell as (a). (c) Cyclic voltammograms (third cycle) recorded in two different cells using the same cell set-up and conditions as (a). (d) Cyclic voltammograms (third cycle) recorded using the cell set-up shown in Figure 3.1a (blue) and in Figure 3.1b (orange) with 0.1 molal LiI + 1 molal LiTFSI in diglyme electrolyte present in both liquid electrolyte compartments; other conditions as in (a).

3.4.4 Cell calibration

The similarity of the voltammograms in Figure 3.5d confirmed that the simplified cell set-up shown in Figure 3.1b could be used to obtain a calibration curve between peak current and iodide concentration, which could then be applied to crossover experiments performed using the cell set-up shown in Figure 3.1a.

Figure 3.6 plots I_3^-/I_2 peak current (first cycle), recorded using the simplified cell set-up shown in Figure 3.1b with different LiI concentrations. For the conversion of molal concentrations (that is, moles per kg of solvent) to molar concentrations (that is, moles per dm^3 of electrolyte),

the density of the electrolyte (1 molal LiTFSI + 0.01 molal LiI in diglyme) was measured experimentally by weighing a fixed volume, obtaining a value of 1.069 g mL^{-1}.

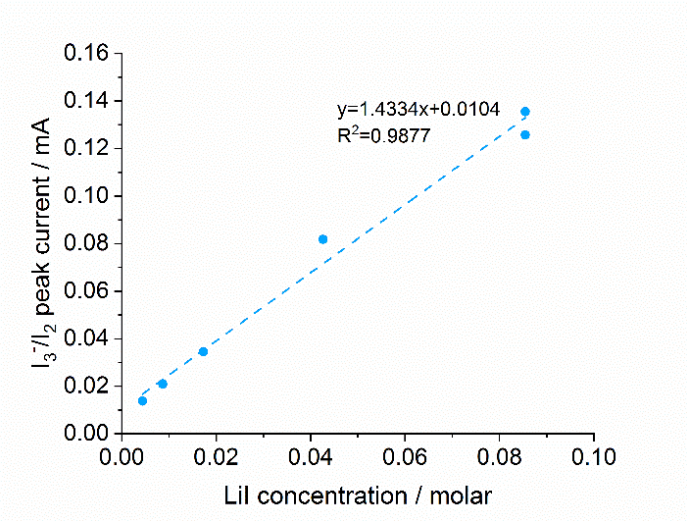

Figure 3.6. I_3^- / I_2 peak current obtained from cyclic voltammograms at a scan rate of 20 mV s^{-1} recorded in cells with electrolytes containing different concentrations of LiI. All other experimental conditions as in Figure 3.5a.

3.4.5 Crossover under open circuit conditions

To test the present model for the variation in concentration of crossover species with time under open circuit conditions, cells were constructed according to Figure 3.1a, with 0.1 molal LiI placed initially in the counter electrode compartment only, and cyclic voltammograms were recorded at approximately 30 minute intervals. The concentration of iodide in the working electrode compartment over time was evaluated from the size of the I_3^-/I_2 peak current in each voltammogram, using the experimentally determined calibration curve in Figure 3.6. The results are plotted in Figure 3.7. As expected, over time the iodide concentration approaches 0.047 molar, as the initial concentrations in the working and counter electrode compartments equilibrate.

Figure 3.8 plots the data according to equation 3.4 and shows that the present model provides an excellent fit. From the slope of the plot, the (average) diffusive permeability, P_m, of iodide in the membrane is evaluated as (5.1 ± 0.3) x 10^{-9} cm^2 s^{-1}. Note that for the data fitting, τ_1 was set to zero. This simplification was made due to the fact that there is a delay between cell assembly and the start of the experiments, and therefore it is not possible to accurately determine from the data the time taken for a linear concentration profile to be established in the

membrane. However the value of τ_1 does not affect the evaluation of the permeability coefficient, only the transference number (see below).

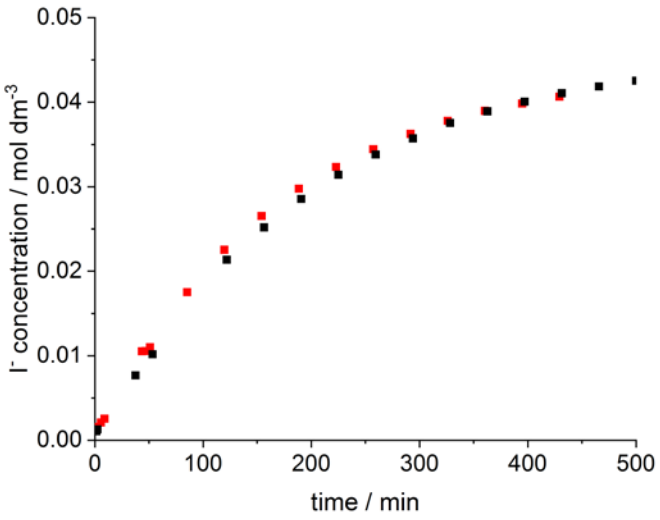

Figure 3.7. Increase over time, evaluated using cyclic voltammetry, in the concentration of iodide in the working electrode compartment of a two-compartment cell, initially containing 0.1 molal LiI in the counter electrode compartment only. The compartments are separated by a Celgard membrane coated on both sides by LITHion. See cell sketch in Figure 3.1a. Other experimental conditions as in Figure 3.5. Concentrations were calculated from I_3^- / I_2 peak currents using the calibration curve in Figure 3.6. The plot shows results from repeat experiments obtained with two different cells.

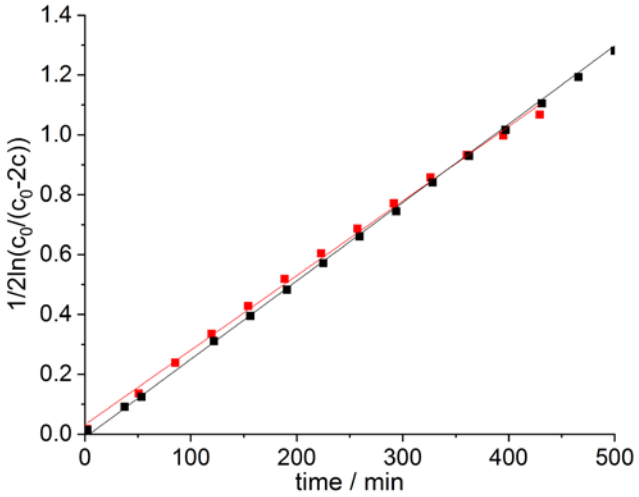

Figure 3.8. Data shown in Fig. 3.6, replotted using equation 3.4, with τ_1 = 0.

In order to test the earlier assumptions (i) that the selective part of the membrane is the coating and therefore the relevant 'membrane' thickness is that of the coating; and (ii) that the rate of mass transport in the electrolyte-soaked separators is much faster than in the Nafion-coated membrane, which is a condition of the present model, Figure 3.9 compares the evolution of iodide concentration in the working electrode compartment of cells containing coated and uncoated Celgard membranes. It can be seen that transport through uncoated Celgard is very fast compared to transport through coated Celgard. Therefore the rate limiting step in the coated membrane must be transport of iodide through the LITHion coating. The value of P_m obtained above might therefore be expected to be similar to values reported in the literature for other forms of lithiated Nafion, and we find that this is the case.[39-40] Combined with the fact that the conductivity of electrolyte-soaked glass fiber separator ($(8.6 \pm 1.0) \cdot 10^{-3}$ S cm^{-1}) is, in turn, larger than that of uncoated Celgard ($(1.4 \pm 0.2) \cdot 10^{-3}$ S cm^{-1}) (see Section 3.4.2), Figure 3.9 also confirms that the rate of mass transport in the electrolyte-soaked separators is much faster than in the Nafion-coated membrane.

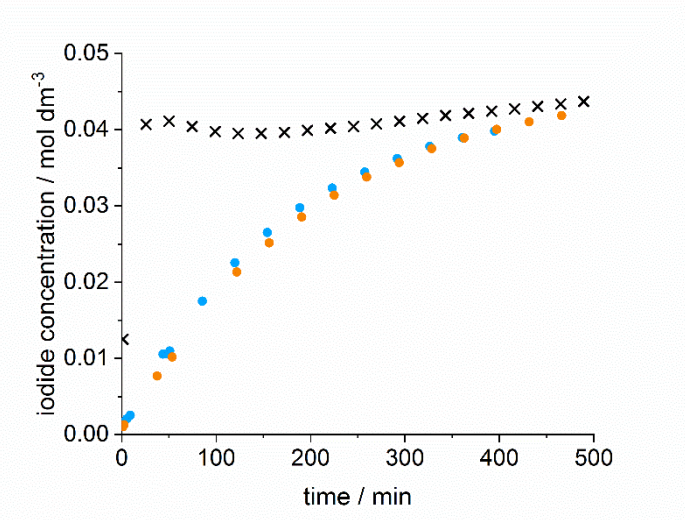

Figure 3.9. Increase over time in the concentration of iodide in the working electrode compartment of a two-compartment cell, initially containing 0.1 molal LiI in the counter electrode compartment only, with compartments separated by either an uncoated Celgard membrane (crosses), or a LITHion-coated membrane (dots, data from Figure 3.6). Other experimental conditions as in Figure 3.5.

3.4.6 Crossover under current flow conditions

To test the model in the case of applied current, cells were constructed as before, according to Figure 3.1a, with 0.1 molal LiI placed initially in the counter electrode compartment only. A constant anodic current was applied to the lithium ring electrode (with the lithium disc as

the counter electrode), and was interrupted at approximately 30 minute intervals to allow cyclic voltammograms to be recorded at the glassy carbon electrode (again with the lithium disc as the counter electrode). Figure 3.10 plots the evolution of the concentration of iodide in the working electrode compartment over time, and compares this with the no-current case. A significant enhancement in the rate of crossover is observed when a positive current is applied, providing clear evidence that the selectivity of the membrane can be overestimated if the measurements are done ex-situ without the application of a current.

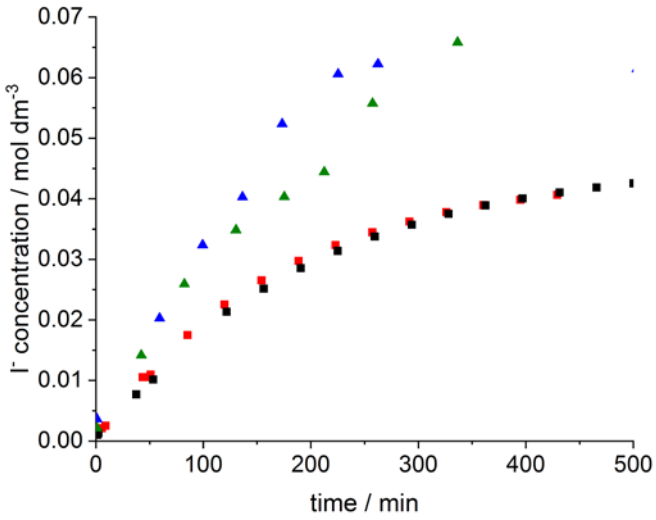

Figure 3.10. Increase over time in the concentration of iodide in the working electrode compartment of a two-compartment cell, initially containing 0.1 molal LiI in the counter electrode compartment only, with compartments separated by a LITHion-coated Celgard membrane, under open circuit conditions (squares, data from Figure 3.7 and on application of current of 1 mA cm^{-2} (triangles). Other experimental conditions as in Figure 3.5. The plot shows results from repeat experiments obtained with two different cells for each condition.

Figure 3.11 plots the data for the applied-current case according to equation 3.8 and again shows that the present model provides an excellent fit. From the slope of the plot, and given the value for P_m of (5.1 ± 0.3) x 10^{-9} cm^2 s^{-1} evaluated earlier, the transference number of iodide in the membrane is evaluated as 0.0193 ± 0.0028. As with the open circuit case in section 3.4.5, the value of τ_1 was again set to zero for the data fitting. Unlike evaluation of the diffusive permeability, evaluation of the transference number is affected by τ_1; however, the effect is modest. For example, using a value of -120 seconds for τ_1 (negative to reflect the delay between cell assembly and the start of the experiment) changes the value of the transference number to 0.0195 $\pm$ 0.0029.

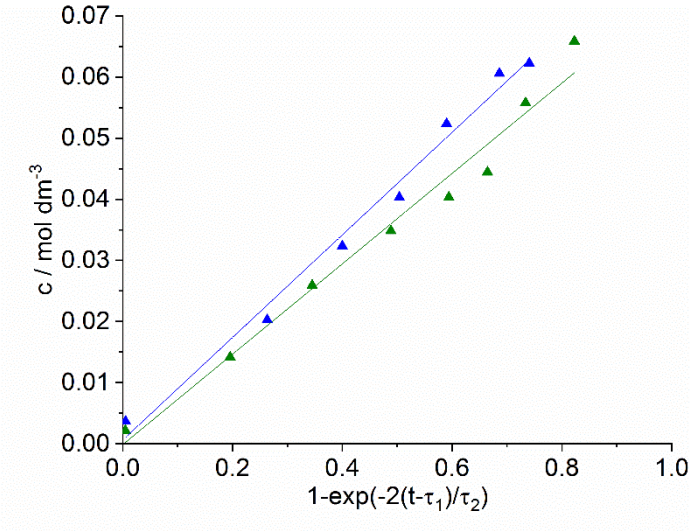

Figure 3.11. Data shown in Fig. 3.10, replotted using equation 3.8.

The current model makes no assumptions about the presence or absence of ion interactions in the membrane. However, it can be shown (see Appendix C) that, in the absence of ion interactions (i.e. where the Nernst-Einstein equation can be used to relate molar conductivities and diffusion coefficients in the membrane), then the transference number of crossover species can also be estimated using equation 3.13:

$$t_c = \frac{P_m F^2 c^*}{RT\sigma_m} \qquad \text{(Eq. 3.13)}$$

(Equation 3.13 was also derived by Su et al[39] and used to estimate the transference number of crossover species in Nafion membranes.)

Given values of $(7.1 \pm 1.9) \cdot 10^{-5}$ S cm^{-1} for σ_m (see Section 3.4.2), $(2.7 \pm 0.4) \cdot 10^{-9}$ cm^2 s^{-1} for P_m, and 0.089 ± 0.004 M for c^*, equation 3.15 provides an estimate of 0.0132 ± 0.004 for the transference number of I^- in the membrane. This is in excellent agreement with the value obtained using the present model based on the rate of crossover of species through the membrane, although, as noted, the Nernst-Einstein equation is not expected to be applicable in the presence of ion-ion interactions.

Finally, using equation 3.9, and the value for $t_{crossover}$ obtained using the present model, we arrive at a value of 0.92 for the transference number of lithium in the membrane, consistent with values reported for other forms of lithiated Nafion.[20]

3.5 Conclusions

In this Chapter, a new approach has been presented that allows the accurate evaluation of the selectivity of lithium conductive membranes under in-operando conditions, that is, while those membranes are used in cells under application of a current. It has been shown that the membrane selectivity can be overestimated if the measurements are restricted to ex-situ conditions where application of a current is not possible. Furthermore, the approach presented also allows an accurate evaluation of the transference number of crossover species, which is obtained from the fit of experimental data with and without current and only requires input from well-known experimental parameters. For highly selective membranes, the approach additionally allows the transference number of lithium to be estimated, which is important for efficient, durable and safe operation of lithium batteries.

In future, the approach could be applied to new membranes and new combinations of membranes, electrolytes and crossover species, including polysulfides. In the latter case, it would be necessary to protect the lithium electrodes in the cell from reaction with polysulfides. This could be achieved, for example, by pre-forming a protective Li_3N layer on the surface of the lithium, which has been shown to block polysulfides, at least temporarily.[20]

3.6 References

1. Bai, S.; Liu, X.; Zhu, K.; Wu, S.; Zhou, H., Metal–organic framework-based separator for lithium–sulfur batteries. *Nature Energy* **2016**, *1*, 1-6.

2. Busche, M. R.; Drossel, T.; Leichtweiss, T.; Weber, D. A.; Falk, M.; Schneider, M.; Reich, M. L.; Sommer, H.; Adelhelm, P.; Janek, J., Dynamic formation of a solid-liquid electrolyte interphase and its consequences for hybrid-battery concepts. *Nature Chemistry* **2016**, *8*, 426-34.

3. Gu, M.; Lee, J.; Kim, Y.; Kim, J. S.; Jang, B. Y.; Lee, K. T.; Kim, B.-S., Inhibiting the shuttle effect in lithium–sulfur batteries using a layer-by-layer assembled ion-permselective separator. *RSC Advances* **2014**, *4*, 46940-46946.

4. Hao, Z.; Yuan, L.; Li, Z.; Liu, J.; Xiang, J.; Wu, C.; Zeng, R.; Huang, Y., High performance lithium-sulfur batteries with a facile and effective dual functional separator. *Electrochimica Acta* **2016**, *200*, 197-203.

5. Huang, J.-Q.; Zhang, Q.; Peng, H.-J.; Liu, X.-Y.; Qian, W.-Z.; Wei, F., Ionic shield for polysulfides towards highly-stable lithium–sulfur batteries. *Energy & Environmental Science* **2014**, *7*, 347-353.

6. Huang, J.-Q.; Zhuang, T.-Z.; Zhang, Q.; Peng, H.-J.; Chen, C.-M.; Wei, F., Permselective Graphene Oxide Membrane for Highly Stable and Anti-Self-Discharge Lithium–Sulfur Batteries. *ACS Nano* **2015**, *9*, 3002-3011.

7. Jin, Z.; Xie, K.; Hong, X., Electrochemical performance of lithium/sulfur batteries using perfluorinated ionomer electrolyte with lithium sulfonyl dicyanomethide functional groups as functional separator. *RSC Advances* **2013**, *3*, 8889-8898.

8. Kumar, J.; Kichambare, P.; Rai, A. K.; Bhattacharya, R.; Rodrigues, S.; Subramanyam, G., A high performance ceramic-polymer separator for lithium batteries. *Journal of Power Sources* **2016**, *301*, 194-198.

9. Li, W.; Hicks-Garner, J.; Wang, J.; Liu, J.; Gross, A. F.; Sherman, E.; Graetz, J.; Vajo, J. J.; Liu, P., V_2O_5 Polysulfide Anion Barrier for Long-Lived Li–S Batteries. *Chemistry of Materials* **2014**, *26*, 3403-3410.

10. Ma, L.; Nath, P.; Tu, Z.; Tikekar, M.; Archer, L. A., Highly Conductive, Sulfonated, UV-Cross-Linked Separators for Li–S Batteries. *Chemistry of Materials* **2016**, *28*, 5147-5154.

11. Song, Z.; Qian, Y.; Otani, M.; Zhou, H., Stable Li-Organic Batteries with Nafion-Based Sandwich-Type Separators. *Advanced Energy Materials* **2016**, *6*, 1501780.

12. Truong, T. T.; Qin, Y.; Ren, Y.; Chen, Z.; Chan, M. K.; Greeley, J. P.; Amine, K.; Sun, Y., Single-crystal silicon membranes with high lithium conductivity and application in lithium-air batteries. *Advanced Materials* **2011**, *23*, 4947-52.

13. Zeng, F.; Jin, Z.; Yuan, K.; Liu, S.; Cheng, X.; Wang, A.; Wang, W.; Yang, Y.-s., High performance lithium–sulfur batteries with a permselective sulfonated acetylene black modified separator. *Journal of Materials Chemistry A* **2016**, *4*, 12319-12327.

14. Babu, D. B.; Giribabu, K.; Ramesha, K., Permselective SPEEK/Nafion Composite-Coated Separator as a Potential Polysulfide Crossover Barrier Layer for Li-S Batteries. *ACS Applied Materials & Interfaces* **2018**, *10*, 19721-19729.

15. Bauer, I.; Thieme, S.; Brückner, J.; Althues, H.; Kaskel, S., Reduced polysulfide shuttle in lithium–sulfur batteries using Nafion-based separators. *Journal of Power Sources* **2014**, *251*, 417-422.

16. Berger, A.; Freiberg, A. T. S.; Siebel, A.; Thomas, R.; Patel, M. U. M.; Tromp, M.; Gasteiger, H. A.; Gorlin, Y., The Importance of Chemical Reactions in the Charging Process of Lithium-Sulfur Batteries. *Journal of the Electrochemical Society* **2018**, *165*, A1288-A1296.

17. Cai, W.; Li, G.; He, F.; Jin, L.; Liu, B.; Li, Z., A novel laminated separator with multi functions for high-rate dischargeable lithium–sulfur batteries. *Journal of Power Sources* **2015**, *283*, 524-529.

18. Cao, Y.; Li, X.; Aksay, I. A.; Lemmon, J.; Nie, Z.; Yang, Z.; Liu, J., Sandwich-type functionalized graphene sheet-sulfur nanocomposite for rechargeable lithium batteries. *Physical Chemistry Chemical Physics* **2011**, *13*, 7660-5.

19. Chen, Y.; Li, Z.; Li, X.; Zeng, D.; Xu, G.; Zhang, Y.; Sun, Y.; Ke, H.; Cheng, H., Harvesting polysulfides by sealing the sulfur electrode in a composite ion-selective net. *Journal of Power Sources* **2017**, *368*, 38-45.

20. Gao, J.; Sun, C.; Xu, L.; Chen, J.; Wang, C.; Guo, D.; Chen, H., Lithiated Nafion as polymer electrolyte for solid-state lithium sulfur batteries using carbon-sulfur composite cathode. *Journal of Power Sources* **2018**, *382*, 179-189.

21. Jin, Z.; Xie, K.; Hong, X.; Hu, Z.; Liu, X., Application of lithiated Nafion ionomer film as functional separator for lithium sulfur cells. *Journal of Power Sources* **2012**, *218*, 163-167.

22. Kim, J. H.; Choi, J.; Seo, J.; Kwon, J.; Paik, U., Two-dimensional Nafion nanoweb anion-shield for improved electrochemical performances of lithium–sulfur batteries. *Journal of Materials Chemistry A* **2016**, *4*, 11203-11206.

23. Li, G.; Cai, W.; Liu, B.; Li, Z., A multi functional binder with lithium ion conductive polymer and polysulfide absorbents to improve cycleability of lithium–sulfur batteries. *Journal of Power Sources* **2015**, *294*, 187-192.

24. Liu, X.; Shan, Z.; Zhu, K.; Du, J.; Tang, Q.; Tian, J., Sulfur electrode modified by bifunctional nafion/γ-Al_2O_3 membrane for high performance lithium–sulfur batteries. *Journal of Power Sources* **2015**, *274*, 85-93.

25. Lu, Y.; Tikekar, M.; Mohanty, R.; Hendrickson, K.; Ma, L.; Archer, L. A., Stable Cycling of Lithium Metal Batteries Using High Transference Number Electrolytes. *Advanced Energy Materials* **2015**, *5*, 1402073.

26. Oh, S. J.; Lee, J. K.; Yoon, W. Y., Preventing the dissolution of lithium polysulfides in lithium-sulfur cells by using Nafion-coated cathodes. *ChemSusChem* **2014**, *7*, 2562-6.

27. Song, J.; Choo, M. J.; Noh, H.; Park, J. K.; Kim, H. T., Perfluorinated ionomer-enveloped sulfur cathodes for lithium-sulfur batteries. *ChemSusChem* **2014**, *7*, 3341-6.

28. Tang, Q.; Shan, Z.; Wang, L.; Qin, X.; Zhu, K.; Tian, J.; Liu, X., Nafion coated sulfur–carbon electrode for high performance lithium–sulfur batteries. *Journal of Power Sources* **2014**, *246*, 253-259.

29. Yu, X.; Joseph, J.; Manthiram, A., Polymer lithium–sulfur batteries with a Nafion membrane and an advanced sulfur electrode. *Journal of Materials Chemistry A* **2015**, *3*, 15683-15691.

30. Zhuang, T. Z.; Huang, J. Q.; Peng, H. J.; He, L. Y.; Cheng, X. B.; Chen, C. M.; Zhang, Q., Rational Integration of Polypropylene/Graphene Oxide/Nafion as Ternary-Layered Separator to Retard the Shuttle of Polysulfides for Lithium-Sulfur Batteries. *Small* **2016**, *12*, 381-9.

31. Bentley, C. L.; Bond, A. M.; Hollenkamp, A. F.; Mahon, P. J.; Zhang, J., Voltammetric Determination of the Iodide/Iodine Formal Potential and Triiodide Stability Constant in Conventional and Ionic Liquid Media. *The Journal of Physical Chemistry C* **2015**, *119*, 22392-22403.

32. Raccichini, R.; Furness, L.; Dibden, J. W.; Owen, J. R.; García-Araez, N., Impedance Characterization of the Transport Properties of Electrolytes Contained within Porous Electrodes and Separators Useful for Li-S Batteries. *Journal of the Electrochemical Society* **2018**, *165*, A2741-A2749.

33. Cannarella, J.; Liu, X.; Leng, C. Z.; Sinko, P. D.; Gor, G. Y.; Arnold, C. B., Mechanical Properties of a Battery Separator under Compression and Tension. *Journal of the Electrochemical Society* **2014**, *161*, F3117-F3122.

34. Kusoglu, A.; Kienitz, B. L.; Weber, A. Z., Understanding the Effects of Compression and Constraints on Water Uptake of Fuel-Cell Membranes. *Journal of the Electrochemical Society* **2011**, *158*, B1504-B1514.

35. Kusoglu, A.; Santare, M. H.; Karlsson, A. M.; Cleghorn, S.; Johnson, W. B., Micromechanics model based on the nanostructure of PFSA membranes. *Journal of Polymer Science Part B: Polymer Physics* **2008**, *46*, 2404-2417.

36. Wijmans, J. G.; Baker, R. W., The solution-diffusion model: a review. *Journal of Membrane Science* **1995**, *107*, 1-21.

37. Bard, A. J.; Faulkner, L. R., *Electrochemical Methods: Fundamentals and Applications, 2nd Edition*; Wiley Textbooks, 2000.

38. Fatouros, N.; Krulic, D., Contribution to the study of square wave voltammetry in the case of simple irreversible reactions. *Journal of Electroanalytical Chemistry* **1998**, *443*, 262-265.

39. Su, L., et al., An Investigation of the Ionic Conductivity and Species Crossover of Lithiated Nafion 117 in Nonaqueous Electrolytes. *Journal of the Electrochemical Society* **2015**, *163*, A5253-A5262.

40. Voropaeva, D. Y.; Novikova, S. A.; Kulova, T. L.; Yaroslavtsev, A. B., Conductivity of Nafion-117 membranes intercalated by polar aprotonic solvents. *Ionics* **2017**, *24*, 1685-1692.

4 Contributions to the resistance of lithium ion transfer at the solid-liquid electrolyte interface

4.1 Overview

In this chapter, four-point impedance measurements of a solid lithium ion conductor immersed in different liquid electrolytes are used to study the rate of ion transfer through the solid-liquid electrolyte interface. An approach is illustrated for identifying the rate-limiting step, which may be desolvation of lithium ions or transport through a solid-liquid electrolyte interphase (SLEI).

4.2 Background

The operation of lithium batteries necessarily involves lithium desolvation reactions. Since lithium ions are small and interact strongly with solvent molecules, desolvation energy could therefore be a rate determining factor during charge/discharge.[1, 2] The role of desolvation at the interface between liquid electrolytes and insertion electrodes has been the focus of a number of studies, and it has been proposed that it slows down the rate of lithium ion transfer between the two phases.[3-17] However this interface is complicated by the various other processes that can affect the overall rate of ion transfer, such as bulk ion diffusion inside the insertion material, SEI formation and growth, redox reactions, structural changes in the insertion material, etc. In comparison, the solid/liquid electrolyte interface is much simpler, and it has therefore been used as a model system to understand the effect of desolvation energy on lithium ion transfer kinetics. Furthermore, understanding the factors that affect lithium ion transfer at the solid/liquid electrolyte interface is essential for the development of conductive solid electrolytes that could be used as protective coatings in hybrid electrolyte batteries.[18]

Previous work on hybrid electrolyte systems has shown that lithium ion transfer at the solid-liquid electrolyte interface may be slower than lithium ion transport within the bulk liquid and solid electrolyte materials.[18-27] In a series of studies, Ogumi and co-workers[19, 20, 22-25, 27] used four-probe impedance measurements to measure the resistance of solid/liquid electrolyte systems. Based on the authors' interpretation of the impedance spectra, interfacial resistances were identified, and activation energies of interfacial lithium-ion transfer were evaluated from the temperature-dependence of these resistances. The activation energies were found to be large

compared to those of lithium-ion transport in solid or liquid electrolytes. Furthermore, the activation energies were found to depend on the electrolyte concentration and solvent species in these studies, leading the authors to infer that the slow lithium ion transfer at the interface may be ascribed to the energy penalty associated with lithium ion desolvation from the liquid electrolyte in order to enter the solid electrolyte.

A different approach was taken by Mehrotra et al[21], who studied polarisation losses at various LATP/organic liquid electrolyte interfaces by comparing measurements of cell potential in symmetric Li-Li cells under different applied current densities, to modelled values excluding these losses. Interestingly, no significant difference in polarisation losses was found when changing solvent or when varying electrolyte concentration in EC:DEC (<=1 M). These observations were attributed, respectively, to what the authors assessed to be similar donor numbers of the solvents used (EC, DEC, PC, DMSO) and to the nature of the solvation shell in mixed cyclic/linear carbonate solvents (citing studies which showed the make-up of the solvation shell in EC:DMC varying only at concentrations >1.5 M).

More recently, the presence of an additional resistance contribution due to the formation of a solid-liquid electrolyte interphase (SLEI) has been demonstrated.[18, 26] A study by Schleutker et al[26] looked at the interface between LLZO:Ta and solutions of $LiPF_6$ in EC:DMC. DC polarisation of a symmetrical 8-electrode cell was used to measure the potential gradients in each phase and extrapolate the potential drops at the interfaces. At low Li^+ concentrations (<0.1 mol L^{-1}), the polarisation resistance R_p was found to decrease with increasing concentration, consistent with Butler-Volmer kinetics and attributed to desolvation. However, at higher concentrations, R_p reached a constant limiting value, greater than the bulk solid electrolyte resistance, attributed to an Ohmic contribution from an SLEI formed by degradation processes.

Busche et al[18] characterised the solid/liquid electrolyte interface between LAGP and 1 M LiTFSI in DOL:DME using a symmetric 4-probe impedance cell with Li electrodes. Temporal development of the impedance spectra, together with surface analysis and depth profiling, indicated that the solid and liquid electrolytes react to form a resistive 3D interphase, with a high capacitance on the order of 10^{-6} F cm^{-2}, suggestive of a thin surface film. Similar results were obtained for LATGP (purchased from Ohara GmbH) in the same liquid electrolyte. It was estimated that the interface resistance would dominate for membrane thicknesses less than 10 µm, with an energy barrier for charge transfer across the interface higher than that for ion transport in LAGP. In this study, lithium desolvation was not identified as a contributor to the interfacial energy barrier.

In the present work, an approach is illustrated for identifying the rate limiting step of ion transfer, by means of a systematic study of the effect of lithium ion concentration and solvent on ion-transfer resistance and activation energy.

4.3 Experimental details

The solid electrolyte used was an Ohara glass-ceramic membrane (AG-01 type, 250 µm thickness, Ohara-GmbH). The main crystalline phase of the membranes is $Li_{1+x}Al_xGe_yTi_{2-x-y}P_3O_{12}$, abbreviated as LATGP, which has a NASICON type structure, with sub phases of $Li_{1+x+3z}Al_x(Ge,Ti)_{2-x}(Si_zPO_4)_3$ and $AlPO_4$.[28]

Impedance measurements of the membrane in contact with liquid electrolytes were obtained in the 4-probe glass cell (PermeGear Ltd.) shown in Figure 4.1a.

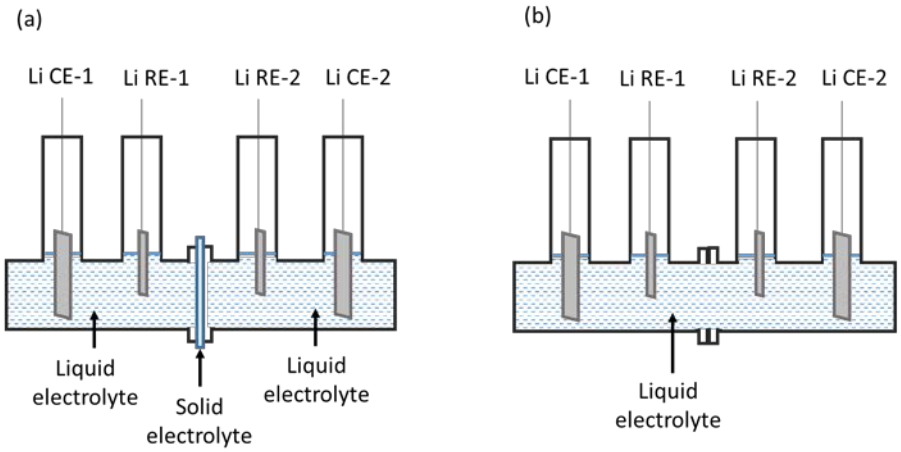

Figure 4.1: Sketch of the cell, with two outer current probes and two inner voltage probes (a) with solid electrolyte and (b) without solid electrolyte.

The membrane is clamped between two liquid electrolyte compartments, each containing 4 ml of electrolyte, with a contact area of 0.7854 cm^2. Outer (current probe) electrodes are spaced at approximately 80 mm and inner (voltage probe) electrodes at approximately 35 mm. Gaskets (Ekraz 9655B, 25 mm outer diameter x 10 mm inner diameter x 0.5 mm thickness, supplied by Polymax Ltd.) coated with a thin layer of vacuum grease (Dow-Corning high vacuum silicone grease) cushion the membrane from the glass joint. The membrane used for all experiments was cleaned by sonicating in isopropyl alcohol (Fisher, 99.5%) and pre-dried overnight at 80 °C under vacuum (Thermo Scientific) prior to each use. Other cell components

were pre-dried overnight at 80 °C at ambient pressure (Genlab). Cells were part-assembled and dried for a further two hours at 80 °C under vacuum before being transferred to an argon filled glovebox (<1 ppm water content, < 10 ppm oxygen content, mBraun). Electrodes were lithium foil (battery grade, 100 µm thickness, Rockwood Lithium), cut to approximately 15 mm x 5 mm for the outer electrodes and 15 mm x 3 mm for the inner electrodes. Outer electrodes were submerged approximately 8 mm below the electrolyte surface and inner electrodes approximately 5 mm below the surface. For the electrolytes, lithium bis(trifluoromethane)-sulfonimide salt (LiTFSI) (99.95%, Sigma-Aldrich) was dried and deoxygenated under vacuum at 120 ^{o}C for 24 hours. 1,3-dioxolane (anhydrous, 99.8%, Sigma-Aldrich) and 1.0 M $LiPF_6$ in EC:DMC (1:1 by volume) ("LP30") (battery grade, Aldrich) were used as received. 1,2-dimethoxyethane (DME) (anhydrous, 99.5%, inhibitor-free, Sigma-Aldrich) and dimethyl sulfoxide (DMSO) (anhydrous, 99.9%, Sigma-Aldrich) were dried for 3 days using molecular sieves (4 Å beads, 4-8 mesh, Sigma-Aldrich) which had been dried under vacuum at 220 ^{o}C for 2 days. Electrolytes (1, 2 and molal LiTFSI in DOL:DME (1:1 by volume), 1 and 3 molal LiTFSI in DMSO) were prepared inside the glovebox and stirred for 24 hours before use.

Impedance measurements of the membrane in contact with blocking electrodes were obtained by coating the membrane on both sides with a thin layer of conductive silver paint (Electrolube) and pressing between two copper current collectors which had been polished with 25, 3.0 and 0.3 µm alumina powder in ethanol.

Impedance measurements of liquid electrolytes were obtained using a conductivity cell (High Temperature Conductivity Cell, BioLogic) containing 1 ml of electrolyte. Prior to each use, the cell was cleaned with acetone and dried overnight at 80 °C at ambient pressure before being transferred to the glovebox. For some electrolytes, bulk resistance was also measured in the 4-probe glass cell (Figure 4.1b) and used to obtain an average scaling factor between the conductivity cell and glass cell. For all electrolytes, this scaling factor was then applied to conductivity cell measurements to obtain values for bulk liquid electrolyte resistance in the 4-probe glass cell.

Impedance measurements were carried out using a BioLogic VMP3 multi-channel potentiostat controlled using ECLab software, with a voltage perturbation of 10 mV and a frequency range of 1 MHz – 10 Hz unless stated, but due to artefacts at high frequencies, the frequency range shown in the graphs is 0.3 MHz – 10 Hz. All measurements were carried out with the cells placed in a climatic chamber (Memmert HPP110) at a temperature of 25 ^{o}C, and the results reported were taken 2 hours after cell assembly, except for the results in Figure 4.8 and

Figure D.1. For measurements nominally at 14 ^{o}C, cells were cooled in a refrigerator at 14 ^{o}C (LMS cooled incubator) before being rapidly (<30 seconds) transferred to the climatic chamber at 25 ^{o}C for measurement. Similarly for measurements nominally at 34 ^{o}C, cells were heated in a climatic chamber at 34 ^{o}C (Gallenkamp incubator) before being rapidly transferred to the climatic chamber at 25 ^{o}C for measurement.

Impedance spectra were fitted with equivalent circuit models using ZView software. In the case of impedance with blocking electrodes, the measured spectra were first fitted in order to obtain parameters for the equivalent circuit components. Modelled spectra excluding the effects of capacitance at the solid electrolyte/blocking electrode interface were then obtained by simulation using these parameter values.

4.4 Results and discussion

4.4.1 Validity of the 4-point impedance method

In the 4-point impedance method, current is passed between two current probes, while two voltage probes measure the potential difference between them. The voltage probe electrodes do not pass current and therefore the measurements exclude any contribution from electrode processes. Figure 4.2 shows impedance spectra measured in the 4-probe impedance cell containing 1 molal LiTFSI in DOL-DME, LP30 or 1 molal LiTFSI in DMSO. As expected, the spectra appear as point measurements, consistent with a resistor whose resistance value is the solution resistance in the cell. This confirms the elimination of any contribution from the electrode/electrolyte interface using the four-probe configuration. (Small deviations from purely Ohmic behaviour at high frequencies are artefacts due to the capacitance of the coaxial cables that connect the electrodes to the potentiostat.[18])

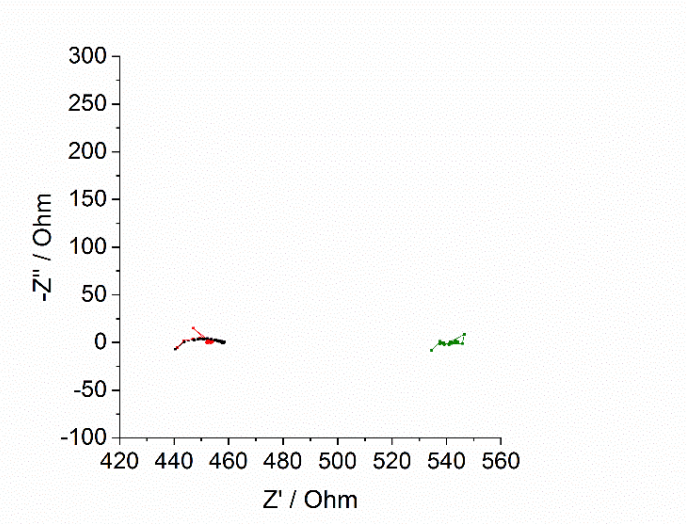

Fig 4.2: Impedance measurements obtained in 4-point impedance cell filled with different liquid electrolytes (1 m LiTFSI in DOL-DME (black), LP30 (red) and 1 m LiTFSI in DMSO (green)), and without Ohara membrane. See cell sketch in Figure 4.1a. All measurements at 25 °C.

4.4.2 Liquid electrolyte resistance

Due to the relatively large volume of electrolyte required for the 4-probe impedance cell, resistance values for other electrolytes were obtained by measuring impedance spectra using a conductivity cell and scaling to account for the different cell constants. A scaling factor between the conductivity cell and the 4-probe cell was obtained by dividing the resistance values from Figure 4.2 by resistance values for the same electrolytes obtained from the conductivity cell, and taking the average of these ratios. An example of an impedance spectrum measured in the conductivity cell is shown in Figure 4.3. In this case, due to the two-electrode configuration with blocking electrodes, the spectrum appears as a near-vertical line (due to double-layer capacitance at the electrode surface) with real-axis intercept (due to the electrolyte solution resistance). The spectrum can be fitted with an equivalent circuit model comprising a resistor in series with a constant phase element, to obtain values for the solution resistance. This was done for each electrolyte, at 14 °C, 25 °C and 34 °C.

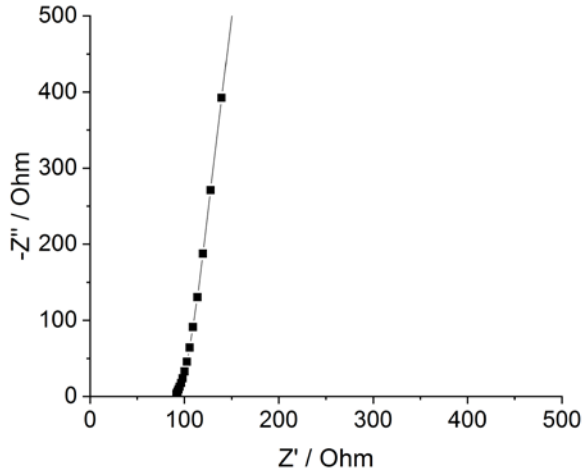

Fig 4.3: Impedance spectrum measured at 25 °C in 2-point conductivity cell with blocking electrodes and containing 1 M LiTFSI in DOL-DME.

4.4.3 Solid electrolyte resistance with blocking electrodes

The 2-point impedance of the solid electrolyte, obtained by coating it with silver conducting paint and pressing it between two copper current collectors, is shown in Figure 4.4 (black curve). Typically for such a configuration we would expect one or more semicircles due to lithium ion transport in the membrane (discussed in more detail below), together with a capacitive spike due to capacitance at the membrane/electrode blocking interface. Depending on the frequency range used, fast transport processes within the membrane may not be resolved, manifesting instead as a high-frequency intercept. The measured spectrum is consistent with this expected behaviour and was fitted using the simple equivalent circuit model shown in the inset. This measurement and fitting process was repeated several times in order to obtain average values for the model parameters. Using the fitted values, the impedance spectrum of the membrane over the whole frequency range, excluding the capacitive behaviour at the solid electrolyte/blocking electrode interface, could then be simulated (blue curve).

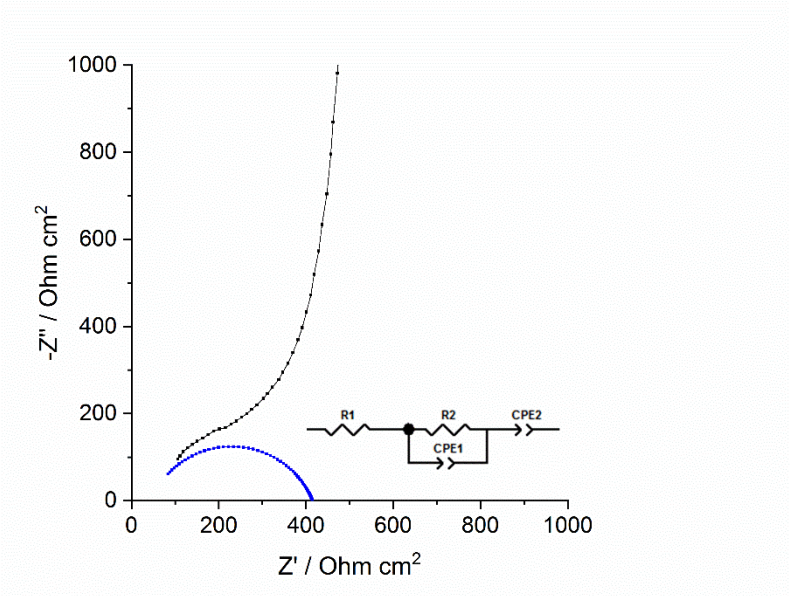

Figure 4.4: Two-point impedance spectrum of an Ohara glass-ceramic membrane measured with blocking electrodes (black), and a corresponding modelled spectrum (blue) excluding the solid electrolyte/blocking electrode interface. All spectra measured at 25 °C.

Before discussing the results in sections 4.4.4 and 4.4.5 it should be noted that subsequent experiments, performed by Dr. Vivek Padmanabhan of the Garcia-Araez group at the University of Southampton, suggest that the present experiments were affected by trace water contamination in the electrolyte. The water content of the anhydrous DOL used for the present experiments was subsequently evaluated by Karl-Fischer analysis, obtaining a result of 165 ppm. The effect of water contamination is discussed briefly in section 4.5. Nevertheless, the methodology and arguments outlined here are put forward as a valid basis for a systematic study into lithium ion transfer kinetics at solid/liquid electrolyte interfaces.

4.4.4 Resistance of the solid electrolyte in contact with liquid electrolyte: effect of lithium ion concentration

Figure 4.5a shows impedance spectra measured in the 4-probe impedance cell containing an Ohara glass-ceramic membrane in contact with 0.5 molal, 1 molal, 2 molal, or 3 molal LiTFSI in DOL-DME. The total cell resistance, R_{cell}, is given by the low frequency intercept. In this case the spectra appear as a depressed and slightly distorted semicircle with a positive offset along the real axis. This offset includes the solution resistance, R_{liquid}, of the liquid electrolyte. In order to better compare the spectra of the membrane in different electrolytes, it is necessary to subtract

off the solution resistance of the liquid electrolyte. In principle, solution resistances could be obtained from the high frequency intercept of the spectra. However, due to instrument limitations, measurements could not be obtained at sufficiently high frequencies to observe this intercept. Another option would be to fit the spectra using an equivalent circuit model in order to obtain R_{liquid}. However, due to artefacts in the measurements at high frequencies (discussed above), accurate fitting was difficult. Solution resistances were therefore obtained from independent measurements either directly using the 4-probe impedance cell, or indirectly using the conductivity cell and scaling to account for the different cell constants, as described above. This assumes that the resistance across the liquid electrolyte is the same in the cell with and without the solid electrolyte membrane (see cell sketches in Figure 4.1), which is reasonable because the thickness of the membrane is much smaller than the length of the liquid electrolyte between the two voltage probes.

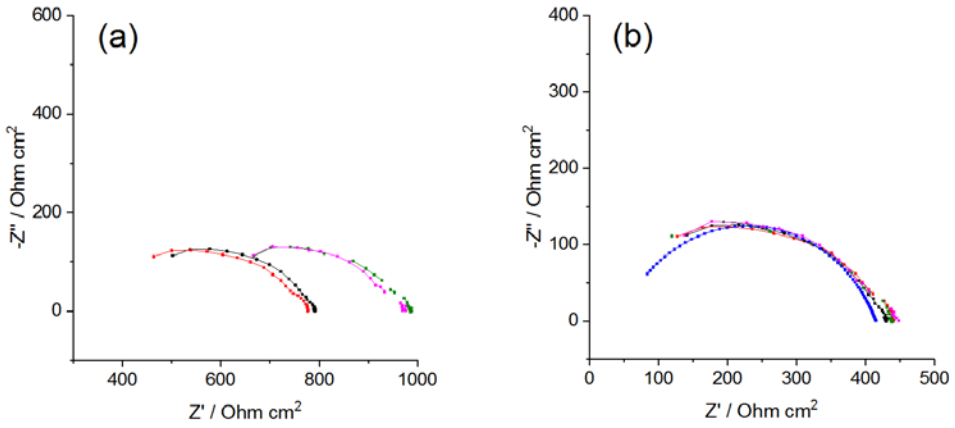

Figure 4.5: (a) Impedance spectra of the Ohara glass-ceramic membrane measured in 4-point impedance cell with 0.5 m (magenta), 1 m (black), 2 m (red) and 3 m (green) LiTFSI in DOL-DME. See cell sketch in Figure 4.1b. (b) Spectra from (a) net of bulk electrolyte resistance, together with the simulated impedance spectrum obtained from measurements with blocking electrodes (blue). All spectra measured at 25 °C.

Figure 4.5b shows the spectra from Figure 4.5a, net of bulk liquid electrolyte resistance, together with the simulated impedance of the solid electrolyte from Figure 4.4. It can be seen that the spectra overlap, except for a small feature in the low-frequency region. Unfortunately this feature is not sufficiently resolved from the main semicircle observed to quantify the two separately. It is only possible to quantify $R_{membrane}$, the total resistance associated with membrane

(including its interfaces in contact with the electrolyte). This is given by the low frequency intercept in Figure 4.5b.

Figure 4.6 plots R_{cell}, R_{liquid}, and $R_{membrane}$, obtained from the data in Figure 4.5. It can be seen that the resistance associated with the liquid electrolyte, R_{liquid}, decreases when the LiTFSI concentration increases from 0.5 to 1 molal, implying an increase in conductivity. This increase in conductivity is due to an increase in the number of charge carriers (lithium ions). In the absence of ion-ion interactions and viscosity effects, we would expect conductivity to be proportional to concentration.[29] Above 1 molal, however, viscosity effects (and possibly ion pairing) begin to offset the increase in the number of charge carriers, so that the resistance is similar for 1 molal and 2 molal solutions, and for the 3 molal solution, the increase in viscosity (and possibly ion pairing) is enough to produce an increase in resistance (decrease in conductivity).[30]

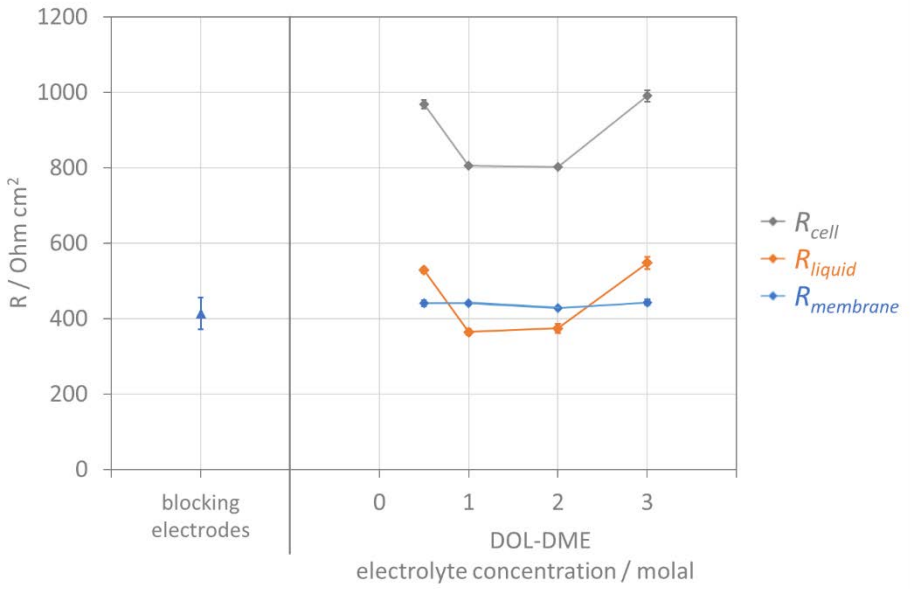

Figure 4.6: Resistance contributions to impedance spectra measured in 4-point impedance cell containing Ohara glass-ceramic membrane and different liquid electrolytes: R_{cell} (grey), R_{liquid} (orange), $R_{membrane}$ (blue). Connecting lines are included as a guide to the eye. Ohara resistance obtained with blocking electrodes is also shown. All spectra measured at 25 °C. Error bars correspond to the standard deviation of repeated measurements. Note: for the 2 m measurements, R_{liquid} and R_{cell} have been adjusted to account for the fact that the length of the liquid electrolyte between the two voltage probes in this cell build was 10% smaller than in other cells.

In contrast to R_{liquid}, the resistance of the membrane in contact with the liquid electrolyte, $R_{membrane}$ is found to be similar for all concentrations, and within the range estimated using

blocking electrodes. $R_{membrane}$ can be considered to comprise three separate contributions: R_{bulk}, due to lithium ion transport in the bulk (grains) of the solid lithium ion conductor; R_{gb}, due to lithium ion transport across the grain boundaries of the solid lithium ion conductor; and $R_{transfer}$, due to lithium ion transfer across the solid-liquid electrolyte interface. R_{bulk} and R_{gb} are not expected to change, and therefore any effect of the electrolyte on the value of $R_{transfer}$ would produce a direct effect on the total resistance of the membrane, $R_{membrane}$. Thus, since $R_{membrane,}$ is similar for all lithium ion concentrations in the liquid electrolyte, we might conclude that, $R_{transfer}$, is also similar for all lithium ion concentrations. (There is of course a caveat to this argument, in that if $R_{bulk} + R_{gb} >> R_{transfer}$ then variations in $R_{transfer}$ might be masked, but we neglect this for the time being.) In contrast, if there was a significant resistance contribution to lithium transfer across the membrane from lithium desolvation, an elementary step following Butler-Volmer kinetics, then we would expect the associated resistance to vary with concentration. It can be shown (see Appendix) that R_{BV} , the resistance associated with desolvation at the solid/liquid electrolyte interface, varies inversely with the lithium ion concentration in the liquid electrolyte according to:

$$R_{BV} = \frac{RT}{k^0 c F^2} \qquad \text{(Eq. 4.1)}$$

where k^0 is the standard rate constant of lithium ion transfer and c is the lithium ion concentration at the liquid electrolyte.

Considering lithium ion transfer as a transport process, as described in previous work,[31-33] it can also be shown (see Appendix) that:

$$R_{BV} = \frac{\delta_{BV}}{\sigma_{BV}} \qquad \text{(Eq. 4.2)}$$

Where σ_{BV} is the lithium ion conductivity of the liquid electrolyte in contact with the SLEI, and δ_{BV} is the characteristic ion transfer distance. Similarly R_{liquid} can be expressed as:

$$R_{liquid} = \frac{\delta_{liquid}}{\sigma_{liquid}} \qquad \text{(Eq. 4.3)}$$

where σ_{liquid} is the lithium ion conductivity in the liquid electrolyte and δ_{liquid} is the length of the liquid electrolyte between the voltage probes in the cell. Equations 4.2 and 4.3 show that R_{BV} and R_{liquid} are expected to show a similar behaviour, since both quantities depend on the conductivity of the liquid electrolyte. Although this conductivity might be different in the bulk liquid and in the

liquid at the interface with the membrane, we might expect the effect of lithium ion concentration to be similar.

4.4.5 Resistance of the solid electrolyte in contact with liquid electrolyte: effect of solvent

If there was a significant resistance contribution to lithium transfer across the membrane from lithium desolvation, we might also expect to see differences in resistance in different electrolytes solvents, with higher resistances in solvents with higher donor numbers (i.e. stronger Li^+-solvent interactions). Figure 4.7 shows impedance spectra measured in the 4-probe impedance cell containing Ohara glass-ceramic membrane with 1 molal LiTFSI in DOL-DME, 1 or 3 molal LiTFSI in DMSO, or LP30. Bulk liquid electrolyte resistances have been subtracted from the raw impedance spectra.

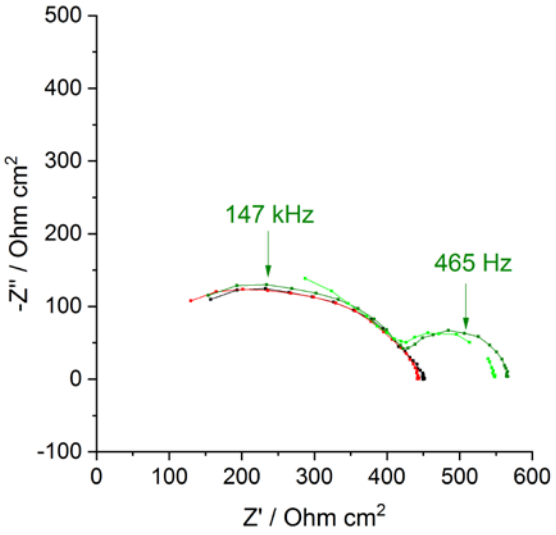

Figure 4.7: Impedance spectra, after subtraction of bulk liquid electrolyte resistance, of Ohara glass-ceramic membrane measured in 4-point impedance cell with 1 m LiTFSI in DOL-DME (black), LP30 (red), 1 m LiTFSI in DMSO (dark green), 3 m LiTFSI in DMSO (lime green). All spectra were measured at 25 °C, approximately 2 hours after cell assembly.

It can be seen that the spectra measured in 1 molal LiTFSI in DOL-DME and in LP30 are very similar, whilst the spectra measured in DMSO-based electrolytes are also similar except for an extra semicircle at low frequencies. However, as shown in Figure 4.8, the width of this semicircle (that is, the resistance of the associated process) is found to increase over time, and

fitting of the spectra reveals that the associated capacitance decreases over time (from ca. 1.5 to 1.0 μF cm^{-2}). It is proposed, therefore, that this extra semicircle is due to the formation of a resistive solid-liquid electrolyte interphase (SLEI) whose thickness increases over time, and not to a lithium desolvation reaction. The formation of an SLEI as a result of degradation reactions and deposition of degradation products has been suggested previously[18, 26, 34-36], and various analytical techniques (XPS, XRD[34-36], SIMS[18], Raman[34, 35], SEM or TEM[34, 35]) have been used to study its composition. Assuming capacitance relates to relative permittivity according to $C = \varepsilon_0 \varepsilon_r A/l$ (where A is the contact area between the solid and liquid electrolyte, l is the thickness of the SLEI layer and ε_r has a typical value of 5) then a capacitance of 1.0 μF cm^{-2} would imply an SLEI thickness of a few hundred nm, suggestive of a 3D extended structure formed by decomposition of electrolyte salt and solvent, as reported by Busche et al.[18] For comparison, thicknesses up to 480 nm have been reported for interphases formed on graphitic surfaces.[37]

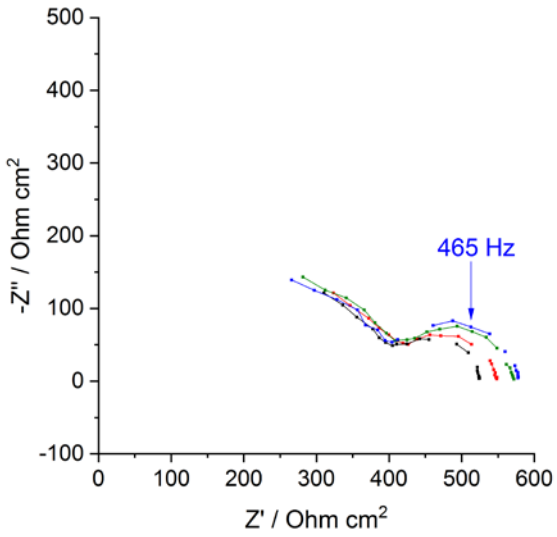

Figure 4.8: Impedance spectra, net of bulk liquid electrolyte resistance, of Ohara glass-ceramic membrane measured in 4-point impedance cell at 25 °C with 3 m LiTFSI in DMSO approximately 30 minutes (black), 2 hours (red), 6 hours (green) and 10 hours (blue) after cell assembly.

In the presence of an SLEI, the overall process of lithium ion transfer can be described as:

Li^+(liquid electrolyte) → Li^+(SLEI) (1)

Li^+(SLEI) → Li^+(solid electrolyte) (2)

where reaction 1 will follow Butler-Volmer kinetics whereas reaction 2 is a more complex process that involves lithium ion diffusion through the SLEI and transfer to the bulk solid electrolyte. Reactions (1) and (2) occur in series, and therefore the total resistance associated with lithium ion transfer from the liquid to the solid electrolyte, $R_{transfer}$, is given by:

$$R_{transfer} = R_{BV} + R_{SLEI} \quad \text{(Eq. 4.4)}$$

where R_{BV} and R_{SLEI} are the resistances associated with processes (1) and (2), respectively. Which of these is dominant will of course depend on their relative values. According to equation 4.1, at low concentrations, R_{BV} will increase and hence the process of lithium ion transfer could become limited by the kinetics of lithium ion desolvation. Similarly, desolvation could become the rate-limiting step for materials with very small values of R_{SLEI}.

As for R_{liquid} and R_{BV}, R_{SLEI} can be expressed according to:

$$R_{SLEI} = \frac{\delta_{SLEI}}{\sigma_{SLEI}} \quad \text{(Eq. 4.5)}$$

Where δ_{SLEI} is its thickness and σ_{SLEI} is its lithium ion conductivity. σ_{SLEI} is a material property that will depend on the composition of the SLEI, which may in turn depend on the liquid electrolyte composition, including concentration e.g. with a greater fraction of lithium salt, vs. solvent, decomposition products at high concentrations.

4.4.6 Analysis of activation energies

Analysis of activation energies of lithium ion transfer can provide further information about the relative importance of R_{BV} and R_{SLEI}. Figure 4.9a is an Arrhenius plot of total membrane resistance $R_{membrane}$, measured in the different liquid electrolyte compositions, and also with blocking electrodes, whilst Figure 4.9b is an Arrhenius plot of bulk liquid electrolyte resistance for the corresponding liquid electrolytes. In line with Buche et al[18], a temperature-dependent pre-exponential factor is used for the solid electrolyte (including interface) and, given the small temperature range of our measurements, a simple Arrhenius dependence (rather than the usual Vogel-Fulcher-Tammann equation) is used for the liquid electrolyte. Resistances were obtained from the impedance spectra shown in Figure D1 in the Appendix. Activation energies can be estimated from the slopes of the plots according to the Arrhenius equation:

$$\sigma = A \exp(-E_a/kT) \quad \text{(Eq. 4.6)}$$

where for the solid electrolyte $A = B/T$ and A and B are constants.

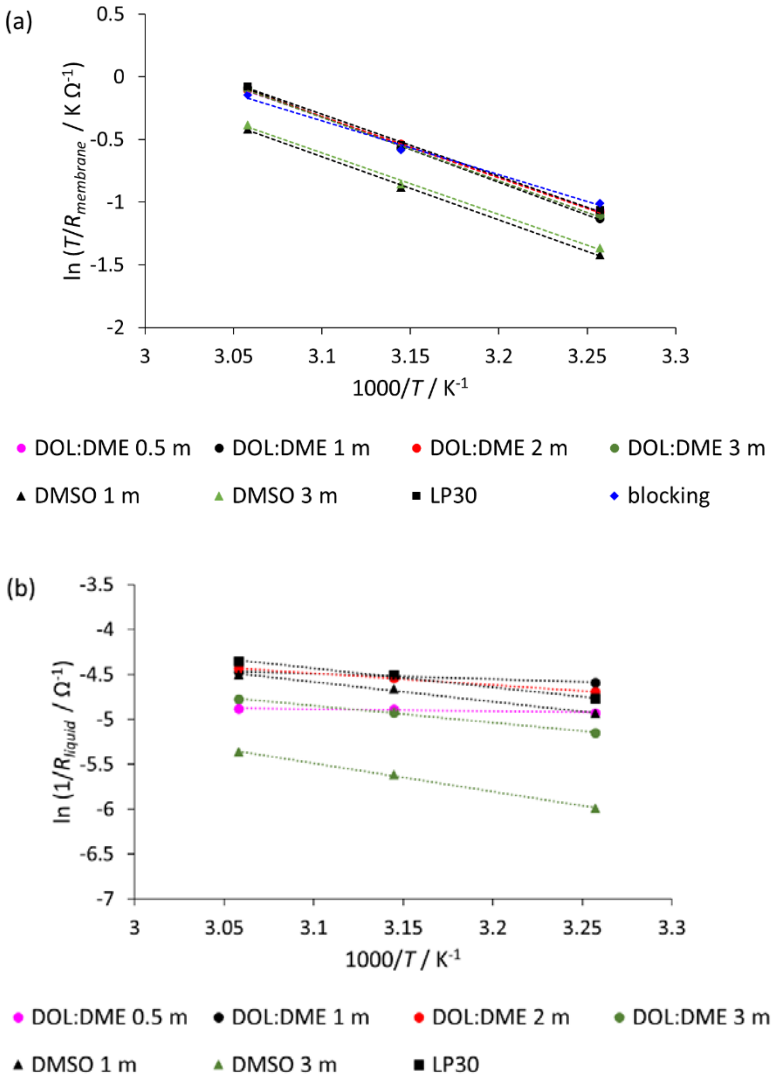

Figure 4.9: Arrhenius plots of (a) $R_{membrane}$ measured in 4-point impedance cell with different electrolytes and measured with blocking electrodes (b) R_{liquid} measured using conductivity cell.

From Figure 4.9b, the activation energy for the bulk liquid electrolyte is found to vary significantly with concentration and solvent. In DOL-DME, values are found to be 21 meV for the 0.5 molal electrolyte, 51 meV for the 1 molal electrolyte (in good agreement with the literature[38]), 111 meV for the 2 molal electrolyte and 162 meV for the 3 molal electrolyte, whilst in DMSO, the values are much higher: 190 meV for 1 molal (in good agreement with the literature[39]) increasing to 272 m eV for 3 molal. (Activation energies in DMSO are discussed further in the Appendix.)

Such variations have been ascribed to differences in ion-ion and ion-solvent interactions.[30, 38, 39] For example, the increase in activation energy with increasing electrolyte concentration reflects an increase in cohesive energy as noted by Angell.[40] In concentrated electrolyte solutions, the degree of ionic association increases, with contact ion pairs and aggregates, rather than solvent-separated ions, becoming predominant in the solvation structure. Where ion pairs/aggregates are predominant, the vehicle-type ion conduction mechanism depicted for dilute solutions, where Li^+ conducts together with its solvation sheath, no longer applies. Instead, Li^+ conduction is expected to occur via a repeated ion dissociation/association process, where Li^+ dissociates from one anion and associates with another.[30] Since Li^+-anion Coulombic interactions will generally be stronger than Li^+-solvent (ion-dipole) interactions, this will result in greater activation energies. Similarly the larger activation energies in DMSO reflect stronger Li^+-solvent interactions than in DOL-DME due to the high donor number of DMSO.[41]

Since ion transfer at the solid/liquid electrolyte interface is expected to involve a similar mechanism, then if there was a significant resistance contribution from lithium desolvation at this interface, we might expect that the total activation energy for lithium ion transfer would also vary with electrolyte concentration and solvent, in a similar way to the activation energy for lithium ion transport in the bulk liquid electrolyte. However, from the slopes in Figure 4.9a, the activation energy for lithium transfer across the membrane is found to be essentially invariant with liquid electrolyte concentration and solvent, and the same when measured with blocking electrodes, with an average value 417 ± 25 meV (corresponding to 40.2 ± 2.5 kJ mol^{-1}), in agreement with previous studies.[42, 43] These values of activation energies are consistent with lithium ion diffusion within a solid conductor.[18, 44]

There is again a caveat arising from the possibility that $R_{bulk}+R_{gb} >> R_{transfer}$. In this case $R_{bulk}+R_{gb}$ might be expected to dominate the temperature response of the membrane resistance, $R_{membrane}$ ($=R_{bulk}+R_{gb}+R_{transfer}$), and thus the evaluation of the activation energy. It would be therefore useful to repeat the present measurements with a thinner membrane, in order to minimise the contribution of $R_{bulk}+R_{gb}$, or preferably to use a membrane for which the characteristic frequencies associated with ion transfer at the solid/liquid electrolyte interface, and with grain boundary conduction within the membrane, are sufficiently different to separate out these processes in the impedance spectra.

In any case, it is noted that variation of the activation energy associated with $R_{transfer}$ is, alone, insufficient to infer the effect of lithium ion desolvation on the kinetics of lithium ion transfer. On the one hand, by analogy with the SEI on electrodes, changing the solvent or even

the lithium ion concentration can produce substantial changes in the composition of the SLEI, which can result in changes in the activation energy.[45] This could erroneously be taken as an indication that lithium ion desolvation is an important factor affecting the kinetics of lithium ion transfer. On the other hand, if the SLEI remains constant, variation of the activation energy of $R_{transfer}$ with lithium ion concentration may also be interpreted erroneously as evidence for the effect of lithium ion desolvation unless a similar variation is also observed in the activation energy for lithium transport in the liquid electrolyte.

4.5 Effect of water contamination

Figure 4.10 shows impedance spectra measured by Dr. Vivek Padmanabhan in the 4-probe impedance cell containing a Ohara glass-ceramic membrane in contact with 1 molal LiTFSI in DOL:DME before and after the addition of a small amount of water to the cell. In this case, both DOL and DME were stored over molecular sieves prior to use. It can be seen that, prior to the addition of water, a second semicircle is present in the impedance spectrum. However, almost instantaneously on addition of water, this semicircle all but disappears, and the spectrum resembles those in Figure 4.5. Collaborative experiments with Dr. Vivek Padmanabhan are currently underway to further investigate the effect of water contamination on the rate of lithium ion transfer across the solid/liquid electrolyte interface.

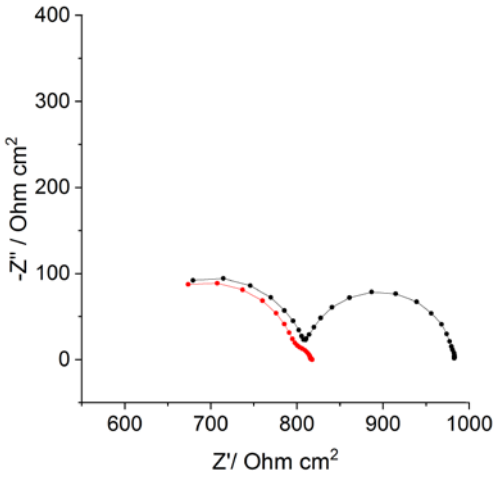

Figure 4.10: Impedance spectra of Ohara glass-ceramic membrane measured in 4-point impedance cell at 25 °C with 1 m LiTFSI in DOL:DME before (black) and after (red) addition of approximately 0.1 vol% water. Note that a different piece of Ohara glass-ceramic membrane was used for these measurements and therefore its bulk and grain boundary impedance contributions may be slightly different to those in the rest of this chapter.

4.6 Conclusions

In this chapter, an approach for studying the rate of lithium ion transfer across the solid/liquid electrolyte interface (or electrode/electrolyte interface) has been developed. Unfortunately the results presented are likely to have been affected by trace water contamination. Nevertheless they serve to illustrate the approach. It is suggested that the effect of lithium ion desolvation on ion transfer kinetics can be analysed by performing a systematic study of the rate of lithium ion transfer (using impedance spectroscopy, for example) as a function of lithium ion concentration. If the ion transfer resistance and activation energy do not change as a function of concentration, this would indicate that desolvation is not the rate-limiting step, which instead may be ion transport through a resistive SLEI (or SEI). If the resistance and activation energy do change as a function of concentration, then additional analysis techniques can be used to identify whether the variation could be attributable to changes in the composition of the SLEI. If, from these analyses, the composition of the SLEI appears to be constant then variation of the resistance and activation energy with lithium ion concentration may indicate that desolvation is important. Then, Butler-Volmer kinetics and ion transport equations can be used to analyse the results, which finally can be compared to the liquid electrolyte case.

4.7 References

1. Xu, K., Nonaqueous liquid electrolytes for lithium-based rechargeable batteries. *Chemical Reviews* **2004**, *104*, 4303-417.

2. Xu, K., Electrolytes and interphases in Li-ion batteries and beyond. *Chemical Reviews* **2014**, *114*, 11503-618.

3. Abe, T.; Fukuda, H.; Iriyama, Y.; Ogumi, Z., Solvated Li-Ion Transfer at Interface Between Graphite and Electrolyte. *Journal of The Electrochemical Society* **2004**, *151*, A1120-A1123.

4. Bruce, P. G.; Saidi, M. Y., The mechanism of electrointercalation. *Journal of Electroanalytical Chemistry* **1992**, *322*, 93-105.

5. Doi, T.; Iriyama, Y.; Abe, T.; Ogumi, Z., Pulse voltammetric and ac impedance spectroscopic studies on lithium ion transfer at an electrolyte/$Li_{4/3}Ti_{5/3}O_4$ electrode interface. *Analytical Chemistry* **2005**, *77*, 1696-700.

6. Doi, T.; Shimizu, Y.; Hashinokuchi, M.; Inaba, M., $LiBF_4$-Based Concentrated Electrolyte Solutions for Suppression of Electrolyte Decomposition and Rapid Lithium-Ion Transfer at

$LiNi_{0.5}Mn_{1.5}O_4$/Electrolyte Interface. *Journal of The Electrochemical Society* **2016**, *163*, A2211-A2215.

7. Kobayashi, S.; Uchimoto, Y., Lithium Ion Phase-Transfer Reaction at the Interface between the Lithium Manganese Oxide Electrode and the Nonaqueous Electrolyte. *The Journal of Physical Chemistry B* **2005**, *109*, 13322-13326.

8. Nakayama, M.; Ikuta, H.; Uchimoto, Y.; Wakihara, M., Study on the AC Impedance Spectroscopy for the Li Insertion Reaction of $Li_xLa_{1/3}NbO_3$ at the Electrode−Electrolyte Interface. *The Journal of Physical Chemistry B* **2003**, *107*, 10603-10607.

9. Nakayama, N.; Nozawa, T.; Iriyama, Y.; Abe, T.; Ogumi, Z.; Kikuchi, K., Interfacial lithium-ion transfer at the $LiMn_2O_4$ thin film electrode/aqueous solution interface. *Journal of Power Sources* **2007**, *174*, 695-700.

10. Okumura, T.; Fukutsuka, T.; Matsumoto, K.; Orikasa, Y.; Arai, H.; Ogumi, Z.; Uchimoto, Y., Lithium-Ion Transfer Reaction at the Interface between Partially Fluorinated Insertion Electrodes and Electrolyte Solutions. *The Journal of Physical Chemistry C* **2011**, *115*, 12990-12994.

11. Xu, K., "Charge-Transfer" Process at Graphite/Electrolyte Interface and the Solvation Sheath Structure of Li^+ in Nonaqueous Electrolytes. *Journal of The Electrochemical Society* **2007**, *154*, A162-A167.

12. Xu, K.; Lam, Y.; Zhang, S. S.; Jow, T. R.; Curtis, T. B., Solvation Sheath of Li^+ in Nonaqueous Electrolytes and Its Implication of Graphite/Electrolyte Interface Chemistry. *The Journal of Physical Chemistry C* **2007**, *111*, 7411-7421.

13. Xu, K.; von Cresce, A.; Lee, U., Differentiating contributions to "ion transfer" barrier from interphasial resistance and Li^+ desolvation at electrolyte/graphite interface. *Langmuir* **2010**, *26*, 11538-43.

14. Xu, K.; von Wald Cresce, A., Li^+-solvation/desolvation dictates interphasial processes on graphitic anode in Li ion cells. *Journal of Materials Research* **2012**, *27*, 2327-2341.

15. Yamada, I.; Miyazaki, K.; Fukutsuka, T.; Iriyama, Y.; Abe, T.; Ogumi, Z., Lithium-ion transfer at the interfaces between $LiCoO_2$ and $LiMn_2O_4$ thin film electrodes and organic electrolytes. *Journal of Power Sources* **2015**, *294*, 460-464.

16. Yamada, Y.; Iriyama, Y.; Abe, T.; Ogumi, Z., Kinetics of lithium ion transfer at the interface between graphite and liquid electrolytes: effects of solvent and surface film. *Langmuir* **2009**, *25*, 12766-70.

17. Yamada, Y.; Miyazaki, K.; Abe, T., Role of edge orientation in kinetics of electrochemical intercalation of lithium-ion at graphite. *Langmuir* **2010**, *26*, 14990-4.

18. Busche, M. R.; Drossel, T.; Leichtweiss, T.; Weber, D. A.; Falk, M.; Schneider, M.; Reich, M. L.; Sommer, H.; Adelhelm, P.; Janek, J., Dynamic formation of a solid-liquid electrolyte interphase and its consequences for hybrid-battery concepts. *Nature Chemistry* **2016**, *8*, 426-34.

19. Abe, T.; Ohtsuka, M.; Sagane, F.; Iriyama, Y.; Ogumi, Z., Lithium Ion Transfer at the Interface between Lithium-Ion-Conductive Solid Crystalline Electrolyte and Polymer Electrolyte. *Journal of The Electrochemical Society* **2004**, *151*, A1950-A1953.

20. Abe, T.; Sagane, F.; Ohtsuka, M.; Iriyama, Y.; Ogumi, Z., Lithium-Ion Transfer at the Interface Between Lithium-Ion Conductive Ceramic Electrolyte and Liquid Electrolyte-A Key to Enhancing the Rate Capability of Lithium-Ion Batteries. *Journal of The Electrochemical Society* **2005**, *152*, A2151-A2154.

21. Mehrotra, A.; Ross, P. N.; Srinivasan, V., Quantifying Polarization Losses in an Organic Liquid Electrolyte/Single Ion Conductor Interface. *Journal of The Electrochemical Society* **2014**, *161*, A1681-A1690.

22. Sagane, F.; Abe, T.; Iriyama, Y.; Ogumi, Z., Li^+ and Na^+ transfer through interfaces between inorganic solid electrolytes and polymer or liquid electrolytes. *Journal of Power Sources* **2005**, *146*, 749-752.

23. Sagane, F.; Abe, T.; Ogumi, Z., Li+-Ion Transfer through the Interface between Li^+-Ion Conductive Ceramic Electrolyte and Li+-Ion-Concentrated Propylene Carbonate Solution. *The Journal of Physical Chemistry C* **2009**, *113*, 20135-20138.

24. Sagane, F.; Abe, T.; Ogumi, Z., Electrochemical Analysis of Lithium-Ion Transfer Reaction through the Interface between Ceramic Electrolyte and Ionic Liquids. *Journal of The Electrochemical Society* **2012**, *159*, A1766-A1769.

25. Sagane, F.; Miyazaki, K.; Fukutsuka, T.; Iriyama, Y.; Abe, T.; Ogumi, Z., Lithium-ion Transfer at the Interface between Solid and Liquid Electrolytes under Applying DC Voltage. *Chemistry Letters* **2010**, *39*, 826-827.

26. Schleutker, M.; Bahner, J.; Tsai, C. L.; Stolten, D.; Korte, C., On the interfacial charge transfer between solid and liquid Li^+ electrolytes. *Phys Chem Chem Phys* **2017**, *19*, 26596-26605.

27. Yamada, Y.; Sagane, F.; Iriyama, Y.; Abe, T.; Ogumi, Z., Kinetics of Lithium-Ion Transfer at the Interface between $Li_{0.35}La_{0.55}TiO_3$ and Binary Electrolytes. *The Journal of Physical Chemistry C* **2009**, *113*, 14528-14532.

28. Nakajima, K.; Katoh, T.; Inda, Y.; Hoffman, B., Lithium Ion Conductive Glass Ceramics: Properties and Application in Lithium Metal Batteries. In *Symposium on Energy Storage Beyond Lithium Ion; Materials Perspective*, Oak Ridge National Laboratory, USA, 2010.

29. Bard, A. J.; Faulkner, L. R., *Electrochemical Methods: Fundamentals and Applications, 2nd Edition*; Wiley Textbooks, 2000.

30. Yamada, Y.; Yamada, A., Review—Superconcentrated Electrolytes for Lithium Batteries. *Journal of The Electrochemical Society* **2015**, *162*, A2406-A2423.

31. Kakiuchi, T., Current—potential characteristic of ion transfer across the interface between two immiscible electrolyte solutions based on the Nernst—Planck equation. *Journal of Electroanalytical Chemistry* **1992**, *322*, 55-61.

32. Kontturi, K.; Manzanares, J. A.; Murtomäki, L.; Schiffrin, D. J., Rate Constant for Ion Transfer in Inhomogeneous Media at the Interface of Immiscible Electrolytes. *The Journal of Physical Chemistry B* **1997**, *101*, 10801-10806.

33. Murtomäki, L.; Kontturi, K.; Schiffrin, D. J., Some remarks on the double layer correction to the kinetics of ion transfer at the interface of immiscible electrolytes. *Journal of Electroanalytical Chemistry* **1999**, *474*, 89-93.

34. Fu, K. K., et al., Stabilizing the Garnet Solid-Electrolyte/Polysulfide Interface in Li–S Batteries. *Chemistry of Materials* **2017**, *29*, 8037-8041.

35. Xu, B.; Duan, H.; Liu, H.; Wang, C. A.; Zhong, S., Stabilization of Garnet/Liquid Electrolyte Interface Using Superbase Additives for Hybrid Li Batteries. *ACS Applied Materials & Interfaces* **2017**, *9*, 21077-21082.

36. Yu, X.; Bi, Z.; Zhao, F.; Manthiram, A., Polysulfide-Shuttle Control in Lithium-Sulfur Batteries with a Chemically/Electrochemically Compatible NaSICON-Type Solid Electrolyte. *Advanced Energy Materials* **2016**, *6*.

37. Cresce, A. v.; Russell, S. M.; Baker, D. R.; Gaskell, K. J.; Xu, K., In Situ and Quantitative Characterization of Solid Electrolyte Interphases. *Nano Letters* **2014**, *14*, 1405-1412.

38. Sun, K.; Wu, Q.; Gan, H., Molecular insights into ether-based electrolytes for Li-FeS_2 batteries. *Energy Storage Materials* **2018**, *12*, 85-93.

39. Kirillov, S. A.; Gorobets, M. I.; Tretyakov, D. O.; Ataev, M. B.; Gafurov, M. M., Phase diagrams and conductivity of lithium salt systems in dimethyl sulfoxide, propylene carbonate and dimethyl carbonate. *Journal of Molecular Liquids* **2015**, *205*, 78-84.

40. Angell, C. A., Fast ion motion in glassy and amorphous materials. *Solid State Ionics* **1983**, *9-10*, 3-16.

41. Gutmann, V., Solvent effects on the reactivities of organometallic compounds. *Coordination Chemistry Reviews* **1976**, *18*, 225-255.

42. Mariappan, C. R.; Gellert, M.; Yada, C.; Rosciano, F.; Roling, B., Grain boundary resistance of fast lithium ion conductors: Comparison between a lithium-ion conductive Li–Al–Ti–P–O-type glass ceramic and a $Li_{1.5}Al_{0.5}Ge_{1.5}P_3O_{12}$ ceramic. *Electrochemistry Communications* **2012**, *14*, 25-28.

43. Mertens, A.; Yu, S.; Schön, N.; Gunduz, D. C.; Tempel, H.; Schierholz, R.; Hausen, F.; Kungl, H.; Granwehr, J.; Eichel, R.-A., Superionic bulk conductivity in $Li_{1.3}Al_{0.3}Ti_{1.7}(PO_4)_3$ solid electrolyte. *Solid State Ionics* **2017**, *309*, 180-186.

44. Bachman, J. C., et al., Inorganic Solid-State Electrolytes for Lithium Batteries: Mechanisms and Properties Governing Ion Conduction. *Chemical Reviews* **2016**, *116*, 140-62.

45. Qian, J.; Henderson, W. A.; Xu, W.; Bhattacharya, P.; Engelhard, M.; Borodin, O.; Zhang, J.-G., High rate and stable cycling of lithium metal anode. *Nature Communications* **2015**, *6*, 6362.

5 Electrochemical observation of polysulfide species in solid polymer electrolytes lithium-sulfur batteries

5.1 Overview

In this chapter, a novel three-electrode cell design is used for direct observation, for the first time, of polysulfide species in PEO-based solid polymer electrolytes, using cyclic voltammetry and electrochemical impedance spectroscopy. Polysulfides are generated by passing current between the sulfur and lithium electrodes, and detected using a glassy carbon probe, allowing operando tracking of the polysulfide intermediates.

5.2 Background

As discussed in Chapter 1, one strategy to tackle the issues of dendrite growth and polysulfide shuttling in Li-S batteries is the use of solid (polymer, inorganic or composite) electrolytes. Solid polymer electrolytes comprise lithium salts dissolved in high-molecular-weight polymers such as PEO. Low conductivity at room temperature means that they must be operated at elevated temperatures (above the melting point of the polymer crystalline phase, e.g. 70 °C). Nevertheless, they offer advantages including mechanical stability, ease of fabrication, a stable interface with lithium metal, and, depending on the modulus of the polymer, suppression of dendrite growth.[1-5]

Recently, Rodriquez et al evaluated the effect of lithium salt on the performance of all-solid state Li-S cells with PEO-based electrolytes.[6] Electrolytes consisting of LiFSI in PEO showed improved cycling performance (high discharge capacity and Coulombic efficiency) compared to those containing the commonly used LiTFSI salt, which was attributed to formation of a stable and polysulfide-resistant SEI between the LiFSI/PEO electrolyte and the lithium metal anode.

The mechanisms of Li-S redox reactions in liquid electrolytes have been studied extensively, using both electrochemical methods and analytical techniques such as XAS, UV-vis, Raman, NMR, and HPLC, as discussed in several recent review papers.[7-9] On the other hand, there have been few studies on polysulfide chemistry in solid polymer electrolytes. Marceau et al[10] used in-operando SEM and UV-vis spectroscopy to study a cell with PEO-based electrolyte containing 7 wt% $LiClO_4$ and 12 wt% SiO_2 nanoparticles, demonstrating the accumulation of various polysulfide species, and the predominant formation of S_4^{2-} and of S_6^{2-} during discharge and charge,

respectively. Wujcik et al[11] used XAS to study Li-S cells containing a diblock copolymer electrolyte polystyrene-poly(ethylene oxide) with $LiClO_4$ (Li:EO = 0.085). A collection of polysulfide radical anions and long polysulfide dianions were found to dominate the electrolyte composition after the early stage of discharge, with the concentration of radical anions decreasing and a mixture of progressively shorter polysulfide dianions appearing at increased depth of discharge.

In this chapter, a novel three-electrode cell design is used for direct observation of polysulfide species in PEO-based solid polymer electrolytes, using electrochemical methods, gaining insight into their reaction mechanisms, kinetics and mass transport.

5.3 Experimental details

Cells were constructed with either two or three electrodes, i.e. without lithium or with lithium. Figure 5.1a shows the details of the cell design with two electrodes. As in previous work[12-13], a glassy carbon electrode (3 mm diameter, type 2, Alfa Aesar) is embedded in a 1-inch diameter borosilicate glass disc attached to a glass tube which fits a standard 1 inch 'Swagelok' cell. A thin copper rod in contact with the back face of the glassy carbon serves as the current collector. On the other side of the cell is a disc-shaped sulfur-PEO composite electrode (11 mm diameter) on top of a stainless steel current collector. Figure 5.1b shows the details of the cell design with three electrodes. In this case, an additional, ring-shaped lithium electrode (20 mm outer dimeter, 10 mm inner diameter), is included on the same side as the sulfur-PEO composite electrode. The sulfur and lithium electrodes are arranged concentrically on top of a special stainless steel current collector, which contains an embedded PEEK tube to maintain electrical isolation between these electrodes.

Prior to each use, glassy carbon electrodes were polished in deionised water (Purite, 18.2 MΩ cm) with 25, 3.0 and 0.3 μm alumina powder and finally on a 'blank' polishing pad, and rinsed with deionised water. They were then dried, along with other cell components, under vacuum at 80 ^{o}C for a minimum of 1 hour before being transferred to an argon filled-glovebox (<1 ppm water content, < 10 ppm oxygen content, mBraun).

The PEO-based solid polymer electrolytes and sulfur composite electrodes used in this work were provided by CIC Energigune according to previously reported procedures.[6] The sulfur loading in the sulfur composite electrode was 0.9 mg cm^{-2}. They were punched by hand to the required diameter and dried for 3 days at 50 ^{o}C under vacuum in a Buchi furnace, before being

transferred to the glovebox. Lithium electrodes (battery grade, 100 µm thickness, Rockwood Lithium) were punched by hand to the required diameters inside the glovebox.

Cells were assembled inside the glovebox before being transferred to an oven at 70 ^{o}C. Cells were allowed to equilibrate for 24 hours prior to measurement. Electrochemical measurements were carried out using Bio-logic VMP2, VMP3 and SP-150 potentiostats. Cyclic voltammograms at the glassy carbon electrode were carried out at a scan rate of 2 – 50 mV s^{-1} as indicated. EIS measurements were carried out with a voltage amplitude of 10 mV and frequencies of 200 kHz – 10 Hz unless stated.

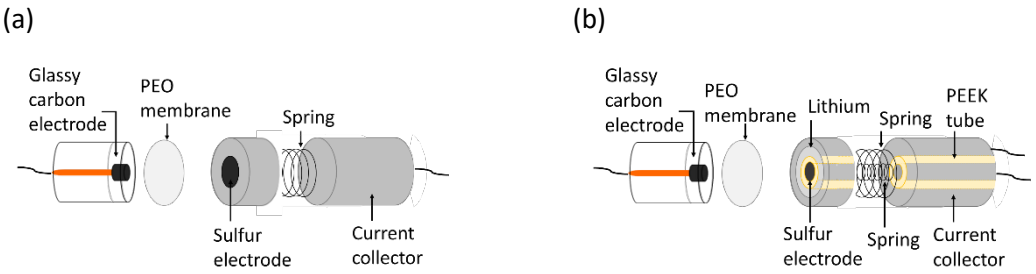

Figure 5.1: Schematic of cell designs with (a) two electrodes (no lithium) and (b) three electrodes (with lithium)

5.4 Results and discussion

5.4.1 Sulfur reduction in polymer electrolyte cells

Initial measurements were performed in cells containing a glassy carbon working electrode, a PEO electrolyte and a sulfur-PEO composite electrode. The cell sketch is shown in Figure 5.1a. The cells were equilibrated at 70 °C for 24 hours prior to measurement, during which time sulfur dissolves into the PEO electrolyte from the sulfur electrode. Cyclic voltammograms were recorded at the glassy carbon working electrode, using the sulfur-PEO composite electrode as both reference and counter electrode, since it has a much higher capacity than the glassy carbon electrode. The characteristic electrochemical behaviour of sulfur dissolved in the PEO electrolytes, containing either LiTFSI or LiFSI as the lithium conductive salt, is shown in Figure 5.2a. It is clear that both lithium salts (LiTFSI and LiFSI) give very similar results (and the differences are within the reproducibility of the measurements, Figure 5.2b). This demonstrates that the different lithium salts do not produce significant differences in the solubility or diffusion coefficient of sulfur dissolved in the polymer electrolyte, nor significant differences in the kinetics of sulfur reduction at the glassy carbon electrode. This is consistent with the hypothesis given by Rodriguez et al that the effect of the lithium salt on the performance of Li-S cell is related to the

effect of the lithium salt on the lithium SEI.[6] Since there is no lithium electrode in these cells, both salts produce the same electrochemical response. The voltammograms show a broad reduction wave centred at around -1.0 V vs. S, with the corresponding oxidation at around -0.8 V vs. S. Taking into account that the potential of sulfur, when measured vs. Li^+/Li in cells containing a Li electrode (cell sketch in Figure 5.1b) is around 3.2 V vs. Li^+/Li, then those potential values correspond to 2.2 and 2.4 V vs. Li^+/Li.

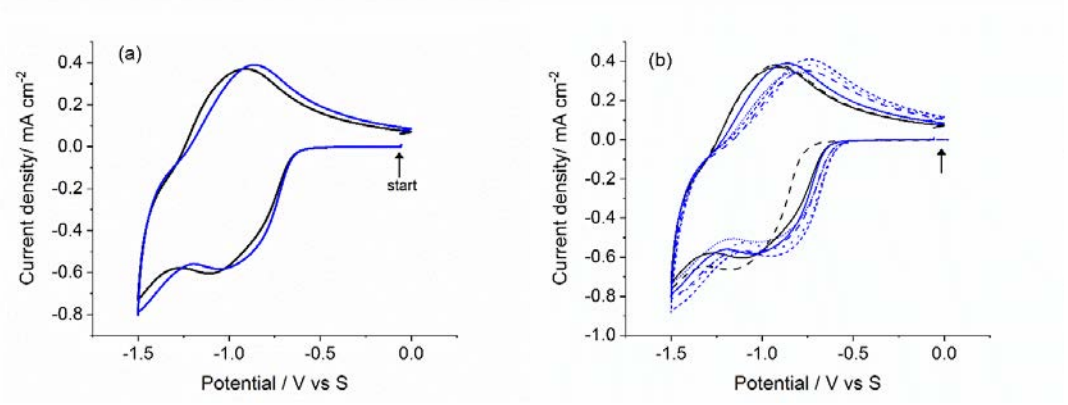

Figure 5.2: (a) First-cycle cyclic voltammograms recorded at a glassy carbon electrode in contact with a sulfur-saturated polymer electrolyte containing LiFSI (black) or LiTFSI (blue), using the cell sketched in Figure 5.1a. Scan rate: 50 mV s^{-1}. (b) Comparison of first-cycle cyclic voltammograms recorded as in (a) in multiple cells. Arrows indicate the start of cycling.

These results demonstrate the sensitivity of the glassy carbon sensor to detect dissolved species in the polymer electrolyte battery. For a more accurate investigation of the mechanisms of sulfur electrochemistry, measurements were also made in cells containing a lithium reference electrode (see cell sketch in Figure 5.1b). Use of this 3-electrode configuration allowed a more accurate estimation of redox potentials vs Li^+/Li. Measurements were done with the cells as prepared, following a 24 hour equilibration period but before any charge had been passed between the sulfur and lithium electrodes.

Note that the distance between the sulfur and lithium electrodes (ca. 1.5 mm) is much larger than the distance between the sulfur and glassy carbon electrodes (i.e. the thickness of the PEO electrolyte, ca. 70 µm). Thus is it possible to detect sulfur at the glassy carbon electrode within the timescale of these experiments (ca. 25 hours), before any possibility of chemical reduction at the lithium electrode. For a diffusion coefficient of ~10^{-6} cm^2 s^{-1}, as reported in the literature[14] for sulfur in liquid electrolytes at room temperature, the time taken to diffuse 1.5 mm would be around 6 hours, compared to around 1 minute to diffuse 70 µm. However, the diffusion

coefficient of sulfur in the solid polymer is expected to be at least an order of magnitude lower than in liquid electrolytes.[4] A diffusion coefficient of 10^{-7} cm^2 s^{-1} would mean that the time taken to diffuse 1.5 mm would be around 60 hours, ruling out chemical reduction of sulfur at the lithium electrode within the timescale of the experiment. On the other hand, even if the diffusion coefficient of sulfur species in the solid polymer was three orders of magnitude lower than in liquid electrolytes (10^{-9} cm^2 s^{-1}), the time taken to diffuse 70 µm would be around 800 minutes or 13.3 hours, thus still allowing detection of sulfur at the glassy carbon electrode within the timescale of the experiment.

Figure 5.3 shows cyclic voltammograms recorded at the glassy carbon electrode in contact with the sulfur-saturated PEO electrolytes, using the 3-electrode configuration. The reproducibility is lower than in the case of the cells without lithium because the construction of the cells is more involved and because lithium might introduce some trace contaminants upon reaction with the electrolyte. Within the reproducibility of the measurements, however, both salts again give similar results. Note that the potential windows used in the measurements in Figures 5.2 and 5.3 are different. The voltammograms in Figure 5.3 show two reduction waves: one centred at around 2.2 V vs. Li$^+$/Li (as for the cells in Figure 5.2) and another at 1.5 V vs. Li$^+$/Li, with an oxidation wave centred at around 2.5 V vs. Li$^+$/Li. There is also a shoulder in the oxidation wave, at around 1.8 V, and possibly another at around 2.2 V suggesting an overlapping of at least two oxidation processes. These voltammograms bear similarity to sulfur CVs recorded in some liquid electrolytes (e.g. DME)[15], although the waves are much broader, as expected for the slow electron transfer kinetics and diffusion in solid state electrolytes.

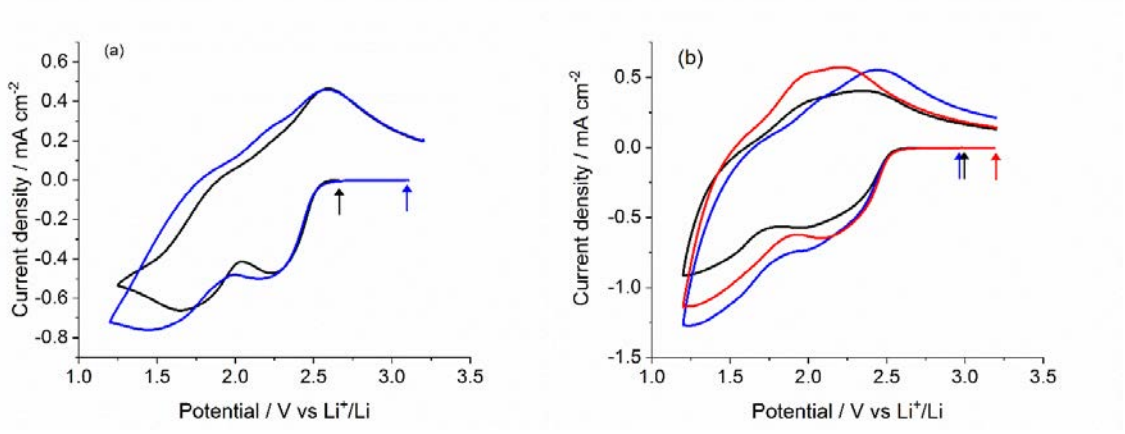

Figure 5.3: First-cycle cyclic voltammograms recorded at a glassy carbon electrode in contact with a sulfur-saturated polymer electrolyte containing LiFSI (a) or LiTFSI (b), using the cell sketched in Figure 5.1b with sulfur as the counter electrode and lithium as the reference electrode. Scan rate: 50 mV s^{-1}. Measurements from two different cells with LiTFSI and three different cells with LiFSI are shown. Arrows indicate the start of cycling.

Figure 5.4 compares the first and second cycles of the cyclic voltammograms, from an example cell in each case (i.e. with LiTFSI-PEO or LiFSI-PEO electrolyte). A small shift of the first reduction wave towards higher potentials is observed in the second cycle, which could be due to the formation of polysulfide species as a result of the cyclic voltammogram experiment, but the first and second cycles are otherwise similar, suggesting only oxidised species (i.e. sulfur) initially present in the electrolytes.

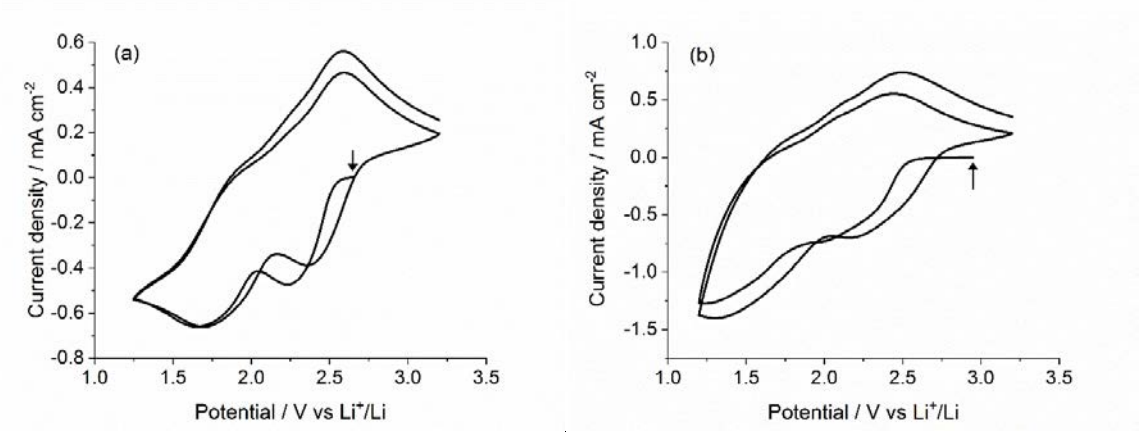

Figure 5.4: First and second-cycle cyclic voltammograms recorded at a glassy carbon electrode in contact with a sulfur-saturated polymer electrolyte containing LiFSI (a) or LiTFSI (b), using the cell sketched in Figure 5.1b with sulfur as the counter electrode and lithium as the reference electrode. Scan rate: 50 mV s^{-1}. Arrows indicate the start of cycling.

5.4.2 Mechanism of sulfur reduction in polymer electrolyte cells

A further advantage of the 3-electrode cell configuration used for the voltammograms in Figure 5.4 is that it allows measurement of the impedance at the glassy carbon electrode, which provides additional information about the mechanism of sulfur reduction. This is illustrated in Figure 5.5, which shows the changing impedance response at the glassy carbon electrode during the course of Staircase Potentio Electrochemical Impedance Spectroscopy (SPEIS) of a cell containing a LiTFSI-PEO electrolyte. Here a linear sweep voltammogram has effectively been conducted by stepping the potential at the working electrode by small increments (ca. 50 mV), and recording impedance spectra 5 seconds after each step (whilst holding the same bias potential). Figure 5.5a shows the current transients after each potential step, whose maxima form a pseudo-voltammogram (see also Figure E.1 in Appendix E), whilst Figure 5.5b shows the measured impedance spectra.

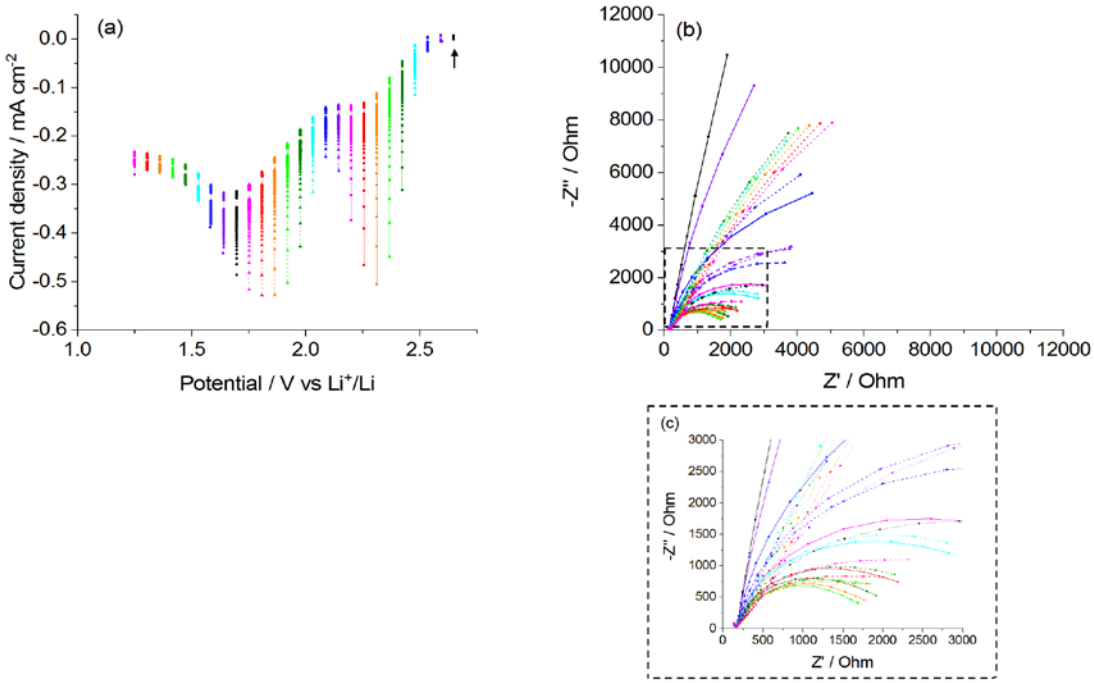

Figure 5.5: Staircase Potentio Electrochemical Impedance Spectroscopy (SPEIS,) recorded at a glassy carbon electrode in contact with a sulfur-saturated polymer electrolyte containing LiTFSI, using the cell sketched in Figure 5.1b with sulfur as the counter electrode and lithium as the reference electrode. (a) Current transients during each ca. 50 mV potential step. Arrow indicates the starting potential. (b) Impedance spectra recorded 5 seconds after applying each potential step (zoom-in to high frequency region is shown in (c)).

Note that SPEIS is usually applied to study electrochemical reaction kinetics along steady-state curves; indeed a criterion for quantitatively valid EIS measurements is that the system under investigation is at steady state.[16] Clearly in this case, the system is not at steady state (the current transients are still changing when each impedance measurement is taken; see also the Kramers-Kronig analyses in Appendix E). Consequently, quantitative interpretation of the data should be treated with caution. Nevertheless, Figure 5.5b shows a striking change in the measured impedance spectra as a function of potential, highlighting the sensitivity of the glassy carbon electrode.

At high potentials, the impedance spectra consist of a small truncated semicircle at high frequencies, attributed to the polymer electrolyte itself, followed by a capacitive spike (or part of a very large semicircle) at lower frequencies, suggesting blocking behaviour (or very high charge transfer resistance) at the glassy carbon electrode. As the potential is stepped towards lower values, the width of the lower-frequency semicircle, which reflects the magnitude of the charge

transfer resistance, R_{ct}, changes significantly, and with some relationship to the peaks in the pseudo-voltammogram. This is highlighted in Figure 5.6a which plots the values of R_{ct} (obtained by fitting an equivalent circuit model to the data (see Appendix E) together with the maxima of the current transients from the pseudo-votammogram, as a function of the electrode potential.

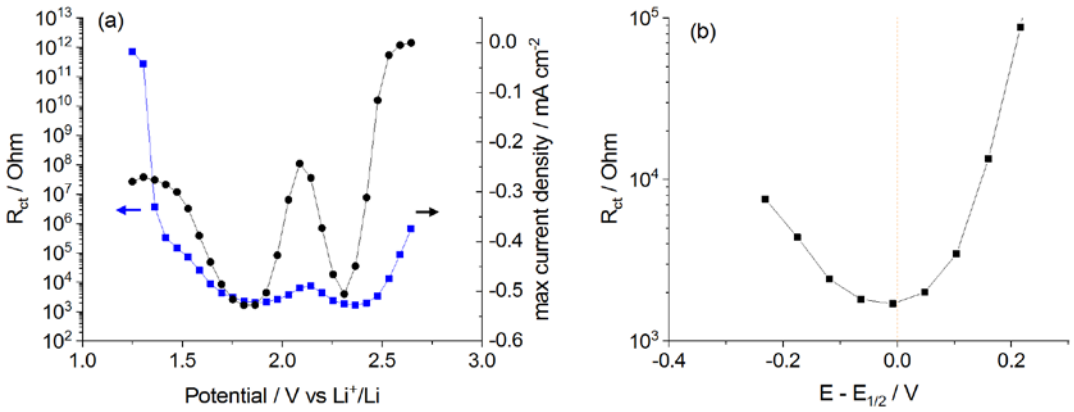

Figure 5.6: (a) Charge transfer resistance and current transient maximum, as a function of electrode potential, from SPEIS data in Figure 5.5. (b) Charge transfer resistance as a function of E-$E_{1/2}$ for the first reduction wave.

It can be shown that, assuming only oxidised species are initially present in the electrolyte, then for a reversible Faradaic reaction in the presence of semi-infinite linear diffusion, R_{ct} is given by (equation 5.1)[17]:

$$R_{ct} = \frac{RT}{n^2F^2k_0c_O^*}\frac{1+\exp[nF(E-E_{1/2})]}{\xi^{\alpha}\exp[(1-\alpha)nf(E-E_{1/2})]} \qquad \text{(Eq. 5.1)}$$

where $\xi = (D_O/D_R)^{1/2}$. It therefore has a minimum at (equation 5.2):

$$E_S = E_{1/2} + \frac{RT}{nF}\ln\frac{\alpha}{1-\alpha} \qquad \text{(Eq. 5.2)}$$

For processes with α = 0.5, R_{ct} therefore has a minimum at the half-wave potential.

For a reversible reaction, the half-wave potential is approximately halfway between the peak and half-peak potential.[18] Values of 2.310 V and 2.438 V vs. Li^+/Li were obtained for the peak and half-peak potentials, respectively, of the first reduction wave in Figure 5.6a, giving an estimate of 2.374 V vs Li^+/Li for the half-wave potential of this wave. Figure 5.6b plots R_{ct} as a function of $E - E_{1/2}$, and is in good agreement with the curve expected from equation (1). The

asymmetry of the curve may be due to effects of the second reduction wave at lower potentials, rather than a value of α different from the assumed value of 0.5. Analysis of the second reduction wave in Figure 5.6a is more complicated, due to its proximity to the first reduction wave, which makes evaluation of the half-wave potential difficult. However, it can be seen qualitatively that, as for the first reduction wave, the minimum value of R_{ct} occurs at approximately the half-wave potential.

Similar results were obtained in a cell containing a PEO electrolyte with LiFSI (Figures 5.7 and 5.8). Unfortunately, a more quantitative analysis of these results is complicated by the sharp increase in the current maxima between the first and second potential steps in Figure 5.7a, making evaluation of half-wave potentials difficult here too. Again, however, it can be seen qualitatively that for both reduction waves, the minimum value of R_{ct} occurs at approximately the half-wave potential (Figure 5.8).

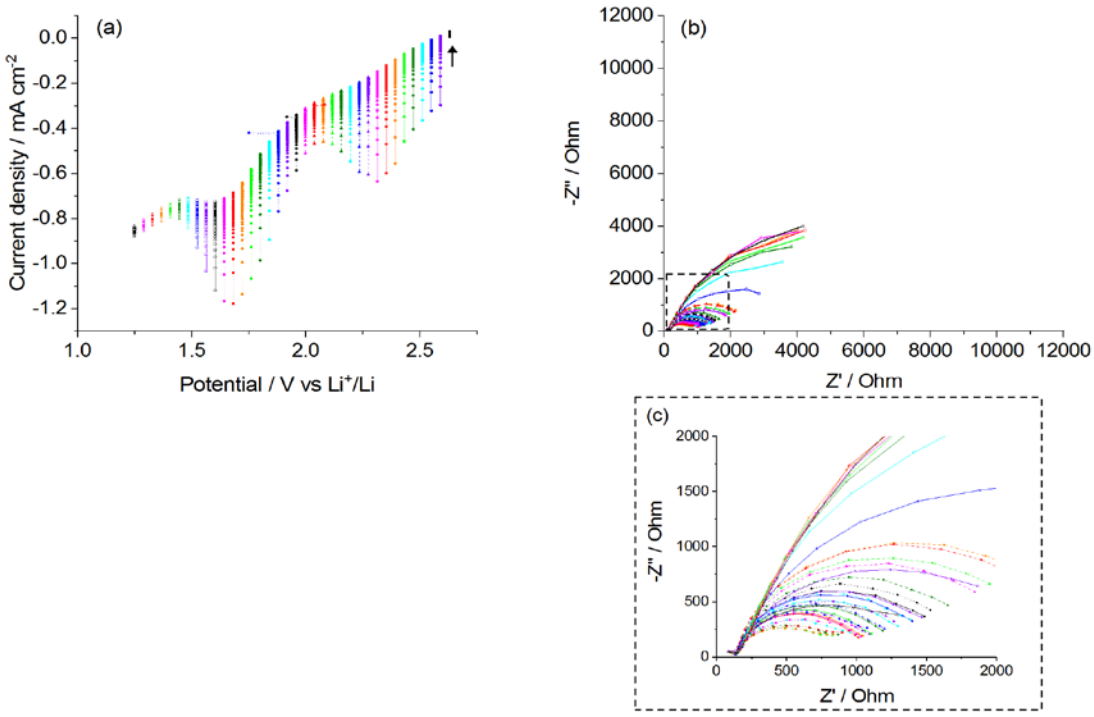

Figure 5.7: As in Figure 5.5 but with a polymer electrolyte containing LiFSI.

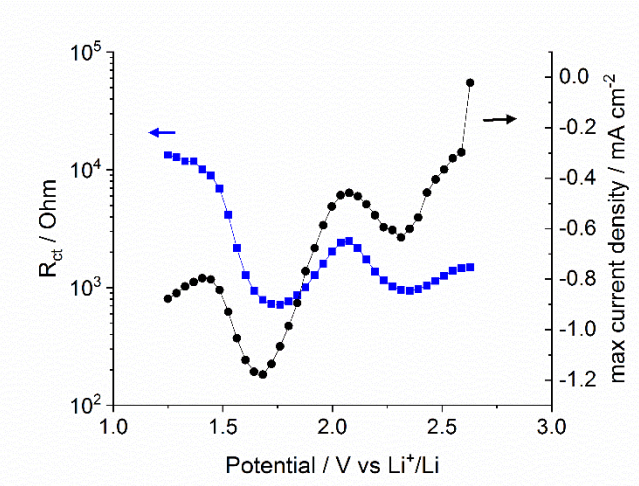

Figure 5.8: Charge transfer resistance and current transient maximum, as a function of electrode potential, from SPEIS data in Figure 5.7.

5.4.3 In-situ detection of polysulfides in Li-S polymer electrolyte cells

We shall now examine the case where polysulfides are present in the polymer electrolyte. For the generation of polysulfides, a lithium ring was incorporated around the sulfur electrode (see cell sketch in Figure 5.1b) and two different electrochemical methods for the reduction of sulfur to polysulfides were explored:

Method 1. Polarization of the sulfur electrode via application of a cyclic voltammogram in which the potential of the sulfur electrode was varied between 0.9 V and 3.2 V vs. Li^+/Li, at a scan rate of 0.2 mV s^{-1}.

Method 2. Application of a series of 10-30 minute potential holds to the sulfur electrode, from 2.5 V to 1.8 V vs. Li^+/Li, where the potential was decreased by 0.1 V in each of the potential holds.

5.4.3.1 Polysulfides generated via cyclic voltammetry of the sulfur electrode

Figure 5.9a shows the voltammogram of the sulfur electrode in a cell containing a PEO electrolyte with LiTFSI, with lithium as the counter-reference electrode, at a very slow scan rate of 0.2 mV s^{-1} (Method 1). The iR drop in this configuration is very high. Nevertheless, peaks are apparent in the voltammogram which broadly correspond to those in Figure 5.3, confirming the reduction of sulfur to polysulfides and their subsequent re-oxidation. Figure 5.9b shows the voltammogram of the sulfur electrode recorded in the same way in a cell containing a PEO electrolyte with LiFSI. In this case the peaks in the voltammogram are less obvious, and we note

again the high iR drop in this cell configuration, where the current path is from the side edges of the sulfur electrode to the side edges of the lithium electrode. This current path also means that cell-to-cell differences may be expected as a result of electrode preparation (manual punching) as well as manual placement of, and hence precise distance between, the sulfur and lithium electrodes.

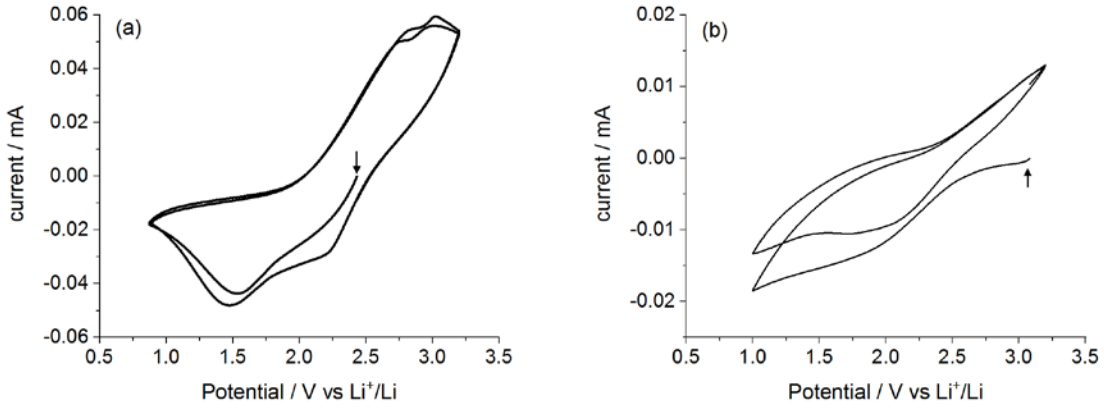

Figure 5.9: Cyclic voltammograms recorded in cells with polymer electrolyte membranes containing LiFSI (a) or LiTFSI (b), using the cell sketched in Figure 5.1b in a 2-electrode configuration with the sulfur electrode as the working electrode and the lithium electrode as the counter-reference electrode. Scan rate 0.2 mV s^{-1}; total scan time 12.8 hours. Arrows indicate the start of cycling.

After cycling the sulfur electrode, the cells were rested before cyclic voltammograms were then recorded at the glassy carbon electrode, with the sulfur electrode now serving as the counter electrode and lithium as the reference. Figure 5.10 shows voltammograms recorded after 4-12 hour intervals at open circuit, in cells containing PEO electrolytes with LiTFSI or LiFSI. For both lithium salts, two observations are immediately apparent when these voltammograms are compared to those in Figure 5.4 (before generation of polysulfides): a dramatic increase in the size of the peak currents (by a factor of more than 10), and a dramatic change in the shape of the peaks, which are now very similar to those reported for sulfur redox behaviour in DOL:DME.[14] In each case, the size and shape of the first reduction peak changes after the first cycle, becoming much larger and sharper. This difference between the first and second cycle demonstrates the presence of redox active polysulfides that can be reduced and oxidized, as will be discussed in section 5.4.4 in more detail. The results in Figure 5.10 demonstrate the formation of polysulfides in the cell as a result of cycling the sulfur electrode, and confirms again the high sensitivity of the glassy carbon electrode sensor.

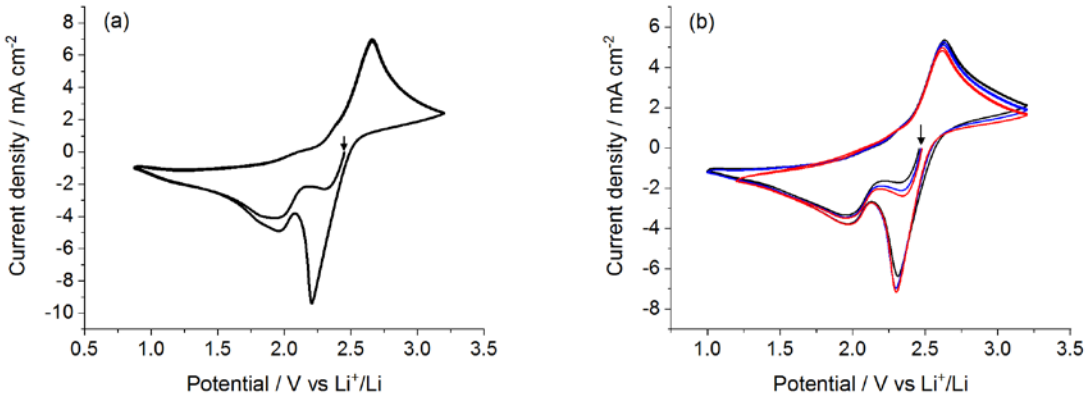

Figure 5.10: First and second-cycle cyclic voltammograms recorded at a glassy carbon electrode in contact with a polysulfide-containing polymer electrolyte containing LiTFSI (a) or LiFSI (b), using the cell sketched in Figure 5.1b, with sulfur as the counter electrode and lithium as the reference electrode, following the passing of the charge between the sulfur and lithium electrode via the voltammograms shown in Figure 5.9. Scan rate: 50 mV s^{-1}. Voltammograms were recorded 12 hours after those shown in Figure 5.9 for the cell with LiTFSI (a) and after 4, 8 and 12 hours for the cell with LiFSI (b). Arrows indicate the start of cycling.

For the cell containing a PEO electrolyte with LiFSI, which was measured at 4, 8 and 12 hour intervals, there was no further change after 4 hours, suggesting that the concentration of polysulfides in the cell had in fact equilibrated within 4 hours. It should be noted that the total scan time associated with the application of a cyclic voltammogram to the sulfur composite electrode was 12.8 hours, which could contribute to the fact that, with four additional hours after the application of the cyclic voltammogram, the polysulfide concentration at the glassy carbon electrode sensor had already reached equilibrium. As described in section 5.4.1, since the thickness of the polymer electrolyte is ca. 70 µm, a diffusion coefficient of 10^{-9} cm^2 s^{-1} would imply that the time required for polysulfides to travel from the sulfur to the glassy carbon electrode sensor would be around 13.3 hours, in agreement with the present results. Since measurements were not performed at shorter times, the present results are also consistent with higher values of the diffusion coefficient.

5.4.3.2 Polysulfides generated via application of potential holds at the sulfur electrode

Similar effects to those in Figure 5.10 were observed in a cell containing an LiTFSI-PEO electrolyte, in which the sulfur electrode was partially discharged via a series of 10-30 minute potential holds vs. Li^+/Li, at 0.1 V intervals between 2.5 V and 1.8 V, and then rested for 12 hours

(Method 2). Figure 5.11 shows cyclic voltammograms recorded at the glassy carbon electrode before and after this procedure. Again, a dramatic increase in the size of the peak currents and a dramatic change in the shape of the peaks is observed after the partial discharge of the sulfur electrode, and the first and second cycle voltammograms are no longer similar, demonstrating the formation of polysulfides. Whilst a quantitative comparison with the voltammograms shown in Figure 5.10 should be approached with care, due to the cell-to-cell variability discussed above, qualitatively the results are remarkably similar.

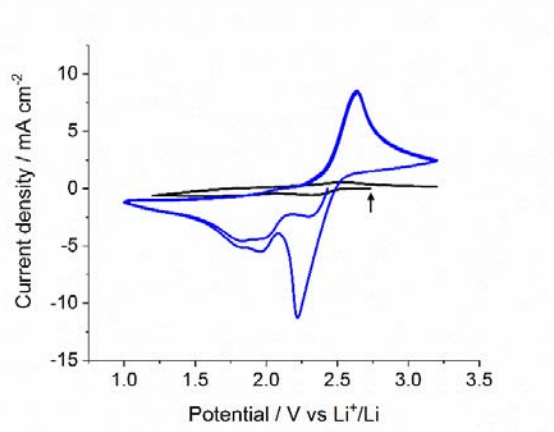

Figure 5.11: First and second-cycle cyclic voltammograms recorded at a glassy carbon electrode in contact with a polysulfide-containing polymer electrolyte containing LiTFSI, using the cell sketched in Figure 5.1b, with sulfur as the counter electrode and lithium as the reference electrode, before (black) and after (blue) partial discharge of the sulfur electrode via a series of potential holds vs. the lithium electrode. Scan rate 50 mV s^{-1}. Arrow indicates the start of cycling.

Figure 5.12a shows voltammograms recorded at the glassy carbon electrode shortly after each of the individual potential holds of the sulfur electrode. A gradual increase in the peak currents is observed as the cell is discharged, suggesting a gradual increase in the concentration of polysulfides. The open circuit potential at the glassy carbon electrode can also be seen to change, moving towards less positive values, which, following the Nernst equation, is consistent with an increase in the concentration of reduced species as a result of sulfur reduction. Caution is needed, however, since the peak potentials also appear to move towards less positive values, suggesting a possible drift in the system.

Figure 5.12b shows impedance spectra measured at open circuit immediately before each of the voltammograms in Figure 5.12a. Initially the spectra comprise a truncated semicircle, attributed the polymer electrolyte itself, followed by a capacitive spike, consistent with blocking (or very high charge transfer resistance) behaviour at the glassy carbon electrode. As the cell is

discharged, and polysulfide species are generated, the capacitive spike in the impedance spectrum becomes a semicircle with progressively decreasing width, suggesting progressively smaller charge transfer resistance of the redox couple involved.

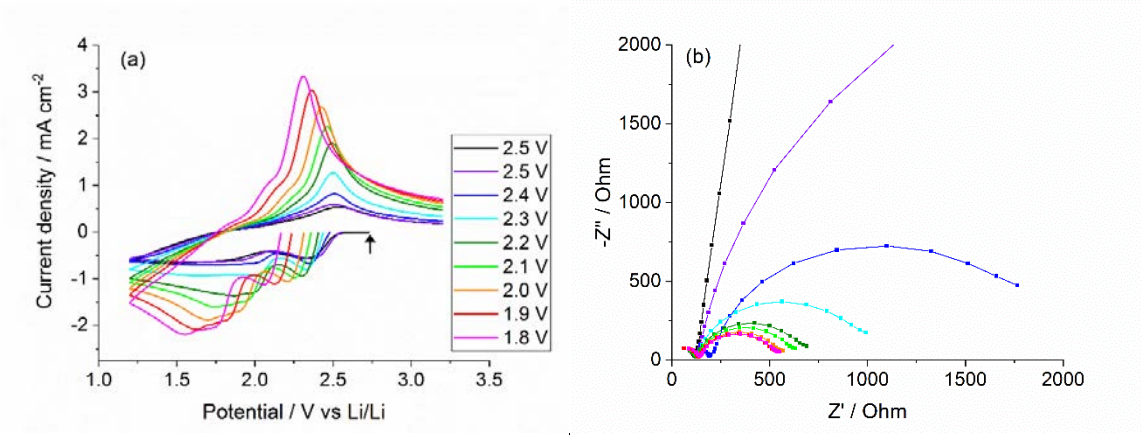

Figure 5.12: (a) First-cycle cyclic voltammograms (scan rate 50 mV s^{-1}, arrow indicates the start of cycling) and (b) impedance spectra recorded at a glassy carbon electrode in contact with a polymer electrolyte containing LiTFSI, using the cell sketched in Figure 5.1b, with sulfur as the counter electrode and lithium as the reference electrode, after each of a series of potential holds of the sulfur electrode vs. the lithium electrode.

As discussed, gradual increases in peak current recorded at the glassy carbon electrode were observed during the course of the potential holds applied to the sulfur electrode. However, a further marked increase was observed after the subsequent 12 hour rest period (compare the first-cycle voltammograms in Figures 5.11 (pink curve) and 5.12 (blue curve) and note the change in the oxidation current, which increases by a factor of 3). This marked increase in current evidences a further increase in the polysulfide concentration (i.e. the concentration of sulfur present as polysulfide species). This could be due to slow chemical reactions, which occurred during the 12 hour rest period, for instance comproportionation reactions between existing polysulfides and dissolved sulfur. Indeed, a previous study by Gasteiger and coworkers showed that some of the chemical reactions involved in the pathway of sulfur reduction to Li_2S are very slow, requiring ca. 17 hour for completion[14]. Gaberscek, Dominko and coworkers reported an impedance analysis of polysulfide solutions with two planar glassy carbon electrodes coupled with in-situ UV measurements and demonstrated that some chemical reactions of polysulfides required ca. 66 hours[19].

An alternative explanation for the marked increase in polysulfide concentration at the glassy carbon electrode after the 12 hour period is continued slow diffusion of polysulfides. As

discussed, for a diffusion coefficient of 10^{-9} cm^2 s^{-1} it would take 13.3 hours for polysulfides to diffuse across the thickness of the electrolyte (see section 5.4.3), compared to a total time of ca. 4.5 hours between the start and end of the measurements in Figure 5.12. In other words, not all of the polysulfides generated at the sulfur electrode would have reached the glassy carbon electrode in this time. (Diffusion coefficients of 10^{-7} cm^2 s^{-1} have been reported in the literature for polysulfides in liquid electrolytes[19-20] but diffusion coefficients in the solid polymer electrolyte are expected to be lower than in the liquids.[4]) Unfortunately, the complicated reaction mechanism of sulfur reduction makes it difficult to distinguish these two possible explanations.

5.4.4 Mechanism of polysulfide electrochemistry in Li-S polymer electrolyte cells

Additional measurements were performed to elucidate the mechanism of the polysulfide redox chemistry, for the polysulfide solutions generated during discharge of the Li-S cells. Figure 5.13 shows impedance spectra recorded at the glassy carbon electrode following the cyclic voltammograms shown in Figure 5.10, i.e. in cells in which polysulfides had been generated via application of a slow cycling voltammogram at the sulfur electrode, followed by a 12 hour rest (Method 1 described above). The spectra again include a truncated semicircle, attributed to the LiTFSI-PEO or LiFSI-PEO electrolyte itself, followed by a semicircle ascribed to charge transfer in parallel with double layer capacitance. The width of this semicircle is very similar for both lithium salts, indicating similar charge transfer resistances in both cases.

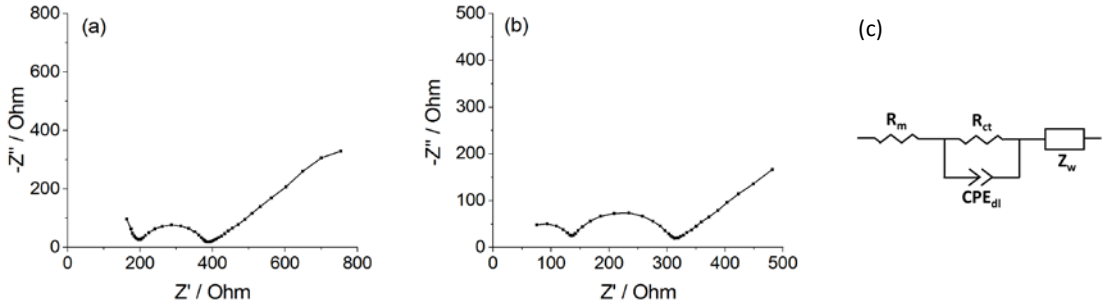

Figure 5.13: Impedance spectra recorded at a glassy carbon electrode in contact with a polysulfide-containing polymer electrolyte containing LiTFSI (a) and LiFSI (b), using the cell sketched in Figure 5.1b, with sulfur as the counter electrode and lithium as the reference electrode. Spectra recorded immediately before the voltammograms shown in blue in Figure 5.10. (c) Equivalent circuit model used to fit the spectra.

In contrast to the impedance results presented so far, the measurements in Figure 5.13 included frequencies as low as 10 mHz. Now, at low frequencies, Warburg behaviour (i.e. a 45 degree line) is clearly apparent, which we ascribe to the diffusion of polysulfides from the bulk of the electrolyte to the glassy carbon electrode surface.

The spectra in Figure 5.13 were fitted using the equivalent circuit model shown. As noted, the impedance spectra exhibits a truncated semi-circle at high frequencies, ascribable to the complex impedance behaviour of the polymer electrolyte (associated with a parallel combination of capacitance and resistor components). Those complications are not included in the model, which treats the electrolyte membrane as a simple resistor, R_m, whilst R_{ct} is the charge transfer resistance and CPE_{dl} is the double layer capacitance at the glassy carbon electrode. The effective, non-complex double layer capacitance of the glassy carbon electrode, C_{dl} is derived from the fitted parameters for R_{ct}, CPE_{dl}-T and CPE_{dl}-P using $C_{dl} = \left(R_{ct} \cdot T\right)^{1/P} \Big/ R_{ct}$.[21] Finally Z_W is the Warburg impedance associated with diffusion of polysulfides. In practice, a CPE with P-value fixed to 0.5 was used for the Warburg impedance, since ZView does not include a semi-infinite Warburg element. The Warburg impedance, σ, is calculated from the fitted CPE_{dl}-T value using $\sigma = 1\big/(T\sqrt{2})$. Table 1 summarises the fitted model parameters.

Parameter	Units	LiTFSI	LiFSI
R_m	Ω	189.5	127.9
	Ω·cm^2	13.4	9.0
R_{ct}	Ω	196.3 +/- 1.7	179.2 +/- 1.4
	Ω·cm^2	13.9 +/- 0.1	12.7 +/- 0.1
CPE_{dl}-T	F·s$^{(n-1)}$	5.17 · 10^{-6} +/- 0.35 · 10^{-6}	4.6 · 10^{-6} +/- 0.3 · 10^{-6}
CPE_{dl}-P		0.81 +/- 0.01	0.84 +/- 0.01
C_{dl}	F·cm^{-2}	13.9 · 10^{-6} +/- 1.2 · 10^{-6}	17.2 · 10^{-6} +/- 1.3 · 10^{-6}
Z_W-σ	Ω ·s$^{1/2}$	96.2 +/- 0.6	136.0 +/- 1.4

Table 5.1: Parameters obtained from equivalent circuit model fitting of the impedance spectra in Figure 5.13.

The fitted parameters provide values of the electrolyte resistance of 9.0 Ω cm^2 for PEO-LiTSFI and 13.4 Ω cm^2 for PEO-LiFSI, which correspond to conductivities of ca. $8 \cdot 10^{-4}$ S cm^{-1} and ca. $5 \cdot 10^{-4}$ S cm^{-1} respectively (taking into account that the electrolyte thickness is ca. 70 μm, and using the geometric electrode area for the calculation), which is in good agreement with previous studies.[6] It is also found that the double-layer capacitance of the glassy carbon electrode, as estimated using the fitted parameters of the CPE element, is around 15-20 μF cm^{-2}, which is as expected for a planar electrode surface (note that the normalization of the capacitance is done using the geometric area of the electrode). The charge-transfer resistance is found to be of the order of 13 Ω cm^2, from which an estimate of the exchange current density for the reaction being probed by the impedance measurements can be obtained using equation 5.3:

$$I_0 = \frac{RT}{nFAR_{ct}} \qquad \text{(Eq. 5.3)}$$

Assuming that the number of electrons involved in the reaction is between 2 and 5,[14] this yields a value of the exchange current density on the order of 0.5–1 mA cm^{-2}. This is larger by 2–3 orders of magnitude than the values of exchange current density reported in previous impedance studies of the redox chemistry of polysulfides in liquid electrolytes using flat electrodes.[19] One possible explanation is that the concentration of polysulfides could be higher in the present measurements. Unfortunately, because we have a mix of oxidised and reduced species in solution, and their relative diffusion coefficients are unknown, we cannot estimate their concentrations from the Warburg parameters in Table 1. However, given a sulfur loading in the electrode of 0.9 mg cm^{-2}, then assuming (i) full dissolution into the PEO membrane, (ii) minimal lateral diffusion, i.e. that the dissolved polysulfides are confined within a membrane volume equal to the area of the sulfur electrode (0.95 cm^2) multiplied by the thickness of the membrane (70 micron) and (iii) that all dissolved polysulfides are present as Li_2S_4, this would give a maximum polysulfide concentration of 0.9 M, compared to a concentration of 0.1 M in ref 19. Another possible explanation for the larger exchange current density observed in the present measurements is the higher temperature used here: 70 °C compared to room temperature in ref 19.

Further insight into the mechanism of the reaction was obtained by measuring cyclic voltammograms at the glassy carbon electrode at different scan rates (Figure 5.14). Taking into account the electrolyte resistance, iR drop effects can be corrected manually, and the results are shown in Figure 5.15. It is observed that all peak potentials are (nearly) independent of the scan rate, indicating that all redox processes are fast. Combined with the fact that, as shown in Figure

5.16, the peak current associated with the main reduction peak is (nearly) proportional to the square root of scan rate, this suggests that the redox couple involved is reversible. (Although the experimental data in Figure 5.16 show a slight curvature, which could indicate a quasi-reversible reaction,[18] the deviation from the reversible case is slight, and could be within the error of the measurements, since the peak currents are derived from the second cycle of the voltammograms, uncorrected for effects from the first cycle.)

At all scan rates, no (significant) oxidation peak corresponding to the second reduction peak is observed. This suggests that the redox process or processes associated with the second reduction peak are followed by a coupled chemical reaction.[14-15, 18] Consistent with this, a small shoulder preceding the main oxidation peak is observed at high scan rates but disappears at low scan rates (seen more clearly in Figures E.4 and E.5 in Appendix E), which can be explained by the longer time available at low scan rates for slower chemical reactions to proceed. In the PEO-LiTFSI electrolyte, the application of lower scan rates also reveals a clearer deconvolution of the second reduction peak into two overlapping processes (Figure E.4), suggesting a complex equilibrium between reducible polysulfide species, and highlighting further the sensitivity of the glassy carbon electrode.

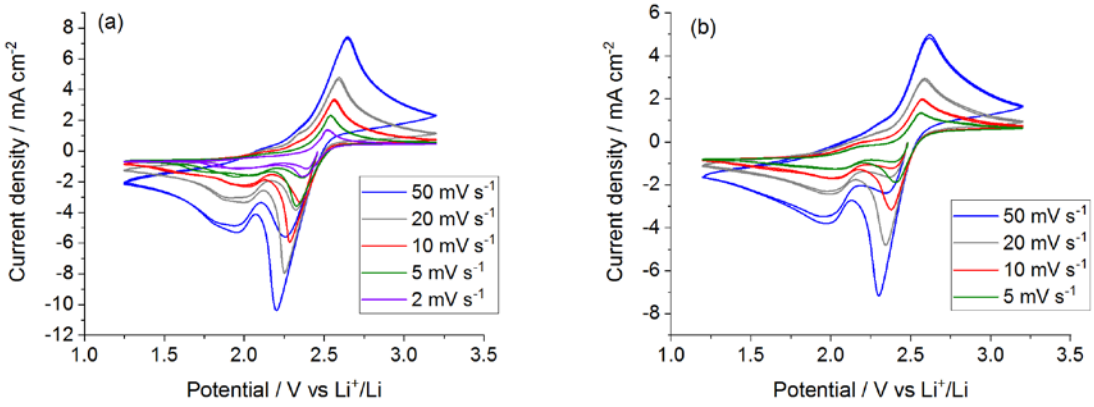

Figure 5.14: First and second-cycle cyclic voltammograms recorded at a glassy carbon electrode in contact with a polysulfide-containing polymer electrolyte containing (a) LiTFSI or (b) LiFSI, using the cell sketched in Figure 5.1b, with sulfur as the counter electrode and lithium as the reference electrode, at a series of decreasing scan rates.

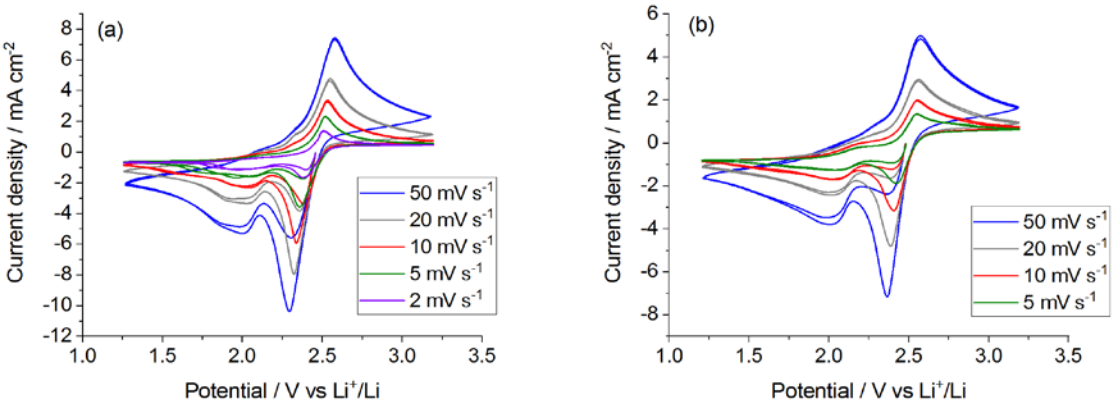

Figure 5.15: Voltammograms from Figure 5.15, corrected for iR drop effects.

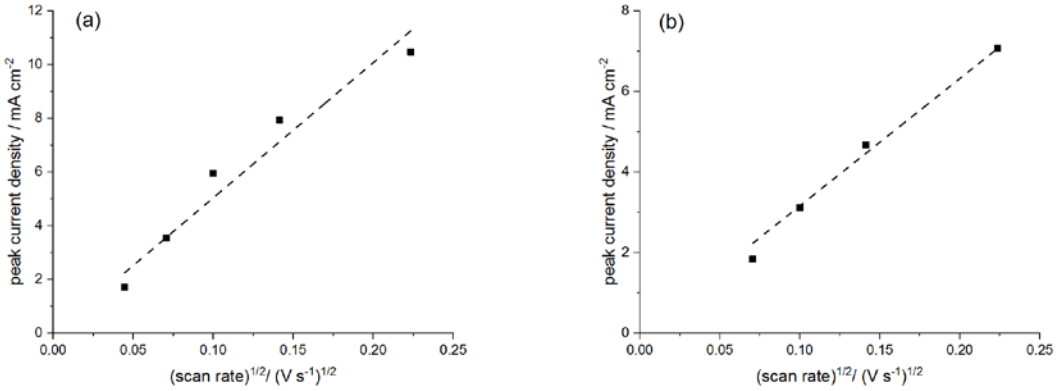

Figure 5.16: Peaks currents from the main reduction peak of the voltammograms in Figure 5.16, vs. the square root of scan rate. Note that the fitted lines were forced to pass through the origin of the axes (0,0).

5.5 Conclusions and future work

In conclusion, sulfur and intermediate polysulfide species have been observed and measured in solid polymer electrolytes for the first time using electrochemical methods. A glassy carbon electrode designed to fit a standard Swagelok cell serves as a powerful electrochemical sensor to detect these species. With only sulfur dissolved in the polymer electrolyte, cyclic voltammograms recorded at the glassy carbon electrode are similar to those recorded in some liquid low-dielectric constant electrolytes, suggesting similar redox mechanisms. Analysis of impedance data as a function of electrode potential suggests that the first reduction wave observed in the voltammograms is associated with a reversible process, usually ascribed to $S_8 +$

$2e^- \rightarrow S_8^{2-}$. A dramatic difference in the cyclic voltammograms is observed in the presence of polysulfides, with a ten-fold increase in the magnitude of the peak currents and a significant change in the shape of the peaks, which now resemble those observed in DOL:DME. The peak potentials are nearly independent of scan rate, indicating fast redox processes. Analysis of the second reduction wave at different scan rates suggests that the redox process or processes associated with this wave are followed by a coupled chemical reaction, and that complex equilibria exist between reducible polysulfide species.

The observations above show that the novel cell design used for this work is therefore well-suited, in terms of sensitivity, to detect polysulfide reaction intermediates. In future, improvements to the cell design could be made both to reduce cell-to-cell variability and to achieve better control of the reaction of the sulfur composite electrode. For example, the lithium ring electrode could be placed on the same side of the cell as the glassy carbon electrode (as in the cell configuration used in Chapter 3), to achieve a better current path between the lithium and sulfur electrodes, which would now be facing each other rather than 'edge-on'. In fact, this configuration was attempted, but the borosilicate glass suffered corrosion, possibly due to the elevated temperature used here compared to the experiments in Chapter 3. However, if a more resistant glass (or other) material was used, then such a configuration might be possible.

5.6 References

1. Judez, X.; Zhang, H.; Li, C.; Eshetu, G. G.; González-Marcos, J. A.; Armand, M.; Rodriguez-Martinez, L. M., Review—Solid Electrolytes for Safe and High Energy Density Lithium-Sulfur Batteries: Promises and Challenges. *Journal of the Electrochemical Society* **2017**, *165*, A6008-A6016.

2. Lin, Z.; Liang, C., Lithium–sulfur batteries: from liquid to solid cells. *Journal of Materials Chemistry A* **2015**, *3*, 936-958.

3. Manthiram, A.; Yu, X.; Wang, S., Lithium battery chemistries enabled by solid-state electrolytes. *Nature Reviews Materials* **2017**, *2*, 16103.

4. Zhang, H.; Li, C.; Piszcz, M.; Coya, E.; Rojo, T.; Rodriguez-Martinez, L. M.; Armand, M.; Zhou, Z., Single lithium-ion conducting solid polymer electrolytes: advances and perspectives. *Chemical Society Reviews* **2017**, *46*, 797-815.

5. Zhang, S.; Ueno, K.; Dokko, K.; Watanabe, M., Recent Advances in Electrolytes for Lithium–Sulfur Batteries. *Advanced Energy Materials* **2015**, *5*, 1500117.

6. Judez, X.; Zhang, H.; Li, C.; Gonzalez-Marcos, J. A.; Zhou, Z.; Armand, M.; Rodriguez-Martinez, L. M., Lithium Bis(fluorosulfonyl)imide/Poly(ethylene oxide) Polymer Electrolyte for All Solid-State Li-S Cell. *The Journal of Physical Chemistry Letters* **2017**, *8*, 1956-1960.

7. Tan, J.; Liu, D.; Xu, X.; Mai, L., In situ/operando characterization techniques for rechargeable lithium-sulfur batteries: a review. *Nanoscale* **2017**, *9*, 19001-19016.

8. Wild, M.; O'Neill, L.; Zhang, T.; Purkayastha, R.; Minton, G.; Marinescu, M.; Offer, G. J., Lithium sulfur batteries, a mechanistic review. *Energy & Environmental Science* **2015**, *8*, 3477-3494.

9. Zheng, D.; Wang, G.; Liu, D.; Si, J.; Ding, T.; Qu, D.; Yang, X.; Qu, D., The Progress of Li-S Batteries-Understanding of the Sulfur Redox Mechanism: Dissolved Polysulfide Ions in the Electrolytes. *Advanced Materials Technologies* **2018**, *3*.

10. Marceau, H., et al., In operando scanning electron microscopy and ultraviolet–visible spectroscopy studies of lithium/sulfur cells using all solid-state polymer electrolyte. *Journal of Power Sources* **2016**, *319*, 247-254.

11. Wujcik, K. H.; Pascal, T. A.; Pemmaraju, C. D.; Devaux, D.; Stolte, W. C.; Balsara, N. P.; Prendergast, D., Characterization of Polysulfide Radicals Present in an Ether-Based Electrolyte of a Lithium-Sulfur Battery During Initial Discharge Using In Situ X-Ray Absorption Spectroscopy Experiments and First-Principles Calculations. *Advanced Energy Materials* **2015**, *5*.

12. Meddings, N.; Owen, J. R.; Garcia-Araez, N., A simple, fast and accurate in-situ method to measure the rate of transport of redox species through membranes for lithium batteries. *Journal of Power Sources* **2017**, *364*, 148-155.

13. Meddings, N.; Owen, J. R.; Garcia-Araez, N., Operando Evaluation of Selectivity and Transference Number of Lithium-Conductive Membranes. *ChemElectroChem* **2019**, *6*, 1-6.

14. Lu, Y.-C.; He, Q.; Gasteiger, H. A., Probing the Lithium–Sulfur Redox Reactions: A Rotating-Ring Disk Electrode Study. *The Journal of Physical Chemistry C* **2014**, *118*, 5733-5741.

15. Jung, Y.; Kim, S.; Kim, B.-S.; Han, D.-H.; Park, S.-M.; Kwak, J., Effect of Organic Solvents and Electrode Materials on Electrochemical Reduction of Sulfur. *International Journal of Electrochemical Science* **2008**, *3*, 566 - 577.

16. Macdonald, D. D., Reflections on the history of electrochemical impedance spectroscopy. *Electrochimica Acta* **2006**, *51*, 1376-1388.

17. Lasia, A., Electrochemical Impedance Spectroscopy and Its Applications. In *Modern Aspects of Electrochemistry*, Conway, B. E.; Bockris, J.; White, R. E., Eds. Kluwer Academic/Plenum: New York, 1999; Vol. 32, pp 143-248.

18. Bard, A. J.; Faulkner, L. R., *Electrochemical Methods: Fundamentals and Applications*; Wiley, 2000.

19. Drvaric Talian, S.; Moskon, J.; Dominko, R.; Gaberscek, M., Reactivity and Diffusivity of Li Polysulfides: A Fundamental Study Using Impedance Spectroscopy. *ACS Applied Materials & Interfaces* **2017**, *9*, 29760-29770.

20. Safari, M.; Kwok, C. Y.; Nazar, L. F., Transport Properties of Polysulfide Species in Lithium-Sulfur Battery Electrolytes: Coupling of Experiment and Theory. *ACS Central Science* **2016**, *2*, 560-8.

21. Busche, M. R.; Drossel, T.; Leichtweiss, T.; Weber, D. A.; Falk, M.; Schneider, M.; Reich, M.-L.; Sommer, H.; Adelhelm, P.; Janek, J., Dynamic formation of a solid-liquid electrolyte interphase and its consequences for hybrid-battery concepts. *Nature Chemistry* **2016**, *8*, 426.

6 Characterising mass transport coefficients: the use of GITT for soluble redox species

6.1 Overview

In a departure from work on membranes and solid electrolytes, this chapter presents the results of experiments in which the cell design from Chapter 2 is used to investigate the suitability of the galvanostatic intermittent titration technique (GITT) for determining quantitative information on mass transport of soluble species, such as polysulfides in Li-S batteries. Various techniques for evaluating diffusion coefficients in this cell are compared, using a model redox system, ethyl viologen. Estimates obtained using cyclic and square wave voltammetry, chronoamperometry and chronopotentiometry are shown to be consistent, providing an accurate value of the diffusion coefficient under conditions that are relevant for battery operation (e.g. minimal electrolyte volume), against which estimates from GITT analysis can be compared.

6.2 Background

A description of GITT is given in Appendix A.4. A key advantage of this technique over other methods for determining diffusion coefficients is that knowledge of the concentration of the reactants and number of electrons involved in the reaction is not required. GITT is therefore of interest as a possible method for determining quantitative information on mass transport in Li-S cells, where the concentration of reactants (in this case polysulfide species) is generally not known. GITT has previously been applied to Li-S cells, but has been limited to evaluating internal resistance[1-2], (quasi) equilibrium voltage profile and qualitative differences in the rates of processes involved in Li-S cell reactions for cells containing different electrolytes, electrodes or at different temperatures[3-6]. The application of GITT to evaluate diffusion coefficients would complement other approaches aimed at understanding kinetics and mass transport in Li-S cells, including XAS[4, 7-9], XRD[10-12], optical imaging[13], UV-vis[7], Raman[14], electrochemical impedance spectroscopy[15-21], and alternative electrochemical methods[22-26].

Whilst GITT has been widely used to evaluate solid-state diffusion coefficients in insertion electrodes, the Li-S battery operates via solution-based redox reactions. The exact mechanisms, however, are complex and poorly understood, involving various unknown polysulfide intermediates with unknown equilibria. Matters are complicated further by phase changes at the

start and end of charge/discharge, and by the varying concentrations of sulfur species dissolved in the electrolyte during charge/discharge, which leads to variations in ion mobility as a result of changes in electrolyte viscosity and ion-ion interactions.[27-29] Therefore, it is instructive to first verify the suitability of the GITT method for evaluating diffusion coefficients of solution-based redox species using a model system. In this chapter, the results of experiments carried out using ethyl viologen as a model reactant are discussed. A Swagelok cell design employing a glassy carbon electrode is used to evaluate the diffusion coefficient of EtV^{2+} using various methods and a comparison of the results is made. Having verified the suitability of the cell for this purpose, an accurate evaluation of the diffusion coefficient in an electrolyte typical of Li-S batteries is made and compared to the results of GITT analysis.

6.3 Experimental details

Experiments were carried out using a Swagelok cell assembly with a glassy carbon working electrode and $Li_{0.5}FePO_4$ counter/reference electrode (Figure 6.1).

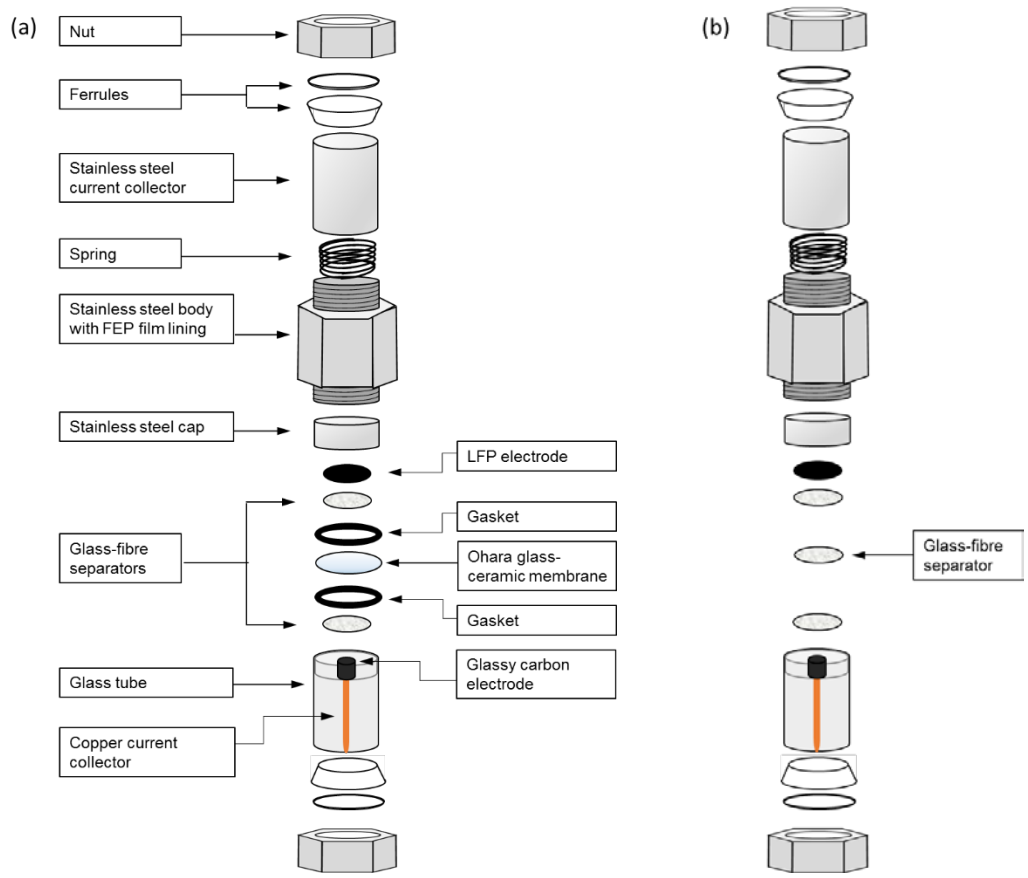

Figure 6.1: Cell configurations used for measurements to determine diffusion coefficient of EtV^{2+} in (a) 100 mM LiTFSI in Pyr14TFSI and (b) 1 M LiTFSI in 1,3-dioxolane.

In the first set of experiments, the cell set-up was as shown in Figure 6.1a, and the electrolyte was 100 mM LiTFSI in $Pyr_{14}TFSI$, with 2 mM $EtV(OTf)_2$ added to the electrolyte in the working electrode compartment. One separator and 50 µL of electrolyte was used on each side of the Ohara glass-ceramic membrane. In the second set of experiments, the cell set-up was as in Figure 6.1b, i.e. without the Ohara membrane, and the electrolyte was 5 mM $EtV(OTf)_2$ with 1 M LiTFSI in 1,3-dioxolane (Sigma-Aldrich, 99.8% purity, anhydrous; used as-received). Three separators and 150 µL of electrolyte were used for each cell. See Chapter 2 for further details on electrode, electrolyte and cell preparation. All experiments were carried out using a Biologic VMP2 potentiostat, controlled using ECLab software.

In the first set of experiments, several techniques were applied, including cyclic voltammetry, chronoamperometry and chronopotentiometry. For chronoamperometry, the potential of the working electrode was stepped from OCV to -1.2 V vs. $Li^+/ Li_{0.5}FePO_4$ (i.e. below the redox potential of the EtV^{2+}/EtV^+ couple but above that of the EtV^+/EtV^0 couple, see Chapter 2) and the resulting current was recorded every 50 nA or 0.1 s for a period of 10 s. For cyclic voltammetry, the potential was scanned from -0.3 V and -2.2 V vs. $Li^+/ Li_{0.5}FePO_4$ (cathodic direction first), at scan rates of 20, 50 and 80 mV s^{-1}. Three cycles were carried out at each scan rate (results are presented from the second cycle[1]) and the cell was allowed to rest for 10 minutes between each scan rate. For chronopotentiometry, the ECLab 'galvanostatic cycling with potential limitation' (GCPL) procedure was applied. Cells were galvanostatically discharged (negative current) then charged (positive current) using a range of current values from -/+ 0.5 µA to -/+ 2.0 µA with cell potential limits of -0.3 V and -1.4 V. Three discharge/charge cycles were carried out for each current value. Prior to the first cycle in each case, cells were slow-charged to a potential limit of -0.3 V using a current of 20 nA in order to fully oxidise all ethyl viologen present to EtV^{2+}. For determination of the double layer capacitance of the glassy carbon electrode (see Appendix F), cyclic voltammetry of a cell without ethyl viologen was conducted. The potential was scanned between 0 and -1.0 V using a range of scan rates between 5 mV s^{-1} and 50 mV s^{-1}, a single cycle in each case, and a rest of 10 minutes between each scan rate. All cells were placed in a climatic chamber at 25 ^oC and allowed to rest for three hours prior to initial measurement.

[1] Strictly analysis the analysis presented is applicable only for the first cycle and for 100% EtV^{2+} present at the start of the experiment; however this was the case only for the first scan rate applied. By analysing the second cycle, the different scan rates are compared on a more equal basis.

In the second set of experiments, cyclic voltammetry was conducted at scan rates of 200, 150, 100, 70, 50 and 20 mV s^{-1}. Cells were allowed to rest for two hours at 25 °C before commencing the experiments. Prior to each scan rate, cells were held at 3.25 V vs Li^+/Li for 15 minutes to ensure 100% concentration of EtV^{2+}. The potential was then scanned to 2.2 V vs Li^+/Li, and back to 3.25 V vs Li^+/Li. Two cycles per scan rate were measured (results presented are from the first cycle). Measurements were done using EC Lab's 'manual IR compensation' function, which automatically applies an iR correction during the measurements, using a manually-inputted value of resistance of 150 Ω, as obtained from the high frequency intercept in impedance measurements, and a correction factor of 80%.

6.4 Results and discussion

6.4.1 Evaluation of diffusion coefficients using different methods in a Swagelok cell with glassy carbon electrode

In the following section, a Swagelok cell design employing a glassy carbon electrode is used to evaluate the diffusion coefficient of EtV^{2+} using various methods and a comparison of the results is made. All experiments in this section were done with the cell shown in Figure 6.1a, containing 2 mM $EtV(OTf)_2$ and 100 mM LiTFSI in Pyr14TFSI.

6.4.1.1 Chronoamperometry

Figure 6.2 shows the chronoamperometric response of the cell following a potential step from OCV to -1.2 V vs. $Li_{0.5}FePO_4$. At short times (t < 1 s), there is an iR drop followed by double layer charging and other slower capacitive process associated with the ionic liquid.[30] At longer times (t >= 1 s), the current decays as the concentration profile supplying EtV^{2+} to the electrode surface expands into the bulk of the solution, the gradient of this profile diminishes, and hence the flux of EtV^{2+} to the surface falls.

For t >= 1 s, a plot of the current vs. $t^{1/2}$ is linear (Figure 6.3), confirming that the reaction is under diffusion control and therefore that the Cottrell equation can be applied in order to determine the diffusion coefficient of EtV^{2+}:[31]

$$D_{EtV^{2+}} = \left(\frac{gradient \times \pi^{1/2}}{nFAc^*_{EtV^{2+}}} \right)^2 = 9.5 \cdot 10^{-8} \text{ cm}^2 \text{ s}^{-1} \qquad \text{(Eq. 6.1)}$$

where n is the number of electrons involved in the electrode reaction, F is Faraday's constant, A is the surface area of the electrode and $c^*_{EtV^{2+}}$ is the bulk concentration of EtV^{2+}.

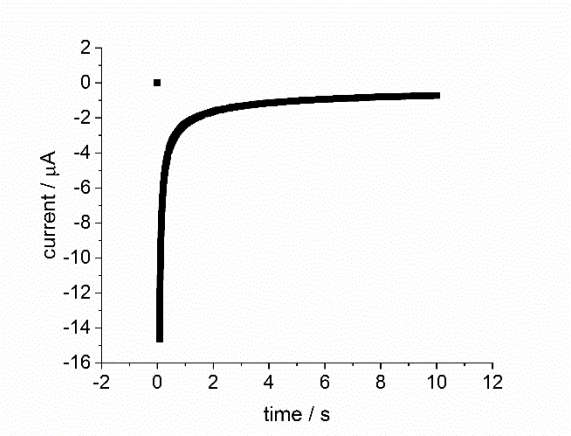

Figure 6.2: Chronoamperometric response of the cell shown in Fig 6.1a, containing 2 mM $EtV(OTf)_2$ and 100 mM LiTFSI in Pyr14TFSI, following a potential step from OCV to -1.2 V.

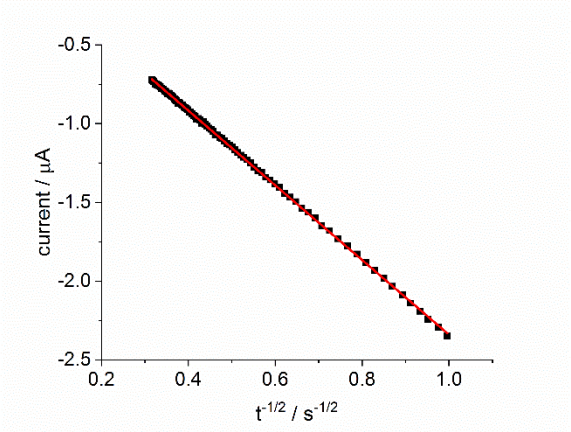

Figure 6.3: Plot of current vs. $t^{-1/2}$ from Figure 6.2, for t >= 1 s.

6.4.1.2 Cyclic voltammetry

Figure 6.4 shows cyclic voltammograms of the reduction and oxidation of ethyl viologen at the glassy carbon electrode, recorded at different scan rates. There are two pairs of redox peaks, centred at -1.0 V and -1.45 V, relating to the EtV^{2+}/EtV^{+} and EtV^{+}/EtV redox couples respectively. The peaks occur at the same potentials for all current densities, indicating electrochemically reversible reactions. This is confirmed by a plot of the anodic and cathodic peak potentials vs. peak current densities for the EtV^{2+}/EtV^{+} couple, which allows the peak separation

at I = 0 to be extrapolated (Figure 6.5). The value of 63 mV is close to the 59 mV for an ideally reversible reaction. Since the reaction is reversible, application of the Randles-Sevcik equation (Equation 6.2) is valid, and the diffusion coefficient of EtV^{2+} can be estimated from the slope of a plot of peak current density vs. the square root of scan rate (Figure 6.6):[31]

$$D_{EtV^{2+}} = \frac{gradient}{2.6\times10^{5} n^{3/2} c^{*}_{EtV^{2+}}} = 5.9\cdot10^{-8}\ \mathrm{cm}^{2}\ \mathrm{s}^{-1} \qquad \text{(Eq. 6.2)}$$

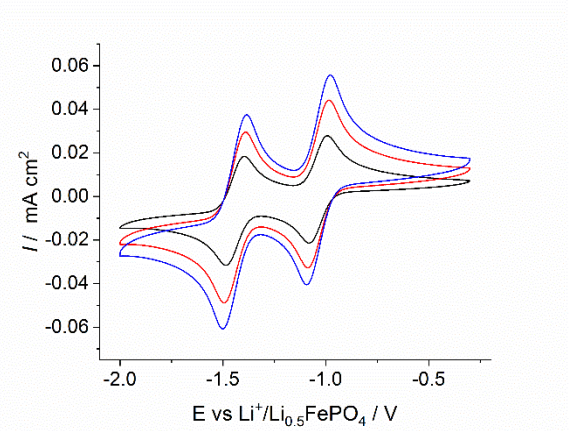

Figure 6.4: Cyclic voltammograms recorded in the cell shown in Figure 6.1a, containing 2 mM $EtV(OTf)_2$ and 100 mM LiTFSI in Pyr14TFSI, at scan rates of 20 mV s^{-1}, 50 mVs^{-1} and 80 mV s^{-1}.

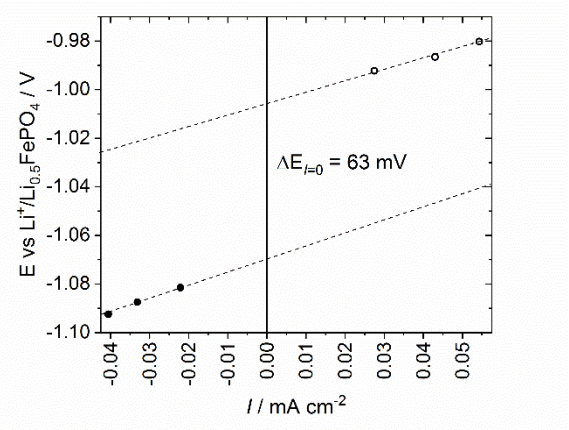

Figure 6.5: Anodic and cathodic peak potentials vs. peak current densities for the EtV^{2+}/EtV^{+} couple at different scan rates, as obtained from Figure 6.4.

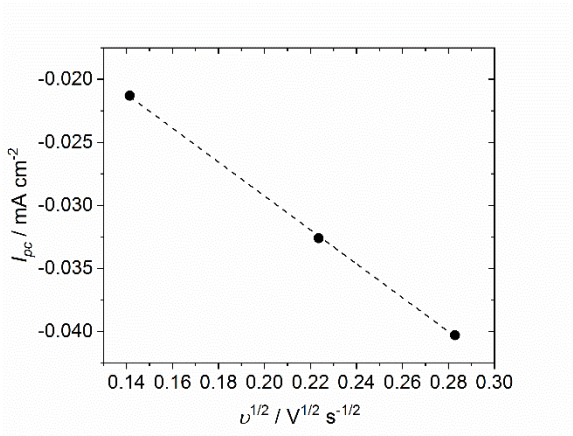

Figure 6.6: Peak current for the reduction of EtV^{2+}, vs. square root of scan rate, as obtained from Figure 6.4.

6.4.1.3 Chronopotentiometry

6.4.1.3.1 Potential response to applied current and determination of transition time

Figure 6.7 shows the potential response of the cell vs. time under a range of applied current values. In the absence of any other effects, we would expect to see an initial IR drop followed by a sharp inflection and then a smooth decrease in potential, according to the Nernst equation, as EtV^{2+} is reduced to EtV^{+} at the electrode surface in order to maintain the applied current. As the surface concentration of EtV^{2+} reaches zero, we would expect another sharp inflection as the potential moves steeply towards the redox potential of another reaction (in this case the reduction of EtV^{+} to EtV^{0}). The time between the two inflection points is the Sand transition time, τ . However, deviations from this ideal behaviour are clearly observed; typically these are due to double layer charging which affects the overall shape of the curve and makes measurement of τ difficult.[31] A more detailed discussion of the deviations from ideal Sand behaviour observed in Figure 6.7 is given in Appendix F.

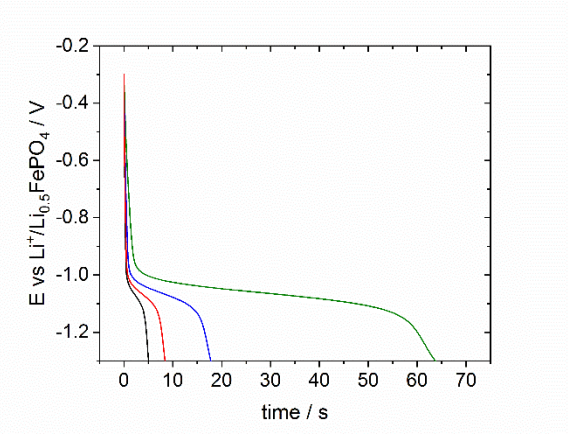

Figure 6.7: Chronopotentiometric response of the cell shown in Fig 6.1a containing 2 mM EtV(OTf)$_2$ and 100 mM LiTFSI in Pyr14TFSI, following a current step of -0.5 µA (green), -1.0 µA (blue), -1.5 µA (red) and -2.0 µA (black).

Various methods have been proposed for determining τ in this situation. Reinmuth[32] suggested fitting three linear regions and taking the transition time τ as the interval between the intersection of the fitted lines (Figure 6.8a). Peters and Burden[33] proposed a method in which τ is calculated from the minimum of the derivative of the potential-time curve (Figure 6.8b) according to equation 6.3. An alternative method is to take τ simply as the interval over which the plateau region is considered linear (Figure 6.8c).

$$\tau = -\frac{27}{8}\frac{RT}{nF}\frac{1}{\left(dE/dt\right)_{\min}} \qquad \text{(Eq. 6.3)}$$

where n is the number of electrons involved in the electrode reaction, F is Faraday's constant, R is the gas constant and T is temperature in Kelvin.

Values of τ were obtained from the data in Figure 6.7 using each of the three methods, and Figure 6.9 plots these values of τ vs. $1/I^2$. The diffusion coefficient of EtV^{2+} could then be estimated from the gradient of the plots of τ vs. $1/I^2$ using the Sand equation:[31]

$$D_{EtV^{2+}} = \left(\frac{2}{\pi^{1/2} nF c^{*}_{EtV^{2+}}}\right)^2 \times gradient \qquad \text{(Eq. 6.4)}$$

In this way, values for $D_{EtV^{2+}}$ of $10.1 \cdot 10^{-8}$ cm^2 s^{-1}, $5.5 \cdot 10^{-8}$ cm^2 s^{-1} and $7.9 \cdot 10^{-8}$ cm^2 s^{-1} were obtained using methods a, b and c respectively. It is important to note that all three methods involve a degree of subjectivity. In particular, since it requires subjective fitting of three separate regions of the potential-time curve (Figure 6.8a), the values of τ obtained using method (a) are

particularly prone to error, as small changes in the slope of these fitted lines can lead to relatively large changes in τ .

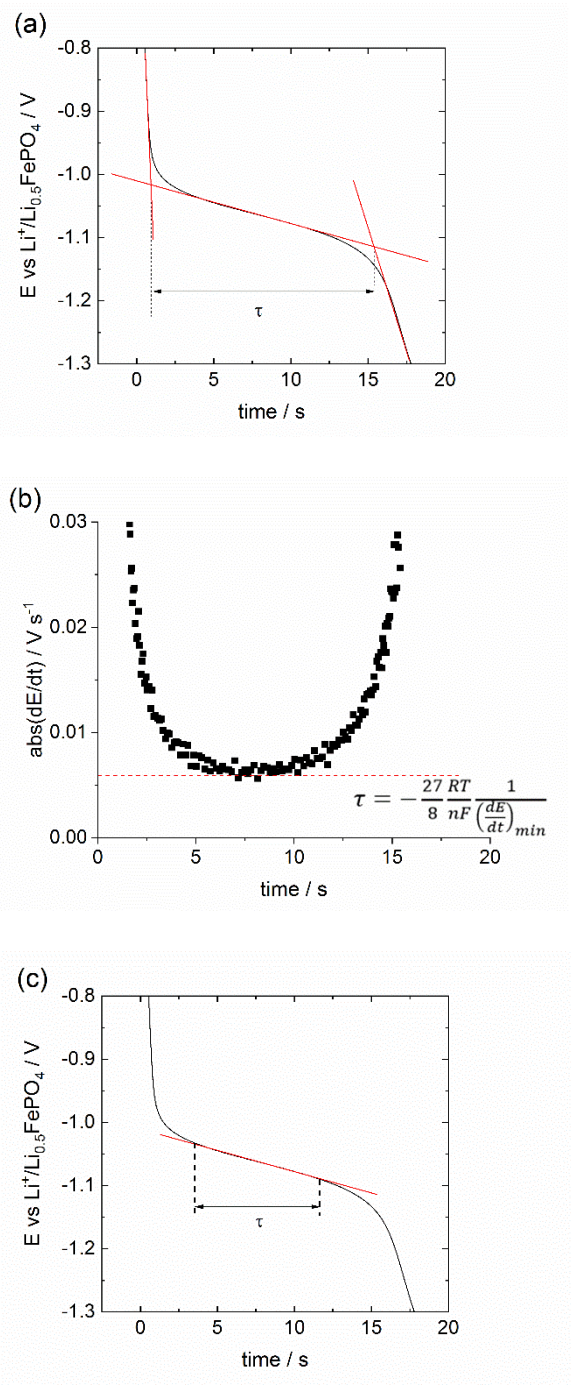

Figure 6.8: Three methods for determining the Sand transition time.

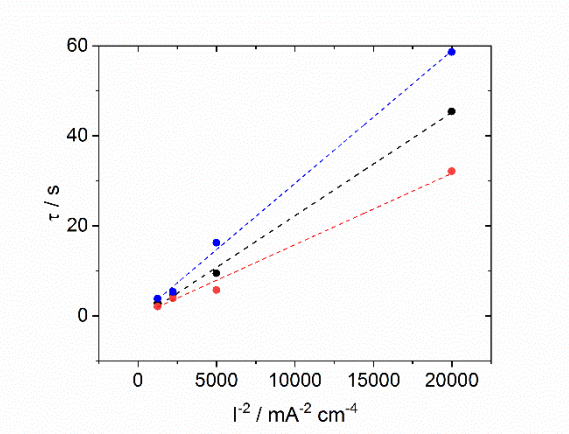

Figure 6.9: Plot of Sand times obtained from the data in Figure 6.7 using method (a) (blue), method (b) (red) and method (c) (black), vs. $I^{-1/2}$

6.4.1.4 Comparison of methods to evaluate the diffusion coefficient

Bringing together the values of the diffusion coefficient obtained using voltammetry (including the value obtained under the same conditions using square wave voltammetry in Chapter 2) and 'chrono' techniques, we now have six different estimates for $D_{EtV^{2+}}$, which agree reasonably well with each other (Table 5.1).

Method		**D / cm^2 s^{-1}**
Cyclic voltammetry		$5.9 \cdot 10^{-8}$
Chronoamperometry		$9.5 \cdot 10^{-8}$
Chronopotentiometry	Method a	$10.1 \cdot 10^{-8}$
	Method b	$5.5 \cdot 10^{-8}$
	Method c	$7.9 \cdot 10^{-8}$
Square wave voltammetry		$7.5 \cdot 10^{-8}$

Table 6.1: Diffusion coefficient of EtV^{2+} (2 mM) in 100 mM LiTFSI in $Pyr_{14}TFSI$ solution estimated using different methods.

In conclusion, the Swagelok cell with glassy carbon electrode is well-suited to determining diffusion coefficients of species using cyclic or square wave voltammetry and chronoamperometry. It is also suitable for chronopotentiometry, though it should be noted that (in general) this method is prone to error due to subjective aspects of the analysis. It can

therefore provide an accurate determination of the mass transport (diffusion) coefficient under conditions that are representative of battery operation (e.g. small electrolyte volume soaked into a separator), that can be used to validate the results of GITT measurements. (The present cell is not, itself, suitable for GITT measurements due to the small area of the glassy carbon electrode relative to that of the electrolyte. As a result, it would be difficult to induce an adequate change in the bulk concentration, and hence equilibrium potential, of the cell, without exhausting the concentration of the reactant at the electrode surface during each applied current pulse (i.e. without reaching Sand's time during the pulse). Furthermore, on the long timescales of GITT measurements, it is unlikely that diffusion would be one dimensional.)

6.4.2 Validation of diffusion coefficients obtained from GITT measurements

In the following section, the cell design used for the previous experiments is used to evaluate the diffusion coefficient of ethyl viologen in an electrolyte typical of Li-S batteries (1 M LiTFSI in 1,3-dioxolane) is evaluated by cyclic voltammetry, and it is shown that analysis of GITT data can provide values of the diffusion coefficient that are consistent with this provided certain conditions are met. Otherwise, using the classical GITT approach proposed by Weppner and Huggins[34] can lead to significant inconsistencies.

This work was part of a collaboration with Mr. (now Dr.) James Dibden, a fellow PhD student in the Garcia-Araez research group, who conducted GITT experiments in a Swagelok cell similar to the one in Figure 6.1a but with a carbon-coated aluminium electrode whose geometrical area (1.77 cm^2), matched that of the electrolyte-soaked separator and was much larger than the area of the glassy carbon electrode (0.07 cm^2) (experimental details for these measurements can be found in ref. 35).

6.4.2.1 Obtaining an accurate diffusion coefficient as a comparator for GITT analysis

Figure 6.10 shows cyclic voltammograms measured at different scan rates at a glassy carbon electrode in a solution containing 5 mM $EtV(OTf)_2$ in 1 M LiTFSI in 1,3-dioxolane. The voltammograms show the characteristic duck-shape of a reversible electrochemical reaction with fast electron transfer.[31] These measurements were done in the cell shown in Figure 6.1b, with the electrolyte soaked into glass fibre separators, and therefore accurately reflect the rate of mass transport of EtV^{2+} in the electrolyte-soaked separator. This allowed a quantitative comparison

with the analysis of the GITT data, which was also obtained (by James Dibden) in a Swagelok cell containing EtV^{2+} present in the electrolyte-soaked glass fibre separator.

In order to improve the accuracy of the analysis of the voltammetric data, the measurements in Figure 6.10 were done with only glass fibre separators between the working and counter electrodes, no Ohara glass-ceramic membrane. (This was possible since EtV^{2+} is stable in contact with the $Li_{0.5}FePO_4$ electrode used, which has a constant potential of 3.45 V vs. Li^+/Li. EtV^+ is oxidized to EtV^{2+} by $Li_{0.5}FePO_4$, but the effect of that reaction on the voltammograms in Figure 6.10 is negligible, since the EtV^+ is only created at the surface of the glassy carbon working electrode, and the time for EtV^+ to diffuse to the $Li_{0.5}FePO_4$, electrode is around L^2/D (where L is the thickness of the three glass fibre separators used in these experiments, ca. 0.1 cm in total), which, given the value of D obtained below, is >1 hour.) In this way, the internal resistance of the cell was relatively small (150 Ω), despite the small area of the glassy carbon electrode (0.07 cm^2), and therefore the effect of iR drop was also small (<12 mV in all cases). Nevertheless, the data in Figure 6.13 have been corrected for IR effects.

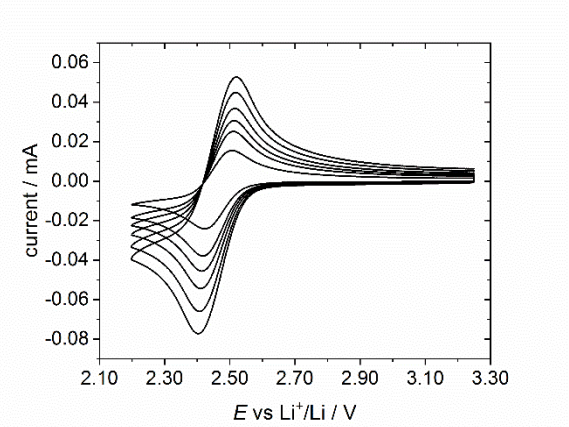

Figure 6.10. Cyclic voltammograms recorded at a glassy carbon electrode in the cell shown in Figure 6.1b, containing 5 mM $EtV(OTf)_2$ + 1 M LiTFSI in 1,3-dioxolane.

Figure 6.11 shows the plot of peak potentials vs. peak currents for the EtV^{2+}/EtV^+ couple, obtained from the data in Figure 6.10. Extrapolation to zero current shows a difference in peak potentials of 69 mV, in reasonable agreement with the 59 mV expected for a fully reversible system. Therefore, the Randles-Sevcik equation was used to evaluate the value of the diffusion coefficient from the peak current. Figure 6.12 shows the plot of peak current vs. the square root of the scan rate. The slope of the plot gives a value of the diffusion coefficient of $3.2 \cdot 10^{-6}$ cm^2 s^{-1}

for EtV^{2+} in the electrolyte-soaked glass fibre separator (equation 6.2). An average value of $(2.8\pm0.4) \cdot 10^{-6}$ cm^2 s^{-1} was obtained upon repetition of these measurements.

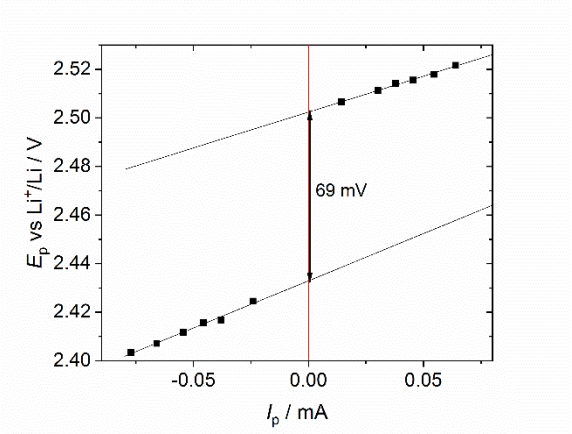

Figure 6.11. Anodic and cathodic peak potentials vs. peak current densities for the measurements shown in Figure 6.14.

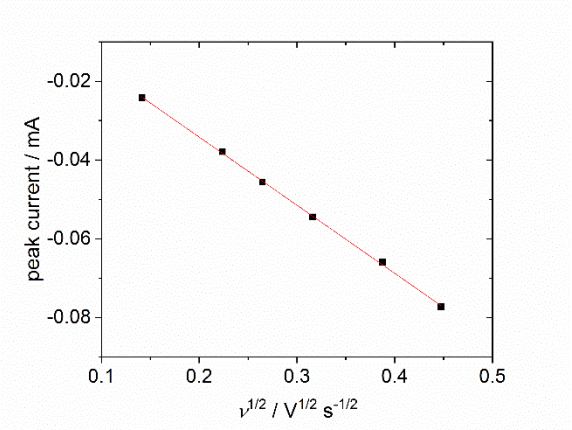

Figure 6.12. Plot of peak potential against the square root of the scan rate, for the measurements shown in Figure 6.14.

6.4.2.2 Comparison of diffusion coefficients from cyclic voltammetry at a glassy carbon electrode and from GITT in a cell with a carbon coated electrode.

Figure 6.13 compares the value of the diffusion coefficient obtained above from cyclic voltammetry in a cell with a glassy carbon electrode, with values obtained by James Dibden from GITT measurements in a cell with a carbon coated electrode (made by coating a carbon-containing slurry onto an aluminium current collector) and initially containing 5 mM $EtV(OTf)_2$.

Values were obtained from GITT data by James Dibden using equation 6.5, which is the classical equation given by Weppner and Huggins (see Appendix A.4).

$$D_{EtV^{2+}} = \left(\frac{4}{\tau\pi}\right)\left(\frac{V}{A}\right)^2\left(\frac{\Delta E_{RELAX}}{\Delta E_{PULSE}}\right)^2 \qquad \text{(Eq. 6.5)}$$

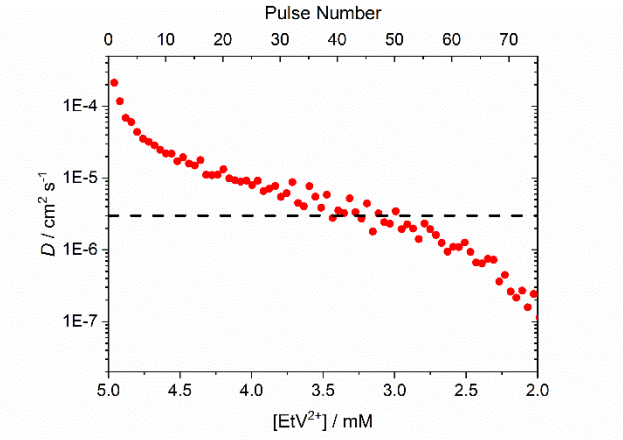

Figure 6.13. Diffusion coefficient of EtV^{2+} as evaluated from cyclic voltammetry data in Figure 6.14 using equation 6.2 (black dashed line) or from GITT data obtained in a cell containing a carbon coated electrode and applying equation 6.5 (red points). GITT data obtained and analysed by James Dibden.

Figure 6.13 shows that, for the GITT analysis, there is a large variation of the diffusion coefficient with state of charge for values obtained using equation 6.5. The reason for this can be explained as follows. The classical analysis of GITT data proposed by Weppner and Huggins (see Appendix A.4) assumes that (Condition 1):

$$\Delta E_{PULSE} = k\Delta c_{PULSE}$$

$$\Delta E_{RELAX} = k\Delta c_{RELAX}$$

where k is a constant. Condition 1 arises from two simplifying assumptions. The first is that a sufficiently small current/pulse length is applied that the resulting change in equilibrium potential ΔE_{RELAX} can be assumed to be proportional to the change in bulk concentration Δc_{RELAX} .. The second is that the change in potential during the current pulse varies linearly with the square root of time for the duration of the pulse. The change in surface *concentration* during the current pulse is expected to vary linearly with $\sqrt{t}$, according to equation 6.6, which comes from solving Fick's second law with the relevant boundary conditions (see Appendix A.4):

$$\left.\begin{aligned} c_O^{x=0} &= c_O^{initial} - \frac{2i_0\sqrt{t}}{nFA\sqrt{D_O\pi}} \\ c_R^{x=0} &= c_R^{initial} - \frac{2i_0\sqrt{t}}{nFA\sqrt{D_R\pi}} \end{aligned}\right\} \quad \left(t \ll \frac{L^2}{D}\right) \qquad \text{(Eq. 6.6)}$$

However, the corresponding change in electrode *potential* will vary linearly with $\sqrt{t}$ only if the change in potential can once again be assumed to be proportional to the change in concentration. The real relationship between potential and concentration is given by the Nernst equation:

$$E = E^{0'} + \frac{RT}{nF}\ln\frac{c_O^{x=0}}{c_R^{x=0}} \qquad \text{(Eq. 6.7)}$$

and in this case an accurate expression for the variation of potential during the pulse is given by:

$$\Delta E_{PULSE} = \frac{RT}{nF}\ln\frac{c_O^{initial} - \frac{2i_0\sqrt{\tau}}{nFA\sqrt{D_O\pi}}}{c_R^{initial}} - \frac{RT}{nF}\ln\frac{c_R^{initial} + \frac{2i_0\sqrt{\tau}}{nFA\sqrt{D_R\pi}}}{c_R^{initial}} \qquad \text{(Eq. 6.8)}$$

Therefore, $dE_{PULSE}/d\sqrt{t}$ will be linear only for (changes in) concentrations at which the Nernst equation can be approximated as linear. Due to the functional form of the Nernst equation, this will be the case only for intermediate states of charge, and only here is the evaluation of the diffusion coefficient reliable. This is confirmed by the fact that the values of $D_{EtV^{2+}}$ obtained from GITT data using equation 6.5 are closest to the 'true' value obtained from cyclic voltammetry when at intermediate states of charge.

6.5 Conclusions and future work

In this chapter, evaluation of the diffusion coefficient of solution-based redox reactants, via application of various electrochemical techniques in a Swagelok cell with glassy carbon electrode, has been investigated. The advantage of this cell configuration is that it allows straightforward analysis of the data using standard equations for semi-infinite diffusion to a planar electrode, since glassy carbon provides a smooth, planar surface, and convection is suppressed by soaking the electrolyte into a separator. The use of a relatively small volume of electrolyte soaked into a separator also means that the Swagelok cell configuration is a better reflection of practical battery operating conditions, when compared to more traditional (e.g. H-cell) configurations.

Since these factors affect the rate of mass transport,[36] the diffusion coefficient evaluated in this way is therefore more accurate for these conditions.

Using a model redox reactant, ethyl viologen, it was found that the cell is well-suited for evaluating diffusion coefficients using cyclic or square-wave voltammetry, chronoamperometry and chronopotentiometry, though the 'chrono' techniques, in particular chronopotentiomentry, involve a degree of subjectivity in the analysis and are therefore prone to error. This is a general limitation of these techniques, however, and not specific to the present system.

The cell was then used to obtain an accurate value of the diffusion coefficient of EtV^{2+} in an electrolyte-soaked glass fibre separator from cyclic voltammetry measurements. In a collaborative piece of work, this value was used as a comparator for values obtained from GITT measurements in a cell with a carbon coated electrode. It was revealed that GITT can provide reliable values for the diffusion coefficient, but only when the cell is at intermediate states of charge. The possibility for using of GITT for evaluating the diffusion coefficient of soluble redox species has therefore been confirmed. This is a first step towards its similar application to polysulfide solutions, which could be explored in future.

6.6 References

1. Lacey, M. J., Influence of the Electrolyte on the Internal Resistance of Lithium–Sulfur Batteries Studied with an Intermittent Current Interruption Method. *ChemElectroChem* **2017**, *4*, 1997-2004.

2. Lacey, M. J.; Edström, K.; Brandell, D., Visualising the problems with balancing lithium–sulfur batteries by "mapping" internal resistance. *Chemical Communications* **2015**, *51*, 16502-16505.

3. Busche, M. R.; Adelhelm, P.; Sommer, H.; Schneider, H.; Leitner, K.; Janek, J., Systematical electrochemical study on the parasitic shuttle-effect in lithium-sulfur-cells at different temperatures and different rates. *Journal of Power Sources* **2014**, *259*, 289-299.

4. Cuisinier, M.; Cabelguen, P. E.; Adams, B. D.; Garsuch, A.; Balasubramanian, M.; Nazar, L. F., Unique behaviour of nonsolvents for polysulphides in lithium–sulphur batteries. *Energy & Environmental Science* **2014**, *7*, 2697-2705.

5. Park, J.-W.; Yamauchi, K.; Takashima, E.; Tachikawa, N.; Ueno, K.; Dokko, K.; Watanabe, M., Solvent Effect of Room Temperature Ionic Liquids on Electrochemical Reactions in Lithium–Sulfur Batteries. *The Journal of Physical Chemistry C* **2013**, *117*, 4431-4440.

6. Waluś, S.; Barchasz, C.; Bouchet, R.; Martin, J. F.; Leprêtre, J. C.; Alloin, F., Non-woven carbon paper as current collector for Li-ion/Li2S system: Understanding of the first charge mechanism. *Electrochimica Acta* **2015**, *180*, 178-186.

7. Dominko, R.; Patel, M. U. M.; Lapornik, V.; Vizintin, A.; Koželj, M.; N. Tušar, N.; Arčon, I.; Stievano, L.; Aquilanti, G., Analytical Detection of Polysulfides in the Presence of Adsorption Additives by Operando X-ray Absorption Spectroscopy. *The Journal of Physical Chemistry C* **2015**, *119*, 19001-19010.

8. Patel, M. U. M.; Arčon, I.; Aquilanti, G.; Stievano, L.; Mali, G.; Dominko, R., X-ray Absorption Near-Edge Structure and Nuclear Magnetic Resonance Study of the Lithium–Sulfur Battery and its Components. *ChemPhysChem* **2014**, *15*, 894-904.

9. Wujcik, K. H.; Wang, D. R.; Pascal, T. A.; Prendergast, D.; Balsara, N. P., In Situ X-ray Absorption Spectroscopy Studies of Discharge Reactions in a Thick Cathode of a Lithium Sulfur Battery. *Journal of The Electrochemical Society* **2017**, *164*, A18-A27.

10. Nelson, J.; Misra, S.; Yang, Y.; Jackson, A.; Liu, Y.; Wang, H.; Dai, H.; Andrews, J. C.; Cui, Y.; Toney, M. F., In Operando X-ray Diffraction and Transmission X-ray Microscopy of Lithium Sulfur Batteries. *Journal of the American Chemical Society* **2012**, *134*, 6337-6343.

11. Yeon, J.-T.; Jang, J.-Y.; Han, J.-G.; Cho, J.; Lee, K. T.; Choi, N.-S., Raman Spectroscopic and X-ray Diffraction Studies of Sulfur Composite Electrodes during Discharge and Charge. *Journal of The Electrochemical Society* **2012**, *159*, A1308-A1314.

12. Zhu, W., et al., Investigation of the reaction mechanism of lithium sulfur batteries in different electrolyte systems by in situ Raman spectroscopy and in situ X-ray diffraction. *Sustainable Energy & Fuels* **2017**, *1*, 737-747.

13. Sun, Y.; Seh, Z. W.; Li, W.; Yao, H.; Zheng, G.; Cui, Y., In-operando optical imaging of temporal and spatial distribution of polysulfides in lithium-sulfur batteries. *Nano Energy* **2015**, *11*, 579-586.

14. Wu, H.-L.; Huff, L. A.; Gewirth, A. A., In Situ Raman Spectroscopy of Sulfur Speciation in Lithium–Sulfur Batteries. *ACS Applied Materials & Interfaces* **2015**, *7*, 1709-1719.

15. Barchasz, C.; Leprêtre, J.-C.; Alloin, F.; Patoux, S., New insights into the limiting parameters of the Li/S rechargeable cell. *Journal of Power Sources* **2012**, *199*, 322-330.

16. Cañas, N. A.; Hirose, K.; Pascucci, B.; Wagner, N.; Friedrich, K. A.; Hiesgen, R., Investigations of lithium–sulfur batteries using electrochemical impedance spectroscopy. *Electrochimica Acta* **2013**, *97*, 42-51.

17. Drvarič Talian, S.; Moškon, J.; Dominko, R.; Gaberšček, M., Reactivity and Diffusivity of Li Polysulfides: A Fundamental Study Using Impedance Spectroscopy. *ACS Applied Materials & Interfaces* **2017**, *9*, 29760-29770.

18. Kolosnitsyn, V. S.; Kuzmina, E. V.; Karaseva, E. V.; Mochalov, S. E., A study of the electrochemical processes in lithium–sulphur cells by impedance spectroscopy. *Journal of Power Sources* **2011**, *196*, 1478-1482.

19. Kolosnitsyn, V. S.; Kuzmina, E. V.; Mochalov, S. E., Determination of lithium sulphur batteries internal resistance by the pulsed method during galvanostatic cycling. *Journal of Power Sources* **2014**, *252*, 28-34.

20. Li, Y.; Zhan, H.; Liu, S.; Huang, K.; Zhou, Y., Electrochemical properties of the soluble reduction products in rechargeable Li/S battery. *Journal of Power Sources* **2010**, *195*, 2945-2949.

21. Yuan, L.; Qiu, X.; Chen, L.; Zhu, W., New insight into the discharge process of sulfur cathode by electrochemical impedance spectroscopy. *Journal of Power Sources* **2009**, *189*, 127-132.

22. Al-Mahmoud, S. M.; Dibden, J. W.; Owen, J. R.; Denuault, G.; Garcia-Araez, N., A simple, experiment-based model of the initial self-discharge of lithium-sulphur batteries. *Journal of Power Sources* **2016**, *306*, 323-328.

23. Cui, Y.; Fu, Y., Polysulfide transport through separators measured by a linear voltage sweep method. *Journal of Power Sources* **2015**, *286*, 557-560.

24. Fan, F. Y.; Carter, W. C.; Chiang, Y.-M., Mechanism and Kinetics of Li2S Precipitation in Lithium–Sulfur Batteries. *Advanced Materials* **2015**, *27*, 5203-5209.

25. Lu, Y.-C.; He, Q.; Gasteiger, H. A., Probing the Lithium–Sulfur Redox Reactions: A Rotating-Ring Disk Electrode Study. *The Journal of Physical Chemistry C* **2014**, *118*, 5733-5741.

26. Safari, M.; Kwok, C. Y.; Nazar, L. F., Transport Properties of Polysulfide Species in Lithium–Sulfur Battery Electrolytes: Coupling of Experiment and Theory. *ACS Central Science* **2016**, *2*, 560-568.

27. Tan, J.; Liu, D.; Xu, X.; Mai, L., In situ/operando characterization techniques for rechargeable lithium–sulfur batteries: a review. *Nanoscale* **2017**, *9*, 19001-19016.

28. Wild, M.; O'Neill, L.; Zhang, T.; Purkayastha, R.; Minton, G.; Marinescu, M.; Offer, G. J., Lithium sulfur batteries, a mechanistic review. *Energy & Environmental Science* **2015**, *8*, 3477-3494.

29. Zheng, D.; Wang, G.; Liu, D.; Si, J.; Ding, T.; Qu, D.; Yang, X.; Qu, D., The Progress of Li–S Batteries—Understanding of the Sulfur Redox Mechanism: Dissolved Polysulfide Ions in the Electrolytes. *Advanced Materials Technologies* **2018**, *3*, 1700233.

30. Roling, B.; Drüschler, M.; Huber, B., Slow and fast capacitive process taking place at the ionic liquid/electrode interface. *Faraday Discussions* **2012**, *154*, 303-311.

31. Bard, A. J.; Faulkner, L. R., *Electrochemical Methods: Fundamentals and Applications*; Wiley, 2000.

32. Reinmuth, W. H., Distortion of Chronopotentiograms from Double Layer and Surface Roughness Effects. *Analytical Chemistry* **1961**, *33*, 485-487.

33. Peters, D. G.; Burden, S. L., Derivative Chronopotentiometry. Reversible and Irreversible Processes at Mercury Pool Electrodes. *Analytical Chemistry* **1966**, *38*, 530-536.

34. Weppner, W.; Huggins, R. A., Determination of the Kinetic Parameters of Mixed-Conducting Electrodes and Application to the System Li3Sb. *Journal of The Electrochemical Society* **1977**, *124*, 1569-1578.

35. Dibden, J. W.; Meddings, N.; Owen, J. R.; Garcia-Araez, N., Quantitative Galvanostatic Intermittent Titration Technique for the Analysis of a Model System with Applications in Lithium−Sulfur Batteries. *ChemElectroChem* **2018**, *5*, 445-454.

36. Raccichini, R.; Furness, L.; Dibden, J. W.; Owen, J. R.; García-Araez, N., Impedance Characterization of the Transport Properties of Electrolytes Contained within Porous Electrodes and Separators Useful for Li-S Batteries. *Journal of The Electrochemical Society* **2018**, *165*, A2741-A2749.

7 Summary of conclusions and future work

The use of lithium protective membranes/separators, coatings and solid electrolytes can address key issues associated with batteries employing a lithium metal electrode. This work has focused on some of the key properties governing performance of such components: ion selectivity and transference number, interfacial resistance, and redox kinetics (mass transport of reactants and/or electron transfer). The main achievement of this research project has been to develop appropriate cell designs and techniques for the evaluation of these properties, via fast, easy, reliable, reproducible, quantitative and in-situ/in-operando measurement. Other applications of the core cell design, to gain further insight into the mechanisms of Li-S battery operation, have also be explored.

In Chapter 2, a convenient, in-situ, direct and quantitative method for measuring the permeability of membranes to crossover species was demonstrated. The method employs a 'Swagelok' cell design equipped with a glassy carbon working electrode, which can be used to evaluate, via voltammetry, the concentration of crossover species that have passed through a membrane separating the working and counter electrode compartments. By testing the method with a model system, ethyl viologen, it was possible to identify the electrode material that gives the most sensitive, reproducible and reliable (free from artefacts) response. It was also possible to show that, for crossover species with reversible redox kinetics, using a differential technique (square wave voltammetry) produces a major increase in the sensitivity of the measurements, compared to cyclic voltammetry. The new cell design allows testing of membrane permeability using small electrolyte volumes (35 µl) and can detect molar quantities less than 10^{-7} moles. The facile, in-situ measurement procedure makes it possible to record passage of redox species through the membrane in real time using a single cell. The quantitative nature of the measurements allows the rate of passage to be determined.

Building on the work in Chapter 2, Chapter 3 presented a new approach that allows the accurate evaluation of the selectivity of lithium conductive membranes in *operando* conditions, that is, under application of a current across a cell. The method employs a similar cell design to the one used in Chapter 2, but with an additional ring-shaped lithium electrode placed concentrically around the glassy carbon sensor. The additional electrode allows charge to be passed, whilst the glassy carbon electrode detects passage of crossover species as a function of this charge. A simple analytical model was presented for the variation in concentration of crossover species with time. By simple fitting of the model to experimental data obtained (i) under open circuit conditions and (ii) when a constant current is applied, values can be obtained

for the diffusive permeability and transference number of crossover species in the membrane. Furthermore, for highly selective membranes, the transference number of lithium in the membrane can also be estimated, which is important for efficient, durable and safe operation of lithium batteries. The method was illustrated with a lithiated Nafion membrane, immersed in 1 molal LiTFSI in diglyme containing 0.1 molal LiI as a model crossover species. It was shown that membrane selectivity can be overestimated if the measurements are restricted to ex-situ conditions where application of a current is not possible. In future, the method can be employed to study new membranes and new combinations of membranes, electrolytes and crossover species.

Chapter 4 focussed on the interfacial resistance between solid and liquid electrolytes, which is highly relevant for hybrid electrolyte systems. Four-probe impedance measurements of a solid lithium ion conductor immersed in different liquid electrolytes were used to study the rate of ion transfer through the solid-liquid electrolyte interface. Unfortunately the results presented are likely to have been affected by trace water contamination. Nevertheless they serve to illustrate a proposed approach for identifying the rate-limiting step, which may be desolvation of lithium ions or transport through a solid-liquid electrolyte interphase (SLEI). The approach involves a systematic study of the rate of lithium ion transfer (using impedance spectroscopy, for example) as a function of lithium ion concentration. If the ion transfer resistance and activation energy do not change as a function of concentration, this would indicate that ion transport through the SLEI, rather than desolvation, is the rate-limiting step. If the resistance and activation energy do change as a function of concentration, then additional analysis techniques can be used to identify whether the variation could be attributable to changes in the composition of the SLEI. If, from these analyses, the composition of the SLEI appears to be constant then variation of the resistance and activation energy with lithium ion concentration may indicate that desolvation is important. Then, Butler-Volmer kinetics and ion transport equations can be used to analyse the results, which finally can be compared to the liquid electrolyte case.

Solid polymer electrolytes for Li-S batteries were investigated in Chapter 5, with a return to the Swagelok cell design equipped with glassy carbon electrode, now modified to allow the placement of two electrodes (a lithium ring and a composite sulfur disc) on the side opposite the glassy carbon probe. This cell design allowed, for the first time using electrochemical methods, the direct observation and measurement of sulfur and intermediate polysulfide species in a solid polymer electrolyte. With only sulfur dissolved in the electrolyte, cyclic voltammograms recorded at the glassy carbon electrode were similar to those recorded in some liquid low-dielectric

constant electrolytes, whilst analysis of impedance data as a function of electrode potential suggested that the first reduction wave is associated with a reversible process. A dramatic difference in the cyclic voltammograms was observed in the presence of polysulfides, with a ten-fold increase in the magnitude of the peak currents and a significant change in the shape of the peaks, now resembling those observed in DOL:DME. The peak potentials were nearly independent of scan rate, indicating fast redox processes, whilst peak shapes suggested that the second reduction wave is followed by a coupled chemical reaction. Its ability to detect polysulfide reaction intermediates proven, the novel cell design used for this work could be refined in future in order to reduce cell-to-cell variability and to achieve better control of the reaction of the sulfur composite electrode.

Finally, in Chapter 6, a version of the Swagelok cell with glassy carbon electrode was used in combination with various electrochemical techniques to evaluate the diffusion coefficient of solution-based redox reactants. Using a model reactant, ethyl viologen, it was found that the cell is well-suited for evaluating diffusion coefficients using voltammetric or 'chrono' techniques. In a collaborative piece of work, an accurate value of the diffusion coefficient of EtV^{2+} in an electrolyte-soaked glass fibre separator, obtained from cyclic voltammetry measurements in the cell, was used as a comparator for values obtained from GITT measurements in a cell with a porous carbon electrode. It was revealed that GITT can provide reliable values for the diffusion coefficient, but only when the cell is at intermediate states of charge. In future, GITT may be used to study other soluble redox species such as polysulfides, provided this and other caveats are noted.

Overall, the use of a Swagelok cell equipped with glassy carbon electrode has proven to be a simple yet powerful tool for studying lithium protective membranes, applicable to Li-S and other advanced lithium batteries; for providing new insights into Li-S redox mechanisms in polymer electrolytes; and for evaluating mass transport properties of soluble redox species in realistic electrolyte conditions. In the case of lithium protective membranes, or solid electrolytes for hybrid electrolyte systems, a new method has been developed for the quantitative evaluation of membrane selectivity and transference numbers under *operando* conditions. Separately, systematic 4-probe impedance measurements have revealed important information about the rate of lithium ion transfer between liquid electrolytes and solid conducting phases, providing a methodology for the study of similar systems in the future. It is hoped that, together, the cell designs and methods developed in this work provide a useful advance in the approaches available for characterising lithium protective membranes, solid electrolytes and beyond.

Appendices

A Appendix A: Experimental techniques used in this work

A.1 Chronoamperometry

In chronoamperometry, the potential at a stationary planar electrode is stepped from a value where no current flows (the equilibrium potential) to a high overpotential where the rate of reaction is diffusion controlled. Considering a simple electron transfer reaction, O + e^- → R, the concentration of O at the electrode surface changes instantaneously to zero as a result of the potential step, creating a concentration profile from the surface to the bulk solution. Initially this profile is steep, leading to a large flux of O to the surface according to Fick's first law of diffusion:

$$J = -D_O \left[\frac{\partial c_O}{\partial x} \right]_{x=0} \qquad \text{(Eq. A.1.1)}$$

where J is the flux, c_O is the concentration of O and D_O is its diffusion coefficient. As time progresses, the concentration profile spreads into the bulk and its gradient decreases. The flux of O to the surface decreases and therefore a falling current vs. time is observed, since the current, i, is related to the flux by:

$$i = IA = nFJA = -nFAD_O \left[\frac{\partial c_O}{\partial x} \right]_{x=0} \qquad \text{(Eq. A.1.2)}$$

where I is the current density, A is the electrode surface area, n is the number of electrons involved in the electrode reaction and F is Faraday's constant. The transient flux, and hence the current, is given by solving, using Laplace transform procedures, Fick's second law of diffusion:

$$\frac{\partial c_O(x,t)}{\partial t} = \frac{\partial^2 c_O(x,t)}{\partial x^2} \qquad \text{(Eq. A.1.3)}$$

with the appropriate initial and boundary conditions:

at $t = 0$ and at all x, $c_O(x,0) = c_O$ (Eq. A.1.4a)

at $t > 0$ and $x = 0$, $c_O(x,t) = 0$ (Eq. A.1.4b)

at $t > 0$ and $x = \infty$, $c_O(x,t) = c_O$ (Eq. A.1.4c)

which leads to the well-known Cottrell equation:

$$i = \frac{nFAD_O^{1/2}c_O}{\pi^{1/2}t^{1/2}} \qquad \text{(Eq. A.1.5)}$$

For a reaction under diffusion control, a plot of i vs $t^{1/2}$ will therefore be linear.

A.2 Cyclic voltammetry

Cyclic voltammetry involves sweeping the potential of the working electrode from a starting potential E_1, at a constant rate, $\boldsymbol{\upsilon}$, through a range where an electrode reaction occurs, to a switching potential E_2, before reversing the scan direction (Figure A.2.1a). The current is measured and plotted as function of potential (Figure A.2.1b, for a simple reversible electron transfer reaction, O + e^- → R. Reversible here means a reaction in thermodynamic equilibrium, i.e. where the rate of electron transfer is sufficiently fast that, at all potentials, the surface concentrations of O and R remain in equilibrium, and the overall rate of the reaction is determined by mass transport of O to the electrode surface.) In general, the number and shape of the peaks on the forward and reverse scans in a cyclic voltammogram, the peak potentials and current densities, the charges associated with each peak, and differences between first, second and subsequent cycles can provide information about the reactions that are occurring.

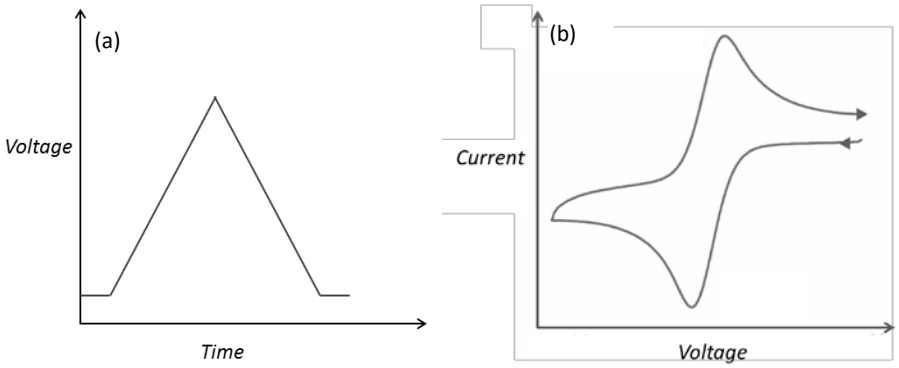

Figure A.2.1: Schematic of (a) typical voltage profile applied in cyclic voltammetry and (b) resulting current response for a reversible one-electron transfer reaction.

Two changes occur simultaneously as the potential is varied on the forward scan: the concentration of O at the electrode surface falls according to the Nernst equation and at the same time, non-steady state diffusion occurs close to the surface to try to minimise the difference in concentration between the surface and the bulk. As the potential decreases (becomes more negative), the surface concentration of O continues to drop; hence the concentration gradient at

the surface increases and therefore the flux of O to the surface (and the current) increases. However, as the potential decreases further, which corresponds to longer times in the experiment, the concentration gradients spread over longer distances (the thickness of the diffusion layer increases), which has the effect of reducing the flux of O to the surface, and consequently the current decreases. Due to these competing effects, a peak in current is observed in the cyclic voltammogram. At higher scan rates, the surface concentration will change more rapidly and the diffusion layer will therefore be thinner, meaning that the current at all potentials, including the peak, will be larger.

The shape of the peak and its dependence on the scan rate comes from the solution to the following equations, based on Fick's second law of diffusion:

$$\frac{\partial c_O(x,t)}{\partial t} = \frac{\partial^2 c_O(x,t)}{\partial x^2} \text{ and } \frac{\partial c_R(x,t)}{\partial t} = \frac{\partial^2 c_R(x,t)}{\partial x^2} \qquad \text{(Eq. A.2.1)}$$

Generally, cyclic voltammetry is carried out with only the oxidised or reduced species in solution; in the former case the initial conditions and boundary conditions are then:

at $t = 0$ and at all x, $c_O(x,0) = c_O$ and $c_R(x,0) = 0$ (Eq. A.2.2a)

at $t > 0$ and $x = \infty$, $c_O(x,t) = c_O$ and $c_R(x,t) = 0$ (Eq. A.2.2b)

at $t > 0$ and $x = 0$:

$$\frac{\partial c_O(0,t)}{\partial x} = -\frac{\partial c_R(0,t)}{\partial x} \qquad \text{(Eq. A.2.2c)}$$

$$\frac{c_O(0,t)}{c_R(0,t)} = \exp\frac{nF(E_1 + \upsilon t - E^{0'})}{RT} \qquad \text{(Eq. A.2.2d)}$$

where $E^{0'}$ is the formal potential for the reaction and equation A.2.2d is a form of the Nernst equation. The solution to these equations shows that, for a reversible system, the peak current is given by the following expression, known as the Randles-Sevcik equation:

$$i_p = 0.4463\left(\frac{F^3}{RT}\right)n^{3/2}AD_O^{1/2}c_O\upsilon^{1/2} = 2.69\times10^5 n^{3/2}AD_O^{1/2}c_O\upsilon^{1/2} \quad \text{at 25 °C} \qquad \text{(Eq. A.2.3)}$$

Furthermore, the peak potential is given by:

$$E_p = E_{1/2} - 1.109\frac{RT}{nF} = E_{1/2} - \frac{28.5}{n}\ \text{mV} \quad \text{at 25 °C} \qquad \text{(Eq. A.2.4)}$$

where $E_{1/2}$ is the half-wave potential:

$$E_{1/2} = E^{0'} + \frac{RT}{nF}\ln\frac{D_O^{1/2}}{D_R^{1/2}} \qquad \text{(Eq. A.2.5)}$$

The half-peak potential, $E_{p/2}$, i.e. the potential at $i_{p/2}$, is given by:

$$E_{p/2} = E_{1/2} + 1.09\frac{RT}{nF} = E_{1/2} + \frac{28.0}{n}\ \text{mV at 25 °C} \qquad \text{(Eq. A.2.6)}$$

Equations A.2.4 and A.2.5 show that for a reversible reaction, peak potential is therefore independent of scan rate.

Beyond the peak, the concentration of O at the surface approaches zero and the current continues to decay as the diffusion layer continues to extend into the bulk. On the reverse scan, as long as the potential is well negative of the formal potential, the surface concentration of O will remain very small and the current will continue to decay. However, near the formal potential, an increase in the concentration of O will be required, according to the Nernst equation, and the only way for this to happen quickly is for R to be oxidised at the surface, creating a flux of R to the surface. The current density will therefore change sign, and will subsequently also pass through a peak due to non-steady state diffusion of R. Evaluation of the peak current on the reverse scan must take account of the 'baseline' created by the forward scan. For an electron-transfer reaction with a stable product, the ratio of the peak currents is equal to 1. For a reversible reaction at 25 °C, the separation, ΔE_p, between the forward and reverse peak potentials is always close to $59/n$ mV. However, distortions due to iR drop (i.e. uncompensated solution resistance, see Section A.4) may affect this, increasing the peak-to-peak separation at higher scan rates.

For an irreversible reaction (i.e. one limited by the rate of electron transfer), changing the potential at the electrode surface will no longer create an instantaneous change in the surface concentrations. Instead, an overpotential is required to drive the reaction in a particular direction, according to the Butler-Volmer equation. Compared to the reversible case, therefore, the reduction peak will shift to more a negative potential and the oxidation peak to a more positive one. Moreover, this effect will increase with increasing scan rate, since there will be less time for the surface concentrations to adjust to the changes in potential and so more of a lag before the surface concentration reaches zero and a peak in the current is observed. The peak potentials will therefore depend on the scan rate, with a larger ΔE_p at higher scan rates.

A.3 Chronopotentiometry

In chronopotentiometry, a constant current step is applied to a cell and the potential response is measured as a function of time. This response can be understood by considering the concentration profiles of the redox species. For a simple electron transfer reaction O + e^- → R, when a current is applied, O is reduced to R at the electrode surface in order to sustain the applied current, and the concentration of O at the electrode decreases. The electrode potential therefore decreases according to the Nernst equation. This continues until the concentration of O at the electrode surface reaches zero, at which point the applied current can no longer be supported by this reaction, and the potential changes to the redox potential of another electron transfer reaction.

The time required for the concentration of O at the electrode surface to reach zero is known as the transition time, τ, and depends on the applied current, i, and on the diffusion coefficient of O and its bulk concentration, c_O^*, according to the Sand equation (see Box A.3.1):

$$\frac{i\tau^{1/2}}{c_O^*} = \frac{nFAD_O^{1/2}\pi^{1/2}}{2} \qquad \text{(Eq. A.3.1)}$$

The measured value of τ at known i (or the values of $i\tau^{1/2}$ obtained at various currents) can be used to determine n, A, c_O^* or D_O.

The transition time constant, $i\tau^{1/2}/c_O^*$, is independent of i or c_O^* for systems that are not affected by coupled chemical reactions, adsorption, or measurement artefacts such as the onset of convection. In most cases, however, double-layer charging leads to deviations from the ideal behaviour represented by the Sand equation. Assuming a constant electrode area then the charging current i_c is given by:

$$i_c = -AC_{dl}\frac{d\eta}{dt} = -AC_{dl}\frac{dE}{dt} \qquad \text{(Eq. A.3.2)}$$

(η is the potential change from the equilibrium position), and only a fraction of the total applied constant current goes to the Faradaic reaction:

$$i_f = i - i_c \qquad \text{(Eq. A.3.3)}$$

Box A.3.1: Derivation of the Sand equation

For a planar electrode in unstirred solution with only species O initially present at the bulk concentration c_o^*, flux of O to the electrode surface (and of R away from the electrode surface) is given by Fick's laws of diffusion:

$$\frac{\partial c_O(x,t)}{\partial t} = D_O\left[\frac{\partial^2 c_O(x,t)}{\partial x^2}\right] \text{ and } \frac{\partial c_R(x,t)}{\partial t} = D_R\left[\frac{\partial^2 c_R(x,t)}{\partial x^2}\right] \quad \text{(Eq. A.3.5)}$$

with the following initial and boundary conditions:

at $t = 0$ and at all x; at $t > 0$ and $x = \infty$:

$$c_O(x,t) = c_O^*;\ c_R(x,t) = c_R^* \quad \text{(Eq. A.3.6)}$$

$$D_O\left[\frac{\partial c_O(x,t)}{\partial x}\right]_{x=0} + D_R\left[\frac{\partial c_R(x,t)}{\partial x}\right]_{x=0} = 0 \quad \text{(Eq. A.3.7)}$$

Since the applied current i is known, the flux at the electrode surface is also known:

$$D_O\left[\frac{\partial c_O(x,t)}{\partial x}\right]_{x=0} = \frac{i}{nFA} \quad \text{(Eq. A.3.8)}$$

Using the Laplace transform method applied to equations A.3.5 and A.3.8, the following expression for $c_O(x,t)$ can be obtained:

$$c_O(x,t) = c_O^* - \frac{i}{nFAD_O^{1/2}}\left\{2\left(\frac{D_O t}{\pi}\right)^{1/2}\exp\left(-\frac{x^2}{4D_O t}\right) - x\,erfc\left[\frac{x}{2\left(D_O t\right)^{1/2}}\right]\right\}$$

(Eq. A.3.9)

At $x = 0$ this simplifies to:

$$c_O(x,t) = c_O^* - \frac{2it^{1/2}}{nFAD_O^{1/2}\pi^{1/2}} \quad \text{(Eq. A.3.10)}$$

At the transition time, τ, $c_O(0,t)$ drops to zero and equation A2.10 becomes the Sand equation:

$$\frac{i\tau^{1/2}}{c_O^*} = \frac{nFAD_O^{1/2}\pi^{1/2}}{2} \quad \text{(Eq. A.3.11)}$$

Since dE/dt is a function of time, i_c and i_f also vary with time, even when the applied current is constant. This effect is greatest immediately after current is applied and just before the transition (when dE/dt is relatively large) and affects the overall shape of the E vs. t curve, making measurement of τ difficult and inaccurate (Figure A.2.1).

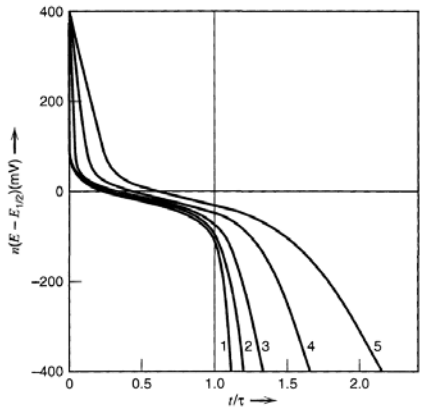

Figure A.2.1: Effect of double layer capacitance on E vs. t curves for a Nernstian reaction. Charging contribution is represented (see Appendix F) by the dimensionless parameter, *K*, with *K* values of (1) 5 X 10^{-4}; (2) 10^{-3}; (3) 2 X 10^{-3}; (4) 5 X 10^{-3} (5) 0.01. Reproduced with permission [2,3]. Copyright (2001) Wiley, (1968) Elsevier.

Various techniques have been proposed for correcting values obtained where double-layer effects are significant. One simple approach is to assume i_c is constant for $0 < t < \tau$ and then it is possible to write:

$$\frac{i\tau^{1/2}}{c_O^*} = \frac{i_f\tau^{1/2}}{c_O^*} + \frac{i_c\tau}{c_O^*\tau^{1/2}} \qquad \text{(Eq. A.3.4)}$$

where $i_f\tau^{1/2}/c_O^*$ is the "true" transition time constant, equal to $\frac{1}{2}nFAD_O^{1/2}\pi^{1/2}$, and $i_c\tau = C_{dl,average}\Delta E$ (where ΔE is the change from the initial potential to the potential when τ is measured). The observed data can then be used to estimate D_O and C_{dl} from a plot of $i\tau$ vs. $\tau^{1/2}$.

A.4 GITT

The galvanostatic intermittent titration technique (GITT) was first developed in 1977 by Weppner and Huggins [4] to determine both kinetic and thermodynamic parameters of lithium ion cells, including the chemical diffusion coefficient of lithium ions in the electrode materials. Typically a cell with lithium metal counter/reference electrode and Li-ion insertion material as the working (positive) electrode is used (Figure A.4.1). A series of current pulses (positive for charge or negative for discharge) is applied, each followed by a relaxation period. Figure A.4.2 illustrates the typical potential response.

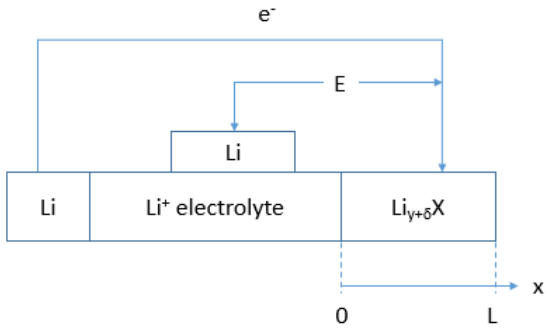

Figure A.4.1: Schematic of cell for determining the chemical diffusion coefficient of lithium ions in electrode materials using GITT.

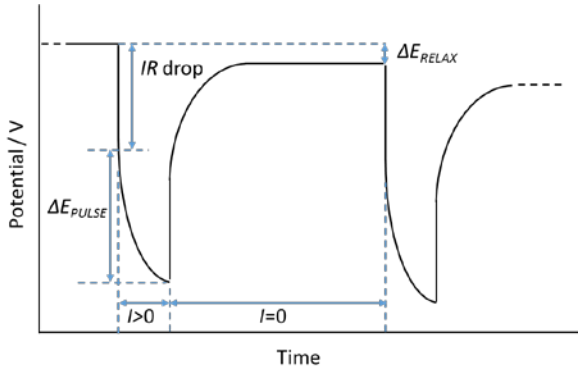

Figure A.4.2: Schematic of potential response during current pulse and relaxation period in GITT.

During each negative current pulse, there is an initial sharp decrease in cell potential, E, due to iR drop (where R is the sum of the uncompensated and charge transfer resistances), followed by a slower decrease due to the galvanostatic discharge current. At the end of the pulse/start of the relaxation period, there is a sharp increase in potential, again due to iR drop. After this the potential increases more slowly until the electrode reaches a new equilibrium ($dE/dt = 0$),

determined by the change in composition caused by the Coulombic titration of Li ions into it (equation A.4.1):

$$\Delta c = \frac{\Delta m}{V} = \frac{i\tau}{nFLA} \qquad \text{(Eq. A.4.1)}$$

where c is the concentration of Li ions in the electrode, m is the number of moles of Li ions in the electrode, V is the volume of the electrode, i is the applied current, τ is the pulse length, n is the number of electrons required to insert each Li ion, F is Faraday's constant, L is the length of the electrode and A is the cross-sectional area of the electrode. This process is repeated until the cell is fully discharged.

Calculating the cell voltage E as a function of time *t* during the pulse involves determining the concentration of lithium ions at the interface $x = 0$ by solving Fick's second law (equation A.4.2):

$$\left[\frac{\partial c(x,t)}{\partial x}\right]_{x=0} = D\left[\frac{\partial^2 c(x,t)}{\partial x^2}\right]_{x=0} \qquad \text{(Eq. A.4.2)}$$

with the following initial and boundary conditions:

$$c(x=0,t=0) = c^{initial} \qquad (0 \le x \le L)$$

$$-D\left[\frac{\partial c(x,t)}{\partial x}\right]_{x=0} = \frac{i}{nFA} \qquad (t \ge 0)$$

$$\left[\frac{\partial c(x,t)}{\partial x}\right]_{x=L} = 0 \qquad (t \ge 0) \qquad \text{(Eq. A.4.3)}$$

(The last condition arises from the assumption that the right-hand phase boundary of the sample is impermeable.)

The solution is known, and for values of $t \ll L^2/D$ is given by equation A.4.4, which is in fact the Sand equation:

$$c(x=0,t) - c^{initial} = \frac{2i\sqrt{t}}{nFA\sqrt{\pi D}} \qquad (t \ll \frac{L^2}{D}) \qquad \text{(Eq. A.4.4)}$$

This yields the following variation of $c(x=0,t)$ with the square root of time:

$$\frac{dc(x=0,t)}{d\sqrt{t}} = \frac{2i}{nFA\sqrt{\pi D}} \qquad (t \ll \frac{L^2}{D}) \qquad \text{(Eq. A.4.5)}$$

This equation could be used to determine the chemical diffusion coefficient D if the variation of the surface concentration with time were known, but this is not usually measurable directly. However, we can expand equation A.4.5 by dE, which *is* measurable, to give:

$$\frac{dE}{d\sqrt{t}} = \frac{dc^{x=0}}{d\sqrt{t}} \cdot \frac{dE}{dc^{x=0}} = \frac{2i}{nFA\sqrt{\pi D}} \cdot \frac{dE}{dc^{x=0}} \qquad (t \ll \frac{L^2}{D}) \qquad \text{(Eq. A.4.6)}$$

Where $c^{x=0}$ is shorthand for $c(x=0,t)$. If a sufficiently small current/pulse length is applied then the resulting change in equilibrium potential ΔE_{RELAX} can be assumed to be proportional to the change in concentration and we can replace dE/dc with $\Delta E_{RELAX}/\Delta c$. Additionally, if $dE/d\sqrt{t}$ is linear over the entire pulse length, τ, then we can replace it with $\Delta E_{PULSE}/\sqrt{\tau}$ where ΔE_{PULSE} is the total change in cell voltage during the pulse, excluding the iR drop. This gives, finally:

$$D = \frac{4}{\pi}\left(\frac{L^2}{\tau}\right)\left(\frac{\Delta E_{RELAX}}{\Delta E_{PULSE}}\right)^2 \qquad (t \ll \frac{L^2}{D}) \qquad \text{(Eq. A.4.7)}$$

Although GITT is typically used for determining the chemical diffusion coefficient in Li-ion insertion materials, it should also be possible to apply it to diffusion of reactants in a liquid electrolyte. This can be visualised by reference to Figure A.4.3. In this example the species of interest, O, diffuses through the electrolyte and is reduced to R at the working electrode. An LICM (Ohara glass) separates the working and counter electrode compartments, providing the impermeable boundary (with respect to R) that underpins the final boundary condition in equation A.4.3, and preventing O (or R) from crossing to the negative electrode and reacting with the lithium metal. The set of assumptions and boundary conditions underpinning equation A.4.7 in this situation can be visualised by reference to Figure A.4.4.

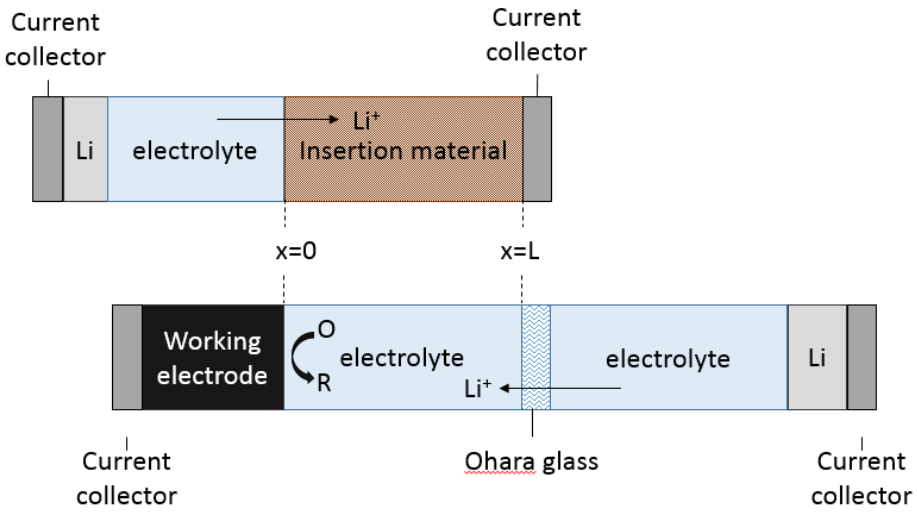

Figure A.4.3: Comparison of GITT cell set-up for determination of diffusion coefficients in Li-ion electrode material vs. liquid electrolyte.

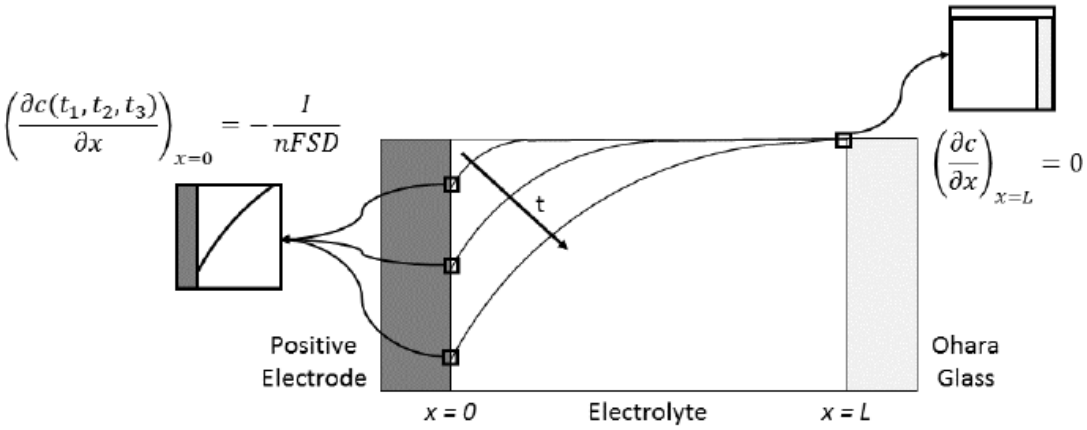

Figure A.4.4: Evolution of concentration profile of O (oxidised species) with time. At the electrode-electrolyte interface (*x = 0*) the concentration gradient is constant with increasing time and at the Ohara-electrolyte interface (*x = L*) the concentration gradient is always zero. The latter holds provided $\tau << L^2/D$.

A.5 Electrochemical Impedance Spectroscopy

According to Ohm's law, resistance is defined in terms of the ratio between voltage, E, and current, i. However, this definition holds only for an ideal resistor, for which resistance is independent of frequency, and AC current and voltage signals are in phase with each other. Impedance is a more generalised measure of the ability of a circuit to resist the flow of electrical current. Electrochemical impedance is usually measured by applying an AC potential to an

electrochemical cell and measuring the resulting current. If a sinusoidal potential excitation is applied, the response will be an AC current at the same frequency but shifted in phase (assuming a pseudo-linear system, which is valid provided the potential excitation is small).

The potential excitation at time t is given by $E = E_0 \sin(\omega t)$ where E_0 is the amplitude and $\omega = 2\pi f$ where f is the frequency. Similarly the current response at time t is given by $i = i_0 \sin(\omega t + \varphi)$ where φ is the phase shift relative to the potential. E and i can be expressed in complex notation as:

$$E = E_0 \left[\cos(\omega t) + j \sin(\omega t) \right] \quad \text{(Eq. A.5.1)}$$

$$i = i_0 \left[\cos(\omega t + \varphi) + j \sin(\omega t + \varphi) \right] \quad \text{(Eq. A.5.2)}$$

Then from Euler's theorem:

$$E = E_0 \exp(j\omega t) \quad \text{(Eq. A.5.3)}$$

$$i = i_0 \exp(j\omega t + j\varphi) \quad \text{(Eq. A.5.4)}$$

And:

$$Z(\omega) = E/i = Z_0 \exp(j\varphi) = Z_0 (\cos\varphi + j \sin\varphi) = Z_{real} + jZ_{im} \quad \text{(Eq. A.5.5)}$$

This allows impedance to be plotted on a Nyquist diagram with the real part of the impedance on the x-axis and the imaginary part on the y-axis. Nyquist diagrams, which contain no information about frequency (unless annotated), can be complemented with a Bode plot of the real and imaginary parts of the impedance vs. log of frequency. This allows for easier interpretation of circuit elements with different time constants. An alternative form of the Bode plot shows the magnitude and the phase angle of the impedance vs. log of frequency.

EIS data are commonly analysed by fitting an equivalent electrical circuit model. This is a combination of common electrical elements (resistors, capacitors etc.) plus some specialised electrochemical elements (e.g. Warburg diffusion elements), which produces the same impedance response as the electrochemical cell. The characteristics of some common circuit elements are set out in Table A.5.1. For linear elements in series, the impedances are summed; for linear elements in parallel, the inverses of the impedances are summed. To be useful, equivalent circuit models should reflect the electrochemical processes occurring in the system.

	Current-voltage relationship	Impedance	Dependence on frequency	Phase angle
Resistor	$V = IR$	$Z = R$	Independent	0^o
Capacitor	$I = C\frac{dV}{dt}$	$Z = \frac{1}{j\omega C}$	Falls with increasing frequency	90^o
Inductor	$V = L\frac{dI}{dt}$	$Z = j\omega L$	Increases with increasing frequency	-90^o

Table A.5.1: Selected characteristics of key circuit elements. V = voltage, I = current, R = resistance, C = capacitance, L = inductance.

A.5.1 Solution resistance

The resistance of an ionic solution depends on its conductivity and the geometry of the area through which the current is carried. For a given volume of area A and length L:

$$R = \rho L / A \qquad \text{(Eq. A.5.6)}$$

where ρ is the solution resistivity $= 1/\sigma$, (σ = conductivity). However most electrochemical cells do not have uniform current distribution through a defined area; solution resistance is therefore determined experimentally from EIS data (see below) rather than calculated from ionic conductivities. Modern potentiostats compensate for the solution resistance between the counter and reference electrodes in a three-electrode cell. However, the solution resistance between the reference and working electrodes (the 'uncompensated' resistance) must be considered.

A.5.2 Double layer capacitance

An electrical double layer exists between the electrode surface and the surrounding electrolyte, formed as ions of opposite charge are attracted to the electrode from the solution. The electrode/electrolyte interface therefore behaves like a capacitor. Modelling double layer charging with an ideal capacitor assumes that the electrode surface is homogeneous, which is not normally the case. This lack of homogeneity is modelled instead with a constant phase element (CPE). Mathematically, a CPE's impedance is given by:

$$Z = 1 / \left[Q^0 \left(j\omega \right)^{\alpha} \right] \qquad \text{(Eq. A.5.7)}$$

where α is a constant ranging from 0 to 1 and $Q^0 = 1/|Z|$ at ω = 1 rad s^{-1}. If $\alpha = 1$ then the CPE is analagous to a capacitor and $Q^0 = C$.

Several theories (surface roughness, "leaky" capacitor, non-uniform current distribution, etc.) have been proposed to account for non-ideal behaviour of the double layer.

A.5.3 Charge transfer resistance

When an electrode is polarised, current also flows as a result of electrochemical reactions. For a kinetically controlled reaction, the relationship between the current and polarisation is given by the Butler-Volmer equation:

$$I = I_0 \left[\frac{c_0}{c_O^*} \exp\left(\alpha \frac{nF}{RT} \eta \right) - \frac{c_R}{c_R^*} \exp\left(-(1-\alpha) \frac{nF}{RT} \eta \right) \right] \qquad \text{(Eq. A.5.8)}$$

Where I is the current density, I_0 is the exchange current density, c_0 and c_R are the concentrations of O and R at the electrode, c_O^* and c_R^* are the concentrations of O and R in the bulk electrolyte, α is the transfer coefficient or symmetry factor, η is the overpotential, n is the number of electrons required to convert O into R, F is Faraday's constant, R is the universal gas constant and T is the temperature. For small values of the overpotential this simplifies to:

$$I = I_0 \frac{nF}{RT} \eta \qquad \text{(Eq. A.5.9)}$$

since $\exp(x) \approx 1 + x$ for $x \approx 0$.

A new parameter, R_{ct}, the charge transfer resistance, can then be introduced:

$$R_{ct} = \frac{RT}{nFI_0} \qquad \text{(Eq. A.5.10)}$$

A.5.4 Diffusion

Impedance can also arise as a result of diffusion, i.e. the need for reactants to diffuse towards the electrode surface. The Warburg impedance was developed to model this phenomenon. Under the assumption of a semi-infinite diffusion layer (i.e. unrestricted diffusion to a large planar electrode), the impedance is given by the infinite Warburg element:

$$Z_W = \sigma\omega^{-1/2}(1-j) \quad \text{(Eq. A.5.11)}$$

Where σ is the Warburg coefficient defined as:

$$\sigma = \frac{RT}{n^2F^2A\sqrt{2}}\left(\frac{1}{c_O^*\sqrt{D_O}} + \frac{1}{c_R^*\sqrt{D_R}}\right) \quad \text{(Eq. A.5.12)}$$

Where D_O and D_R are the diffusion coefficients of the oxidised and reduced species respectively. The Warburg impedance is an example of a CPE for which the real and imaginary parts are equal, i.e. the phase angle is 45° ($\alpha = 0.5$). Its magnitude is inversely proportional to the square root of frequency. At high frequencies, diffusing reactants don't have to travel far and the Warburg impedance is small, whilst at low frequencies, the reactants have to diffuse farther, and the Warburg impedance increases. This form of the Warburg impedance is only valid if the diffusion layer has an infinite thickness. If the diffusion layer is bounded, the impedance at low frequencies no longer obeys the equation above. Instead the impedance is described by the finite Warburg element which can be either 'open' (e.g. for an electrode facing an inert wall) or 'closed' (e.g. for a thin layer cell with two electrodes):

$$Z_{oW} = \sigma\omega^{-1/2}(1-j)\coth\left[\left(j\omega L^2/D\right)^{1/2}\right] \quad \text{(Eq. A.5.13)}$$

$$Z_{cW} = \sigma\omega^{-1/2}(1-j)\tanh\left[\left(j\omega L^2/D\right)^{1/2}\right] \quad \text{(Eq. A.5.14)}$$

Where L is the effective diffusion thickness and D is the average value of the diffusion coefficients of the diffusing species. For high frequencies where $\omega \to \infty$, or for an infinite thickness of the diffusion layer where $L \to \infty$, the final term $\to$ 1 and these expressions simplify to Equation A.5.11.

A.5.5 Simplified Randles circuit

The simplest model of an electrochemical interface is the simplified Randles circuit, which consists of the electrolyte solution resistance in series with the double layer capacitance and charge transfer resistance (Figure A.5.1). The double layer capacitance, C_{dl}, and charge transfer resistance, R_{ct}, are in parallel as they represent two competing 'pathways' for current to flow.

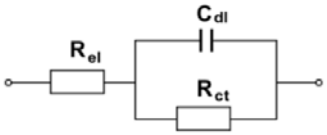

Figure A.5.1: Simplified Randles circuit

For a general parallel RC circuit, according to Kirchoff's law the potential across the parallel branches is equal while the current that flows through each branch depends on the impedance. At high frequencies, the impedance of C tends to zero and all current effectively flows through it, bypassing R. At low frequencies, the impedance of C becomes very large and all current flows through R.

The total current is equal to the sum of the current through each branch:

$$i(t)=\frac{V(t)}{Z}=\frac{V(t)}{R}-\frac{\omega CV(t)}{j}=V(t)\left(\frac{1}{R}-\frac{\omega C}{j}\right)=V(t)\frac{1+\left(\omega RC\right)^2}{R-j\omega R^2C} \qquad \text{(Eq. A.5.15)}$$

The resulting impedance therefore has a real part and an imaginary part:

$$Z_{real}(\omega)=\frac{R}{1+\left(\omega RC\right)^2} \qquad \text{(Eq. A.5.16a)}$$

$$Z_{im}(\omega)=\frac{\omega R^2C}{1+\left(\omega RC\right)^2} \qquad \text{(Eq. A.5.16b)}$$

On a Nyquist plot, this appears as a semicircle whose diameter is equal to R. (The solution resistance in the Randles circuit appears as a high-frequency intercept on the real axis). At a characteristic frequency $\omega_c=2\pi f_c$ the real and imaginary impedances of the parallel RC circuit are equal, $|Z_{im}|=|Z_{real}|$ (i.e. the midpoint of the semicircle on a Nyquist plot). At this point $R=\omega R^2C$ i.e. $\omega_c=1/RC$. RC is the time constant, τ, of the circuit. Each semicircle on a Nyquist plot is characteristic of a different time constant.

A.6 References

[1] D. Pletcher, A First Course in Electrode Processes, Royal Socety of Chemistry, Cambridge, UK, 2009.

[2] A.J. Bard and L.R. Faulkner, Electrochemical Methods Fundamentals and Applications, John Wiley & Sons, New York, NY, USA, 2001.

[3] De Vries, W. T., Double-layer charging in constant-current chronopotentiometry at a mercury-film electrode. *Journal of Electroanalytical Chemistry and Interfacial Electrochemistr*y **1968**, 19, 41-53.

[4] W. Weppner, R.A. Huggins, Determination of the Kinetic Parameters of Mixed-Conducting Electrodes and Application to the System LLSb, J. Electroanal. Chem. 124 (1977) 1569–1578.

[5] Wen, C. J., Boukamp, B. A., Huggins, R. A. & Weppner, W. Thermodynamic and mass transport properties of LiAl. *Journal of the Electrochemical Society* 126 (1979) 2258–2266.

[6] Gamry Instruments, Basics of electrochemical impedance spectroscopy. Available at https://www.gamry.com/application-notes/EIS/basics-of-electrochemical-impedance-spectroscopy/ . Accessed 15 January 2016.

[7] V.F. Lvovich, Impedance Spectroscopy: Applications to Electrochemical and Dielectric Phenomena, John Wiley & Sons, Somerset, NJ, USA, 2012.

B Appendix B: Appendix to Chapter 1

B.1 Bruce-Vincent method for determining transport numbers

A method for determining ion transport numbers in SPEs was developed by Bruce, Evans and Vincent, based on DC polarisation and utilising the fact that, unlike liquid electrolytes, polymer electrolytes can sustain stable concentration gradients, since convection is negligible [1]. For a symmetrical Li/polymer electrolyte/Li cell under a small (<= 10 mV), constant applied voltage, ΔV, the initial current i^0 (due to migration of cations and anions) falls with time towards a steady state i^{SS}, as a salt concentration gradient is established across the cell due to anion accumulation at the positive electrode. The concentration gradient generates an e.m.f. that opposes ΔV and reduces the migration current. It also leads to diffusion of both ion species away from the positive electrode; for anions this is in the opposite direction to migration and steady state is reached when there is zero net anion motion. The steady state current is thus carried entirely by cation motion (migration plus diffusion in the same direction, with diffusion compensating for the reduction in migration current), and the transport number is given simply by:

$$T_+ = \frac{i^{SS}}{i^0} \qquad \text{(Eq. B.1)}$$

In practice, the fall in current from $t = 0$ until steady state also arises from the growth of an SEI on the electrode surface, to a limiting thickness. In this case the initial and steady-state currents are given by [2]:

$$i^0 = \frac{\Delta V}{\left(R^0_{SEI} + R_{el}\right)} = \frac{\Delta V}{\left(R^0_{SEI} + \frac{k}{\sigma}\right)} \qquad \text{(Eq. B.2)}$$

and:

$$i^{SS} = \frac{\Delta V}{\left(R^{SS}_{SEI} + \frac{k}{t_+\sigma}\right)} \qquad \text{(Eq. B.3)}$$

where ΔV is the potential applied across the cell, k is the cell constant, t_+ is the cationic transport number, σ is the (d.c.) conductivity of the electrolyte (R_{el} is its resistance), and R^0_{SEI} and R^{SS}_{SEI} are the initial and steady-state resistances of the SEI. From equation B.3:

$$\sigma = \frac{i^0 k}{\left(\Delta V - i^0 R_{SEI}^0\right)} \qquad \text{(Eq. B.4)}$$

Hence from equations B.2 and B.4:

$$T_+ = \frac{i^{SS}\left(\Delta V - i^0 R_{SEI}^0\right)}{i^0\left(\Delta V - i^{SS} R_{SEI}^{SS}\right)} \qquad \text{(Eq. B.5)}$$

R_{SEI}^0 and R_{SEI}^S can be determined from electrochemcial impedance spectroscopy before and after polarisation. Evaluation of i^0, using equation B.2 with values of R_{el} and R_{SEI}^0 determined from impedance data before polarisation, is preferable to determination of i^0 from the measured i vs. t curve since the latter is prone to error; in particular double layer charging current may lead to overestimation [3].

It is also possible to measure transport number using an analogous galvanostatic polarisation method [4]. In this case, transport number is given by:

$$T_+ = \frac{iR_{TOTAL}^0 - iR_{SEI}^0}{U^{SS} - iR_{SEI}^{SS}} \qquad \text{(Eq. B.6)}$$

Where i is the applied current, $R_{TOTAL}^0 = R_{SEI}^0 + R_{el}$ and U^{SS} is the steady state voltage.

B.2 References

[1] Bruce, P. G.; Vincent, C. A., Steady state current flow in solid binary electrolyte cells. Journal of Electroanalytical Chemistry and Interfacial Electrochemistry 1987, 225, 1-17.

[2] Evans, J.; Vincent, C. A.; Bruce, P. G., Electrochemical measurement of transference numbers in polymer electrolytes. Polymer 1987, 28, 2324-2328.

[3] [5] M. M. Hiller, et al., The influence of interface polarization on the determination of lithium transference numbers of salt in polyethylene oxide electrolytes. Electrochimica Acta, 114 (2013) 21-29.

[4] J. Popovic, G Hasegawa, I. Moudrakovski and J. Maier, Infiltrated porous oxide monoliths as high lithium transference number electrolytes, J. Mater. Chem. A, 4 (2016) 7135

C Appendix C: Appendix to Chapter 3

C.1 Comparison of cyclic voltammetry and square voltammetry of iodide

Figure C.1 illustrates the greatly enhanced signal achieved with cyclic voltammetry vs. square voltammetry in the case of iodide, which has slow redox kinetics. This reason for the can be understood from Figure C.2, which shows the sampled forward and reverse currents from the square wave voltammogram. It can be seen that rather than a reversal of the current direction on the reverse pulse, there is simply a reduction in its magnitude. Accordingly, taking the difference between the forward and reverse current no longer 'amplifies' the signal from the Faradaic reaction, and in this case staircase (i.e. digital cyclic) voltammetry provides a better response.

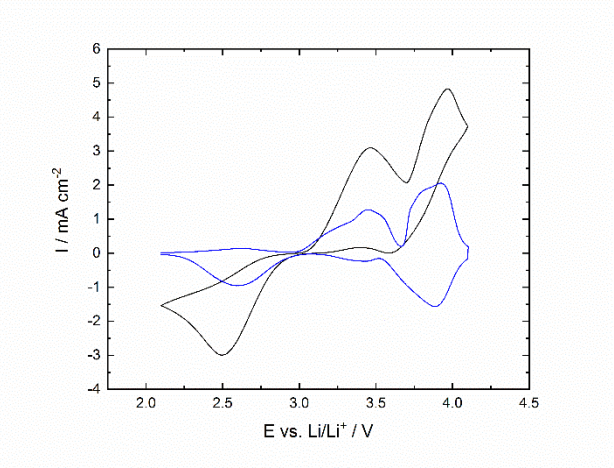

Figure C.1: Voltammetry of LiI (0.4 M in 1 M LiTSI in diglyme). Black line: cyclic voltammogram, scan rate 20 mV s^{-1}. Blue line: Square wave voltammogram. ΔE_s = 4 mV, ΔE_p = 25 mV, t_p = 100 ms. Cell used is shown in Fig 2.1(b).

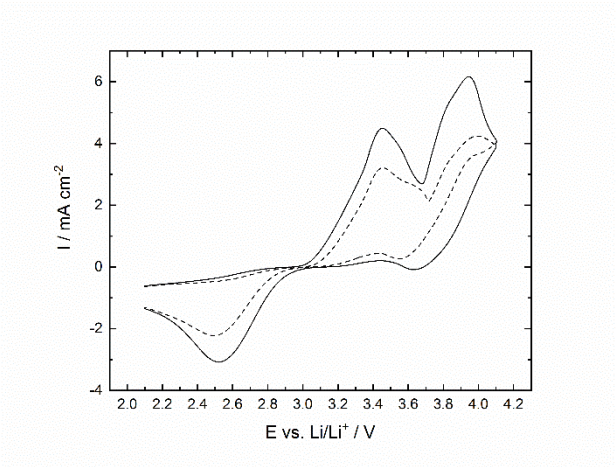

Figure C.2 Forward (solid line) and reverse (dashed line) currents corresponding to SWV in Fig C.1.

C.2 Stack pressure inside Swagelok cell

The stack pressure in the cell comes from compressing a spring (LC 050K 03, Lee Spring Ltd.) with the following properties:

free length / mm	25.4
solid height / mm	5.32
spring rate / kg mm^{-1}	0.167

Table C.1: Properties of spring used to apply stack pressure in half-in Swagelok cells

From Hooke's law, the force needed for full compression of the spring is therefore ((25.4 – 5.32) mm * 0.167 kg mm^{-1}) * 9.81 N kg^{-1} = 32.9 N. Given a current collector area of 4.9 cm^2 (4.9 · 10^{-4} m^2), this amounts to a pressure of 0.7 MPa.

C.3 Estimating transference number based on the Nernst-Einstein equation

This section is adapted from the supporting information to ref 1. The derivations in this section were made by Dr. Nuria Garcia-Araez.

In the absence of ion interactions, the Nernst-Einstein equation can be used to evaluate the molar conductivity of crossover species inside the membrane:

$$\Lambda_c = \frac{D_c F^2}{RT} \qquad \text{(Eq. C.1)}$$

where Λ_c and D_c are the molar conductivity and diffusion coefficient of crossover species inside the membrane, F is Faraday's constant, R is the gas constant and T is absolute temperature. Then, the transference number of crossover species can be obtained as:

$$t_c = \frac{\Lambda_c c_{c,m}}{\sigma_m} = \frac{D_c F^2 c_{c,m}}{RT\sigma_m} \qquad \text{(Eq. C.2)}$$

where $c_{c,m}$ is the concentration of crossover species inside the membrane and σ_m is the membrane conductivity. The concentration of crossover species inside the membrane, $c_{c,m}$, is related to the concentration of crossover species in the liquid electrolyte, $c_{c,l}$, by [2]:

$$c_{c,m} = \frac{\gamma_{c,l} c_{c,l}}{\gamma_{c,m}} = K c_{c,l} \qquad \text{(Eq. C.3)}$$

where $\gamma_{c,m}$ and $\gamma_{c,l}$ are the activity coefficients of the crossover species inside the membrane and the liquid electrolyte, respectively, and *K* is the sorption coefficient [2]. Therefore, the transference number can be obtained as:

$$t_c = \frac{D_c F^2 K c_{c,l}}{RT\sigma_m} = \frac{P_m F^2 c_{c,l}}{RT\sigma_m} \qquad \text{(Eq. C.4)}$$

where it has been taken into account that the diffusive permeability or permeability coefficient P_m equals the product of the diffusion coefficient of the crossover species inside the membrane, D_c, and the sorption coefficient, K, [2]:

$$P_m = D_c K \qquad \text{(Eq. 3.5)}$$

C.4 References

[1] Meddings, N.; Owen, J. R.; Garcia-Araez, N., Operando Evaluation of Selectivity and Transference Number of Lithium-Conductive Membranes. ChemElectroChem 2019, 6, 1678-1682.

[2] Wijmans, J. G.; Baker, R. W., The solution-diffusion model: a review. J. Memb. Sci. 1995, 107, 1-21.

D Appendix D: Appendix to Chapter 4

D.1 Ion transfer in a liquid/solid/liquid electrolyte system described by Butler-Volmer kinetics

This section is adapted from the supporting information of an article in preparation. The derivations in this section were made by Dr. Nuria Garcia-Araez.

In Chapter 4, four-point impedance measurements are used to characterize the rate of lithium ion transfer from one liquid electrolyte compartment (phase 1), through a lithium-selective solid ion conductor (membrane), to another liquid electrolyte compartment (phase 2).

The flux of lithium ions will be given by:

$$J = k^0 \left[c_1 \exp\left(\frac{\alpha F}{RT} \left(\Delta_2^1\phi - \Delta_2^1\phi^0 \right) \right) - c_2 \exp\left(\frac{(\alpha - 1) F}{RT} \left(\Delta_2^1\phi - \Delta_2^1\phi^0 \right) \right) \right] \qquad \text{(Eq. D.1)}$$

where k^0 is the standard rate constant of lithium ion transfer, α is a transfer coefficient, c_1 and c_2 are the lithium concentrations in the liquid electrolyte phases 1 and 2, respectively, $\Delta_2^1\phi$ is the potential drop between phases 1 and 2, and $\Delta_2^1\phi^0$ is the potential drop between phases 1 and 2 under standard conditions ($c_1 = c_2 = 1$ M).

Under equilibrium conditions, $\Delta_2^1\phi = \Delta_2^1\phi^{equil}$, which is related to $\Delta_2^1\phi^0$ by the Nernst equation:

$$\Delta_2^1\phi^{equil} = \Delta_2^1\phi^0 + \frac{RT}{F} \ln\left(\frac{c_2}{c_1} \right) \qquad \text{(Eq. D.2)}$$

Combining equations D.1 and D.2, the flux of lithium ions can also be expressed as a function of the applied overpotential, $\eta = \Delta_2^1\phi - \Delta_2^1\phi^{equil}$:

$$J = k^0 c_1^{1-\alpha} c_2^{\alpha} \left[\exp\left(\frac{\alpha F}{RT} \eta \right) - \exp\left(\frac{(\alpha - 1) F}{RT} \eta \right) \right] \qquad \text{(Eq. D.3)}$$

When $c_1 = c_2$, as is the case for the present impedance measurements, equation D.3 simplifies to the following expression, taking into account that in the impedance measurements, the overpotential is equal to the applied potential perturbation, ΔE.

$$J = k^0 c\left[\exp\left(\frac{\alpha F}{RT}\Delta E\right) - \exp\left(\frac{(\alpha - 1)F}{RT}\Delta E\right)\right] \quad \text{(Eq. D.4)}$$

Taking into account also that ΔE is small, the flux can be simplified to:

$$J = k^0 c\frac{F}{RT}\Delta E \quad \text{(Eq. D.5)}$$

The associated current density, I, will be given by:

$$I = k^0 c\frac{F^2}{RT}\Delta E \quad \text{(Eq. D.6)}$$

And the associated resistance, $R_{BV} = \Delta E / I$, will be given by:

$$R_{BV} = \frac{RT}{k^0 c F^2} \quad \text{(Eq. D.7)}$$

It is worth mentioning that studies of lithium ion insertion into insertion electrodes have been done previously by performing impedance measurements at a constant potential vs. Li^+/Li, so that the activity of lithium ions inside the host insertion material can be considered constant [1]. Under those conditions, the flux of lithium ions is expected to be proportional to c^α, where c is the lithium ion concentration (or more accurately, activity) in the liquid electrolyte and the transfer coefficient, α, is typically close to 0.5. Indeed, the resistance associated with ion transfer into the host material has been found to be inversely proportional to the square root of the lithium ion concentration in a number of cases [1-3].

Note that equation D.4 will only strictly be true for ideal solutions where activity coefficients are expected to be unity. In order to study ion transfer in the presence of more complex effects such as ion-ion interactions, it is convenient to consider ion transfer as a transport process, which is discussed next.

D.2 Ion transfer as a transport process

This section is adapted from the supporting information of an article in preparation. The derivations in this section were made by Dr. Nuria Garcia-Araez.

We have seen that ion transfer can be described using Butler-Volmer kinetics. Equivalent expressions can also be obtained considering that ion transfer can be described as a transport

process. In this context, the standard rate constant k^0 is interpreted as D/δ where D is the lithium ion diffusion coefficient and δ is the characteristic transport layer thickness, as described in previous work [4-6].

The current associated with lithium ion transport will be given by the product of the lithium ion conductivity, σ, and the potential gradient, $\Delta E/\delta$:

$$I = \sigma \frac{\Delta E}{\delta} \qquad \text{(Eq. D.8)}$$

The associated resistance, $R = \Delta E / I$, can therefore be written as a function of the lithium ion conductivity:

$$R = \frac{\Delta E}{I} = \frac{\delta}{\sigma} \qquad \text{(Eq. D.9)}$$

The lithium ion conductivity can be described by the Nernst-Einstein equation:

$$\sigma = \frac{DF^2 c}{RT} \qquad \text{(Eq. D.10)}$$

Thus, combining equations (D.5) and (D.6), the ion transfer resistance can be expressed as:

$$R = \frac{RT\delta}{DcF^2} \qquad \text{(Eq. D.11)}$$

As pointed out in previous studies [4-6], equation (D.11) is mathematically equivalent to equation (D.7), considering that $k^0 = D/\delta$.

Taking into account the Stokes-Einstein equation, the diffusion coefficient can be expressed as:

$$D = \frac{kT}{6\pi v r} \qquad \text{(Eq. D.12)}$$

where v is the viscosity and r is the hydrodynamic radius. Equation D.11 can then be rewritten as:

$$R = \frac{6\pi v r N_{av} \delta}{cF^2} \qquad \text{(Eq. D.9)}$$

where N_{av} is Avogadro's number.

Equation D.9 shows that an increase in the viscosity of the solution is expected to increase the ion transfer resistance. The rate of ion transport can also be complicated by other effects such as ion pairing. Consequently, the lithium ion conductivity, σ, might not be proportional to the lithium ion concentration, c. Instead, σ could scale with $c^{1/2}$ as a result of ion pair formation, or with $c^{3/2}$ as a result of triple ion pair formation [7-8], meaning the ion transfer resistance would scale with $c^{-1/2}$ or with $c^{-3/2}$ respectively. Moreover, in most situations, the conductivity is correlated with the viscosity, according to the fractional Walden rule:

$\Lambda \nu^{\gamma}$ = constant (Eq. D.10)

where Λ is the molar conductivity and the exponent γ varies between 0 and 1. According to equation D.9, this would mean the ion transfer resistance scales with ν^{γ}.

D.3 Impedance spectra of Ohara glass-ceramic membrane measured in 4-point impedance cell with different liquid electrolytes at different temperatures

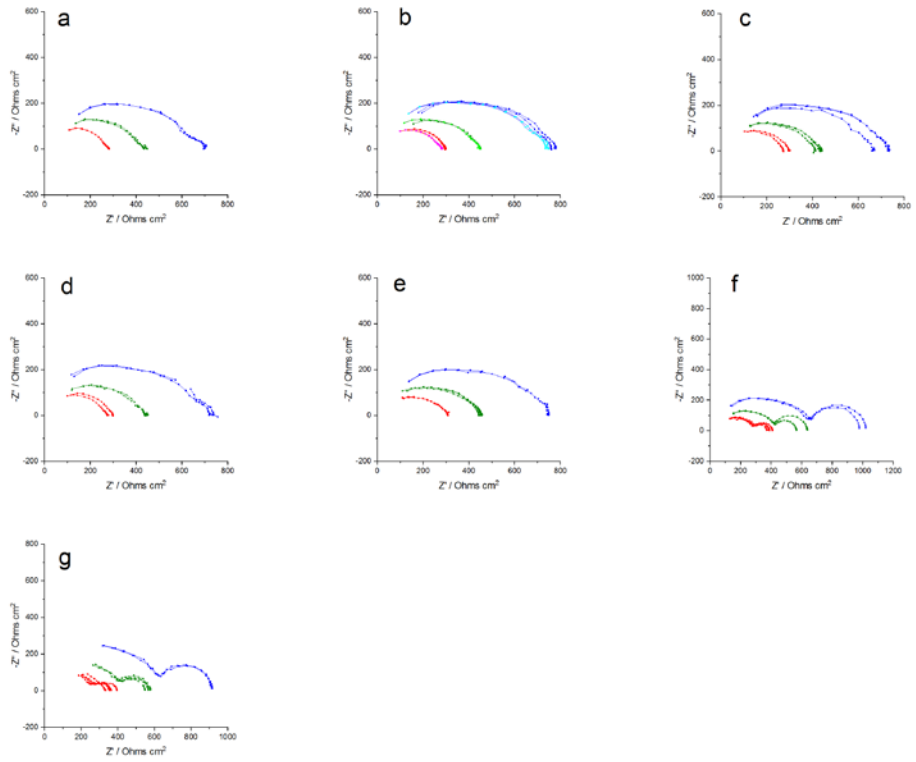

Fig D.1: Impedance spectra of Ohara glass-ceramic membrane measured in 4-point impedance cell at 25 °C (green), 14 °C (red/pink) and 34 °C (blue), with LiTFSI in DOL-DME ((a) 0.5 m, (b) 1 m, (c) 2 m, (d) 3 m); LP30 (e); or LiTFSI in DMSO ((f) 1 m, (g) 3 m). Spectra are net of bulk liquid electrolyte resistance. Multiple lines show multiple measurements over time at each temperature. In (b), lighter and darker coloured lines are from two separate cells. In (f) initial measurement at 25 °C was followed by two @ 14 °C, two @ 34 °C, one @ 25 °C. In (g) initial measurement at 25 °C was followed by two @ 14 °C, two @ 25 °C, two @ 34 °C, one @ 25 °C. 1 hour between each measurement in both cases.

D.4 Activation energies of lithium ion transfer at the solid/liquid electrolyte interface in DMSO

As discussed in Chapter 4, the spectra measured in DMSO-based electrolytes were very similar to those measured in the other electrolytes, except for an extra semicircle at low frequencies which in Chapter 4 was attributed to deposition of additional degradation products rather than to lithium ion desolvation. Further evidence for this is obtained by analysing the individual activation energies of the processes associated with each of the semicircles (Figure

D.2a). The activation energy of the first process (which we identified in Chapter 4 as ion transport through the membrane) is very similar in 1 molal and 3 molal electrolytes (375 meV and 379 meV respectively) and close to that obtained in the other electrolytes. The activation energy of the second process is also similar in 1 molal and 3 molal electrolytes (567 meV and 546 meV respectively). If this second process was lithium ion desolvation, then we would expect its activation energy to vary with lithium ion concentration as observed for ion transport in the bulk liquid electrolyte (Figure D.2b). Moreover the values of 567 and 546 meV are much larger than the activation energies found for the corresponding bulk liquid electrolytes (190 and 272 meV respectively), and more consistent with ion transport in a solid conductor [10-11].

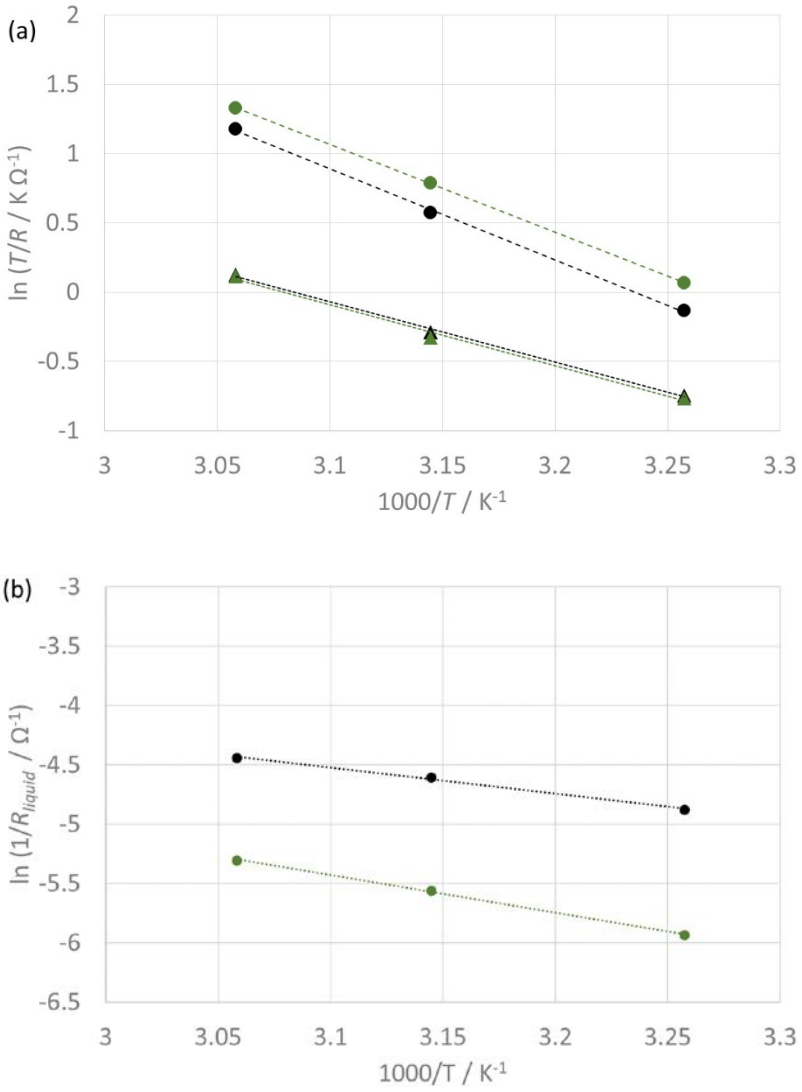

Fig D.2: Arrhenius plots of (a) resistance associated with the first semicircle (triangles) and second semicircle (circles) in impedance spectra measured in 4-probe cell containing Ohara membrane with 1 m (black), and 3 m (green) LiTFSI in DMSO, (b) bulk liquid electrolyte resistance of 1 m (black) and 3 m (green) LiTFSI in DMSO, measured using conductivity cell.

D.5 References

[1] Kobayashi, S.; Uchimoto, Y., Lithium Ion Phase-Transfer Reaction at the Interface between the Lithium Manganese Oxide Electrode and the Nonaqueous Electrolyte. *The Journal of Physical Chemistry B* **2005**, 109, 13322-13326.

[2] Nakayama, M.; Ikuta, H.; Uchimoto, Y.; Wakihara, M., Study on the AC Impedance Spectroscopy for the Li Insertion Reaction of $Li_xLa_{1/3}NbO_3$ at the Electrode−Electrolyte Interface. *The Journal of Physical Chemistry B* **2003**, 107, 10603-10607.

[3] Okumura, T.; Fukutsuka, T.; Matsumoto, K.; Orikasa, Y.; Arai, H.; Ogumi, Z.; Uchimoto, Y., Lithium-Ion Transfer Reaction at the Interface between Partially Fluorinated Insertion Electrodes and Electrolyte Solutions. *The Journal of Physical Chemistry C* **2011**, 115, 12990-12994.

[4] Kakiuchi, T., Current—potential characteristic of ion transfer across the interface between two immiscible electrolyte solutions based on the Nernst—Planck equation. *Journal of Electroanalytical Chemistry* **1992**, 322, 55-61.

[5] Kontturi, K.; Manzanares, J. A.; Murtomäki, L.; Schiffrin, D. J., Rate Constant for Ion Transfer in Inhomogeneous Media at the Interface of Immiscible Electrolytes. *The Journal of Physical Chemistry B* **1997**, 101, 10801-10806.

[6] Murtomäki, L.; Kontturi, K.; Schiffrin, D. J., Some remarks on the double layer correction to the kinetics of ion transfer at the interface of immiscible electrolytes. *Journal of Electroanalytical Chemistry* **1999**, 474, 89-93

[7] Fuoss, R. M.; Kraus, C. A., Properties of Electrolytic Solutions. IV. The Conductance Minimum and the Formation of Triple Ions Due to the Action of Coulomb Forces. *Journal of the American Chemical Society* **1933**, 55, 2387-2399.

[8] Raccichini, R.; Dibden, J. W.; Brew, A.; Owen, J. R.; García-Aráez, N., Ion Speciation and Transport Properties of LiTFSI in 1,3-Dioxolane Solutions: A Case Study for Li–S Battery Applications. *The Journal of Physical Chemistry B* **2018**, 122, 267-274.

[9] Angell, C. A.; Ansari, Y.; Zhao, Z., Ionic Liquids: Past, present and future. *Faraday Discussions* **2012**, 154, 9-27.

[10] Busche, M. R.; Drossel, T.; Leichtweiss, T.; Weber, D. A.; Falk, M.; Schneider, M.; Reich, M. L.; Sommer, H.; Adelhelm, P.; Janek, J., Dynamic formation of a solid-liquid electrolyte interphase and its consequences for hybrid-battery concepts. *Nature Chemistry* **2016**, 8, 426-34.

[11] Bachman, J. C., et al., Inorganic Solid-State Electrolytes for Lithium Batteries: Mechanisms and Properties Governing Ion Conduction. *Chemical Reviews* **2016**, 116, 140-62.

E Appendix E: Appendix to Chapter 5

E.1 Comparison of cyclic and pseudo-voltammograms of sulfur reduction

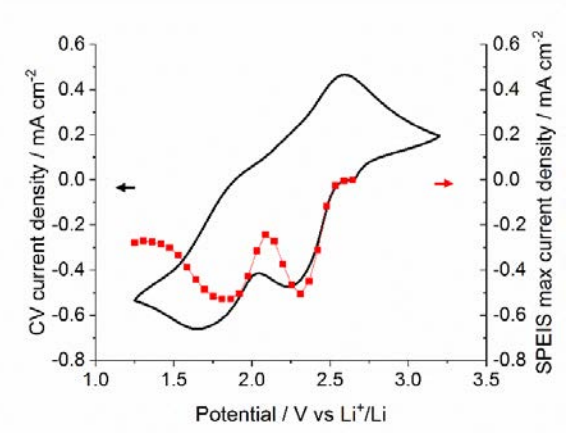

Figure E.1 – Comparison of the first-cycle cyclic voltammogram from Figure 4a (black) and the pseudo-voltammogram produced by the SPEIS current maxima in Figure 5a (red) in a cell with PEO-LiTFSI membrane.

E.2 Analysis of impedance spectra measured using SPEIS of sulfur reduction

E.2.1 Kramers-Kronig analysis

For a causal, stable, linear, time-invariant (stationary) system, whose impedance is finite when $\omega \to 0$ and $\omega \to \infty$, it is possible to determine the imaginary part of the impedance from the real part and vice versa using Kramer-Kronig (KK) transforms. Comparison of the calculated impedance Z_{KK} with the experimental impedance Z can then be used check the validity of the impedance measurement with respect to the conditions of applicability of KK transforms.[1,2] Figure E.2 compares the experimental and calculated impedance for selected cycles from Figure 5b in Chapter 5. It is observed that the calculate values deviate from the experimental ones at low frequencies. This can be explained by the non-stationarity of the system when the measurements were taken.

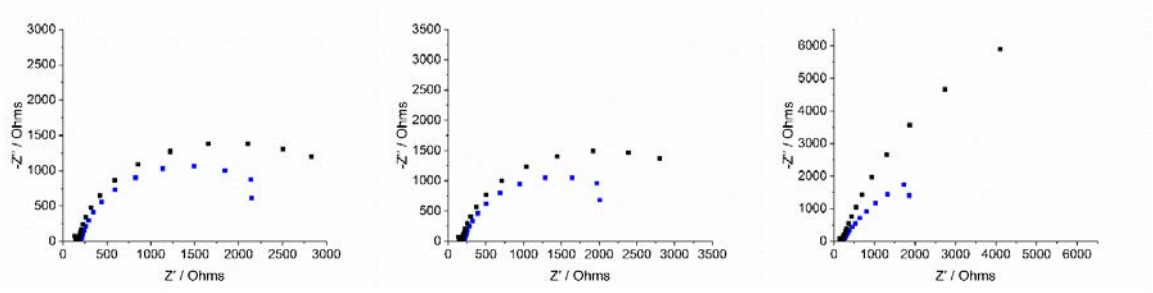

Figure E.2 – Experimental (black) and calculated (blue) impedance spectra for (left to right) steps 4, 12 and 20 from Figure 5.5b, corresponding to electrode potentials of 2.48 V, 2.03 V and 1.58 V vs. Li^+/Li.

E.2.2 Equivalent circuit model fitting

The impedance spectra in Figures 5.5b and 5.7b in Chapter 5 were fitted using the equivalent circuit model shown below, where R_m is the resistance of the polymer membrane, R_{ct} is the charge transfer resistance and CPE_{dl} is the double layer capacitance at the glassy carbon electrode. (Whilst the impedance spectra exhibit a truncated semi-circle at high frequencies, ascribable to the complex impedance behaviour of the membrane (associated with a parallel combination of capacitance and resistor components), those complications are not included in the model, which treats the membrane as a simple resistor.)

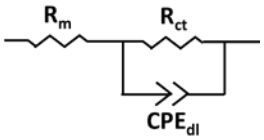

Figure E.3: Equivalent circuit model used to fit impedance spectra in Figures 5.5b and 5.7b

Note that in some cases, the semicircle ascribed to charge transfer in parallel with double layer capacitance appears to be drawn out along the Z' axis, with a slight upturn at low frequencies. This apparent behaviour could be the result of an increasing charge transfer resistance during the measurement [1], since the system was not at steady state. In such cases, low frequency data points were excluded from the model fit.

E.3 Effect on scan rate on cyclic voltammograms of polysulfides

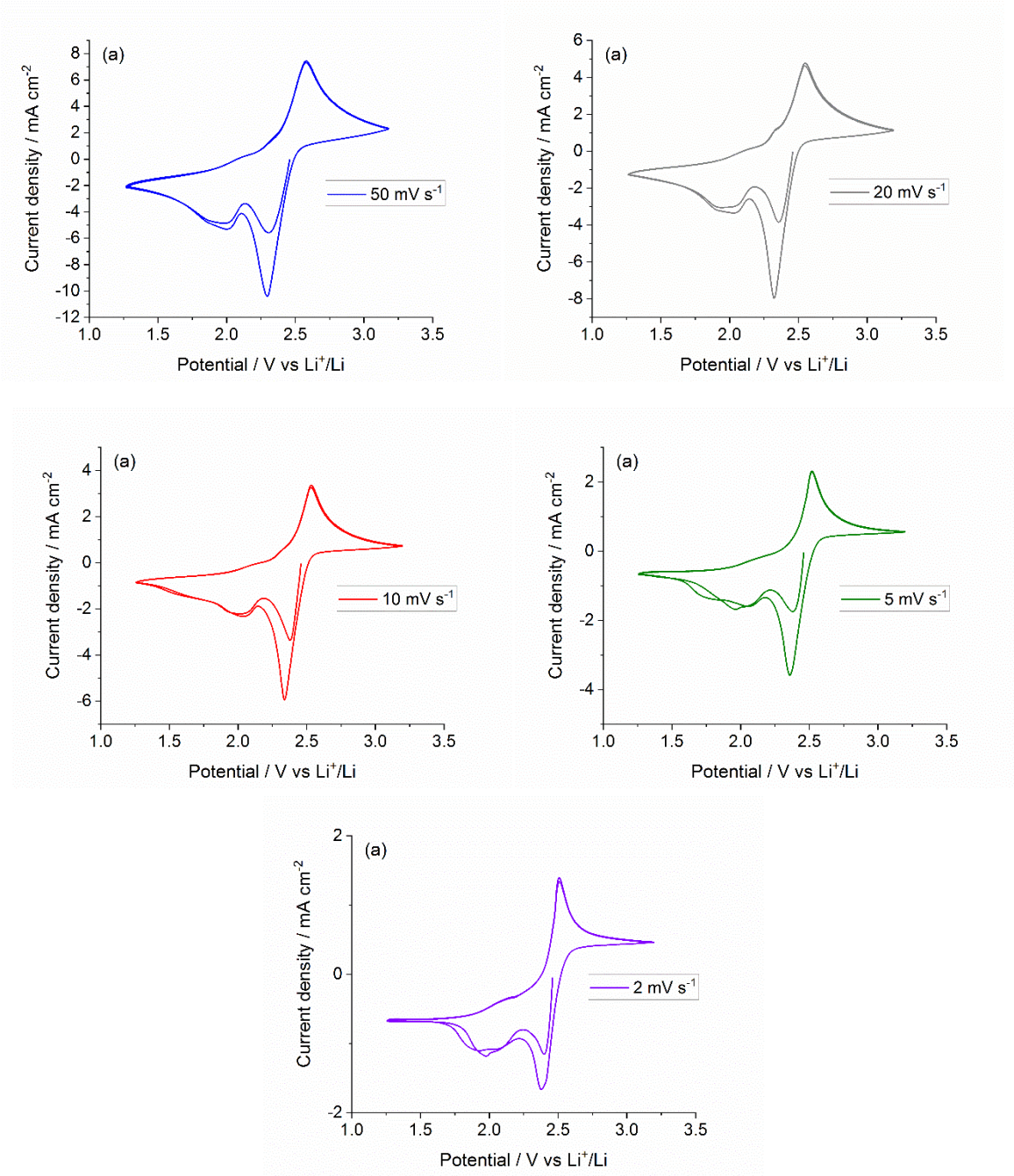

Figure E.4: Data re-plotted from Figure 5.15a, with a separate plot for each scan rate.

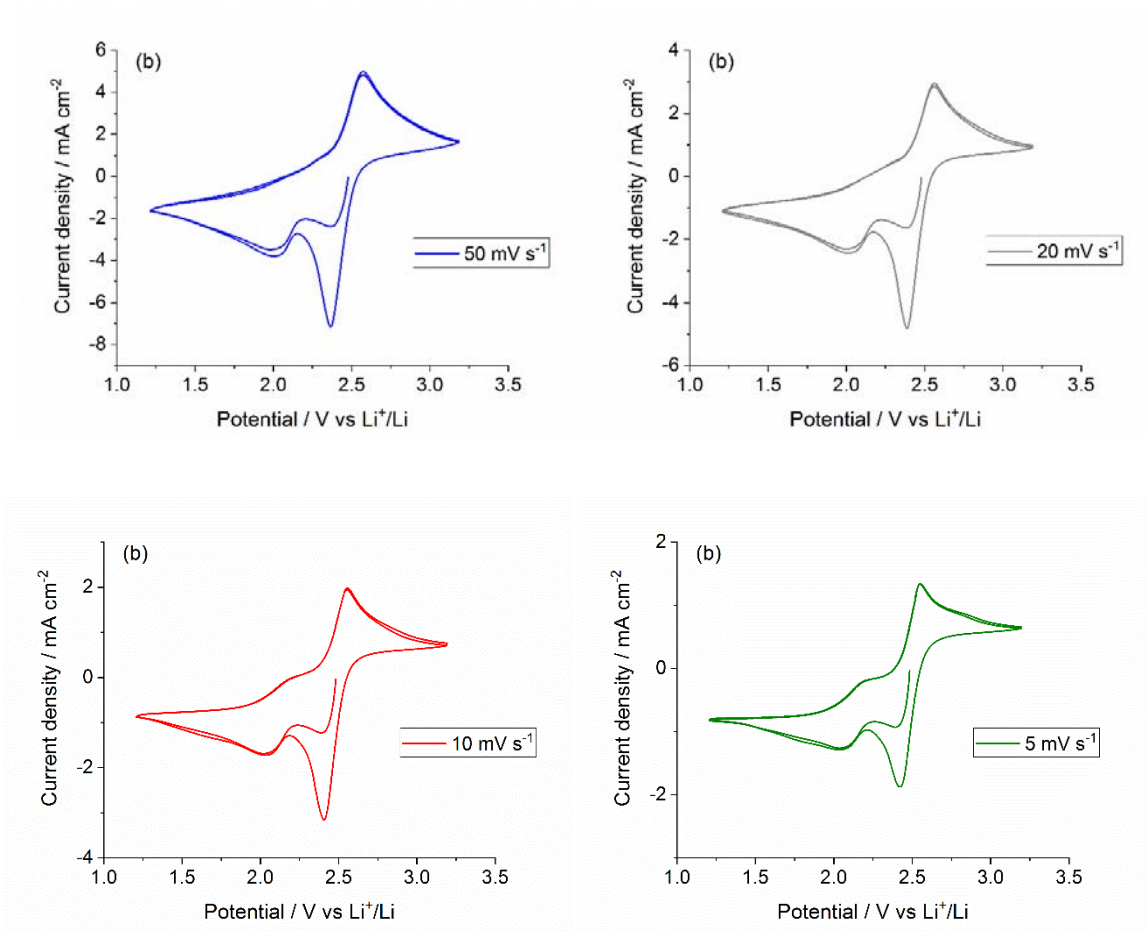

Figure E.5 – Data re-plotted from Figure 5.15b, with a separate plot for each scan rate.

E.4 References

[1] Lasia, A., Electrochemical Impedance Spectroscopy and Its Applications. In Modern Aspects of Electrochemistry, Conway, B. E.; Bockris, J.; White, R. E., Eds. Kluwer Academic/Plenum: New York, 1999; Vol. 32, pp 143-248.

[2] Application note #55. Interpretation problems of impedance measurements made on time variant systems. Downloaded from https://www.bio-logic.net/application-notes-2/ .

F Appendix F: Appendix to Chapter 6

F.1 Evaluating diffusion coefficient using chronopotentiometry – deviation from ideal Sand behaviour

As discussed in Chapter 6, deviations from ideal Sand behaviour were observed in the chronopotentiometric response of a cell with glassy carbon working electrode containing 2 mM EtV^{2+} under constant applied current (Figure 6.7 in Chapter 6). Such deviations are typical of double layer charging (see Appendix A.3), whose effects are illustrated in Figure A3.2 and can be represented using a dimensionless parameter, K:

$$K = \frac{RT}{nF}\frac{C_{dl}}{nFc_O^*\left(\pi D_O \tau\right)^{1/2}} \qquad \text{(Eq. F.1)}$$

Double layer capacitance, C_{dl}, can be estimated using cyclic voltammetry of a 'blank' electrolyte (no ethyl viologen present) at different scan rates (Figure F.1a). Since $i = dQ/dt = C_{dl}dV/dt$, C_{dl} is given directly by the gradient of a plot of current vs. scan rate. The average of the absolute 'anodic' and 'cathodic' currents (read at an arbitrary point along the x-axis = -0.7 V) are plotted vs. scan rate in Figure F.1b, giving a value for C_{dl} of 22 µF cm^{-2}.

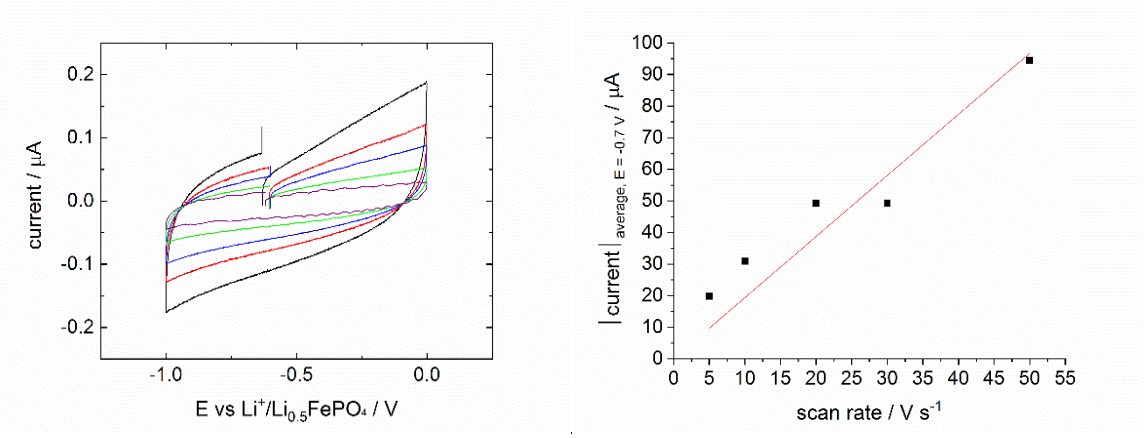

Figure F.2: (a) Cyclic voltammetry of 'blank' cell (no EtV(OTf)2 at scan rate of 50 mV s^{-1} (–), 30 mV s^{-1} (–), 20 mV s^{-1} (–), 10 mV s^{-1} (–), 5 mV s^{-1} (–); (b) Plot of average of 'cathodic' and 'anodic' current at -0.7 V, vs. scan rate; the intercept was set to zero for the data fitting.

We can now use this value of C_{dl} to estimate the dimensionless parameter K, using $D_{EtV^{2+}}$ determined previously using square wave voltammetry (see Chapter 2), on the grounds that SWV essentially eliminates double layer charging effects. For an applied current of 0.5 μA, this gives *K* = 0.00365, which roughly corresponds to line 3 in Figure A.2.2. This represents a fairly modest deviation from ideal Sand behaviour due to double layer charging (assuming that $i\tau = C_{dl,average}\Delta E$, where ΔE is the change from the initial potential to the potential when τ is measured, then our value of C_{dl} implies that the proportion of applied current going to the Faradaic process is ca. 90%). Referring again to Figure 6.7 in Chapter 6, there is a more pronounced deviation at the end of the curve that at the start, whereas in Figure A.2.2, the deviation is relatively symmetrical at either end of the curve. Possibly, then, the deviation at the end of the curve in Figure 6.4 is due to the onset of the next reduction reaction ($EtV^{+} \rightarrow EtV^{0}$) rather than to a strong contribution from double layer charging.

F.2 References

[1] A.J. Bard and L.R. Faulkner, Electrochemical Methods Fundamentals and Applications, John Wiley & Sons, New York, NY, USA, 2001.